BERGISCHE
UNIVERSITÄT
WUPPERTAL

Fakultät für Mathematik
und Naturwissenschaften

Search for Top Squarks in Compressed Scenarios of Supersymmetry with the ATLAS Experiment

Dissertation

Daniela Börner

Die Dissertation kann wie folgt zitiert werden:

urn:nbn:de:hbz:468-20180725-135946-6
[http://nbn-resolving.de/urn/resolver.pl?urn=urn%3Anbn%3Ade%3Ahbz%3A468-20180725-135946-6]

Referent:	Prof. Peter Mättig
Koreferent:	Prof. Tobias Golling
Koreferent:	Prof. Dan Tovey

Abgabe:	01.03.2018
Prüfungsdatum:	27.06.2018

Für Jan

Contents

I Introduction **1**

II The Theory of Particle Physics **7**

1 The Standard Model **9**
1.1 General Introduction . . . 9
1.2 Electroweak Theory . . . 11
1.3 The Higgs Mechanism . . . 12
1.4 Quantum Chromodynamics . . . 14
1.5 Experimental Success of the Standard Model . . . 16
1.6 Limitations of the Standard Model . . . 18

2 Supersymmetry **21**
2.1 Phenomenology of the MSSM . . . 22
2.1.1 Higgs Mass Corrections . . . 24
2.2 Supersymmetric Models . . . 25
2.2.1 Bino LSP . . . 27
2.2.2 Higgsino LSP . . . 28
2.2.3 Well-tempered Neutralino LSP . . . 29

3 Event Simulation **31**
3.1 Simulation of *pp* Collisions . . . 31
3.1.1 Factorisation Theorem . . . 32
3.1.2 Matrix Element . . . 33
3.1.3 Parton Shower . . . 33
3.1.4 Matching and Merging . . . 34
3.1.5 Hadronisation . . . 34
3.1.6 Underlying Event and Pile-Up . . . 35
3.2 ATLAS Detector Simulation . . . 35

4 Statistical Techniques **37**
4.1 Unfolding . . . 37
4.2 Hypothesis Testing and Profile Likelihood Fit . . . 39

4.3 Boosted Decision Trees . . . 41

III The ATLAS Experiment at the Large Hadron Collider 43

5 The Large Hadron Collider 45

6 The ATLAS Experiment 49
6.1 ATLAS Coordinate System . . . 50
6.2 Inner Detector . . . 51
6.3 Calorimeters . . . 52
6.4 Muon Spectrometer . . . 53
6.5 Magnets . . . 54
6.6 Luminosity Measurement . . . 54
6.7 Trigger System . . . 55
6.7.1 Minimum Bias Trigger . . . 55
6.8 Data Quality . . . 56

7 Event Reconstruction 57
7.1 Tracks and Primary Vertex . . . 57
7.2 Electrons . . . 59
7.3 Muons . . . 60
7.4 Jets . . . 61
7.5 Flavour Tagging . . . 64
7.6 Hadronically Decaying τ Leptons . . . 65
7.7 Missing Transverse Momentum . . . 66
7.8 Overlap Removal . . . 66

IV Charged-particle Measurements 69

8 Introduction 71

9 Event Selection 73
9.1 Data and Monte Carlo Samples . . . 73
9.2 Event Selection . . . 74
9.3 Background Estimation . . . 76
9.4 Trigger and Vertex Reconstruction Efficiency . . . 77
9.5 Track Reconstruction Efficiency . . . 79

10 Correction Procedure 81
10.1 Detailed Unfolding Procedure . . . 81
10.2 Closure Tests . . . 83
10.3 Systematic Uncertainties . . . 88

11 Results and Outlook 93
11.1 Results . . . 93
11.2 Summary and Comparison . . . 95

V Search for Supersymmetry **99**

12 Introduction **101**
12.1 Simplified Supersymmetric Model . . . 101
12.2 Basic Strategy . . . 102

13 Common Analysis Strategy **103**
13.1 Data and Simulated Samples . . . 103
13.2 Preselection . . . 105
13.3 Variables Separating between Signal and Background . . . 109
13.4 Systematic Uncertainties . . . 114
13.4.1 Experimental Systematic Uncertainties . . . 115
13.4.2 Theoretical Systematic Uncertainties . . . 115

14 Intermediate Top Squark Masses **117**
14.1 Optimisation Algorithm . . . 118
14.2 tN_med Signal Region . . . 119
14.3 Background Estimation . . . 124
14.3.1 Control Regions . . . 125
14.3.2 Validation Regions . . . 134
14.4 Impact of Systematic Uncertainties . . . 137
14.5 Results . . . 138
14.5.1 Combination . . . 140

15 Compressed Region **143**
15.1 Analysis Strategy . . . 143
15.2 Training of the BDT . . . 144
15.3 Background Estimation . . . 149
15.4 Validation . . . 152
15.4.1 Validation with 2L and 1L1τ Selections . . . 157
15.4.2 Summary of the BDT Validation . . . 159
15.5 Impact of Systematic Uncertainties . . . 159
15.6 Fit Setup . . . 161
15.7 Results . . . 165
15.7.1 Comparison to Similar Search Regions . . . 167
15.7.2 Low Mass BDT . . . 168

16 Comparison of the Full Result **171**

VI Conclusion **173**

Appendix **177**

A Monitoring for the IBL Detector **179**
A.1 Cross-talk Scan . . . 179
A.2 Quick Status – A Monitoring Tool . . . 180

B Charged-particle Measurements **183**
B.1 Closure Tests . . . 183
B.2 Comparison Including Strange Baryons . . . 187
B.3 Comparison with Other Generators . . . 188

C Search for Supersymmetry **189**
C.1 Preselection Plots for tN_med . . . 189
C.2 Control Region Plots for tN_med . . . 192
C.3 Validation Region Plots for tN_med . . . 197
C.4 Modelling in the tN_med Signal Region . . . 203
C.5 Combination of tN_med and the bCsoft Selections . . . 205
C.6 Preselection Plots for the Compressed Signal Region . . . 209
C.7 Validation Plots . . . 212
C.7.1 VR for Discovery Fit Setup . . . 212
C.7.2 Validation Plots for Low BDT Values . . . 214
C.7.3 Profile Plots . . . 222
C.7.4 Correlation Plots for BDT Input Variables . . . 224
C.8 JES Dependence of the BDT Fit . . . 228
C.9 Results for Low Mass BDT . . . 229

Bibliography **233**

Acknowledgements **243**

Introduction

Nothing in life is to be feared, it is only to be understood. Now is the time to understand more, so that we may fear less.

Marie Curie

Particle physics aims to describe and understand the properties and interactions of elementary particles. The theoretical basis of particle physics is combined in the Standard Model. Its predictions and implications are tested at the Large Hadron Collider at which the collisions of high energy protons are recorded by experiments. The latest confirmation of the Standard Model was the discovery of the Higgs boson in 2012, which was a milestone in high-energy physics. The Higgs discovery completes the Standard Model, but also opens further questions to the theory. Theoretical considerations motivate extensions of the theory, such as the susceptibility of the Higgs mass to radiative corrections which require finely tuned cancellation effects. Cosmological observations necessitate a large amount of non-luminous, so-called Dark Matter, which is not described by the Standard Model. At the Large Hadron Collider, dedicated searches for new particles are performed in order to find explanations for these effects.

The Large Hadron Collider was upgraded during a long shutdown before 2015. The centre-of-mass energy was increased to 13 TeV, which opened new possibilities for measurements and searches. At the same time, the experiments were improved to achieve a better precision. A measurement using low-momentum charged-particles as well as two searches for new particles predicted from Supersymmetry are discussed in this dissertation.

The measurement performed at the ATLAS experiment constrains inclusive QCD effects and forms the basis for the understanding of the detector response as well as the physics involved. Initially performed with charged-particles with a transverse momentum of 500 MeV, this so-called Minimum Bias measurement was then extended to even lower momentum of 100 MeV. This latter analysis is presented in this dissertation and can be used to constrain and improve QCD-inspired models. These models are used to describe the low energy effects of QCD, for which more accurate, perturbative calculations are impossible. The primary charged-particle multiplicity is compared between the measured data and various model predictions as function of the pseudorapidity η and the transverse momentum p_{T}. Furthermore, the primary charged-particle multiplicity and the mean transverse momentum are compared. The understanding of the measured data is crucial for simulating single pp interactions and the effects of simultaneous multiple pp interactions. The improved simulation is an important input for all further precision measurements and searches.

For the measurement, the observed data are corrected and unfolded in order to take any detector effects and inefficiencies into account. The unfolding procedure is tested and validated before its application to data. A challenging aspect of the measurement is the correct estimation of the associated uncertainties and the propagation through the unfolding procedure.

A possible extension of the Standard Model is Supersymmetry, which is an extension of the space-time symmetries and relates bosons and fermions. In the Minimal Supersymmetric Standard Model, each known particle is related to a new particle differing by a half-integer spin. The radiative corrections to the Higgs mass cancel when considering the contributions of both the particle and the superparticle. The lightest supersymmetric particle is also a viable candidate to explain Dark Matter.

In this dissertation, two searches for Supersymmetry are presented, both targeting a model with a top squark, which is the superpartner of the top quark. The top squark mass is assumed to be below 1 TeV. In the simplified model targeted by the analyses only the top squark and the neutralino as lightest supersymmetric particle are considered.

The first analysis concentrates on intermediate to high top squark masses with varying neutralino masses. Here, the top squark decays into a top quark and a neutralino. The pair production gives rise

to a final state similar to that of top quark pair production, but with additional missing transverse momentum, due to the undetectable neutralinos. The shape information of this missing transverse momentum is used to gain sensitivity to a broad range of signal masses.

In the second analysis, a compressed mass spectrum is assumed, considering only small mass differences between the top squark and its decay products. This creates a challenging final state, which is kinematically close to the Standard Model background dominated by top quark pair production. Models in which the top squark decays into a bottom quark, a W boson and a neutralino via an off-shell top quark are also considered. The separation between the signal and the Standard Model backgrounds is achieved by using a Boosted Decision Tree. This multivariate method also includes the correlation of different observables to build a strong classifier.

The data recorded by the ATLAS experiment in 2015 and 2016, resulting in an integrated luminosity of 36.1 fb^{-1}, are used for the searches. Using profile-likelihood estimates, sensitivity to the compressed scenario as well as to larger top squark masses is achieved. The normalisation of the dominant Standard Model backgrounds is simultaneously estimated based on dedicated control regions. The sensitivity to the general signature of a top quark pair and missing transverse momentum is used to constrain further, less simplified models of Supersymmetry.

Contributions

The author has contributed to the following publications by the ATLAS collaboration

- ATLAS Collaboration, *Search for top squarks in final states with one isolated lepton, jets, and missing transverse momentum in* $\sqrt{s}$ = 13 *TeV pp collisions with the ATLAS detector*, Phys. Rev. D **94**.5 (2016) p. 052009, arXiv: 1606.03903 [hep-ex]
- ATLAS Collaboration, *Charged-particle distributions in* $\sqrt{s}$ = 13 *TeV pp interactions measured with the ATLAS detector at the LHC*, Phys. Lett. B **758** (2016) p. 67, arXiv: 1602.01633 [hep-ex]
- ATLAS Collaboration, *Search for pair production of vector-like top quarks in events with one lepton, jets, and missing transverse momentum in* $\sqrt{s}$ = 13 *TeV pp collisions with the ATLAS detector*, JHEP **08** (2017) p. 052, arXiv: 1705.10751 [hep-ex]

The further contributions of the author to the following two publications are discussed in detail in this dissertation

- ATLAS Collaboration, *Charged-particle distributions at low transverse momentum in* $\sqrt{s}$ = 13 *TeV pp interactions measured with the ATLAS detector at the LHC*, Eur. Phys. J. C **76**.9 (2016) p. 502, arXiv: 1606.01133 [hep-ex]
- ATLAS Collaboration, *Search for top-squark pair production in final states with one lepton, jets, and missing transverse momentum using 36* fb^{-1} *of* $\sqrt{s}$ = 13 *TeV pp collision data with the ATLAS detector*, JHEP **06** (2018) p. 108, arXiv: 1711.11520 [hep-ex]

In addition, the author contributed to the development of the monitoring for the IBL detector (see Appendix A), as well as to performance studies of the tracking with the upgraded inner detector and the reduced representation of the ATLAS jet energy scale uncertainty, as documented in

- ATLAS Collaboration, *Track Reconstruction Performance of the ATLAS Inner Detector at* $\sqrt{s}$ = 13 *TeV*, ATL-PHYS-PUB-2015-018, 2015, URL: http://cds.cern.ch/record/2037683
- ATLAS Collaboration, *A method for the construction of strongly reduced representations of ATLAS experimental uncertainties and the application thereof to the jet energy scale*, ATL-PHYS-PUB-2015-014, 2015, URL: https://cds.cern.ch/record/2037436

The Theory of Particle Physics

The thing that doesn't fit is the thing that's the most interesting: the part that doesn't go according to what you expected.

Richard P. Feynman

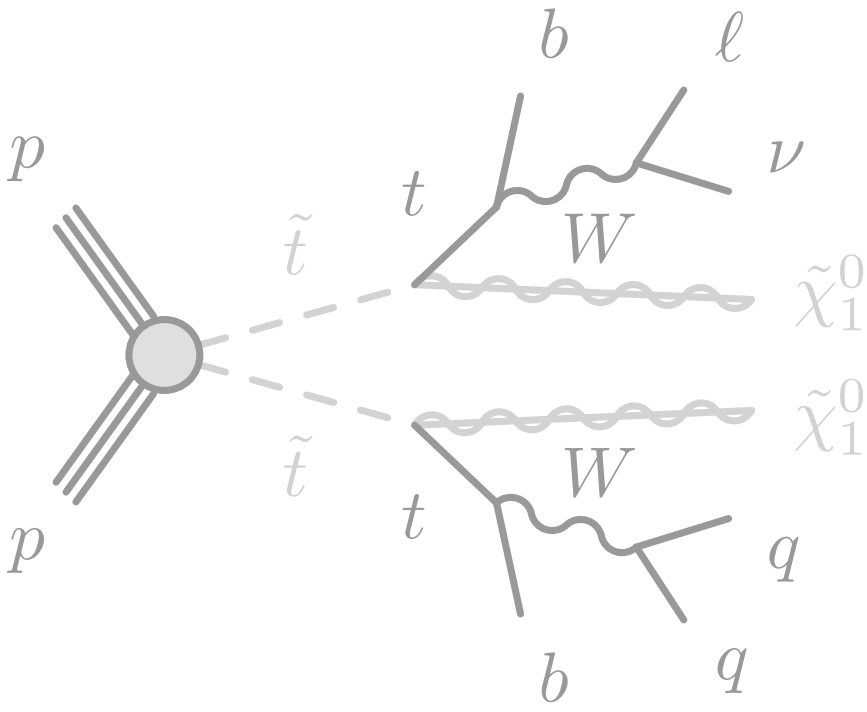

1 The Standard Model

The Standard Model of particle physics provides a precise description of the subatomic world. Since 1960, it has been developed and tested and various predictions have been confirmed [8–13]. The latest confirmation of the Standard Model was the discovery of the Higgs boson by the ATLAS and CMS collaborations [14, 15].

In this section, the Standard Model (SM) and the corresponding particles are introduced. The different components of the SM are shortly explained. In the end, the success, but also the limitations of this theory, are discussed.

1.1 General Introduction

The SM can be described using a renormalisable quantum field theory which is invariant under the following gauge group

$$SU(3)_{\mathrm{C}} \otimes SU(2)_{\mathrm{L}} \otimes U(1)_{\mathrm{Y}} \,, \tag{1.1}$$

where $SU(3)_{\mathrm{C}}$ is the symmetry group for the strong interaction and $SU(2)_{\mathrm{L}} \otimes U(1)_{\mathrm{Y}}$ is the symmetry group for the electroweak interaction.

In the theory, particles are described as fields, functions of space-time coordinates. Fermions are half-integer spin particles and build the matter in this theory, whereas bosons describe the exchange of force mediators as integer spin particles. Gravity and a possible graviton as force mediator are not included into the SM, as there is no known corresponding renormalisable quantum field theory.

The properties of the fermions and the gauge bosons are listed in Table 1.1 and 1.2, respectively. There are three generations of fermions which are copies with the same quantum numbers. Only the mass increases for the second and the third generation. The heavier generation quarks as well as the muon and the τ lepton can decay to the lighter SM particles, and thus the first generation is stable. Also, for each fermion a corresponding anti-particle is assigned, doubling the number of fermions in the SM. Anti-particles have the same mass as the particle, but opposite quantum numbers, for example electrical charge. In addition to the electrical charge, quarks carry one of three possible colour charges (usually called red, blue and green) or the corresponding anti-colour. Only colour-neutral combinations of particles, so-called hadrons, have been directly observed so far.

Table 1.1: Overview of the leptons and quarks in the Standard Model, with their electrical charges and masses [16]. The neutrino mass limit comes from the 95 % CL upper limit on the sum of all neutrino masses.

	Leptons			Quarks		
Generation	Name	Charge	Mass	Name	Charge	Mass
I	electron (e)	-1	511 keV	up (u)	$+2/3$	2.2 MeV
	e neutrino (ν_e)	0	< 0.23 eV	down (d)	$-1/3$	4.7 MeV
II	muon (μ)	-1	106 MeV	charm (c)	$+2/3$	1.28 GeV
	μ neutrino (ν_μ)	0	< 0.23 eV	strange (s)	$-1/3$	96 MeV
III	tau (τ)	-1	1.78 GeV	top (t)	$+2/3$	173.1 GeV
	τ neutrino (ν_τ)	0	< 0.23 eV	bottom (b)	$-1/3$	4.18 GeV

Table 1.2: Overview of the gauge bosons in the Standard Model, with their masses, interactions and electrical charges [16].

Particle	Mass	Interaction	Charge
photon (γ)	0 GeV	electromagnetic	0
gluon (g)	0 GeV	strong	0
W boson	80.39 GeV	weak	± 1
Z boson	91.19 GeV	weak	0

Interactions between the fundamental particles are mediated by gauge bosons. The electromagnetic interaction is mediated by the photon with the $U(1)_{\mathrm{EM}}$ symmetry group. The photon couples only to electrical charge and as it is not charged itself, no self-coupling is possible. Since the photon is a massless spin-1 particle, the range of the electromagnetic interaction is infinite. The symmetry group of the weak force is the $SU(2)_{\mathrm{L}}$ and is mediated by the $W^{\pm}$ and the Z bosons. It interacts via the weak isospin and is the only interaction in which neutrinos participate. The range of the weak interaction is small due to the mass of the corresponding gauge bosons. The strong force acts on the colour charge and thus influences only the quarks and the corresponding mediator, the gluon. The gluon is massless and electrically neutral, but has eight different colour states.

The full SM Lagrangian can be split into two terms

$$\mathcal{L}_{\mathrm{SM}} = \mathcal{L}_{\mathrm{EW}} + \mathcal{L}_{\mathrm{QCD}} \,. \tag{1.2}$$

The theory for the electroweak force and the one for quantum chromodynamics (QCD) are described separately below.

1.2 Electroweak Theory

The electroweak theory describes the weak and the electromagnetic interaction with the $SU(2)_\mathrm{L} \otimes U(1)_\mathrm{Y}$ symmetry group. Fermions can be expressed as spin-$1/2$ Dirac field with the Lagrangian

$$\mathcal{L} = \bar{\psi}(i\gamma^\mu \partial_\mu - m)\psi \tag{1.3}$$

with the fermion field ψ, the Dirac matrices γ^μ and the fermion mass m. The Lagrangian should be invariant under local gauge transformations and for this purpose gauge fields are introduced.

The symmetry group of the weak interaction is the $SU(2)_\mathrm{L}$ group with a new quantum number T. The generators of this group are the weak isospin operators $\hat{T}_i = \sigma_i/2$ ($i = 1, 2, 3$) with the Pauli matrices σ_i. Neutrinos and up-type quarks carry a weak isospin of $T_3 = 1/2$ while the charged leptons and down-type quarks have an isospin of $T_3 = -1/2$.

The left- and right-handed components of a fermion field ψ are defined as

$$\psi_{\mathrm{L,R}} = \frac{1}{2}(1 \mp \gamma^5)\psi \ . \tag{1.4}$$

They transform differently under the operators of the weak symmetry group as the left-handed component transforms as doublet, while the right-handed transforms as singlet. This describes the parity violating nature of the weak interaction.

$$f_\mathrm{L}^i = \begin{pmatrix} \nu_\mathrm{L}^i \\ \ell_\mathrm{L}^i \end{pmatrix}, \begin{pmatrix} u_\mathrm{L}^i \\ d_\mathrm{L}^i \end{pmatrix}, \tag{1.5}$$

$$f_\mathrm{R}^i = \ell_\mathrm{R}^i, u_\mathrm{R}^i, d_\mathrm{R}^i \ , \tag{1.6}$$

where u stands for up-like and d for down-like quarks, l stands for a charged lepton and ν for a neutrino. The three families are considered using $i = 1, 2, 3$. The index L for $SU(2)_\mathrm{L}$ is assigned as only left-handed fermions interact through the weak force.

For the symmetry group $U(1)_\mathrm{Y}$, the hypercharge Y is introduced as a new quantum number. The hypercharge, the electrical charge and the third component of the weak isospin T_3 can be related using the Gell-Mann Nishijima relation

$$\hat{Q} = \hat{T}_3 + \hat{Y} \ . \tag{1.7}$$

In order to assure the local invariance under the gauge group, the covariant derivative from Equation 1.3 can be written as

$$D_\mu = \partial_\mu - igT_i W_\mu^i - ig'YB_\mu \ , \tag{1.8}$$

where g and g' are the coupling constants for the $SU(2)_\mathrm{L}$ and $U(1)_\mathrm{Y}$ group respectively. The gauge fields of the symmetry groups are therefore the W_μ^i and B_μ.

A kinetic term for the gauge fields has to be added to the Lagrangian

$$\mathcal{L}_{\text{gauge}} = -\frac{1}{4} W^i_{\mu\nu} W_i^{\mu\nu} - \frac{1}{4} B_{\mu\nu} B^{\mu\nu} \,, \tag{1.9}$$

with $i = 1, 2, 3$ and the field tensors defined as

$$W^i_{\mu\nu} = \partial_\mu W^i_\nu - \partial_\nu W^i_\mu + g\epsilon^{ijk} W^j_\mu W^k_\nu \,, \tag{1.10}$$

$$B_{\mu\nu} = \partial_\mu B_\nu - \partial_\nu B_\mu \,, \tag{1.11}$$

with the Levi-Civita tensor ϵ^{ijk}. The field tensors can be translated into the known gauge bosons using the following relations

$$W^\pm_\mu = \frac{1}{\sqrt{2}} (W^1_\mu \mp i W^2_\mu) \,, \tag{1.12}$$

$$\begin{pmatrix} Z_\mu \\ A_\mu \end{pmatrix} = \begin{pmatrix} \cos\theta_W & -\sin\theta_W \\ \sin\theta_W & \cos\theta_W \end{pmatrix} \begin{pmatrix} W^3_\mu \\ B_\mu \end{pmatrix} \,. \tag{1.13}$$

The angle θ_W is the weak mixing angle and A stands for the photon field. Considering Equation 1.8, the W_μ field tensors couple only to the left-handed components, while the B_μ couples only to the right-handed components. The W^3 boson describes the interaction between only up- or only down-type particles, where the combination of $W^{1,2}$ known as $W^\pm$ allows flavour-changing interactions. The Levi-Civita tensor leads to the non-Abelian nature of the weak interaction as it allows the self-coupling of the W^i tensors.

The final electroweak Lagrangian can be written as

$$\mathcal{L}_{\text{EW}} = \sum_{f=l,q} \bar{f} i\gamma^\mu D_\mu f + \mathcal{L}_{\text{gauge}} \,. \tag{1.14}$$

In this Lagrangian, no mass terms for the fermions or the gauge fields are included. Adding any mass term would break the local $SU(2)_{\text{L}} \otimes U(1)_{\text{Y}}$ invariance and thus the full SM theory would not be renormalisable anymore. Therefore another mechanism is needed to introduce the measured non-zero masses for fermions and bosons (see Table 1.1 and 1.2).

1.3 The Higgs Mechanism

Massive particles can be introduced without breaking the gauge invariance with a Spontaneous Symmetry Breaking mechanism. The $SU(2)_{\text{L}} \otimes U(1)_{\text{Y}}$ symmetry group can be reduced to the $U(1)_{\text{EM}}$ group at low energies. For this, a new isospin doublet of complex scalar fields is introduced

$$\Phi = \begin{pmatrix} \phi^+ \\ \phi^0 \end{pmatrix} \,. \tag{1.15}$$

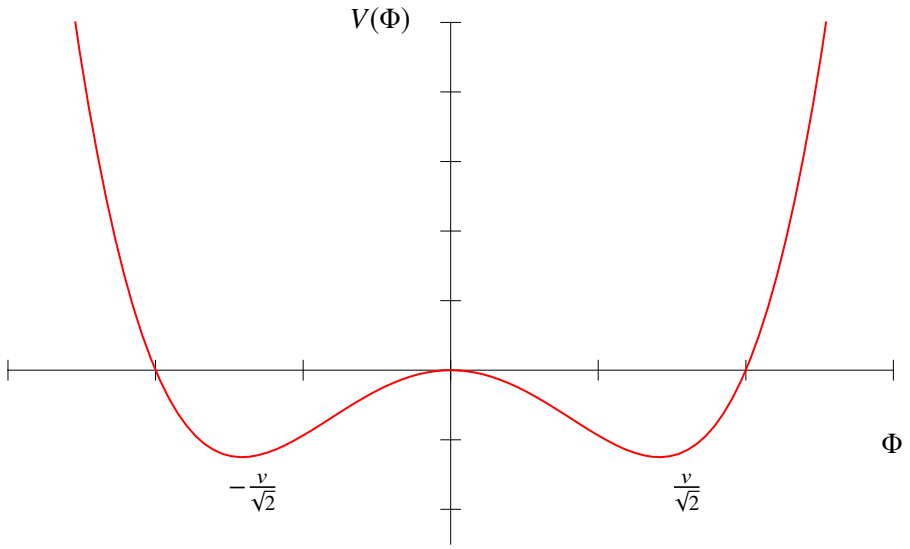

Figure 1.1: Sketch of the "mexican hat" Higgs potential in one dimension.

The indices indicate the electrical charge of the fields. The kinetic and potential terms for this new field are added to the Lagrangian

$$\mathcal{L}_\Phi = (D_\mu \Phi)^\dagger (D^\mu \Phi) - V(\Phi)\,, \tag{1.16}$$

$$V(\Phi) = \mu^2 \Phi^\dagger \Phi + \lambda (\Phi^\dagger \Phi)^2\,. \tag{1.17}$$

The Lagrangian depends on μ^2 and λ. The case for $\lambda < 0$ is unphysical and leads to non-stable maxima, thus λ is larger than 0. In the case of $\mu^2 > 0$, a single minimum at $|\Phi| = 0$ is expected with a vacuum expectation value (VEV) of $\langle\Phi\rangle_0 = \langle 0|\Phi|0\rangle = 0$. Therefore the interesting part is the case with $\mu^2 < 0$, where the minimum of the potential is at

$$\Phi^\dagger \Phi = -\frac{\mu^2}{2\lambda} = \frac{v^2}{2} \tag{1.18}$$

with a non-zero VEV of $\langle\Phi\rangle_0 = v/\sqrt{2}$. There is no unique minimum and the potential of the field has the typical Mexican hat structure as illustrated in Figure 1.1. As this VEV is not invariant under the symmetry group of $SU(2)_\mathrm{L} \otimes U(1)_\mathrm{Y}$, the symmetry is broken spontaneously.

The Goldstone theorem [17, 18] declares that a broken symmetry always results in massless scalars, referred to as Goldstone bosons. These can be absorbed by a gauge field as the longitudinal polarisation component and the gauge field acquires mass. The minimum of the potential is chosen such that the neutral Higgs field acquires a VEV

$$\Phi_0 = \frac{1}{\sqrt{2}} \begin{pmatrix} 0 \\ v \end{pmatrix}\,. \tag{1.19}$$

When expanding the theory around the true minimum with $H(x)$ as a ground state fluctuation, the complex field Φ changes to

$$\Phi(x) = \frac{1}{\sqrt{2}} \begin{pmatrix} 0 \\ v + H(x) \end{pmatrix}\,. \tag{1.20}$$

The field $H(x)$ does describe a massive, scalar boson. The Higgs can couple to the fermions and the corresponding interaction is added to the Lagrangian

$$\mathcal{L}_Y = \sum_{f=l,q} y_f \left[\bar{f}_\mathrm{L} \Phi f_\mathrm{R} + \bar{f}_\mathrm{R} \bar{\Phi} f_\mathrm{L} \right] , \tag{1.21}$$

with the Yukawa matrices y_f describing the coupling between the Higgs doublet and fermions. This Lagrangian is gauge-invariant as both summands are $SU(2)_\mathrm{L}$ singlets.

Combining the expansion of the theory around the true minimum with the Lagrangian gives the tree level prediction for the masses of the fermions

$$m_f = y_f \frac{v}{\sqrt{2}} , \tag{1.22}$$

where f stands for the different fermions. The flavour eigenstates of the quarks do not correspond directly to their mass eigenstates, but they are linear combinations of those. The combination factors are given by the unitary Cabibbo-Kobayashi-Maskawa (CKM) matrix.

The tree level mass of the Higgs boson can be calculated from Equation 1.16 and calculates to

$$m_H = \sqrt{-2\mu^2} = \sqrt{2\lambda} v . \tag{1.23}$$

The parameter λ is not predicted by the SM, and therefore also the Higgs mass is not predicted by the theory and an experimental determination is needed.

The gauge boson masses can be calculated from the first term of Equation 1.16 evaluated at the VEV

$$\Delta\mathcal{L} = \frac{1}{2}\frac{v^2}{4} \left[g^2 (W_\mu^1)^2 + g^2 (W_\mu^2)^2 + (-g W_\mu^3 + g' B_\mu)^2 \right] . \tag{1.24}$$

With the previous introduced relation between the gauge fields and the gauge bosons, the masses result to

$$m_W = \frac{vg}{2} , \tag{1.25}$$

$$m_Z = v \frac{\sqrt{g^2 + g'^2}}{2} , \tag{1.26}$$

$$m_\gamma = 0 . \tag{1.27}$$

1.4 Quantum Chromodynamics

The symmetry group for Quantum Chromodynamics (QCD) is the $SU(3)_\mathrm{C}$ group. As a new quantum number, colour is introduced where quarks can have three different states.

The local gauge symmetry is introduced with the covariant derivative

$$D_\mu = \partial_\mu - i g_s T^a G_\mu^a , \tag{1.28}$$

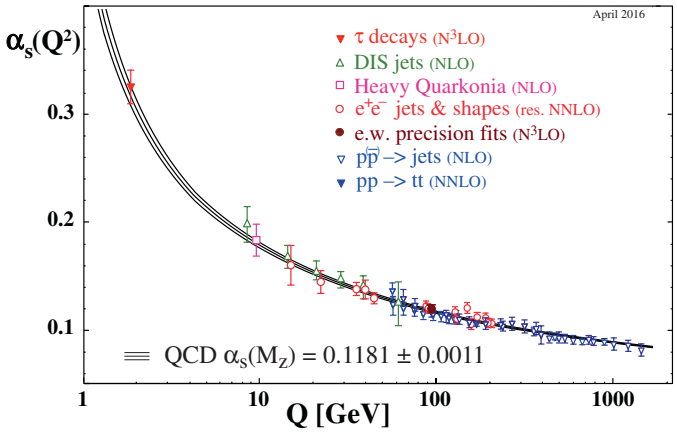

Figure 1.2: Measurements of α_s as a function of the energy scale Q [16].

where g_s is the coupling strength of the strong interaction and is commonly given as $\alpha_s = g_s^2/4\pi$. The $SU(3)_C$ generators are T_a, where $a = 1, ..., 8$ and G_μ are the gluon fields.

The QCD Lagrangian can be written as

$$\mathcal{L}_{\text{QCD}} = \bar{q}(i\gamma^\mu D_\mu)q - \frac{1}{4}G^a_{\mu\nu}G^{a\mu\nu}\,, \tag{1.29}$$

with the Dirac matrices γ^μ, and the vector q with three components corresponding to the different colours of a given quark type. Gluons transform under the adjoint representation and quarks transform under the fundamental representation of the $SU(3)_C$ group. The interaction between the quarks and gluons is described with the covariant derivative with the field tensor defined as

$$G^a_{\mu\nu} = \partial_\mu G^a_\nu - \partial_\nu G^a_\mu - g_s f^{abc} G^b_\mu G^c_\nu\,. \tag{1.30}$$

The structure constant f_{abc} is responsible for the non-Abelian structure of QCD as it describes the self-interaction between gluons. This self-interaction creates an energy scale dependence of the strong coupling constant which can be described at leading order as

$$\alpha_s(Q^2) = \frac{12\pi}{(33 - 2n_f)\cdot \log\left(\frac{Q^2}{\Lambda^2_{\text{QCD}}}\right)} \tag{1.31}$$

with the number of active flavour quarks n_f, that is the number of quarks with $m_q < Q$. The infrared cut-off scale Λ_{QCD} gives the scale where the perturbative approximation becomes incorrect due to the size of α_s.

In the high energy regime, α_s becomes small and the perturbation theory is valid and the theory has predictive power. In the case of $Q^2 \to \infty$, the coupling nearly vanishes and the quarks are quasi free. This is called *asymptotic freedom*. At low energies, the coupling increases up to infinity and the quarks and gluons are not free. This effect is known as *confinement*. When partons with colour charge start to separate, the potential energy increases due to the strong coupling. At some point, it is preferable to create a new quark-anti-quark pair. Therefore coloured partons show up as collimated streams of hadrons, referred to as jets in experiments. The coupling α_s was measured at various energy scales Q and the described dependence was verified, as can be seen in Figure 1.2.

1.5 Experimental Success of the Standard Model

The SM theory has evolved over time, e.g. more particles have been predicted and searched for in various experiments. In addition, the precision of the measurements has increased in order to measure several particle properties as their mass, spin and their production rate.

The charm quark was predicted by the SM in order to explain the absence of flavour-changing neutral currents. It was discovered at SLAC [19] and the MIT [20]. A natural mechanism for CP violation [21] can be explained with a third family of fermions which was confirmed with the discovery of the τ lepton [22] and the bottom quark [23]. Furthermore, the W and Z boson were predicted and discovered at CERN [24], as well as the top quark at Tevatron [25, 26]. The latest discovery has been the Higgs boson at CERN [14, 15].

Precision measurements are used to check the consistency of the SM theory in more detail where only few results are shown below. An electroweak fit is performed in order to validate that all

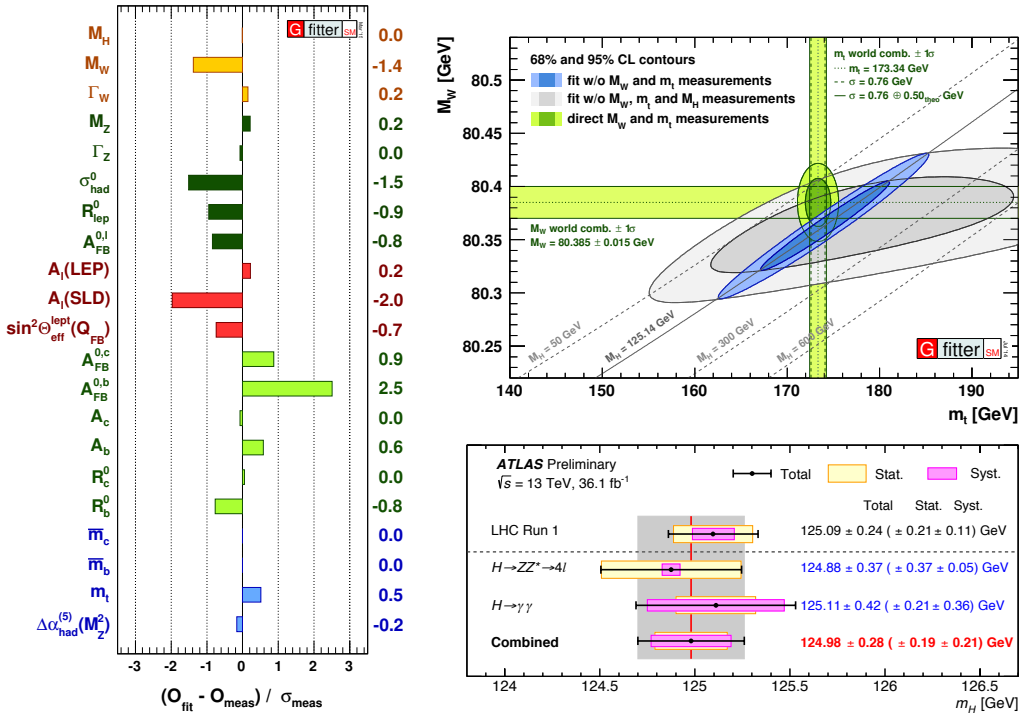

Figure 1.3: Comparing the fit results with direct measurements, i.e. deviations between experimental measurements and theoretical calculations in units of the experimental uncertainty (left) [27].
Contours of 68% and 95% confidence level obtained from scans for the W boson and top quark masses. The blue and larger grey areas are the allowed regions of the fit including and excluding the Higgs boson mass measurement respectively (top right) [27].
Summary of the Higgs boson mass measurements from individual and combined analyses (bottom right). The red vertical line and corresponding grey shaded column indicate the central value and the total uncertainty of the combined measurement (bottom right) [28].

measured quantities agree with the prediction from the SM theory. In Figure 1.3 on the left-hand side, the results of this fit are shown [27]. The deviations between the experimental measurement and the theoretical calculations are smaller than three standard deviations for all quantities.

Radiative corrections can influence masses of particle predictions, even if they are not directly involved in the process. The top quark and W boson masses are compared between direct mass measurements and electroweak precision measurements when including and excluding the Higgs boson mass into the fit. The result is shown in Figure 1.3 on the top right-hand side. The direct and indirect measurements agree and confirm the theory describing these radiative corrections.

The Higgs boson mass is measured for different production and decay modes. The combined Run 1 result, as well as the individual results from the $H \rightarrow ZZ^* \rightarrow 4\ell$ and $H \rightarrow \gamma\gamma$ analyses are shown in Figure 1.3 on the bottom right. In addition, the combined mass is shown. A great success of the SM is the possibility to measure the Higgs boson, and beside the mass, the couplings and cross-sections are also measured.

The cross-section is measured precisely for various production modes as shown in Figure 1.4. The results are shown for the ATLAS measurements from different years compared to the theory prediction. Overall, a good agreement between the measurement and the prediction can be seen for several orders of magnitudes in the cross-section.

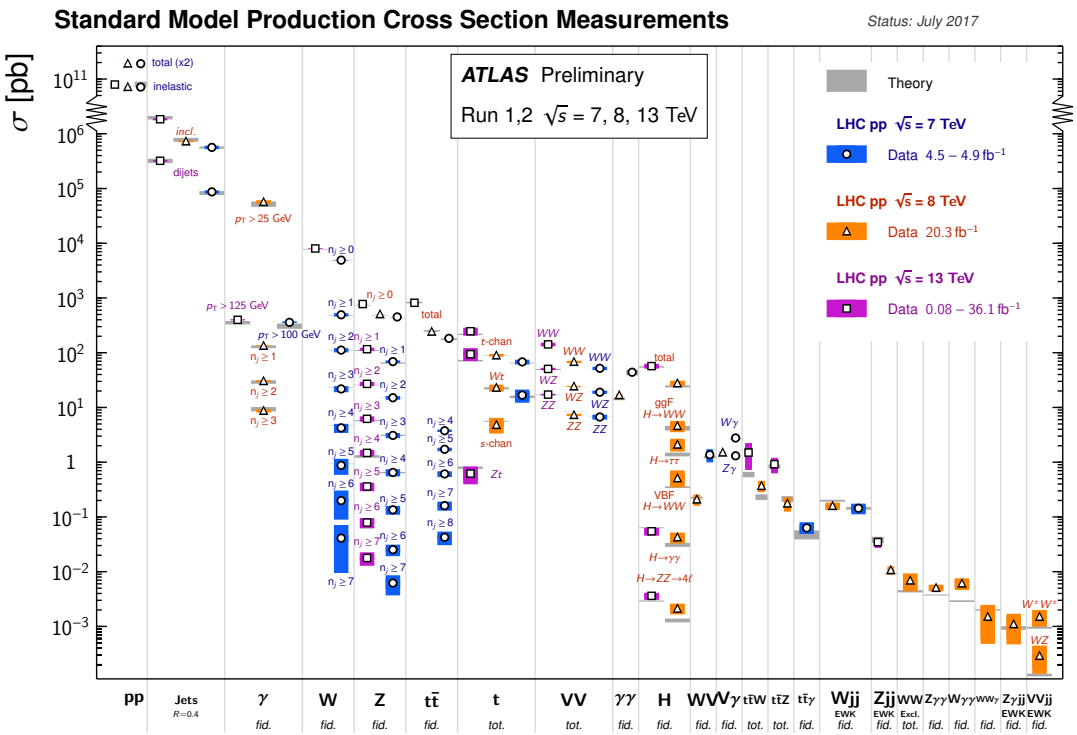

Figure 1.4: Summary of several SM production cross-section measurements, corrected for leptonic branching ratios and compared to the corresponding theoretical expectations. The theoretical expectations are calculated at NLO or higher and their uncertainties are taken from the original measurement [29].

1.6 Limitations of the Standard Model

The SM was tested precisely and a good agreement was observed. Nonetheless, there are observations which can not be explained by the SM theory. And thus a more general, but so far unknown, theory is needed in order to explain the problems and limitations which are not predicted and explained by the SM:

- Neutrino oscillations: The neutrino masses are not measured precisely, but from oscillation measurements [30] a mass difference between the neutrinos is required. The SM does not introduce any mass term, but a full valid theory needs to include those masses.
- Gravity: The effects of gravity and a possible force particle are not included in the SM, but would be needed for a general theory.
- Matter-anti-matter asymmetry: The asymmetry between the amount of matter and anti-matter can be partially explained by CP-violation. But this effect is not large enough to produce the large asymmetry observed.
- Naturalness: The SM has several free parameters. In some cases, e.g. the fermion masses, the value of the parameters range from 1 MeV up to 173 GeV. This is not an immediate problem, but seen as unnatural, as there is no direct explanation for the range of the parameters.

These are smaller problems of the SM theory, but there are also two more crucial problems. First, measurements of rotation curves and observation of gravitational lensing show the existence of non-luminous matter in the Universe, so-called *Dark Matter*. With cosmic microwave background measurements, the amount of Dark Matter was determined to be five times larger than the ordinary matter [31]. So far, none of the SM particles can explain the origin of this Dark Matter and thus theories are developed providing particles to explain the existence of Dark Matter.

Another relevant problem is the so-called *hierarchy problem*. The weak and the Planck scale (10^{19} GeV) differ, which is part of the naturalness problem. The problem occurs as the Higgs boson field is very sensitive to any theory beyond the Standard Model (BSM). The Higgs boson is not protected against radiative corrections by any chiral or gauge symmetry, and the mass can be expressed as

$$m_H^2 = (m_H)_0^2 + \Delta m_H^2 \tag{1.32}$$

with the bare mass $(m_H)_0$ and the Higgs boson mass correction Δm_H^2. The correction for e.g. a fermion loop as illustrated in Figure 1.5 calculates to

$$\Delta m_H^2 = -\frac{|y_f|^2}{16\pi^2}\left[2\Lambda^2 + O\left(m_f^2 \ln\left(\frac{\Lambda}{m_f}\right)\right)\right] \tag{1.33}$$

leading to quadratic divergences [32]. The Yukawa coupling y_f is proportional to the fermion mass and therefore the largest correction to the Higgs boson mass is due to the top quark as heaviest particle of the SM

$$y_t = \frac{\sqrt{2}m_t}{v} = 0.996 \pm 0.005\ . \tag{1.34}$$

The cutoff scale Λ is the energy scale at which new physics enter and the SM is not valid. The correction term for gauge bosons is similar to the one for fermions.

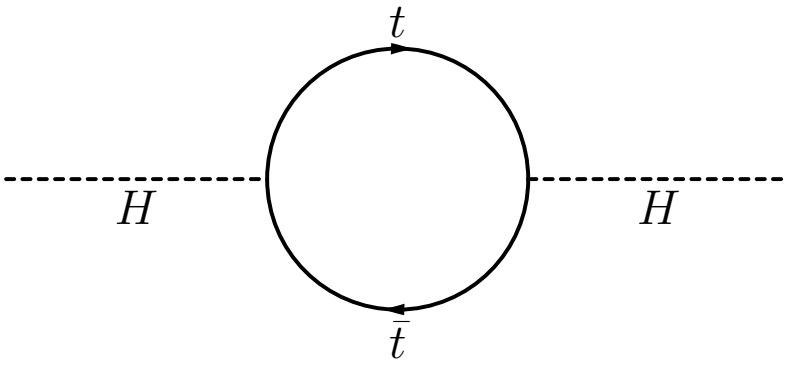

Figure 1.5: One-loop correction for the Higgs mass with top quarks in the loop.

If the SM theory as known today were valid up to the Planck scale, the corrections to the Higgs mass squared would be 30 orders larger than the measured mass squared. Following Equation 1.32, the bare Higgs mass and the corrections need to cancel exactly over 16 order of magnitude which leads to the so-called *fine-tuning* problem. Therefore new physics models with light particles ($\lesssim$ 1 TeV) are motivated in order to explain the Higgs mass at the electroweak scale.

2 Supersymmetry

Supersymmetry (SUSY) is a possible extension of the SM which can explain the hierarchy problem and predict possible Dark Matter candidates. The Minimal Supersymmetric Standard Model (MSSM) is the SUSY model, which adds the smallest amount of new particles. A detailed review can be found in [32].

SUSY is a symmetry relating fermions and bosons with an anti-commuting operator Q

$$Q\,|\text{fermion}\rangle = |\text{boson}\rangle\ ,\quad Q\,|\text{boson}\rangle = |\text{fermion}\rangle\ . \tag{2.1}$$

The operator Q and the hermitian conjugate $Q^\dagger$ are both fermionic operators and carry spin angular momentum $1/2$. SUSY is the only viable generalisation of the Lorentz symmetry as spacetime symmetry [33, 34]. For realistic theories, the generators Q and $Q^\dagger$ have to satisfy the commutation relations as

$$\{Q,\ Q^\dagger\} = P^\mu\,, \tag{2.2}$$

$$\{Q,\ Q\} = \{Q^\dagger,\ Q^\dagger\} = 0\,, \tag{2.3}$$

$$[P^\mu,\ Q] = [P^\mu,\ Q^\dagger] = 0\,, \tag{2.4}$$

with P^μ as the four-momentum generator of spacetime translations. The single particle states are called supermultiplets, each supermultiplet contains both fermionic and bosonic states which are the superpartner of each other. The squared mass operator P^2 commutes with the operators Q and $Q^\dagger$, and the spacetime rotation and translation operators, and therefore particles from the same multiplet have equal masses. Furthermore, the generators of gauge transformation commute with Q and $Q^\dagger$ and thus particles from the same multiplet are in the same representation of the gauge group, resulting into same electrical charges, weak isospin and colour degrees of freedom. The relation

$$n_B = n_F \tag{2.5}$$

follows taking into account the completeness relation and the commutation algebra. This means that the number of bosonic and fermionic degrees of freedom have to be the same. This can be achieved with *chiral* or *gauge* supermultiplets, which are the two irreducible multiplets of Supersymmetry. The chiral supermultiplets consist of a spin-$1/2$ fermion with two helicity states and a complex scalar field. A gauge multiplet consists of a massless spin-1 boson and a massless spin-$1/2$ fermion, both with two helicity states.

The vector bosons of the SM are associated with their fermionic superpartners, the *gauginos*, into gauge supermultiplets. The superpartners of the $W^\pm$, W^3 and B are called *winos* and *binos*. All

Table 2.1: Gauge supermultiplets in the MSSM.

Names	Spin 1/2	Spin 1	$SU(3)_C,\ SU(2)_L,\ U(1)_Y$
Gluino, gluon	$\tilde{g}$	g	8, 1, 0
Winos, W bosons	$\widetilde{W}^{\pm},\ \widetilde{W}^3$	$W^{\pm},\ W^3$	1, 3, 0
Bino, B boson	$\widetilde{B}$	B	1, 1, 0

Table 2.2: Chiral supermultiplets in the MSSM.

Names	Spin 0	Spin 1/2	$SU(3)_C,\ SU(2)_L,\ U(1)_Y$
Squarks, quarks	$(\tilde{u}_L\ \ \tilde{d}_L)$	$(u_L\ \ d_L)$	$3,\ 2,\ 1/6$
(×3 families)	$\tilde{u}_R^*$	$u_R^\dagger$	$\bar{3},\ 1,\ -2/3$
	$\tilde{d}_R^*$	$d_R^\dagger$	$\bar{3},\ 1,\ 1/3$
Sleptons, leptons	$(\tilde{\nu}\ \ \tilde{e}_L)$	$(\nu\ \ e_L)$	$1,\ 2,\ -1/2$
(×3 families)	$\tilde{e}_R^*$	$e_R^\dagger$	1, 1, 1
Higgs, higgsinos	$(H_u^+\ \ H_u^0)$	$(\tilde{H}_u^+\ \ \tilde{H}_u^0)$	$1,\ 2,\ 1/2$
	$(H_d^0\ \ H_d^-)$	$(\tilde{H}_d^0\ \ \tilde{H}_d^-)$	$1,\ 2,\ -1/2$

gauge supermultiplets are summarised in Table 2.1 and the chiral supermultiplets are summarised in Table 2.2. The SM fermions are in chiral supermultiplets in order to keep the different couplings for the left- and right-handed particles. The partners of the quarks and leptons are called *squarks* and *sleptons*, respectively. The Higgs boson as a scalar has the Higgsino as its superpartner with spin 1/2 and is also a chiral supermultiplet. In order to avoid any gauge anomaly, two Higgs supermultiplets (H_u and H_d) are defined. The scalar fields then mix and form mass eigenstates, of which the lightest corresponds to the Standard Model Higgs boson.

The masses of the SM particles and their superpartners cannot be equal, as no superpartners have been found so far. This means that SUSY is broken at some scale. Most models assume a *soft* SUSY breaking by introducing mass terms and coupling parameters with only positive mass dimension. This retains dimensionless couplings in the theory. SUSY breaking is assumed to be spontaneous, and is usually parametrised as additional terms in the effective Lagrangian density which do not depend on a specific model. These parameters are gaugino and scalar mass terms, as well as coupling parameters for three-scalar interactions.

2.1 Phenomenology of the MSSM

The Minimal Supersymmetric Standard Model contains the minimal set of supermultiplets extending the SM. In general 105 independent, free parameters are included in addition to the 19 SM parameters. These parameters are mostly part of the later introduced SUSY breaking terms of the Lagrangian

and can be expressed as masses, mixing angles and phases. Precision measurements can be used to strongly constrain the parameters.

The Higgs fields H_u^0 and H_d^0 acquire vacuum expectation values due to the electroweak symmetry breaking in the MSSM which add up to the SM value, $v^2 = v_u^2 + v_d^2$. Usually their ratio $\tan\beta = {}^{v_u}/_{v_d}$ is used. This ratio, the higgsino mass parameter μ, and the gaugino mass parameters M_1, M_2 and M_3 are not constrained by any precision measurements.

As in the SM, the MSSM parameters are energy dependent. Due to additional particles, the evolution of the coupling constants changes. Figure 2.1 shows the energy dependence of the inverse coupling constants. In the MSSM, the couplings unify at a scale of 1.5×10^{16} GeV.

The soft SUSY breaking Lagrangian can include baryon and lepton number violating terms which would lead to possible proton decays. This is incompatible with experimental results where the proton lifetime is measured at 90% confidence level to $\tau > 1.6 \times 10^{34}$ years for the decay $p \to e^+\pi^0$ [35]. An additional symmetry is introduced, as part of the MSSM, in order to include the suppression of the proton decay. The so-called R-parity is a multiplicative, conserved quantum number defined as

$$P_R = (-1)^{3(\mathrm{B}-\mathrm{L})+2s} \tag{2.6}$$

with the baryon (B) and lepton (L) number of the particle and its spin s.

R-parity is a discrete symmetry and commutes with the SUSY generator Q. All SM particles and the additional Higgs bosons have $P_R = +1$, while the supersymmetric particles have $P_R = -1$. Therefore, sparticles can only be produced as pairs and the *lightest supersymmetric particle* (LSP) has to be stable as it cannot exclusively decay into SM particles. It is usually assumed to be only weakly interacting and is thus a possible Dark Matter particle candidate.

In the MSSM, the Higgs sector is defined including four complex fields resulting into eight scalar degrees of freedom. Three of these become the longitudinal modes of the massive, weak bosons after electroweak symmetry breaking. The remaining five fields mix into five different mass eigenstates: two CP-even neutral scalar bosons h^0 and H^0, one CP-odd neutral scalar A^0, and two charged

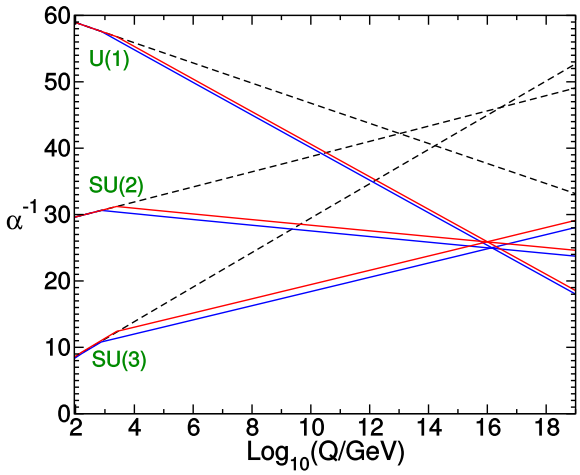

Figure 2.1: Two-loop renormalisation group evolution of the inverse of the gauge couplings $\alpha(Q)$ in the SM (dashed lines) and the MSSM with some sparticle mass variations applied (solid lines) [32].

scalars $H^{\pm}$. The mixing angle and the vacuum expectation ratio $\tan\beta$ relate the gauge eigenstates. At tree-level, the mass of the lightest scalar boson is bound by the mass of Z boson

$$m_{h^0} < m_Z \cdot |\cos(2\beta)| \,. \tag{2.7}$$

This bound is changed by radiative corrections as the previously discussed correction from e.g. top quark loops. The upper bound results to $m_{h^0} \lesssim 135\,\text{GeV}$ and agrees well with the observed mass of 125 GeV [14, 15].

The effects of the electroweak symmetry breaking lead to a mixing of the electroweak gauginos and the higgsinos. The charged mass eigenstates are called *charginos* $\tilde{\chi}_i^{\pm}$ (with $i = 1, 2$) and are the mixtures of $\widetilde{H}^{\pm}$ and $\widetilde{W}^{\pm}$. The four neutral mass eigenstates are referred to as *neutralinos* $\tilde{\chi}_i^0$ (with $i = 1 - 4$) and are the mixtures of $\widetilde{H}_u^0$, $\widetilde{H}_d^0$, $\widetilde{B}$ and $\widetilde{W}^3$. The neutralino masses depend on the parameters M_1, M_2, μ, the gauge couplings g and g', as well as the vacuum expectation values v_u and v_d. The mixing matrix is

$$\begin{pmatrix} \tilde{\chi}_1^0 \\ \tilde{\chi}_2^0 \\ \tilde{\chi}_3^0 \\ \tilde{\chi}_4^0 \end{pmatrix} = \begin{pmatrix} M_1 & 0 & -g'v_d/\sqrt{2} & g'v_u/\sqrt{2} \\ 0 & M_2 & gv_d/\sqrt{2} & -gv_u/\sqrt{2} \\ -g'v_d/\sqrt{2} & gv_d/\sqrt{2} & 0 & -\mu \\ g'v_u/\sqrt{2} & -gv_u/\sqrt{2} & -\mu & 0 \end{pmatrix} \begin{pmatrix} \widetilde{B} \\ \widetilde{W}^3 \\ \widetilde{H}_d^0 \\ \widetilde{H}_u^0 \end{pmatrix} . \tag{2.8}$$

Only small mixing effects are expected for the neutralinos and charginos, assuming $m_Z \ll |\mu|, M_1, M_2$. Therefore almost pure mass eigenstates are expected. Many models predict that the lightest neutralino state is mostly bino like. The masses of the lightest and the second lightest neutralino can be related as $M_2 = 2 \times M_1$ when considering models with a unification of the gauge couplings. The mass of the lightest chargino is expected to be similar to the mass of the second lightest neutralino as they are both wino states.

The left- and right-handed up-type and down-type squarks can mix and form mass eigenstates. The handedness of a squark refers to that of its fermionic partner. The mixing of the first and second generation is small due to the small Yukawa coupling. Due to the larger Yukawa coupling, third generation squarks can have different masses.

The mixing of the top squark can be expressed with the mixing angle $\theta_{\tilde{t}}$

$$\begin{pmatrix} \tilde{t}_1 \\ \tilde{t}_2 \end{pmatrix} = \begin{pmatrix} \cos\theta_{\tilde{t}} & -\sin\theta_{\tilde{t}} \\ \sin\theta_{\tilde{t}} & \cos\theta_{\tilde{t}} \end{pmatrix} \begin{pmatrix} \tilde{t}_\text{L} \\ \tilde{t}_\text{R} \end{pmatrix} \tag{2.9}$$

with the two mass eigenstates $\tilde{t}_1$ and $\tilde{t}_2$ with $m_{\tilde{t}_1} < m_{\tilde{t}_2}$. Due to constraints from the Higgs measurement, a large mixing for top squarks is needed. The lighter mass eigenstate is mainly composed of the right-handed top squark in many models. The top squarks are usually expected to be lighter than the other squarks due to renormalisation group effects.

2.1.1 Higgs Mass Corrections

For unbroken Supersymmetry, any fermionic or bosonic contributions to the radiative scalar mass corrections cancel exactly to any order. In case that SUSY is broken, the Higgs mass correction due

to a boson loop is

$$\Delta m_H^2 = \frac{|y_S|^2}{16\pi^2}\left[2\Lambda^2 + O\left(m_S^2 \ln\left(\frac{\Lambda}{m_S}\right)\right)\right], \tag{2.10}$$

with y_S as the corresponding Yukawa coupling. This is shown in Figure 2.2 for a top squark loop. Assuming that the Yukawa coupling for the fermion and the bosonic superpartner is equal ($y_f = y_S$), the residual mass correction for the Higgs boson calculates to

$$\Delta m_H^2 = \frac{|y_f|^2}{16\pi^2}\left|m_S^2 - m_f^2\right| \ln\left(\frac{\Lambda}{m_S}\right) \tag{2.11}$$

and depends only on the mass difference between the particle and the superparticle and does not result in the quadratic corrections known from the hierarchy problem. In soft SUSY breaking models, the relation of the coupling parameters is not modified by the breaking mechanism, and they remain exactly equal. Arguing with the naturalness problem, this suggests to have light superparticles even when SUSY is broken.

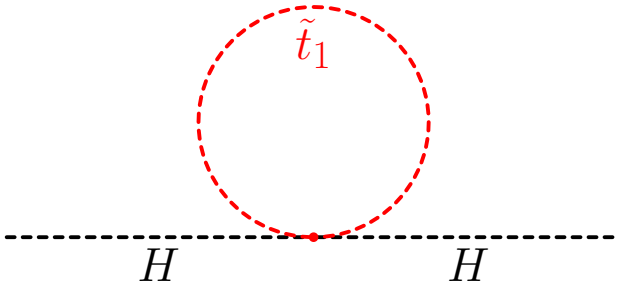

Figure 2.2: One-loop correction for the Higgs mass with a top squark loop.

2.2 Supersymmetric Models

The MSSM introduces 105 additional parameters to the SM. A reduced dependence on the models is achieved by targeting simplified models [36, 37], in which only a few supersymmetric particles are assumed to be accessible, while all others are decoupled. As the mass difference between the top squark and the top quark contributes to the residual fine-tuning, a large effort is put into searches for light top squarks.

Different models are considered for this dissertation and details of those are given below. The phenomenology and search strategy depend strongly on the composition of the lightest supersymmetric particles considered. The three models considered either have a bino LSP, a higgsino LSP or a bino-higgsino mixture. The masses of the SUSY particles strongly affect the phenomenology and are varied in order to search for a broad spectrum. For this dissertation, the models considered have the same general signature, leading to $t\bar{t} + E_{\mathrm{T}}^{\mathrm{miss}}$ in the final state.

The top squark pair is produced in leading order from an initial qq or gg state for all models considered as shown in Figure 2.3. The production cross-section for the bino LSP model is shown in Figure 2.4 in dependence of the top squark mass. The cross-section is calculated at next-to-leading order (NLO) accuracy, including the resummation of soft gluon emission at next-to-leading logarithmic accuracy (NLL) [38].

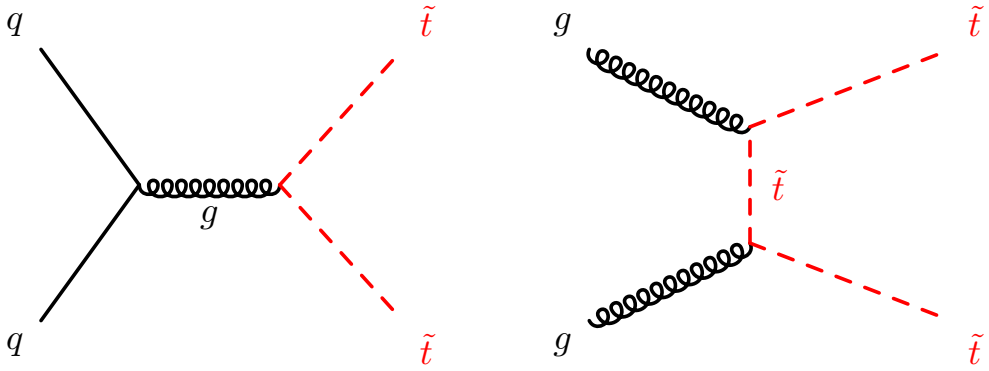

Figure 2.3: Feynman diagrams as example of the production of a top squark pair with an initial qq (left) or gg (right) state.

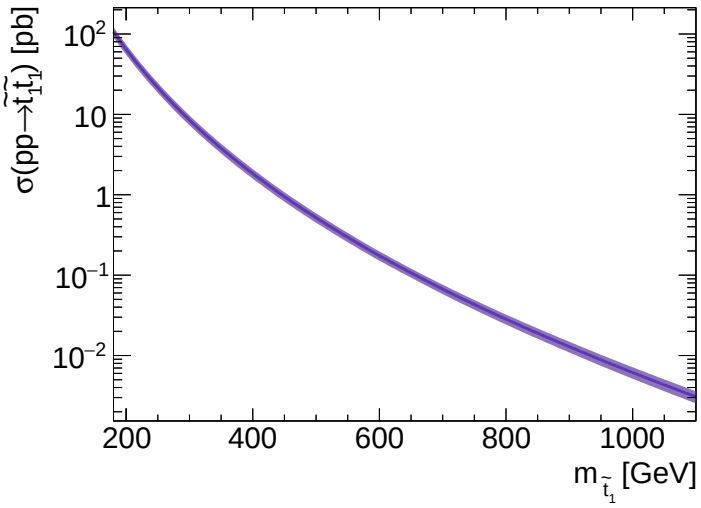

Figure 2.4: Production cross-section for top squark pair production in dependence of the top squark mass at NLO+NLL accuracy [38]. The width of the line gives the uncertainty due to scale and PDF choices.

2.2.1 Bino LSP

The first model is a simplified model where all sparticles are decoupled, and thus the masses of all sparticles are set to high values except the ones involved in the decay chain. The only light sparticles are the top squark and the lightest neutralino. As the chirality of the top squark affects the kinematic, the light top squark is chosen to be mostly right-handed (70%), corresponding to a mixing angle of $\theta_{\tilde{t}} = 56°$. The neutralino mixes such that it is mostly bino like.

The possible top squark decays are

$$\tilde{t}_1 \rightarrow t\tilde{\chi}_1^0 \qquad \text{for } m_{\tilde{t}_1} > m_t + m_{\tilde{\chi}_1^0}, \tag{2.12}$$

$$\tilde{t}_1 \rightarrow bW\tilde{\chi}_1^0 \qquad \text{for } m_{\tilde{t}_1} > m_W + m_{\tilde{\chi}_1^0}, \tag{2.13}$$

$$\tilde{t}_1 \rightarrow bff'\tilde{\chi}_1^0 \qquad \text{else.} \tag{2.14}$$

The top squark decays with a branching ratio of 100% to a top quark and the neutralino. Given that the coupling depends on the hypercharge, it is favoured even when other weak decay modes would exists, due to the large hypercharge for the right-handed top squark. This two-body decay is possible as long as the top squark mass is larger than the sum of the top quark and the neutralino mass. For this scenario intermediate to high top squark masses are analysed for varying neutralino masses. The decay is illustrated in Figure 2.5 on the left-hand side.

If the previously discussed decay is kinematically forbidden, the top squark decays into a bottom quark, W boson and the neutralino via an off-shell top quark (three-body decay) as illustrated in Figure 2.5. When $m_{\tilde{t}_1} \simeq m_{\tilde{\chi}_1^0} + m_t$, the signature and event kinematics become very similar for top squark pair production and the main SM background, $t\bar{t}$ production. This region is referred to as *diagonal region*. The dedicated analysis targeting this compressed area on the two- and three-body decay side is detailed in this dissertation.

When the three-body decay is also kinematically forbidden, the top squark decays via a four-body decay with two distinct fermions or via flavour-changing neutral currents in the loop-suppressed decay $\tilde{t}_1 \rightarrow c\tilde{\chi}_1^0$. In this dissertation, the four-body decay is not further studied.

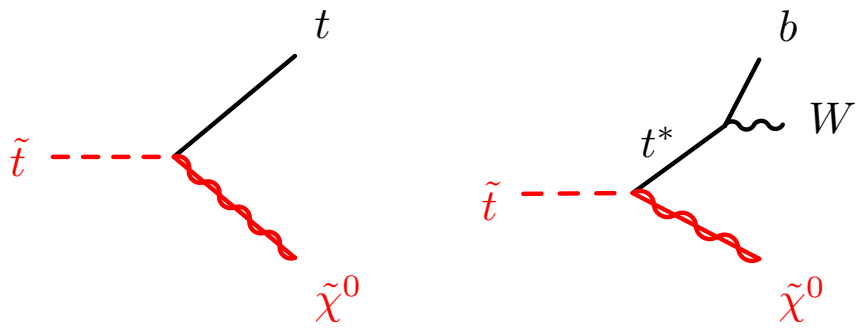

Figure 2.5: Decay modes of a top squark via direct decay into a top quark and a neutralino (tN, left) and via a three-body decay (bWN, right) with an off-shell top quark into a b quark, a W boson and a neutralino.

An alternative model additionally contains a wino as the next-lightest supersymmetric particle (NLSP). For mostly left-handed top squarks, the decay $\tilde{t}_1 \rightarrow b + \tilde{\chi}_1^{\pm}$ is favoured. The mass of the wino NLSP is set to twice that of the bino, inspired by models of gauge coupling unification. An interpretation of this model is performed in the publication in which the analyses discussed here are part of [5].

2.2.2 Higgsino LSP

Naturalness arguments suggest light higgsinos [39]. As a further model, thus a higgsino LSP is assumed, implicating light states for the $\tilde{\chi}_1^0$, $\tilde{\chi}_2^0$ and the $\tilde{\chi}_1^{\pm}$. The top squark is still assumed to be light, but with a larger mass than the neutralinos and charginos, and thus the top squark can decay into all of these sparticles.

$$\tilde{t}_1 \rightarrow b\tilde{\chi}_1^{\pm},\ t\tilde{\chi}_{1,2}^0 \tag{2.15}$$

$$\tilde{\chi}_1^{\pm} \rightarrow W^*\tilde{\chi}_1^0 \tag{2.16}$$

$$\tilde{\chi}_2^0 \rightarrow Z^*/h^*\tilde{\chi}_1^0 \tag{2.17}$$

The $\tilde{\chi}_1^{\pm}$ and $\tilde{\chi}_2^0$ decay through the emission of an off-shell W, Z or h boson. The decays are illustrated in Figure 2.6.

Typically, a small mass splitting between the chargino and the neutralino from a few hundred MeV to several GeV is assumed. In the model considered, mass differences of

$$\Delta m(\tilde{\chi}_1^{\pm}, \tilde{\chi}_1^0) = 0.5 \cdot \Delta m(\tilde{\chi}_2^0, \tilde{\chi}_1^0) < 30\,\text{GeV} \tag{2.18}$$

are taken into account. The decay branching ratio depends in general on the left- and right-handed composition of the top squark. The decay into a bottom quark and a chargino is preferred for the mostly right-handed top squarks. In case of left-handed top squarks, the decay into a top quark and a neutralino is favoured. In this dissertation, three different higgsino LSP models are considered using different branching ratios as listed in Table 2.3.

Table 2.3: Decay branching ratios of the three higgsino LSP models.

Model	$\mathcal{B}(\tilde{t}_1 \rightarrow t + \tilde{\chi}_2^0)$	$\mathcal{B}(\tilde{t}_1 \rightarrow b + \tilde{\chi}_1^{\pm})$	$\mathcal{B}(\tilde{t}_1 \rightarrow t + \tilde{\chi}_1^0)$
$\tilde{t}_1 \sim \tilde{t}_R$	25%	50%	25%
$\tilde{t}_1 \sim \tilde{t}_L$	45%	10%	45%
$\tilde{t}_1 \sim \tilde{t}_L$, large $\tan\beta$	33%	33%	33%

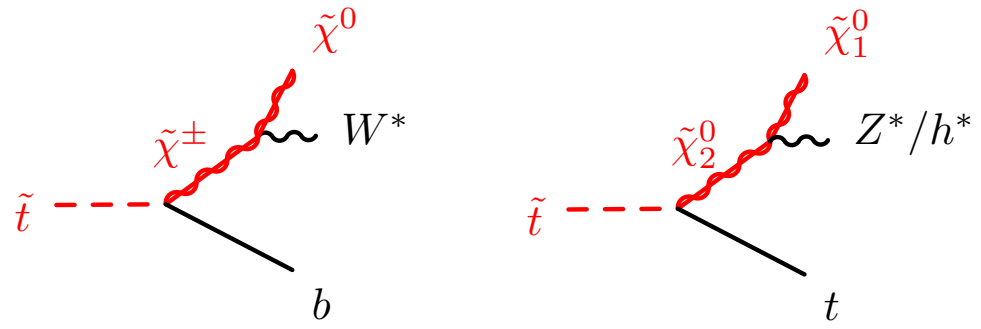

Figure 2.6: Decay of a top squark into a bottom quark, a W boson and a neutralino via a $\tilde{\chi}_1^{\pm}$ (left). Decay of a top squark into a top quark, a neutralino and a neutral boson via a $\tilde{\chi}_2^0$ (right).

2.2.3 Well-tempered Neutralino LSP

Another model is based on the phenomenological MSSM (pMSSM) [40, 41]. The number of parameters is reduced to 19 SUSY parameters at the electroweak scale by incorporating constraints from measurements of the Z and Higgs bosons, b-quark physics, astrophysics as well as direct searches for dark matter and supersymmetric particles. In order to design specific models, most of the parameters are set to fixed values and only two remaining ones are scanned.

When the mass parameters M_1 and μ are comparably small, the lightest neutralino is a mixed state, so-called *well-tempered neutralino* [42]. The typical mass-splitting considered for the bino and higgsino state is between 20-50 GeV.

Two cases are considered, in which the top squark is either mostly left-handed or mostly right-handed. In the former case, the lightest bottom squark ($\tilde{b}_1$) is close in mass to the top squark, and the production of bottom squark pairs is considered as well. The right-handed bottom quark is fully independent from the right-handed top quark and thus the mass of the right-handed bottom squark is independent and is assumed to be decoupled.

The following decay modes are considered for this model

$$\tilde{t}_1 \rightarrow b\tilde{\chi}_1^{\pm},\ t\tilde{\chi}_{1,2,3}^0\,, \tag{2.19}$$

$$\tilde{b}_1 \rightarrow t\tilde{\chi}_1^{\pm},\ b\tilde{\chi}_{1,2,3}^0\,, \tag{2.20}$$

$$\tilde{\chi}_1^{\pm} \rightarrow W^*\tilde{\chi}_{1,2}^0\,, \tag{2.21}$$

$$\tilde{\chi}_3^0 \rightarrow W^*\tilde{\chi}_1^{\pm},\ Z^*/h^*\tilde{\chi}_{1,2}^0\,, \tag{2.22}$$

$$\tilde{\chi}_2^0 \rightarrow Z^*/h^*\tilde{\chi}_1^0\,. \tag{2.23}$$

The first two discussed models do not predict a correct value of the dark matter density. The well-tempered model is designed such that it provides a viable dark-matter candidate. The annihilation rate of the neutralinos is consistent with the observed dark matter relic density [43] while still addressing the naturalness problem when introducing the admixture of bino and higgsino LSP.

3 Event Simulation

The observed data and the theoretical predictions are compared in order to verify the consistency of the SM or to search for new physics. For this, physics processes are simulated and the interaction of the particles with the detector are modelled. Monte Carlo (MC) generators reproduce the predicted distributions on average by using pseudo random numbers. The MC generators is used to simulate various physics processes and also the interaction of particles with the detector material.

An overview of the simulation of pp collisions and the ATLAS detector simulation is presented.

3.1 Simulation of pp Collisions

In order to simulate pp collisions, physic processes are described at different energy scales by different generators [44]. Deep-inelastic scattering between the partons in the protons is described at high energy scales, while low energy scales of the final state are needed when partons evolve into stable hadrons.

The simulation can be factorised into different steps. These individual steps are solved independently and are illustrated in Figure 3.1. As a first step, the partons in the proton are modelled using parton

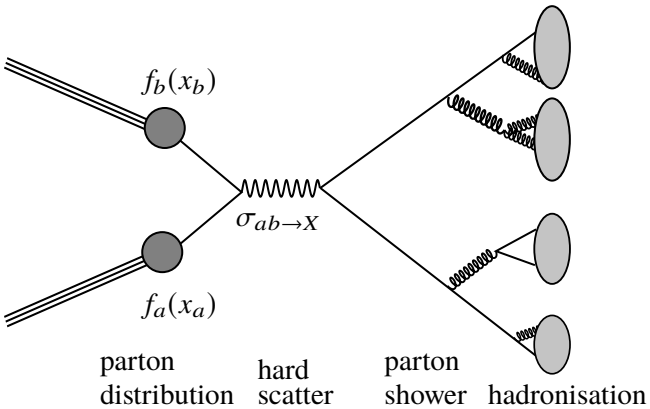

Figure 3.1: Sketch of a pp collision illustrating the different steps of the event simulation.

distribution functions. The hard interaction of the partons is calculated up to a fixed order in perturbative theory as a large momentum transfer occurs.

In the collision, these partons are colour charged and can emit gluons which can radiate further gluons and split into quark-anti-quark pairs, and will thereby create parton showers. The radiation processes progress until the parton reaches an energy scale of $Q \simeq 1\,\text{GeV}$. At lower scales, partons recombine into colourless hadrons, so-called hadronisation. These two processes are at softer scales where the perturbative QCD is no longer valid. As no analytic description is possible, phenomenological models are needed.

The hadrons decay further into final state particles which then interact with the detector.

3.1.1 Factorisation Theorem

Following the factorisation theorem [45], short- and long-distance effects can be split at the factorisation scale μ_F. The cross-section of a hadron collision with final state X can then be calculated as

$$\sigma_{pp\to X} = \sum_{a,b} \int dx_a dx_b f_a(x_a, \mu_F) f_b(x_b, \mu_F) \hat{\sigma}_{ab\to X}(x_a, x_b, \sqrt{s}, \mu_F, \mu_R), \tag{3.1}$$

with a and b as parton types initiating the process. The integration is performed over the corresponding Bjorken variables. The parton-level cross-section $\hat{\sigma}_{ab\to X}$ depends on the momenta of the partons. It can be calculated by the product of the scattering matrix element squared, and averaged over the initial-state spin and the possible colours. The matrix element (ME) depends on the renormalisation scale μ_R where usually $\mu_F = \mu_R$ is chosen.

The parton density function (PDF) $f_i(x_i, \mu_F)$ is the probability of finding a parton of type i within the proton where the parton carries a specific fraction of the proton momentum x_i. The PDFs are

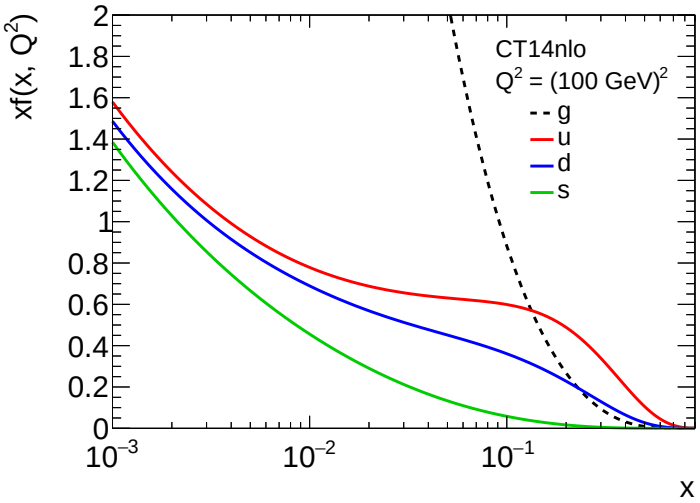

Figure 3.2: The CT14 parton density functions [46, 47] for gluons, up, down and strange quarks at $Q^2 = (100\,\text{GeV})^2$.

universal and do not depend on the physic process. No analytic solutions exist for PDFs, therefore parametrised functions are fitted to measurements of deep inelastic scattering processes and from hadron colliders. The dependence of the PDFs on the energy scale Q is given by the QCD evolution equations (DGLAP) [48–50]. The PDF for up, down and strange quarks and the gluon is shown in Figure 3.2 at $Q^2 = (100\,\text{GeV})^2$.

3.1.2 Matrix Element

The inclusive cross-section of the inclusive production of a final state X can be calculated as

$$\sigma_{ab\to X} \sim \sum_{k=0}^{\infty} \int d\Phi_{X+k} \left| \sum_{l=0}^{\infty} \mathcal{M}^{l}_{X+k} \right|^2 , \tag{3.2}$$

with the sum over all legs (k) corresponding to the real emission and the sum over all loops (l) corresponding to virtual corrections. The phase-space Φ_{X+k} matches to the configuration with k legs. The KLN theorem [51, 52] states that divergences in the loops cancel exactly those from the real emission for each order in perturbative theory. In order to reduce the complexity of this calculation, the nested sums are limited.

The case with $k = l = 0$ relates to the leading order for the inclusive X production, where $k = n, l = 0$ corresponds to the leading order for the $X + n$ jet production. Increasing the number of summands improves the accuracy of the prediction. When calculating the order N^nLO for X production, $k + l \leq n$ is used. This includes N^{n-1}LO for X+1 jet, N^{n-2}LO for X+2 jet, to LO for X+n jets.

3.1.3 Parton Shower

The idea of the parton shower (PS) is to account for higher order contributions. The emission of quarks and gluons from the partons in the final or initial state is assumed to be independent. For this, the probability for each parton in the hard interaction to split into two partons with a fraction of the momentum of the initial parton can be calculated as

$$d\sigma_{n+1} \simeq \sigma_n \sum_{\text{partons}} \frac{\alpha_s}{2\pi} \frac{d\theta^2}{\theta^2} dz P_{ji}(z, \phi) d\phi. \tag{3.3}$$

The $P_{ji}(z)$ are the Altarelli-Parisi splitting functions [50] which are a set of universal, but flavour- and spin-dependent functions. As infinity occurs for $z = 1$ and 0, a cut-off is introduced. MC programs use Sudakov form factors for this, defined as

$$\Delta_i(Q^2, q^2) = \exp\left(- \sum_j \int_{q^2}^{Q^2} \int_{z_{\min}}^{z_{\max}} dP_{ij}(z, q) \right). \tag{3.4}$$

The $\Delta_i(Q^2, q^2)$ represents the probability that an outgoing parton evolves from the initial scale Q to a lower scale q where $z_{\min}$ and $z_{\max}$ correspond to the introduced cut-off.

The shower algorithm applies the parton radiation to a lower scale q following the Sudakov form factor. If the new scale q is below the hadronisation scale of 1 GeV, no further shower development is performed. Otherwise, the splitting procedure is applied for each new parton with the new scale.

In order to determine initial state radiation from incoming partons, the *backward evolution* is applied. The energy scale entering the hard interaction is known and thus the shower is developed backwards gaining energy at each emission.

3.1.4 Matching and Merging

The matrix element is calculated at higher order in order to achieve a good precision, applying the infrared cut-off to prevent divergences from soft and collinear emissions. The parton shower evaluation can not be simply added to the ME calculation as it can lead to possible double counting. The final state with e.g. one additional emission can be calculated from ME term with $X + 1$ parton or from the first radiation of the parton shower for the ME term with $X + 0$ partons.

The overlap has to be removed, therefore a procedure is needed to distinguish between hard and large-angle emissions (as from the ME calculation) and soft, collinear emission (as from PS). Two different ideas – *matching* and *merging* – are developed for this.

For merging, the parton shower is added on top of the calculations for different hard jet multiplicities. At lower scale, usually only the parton shower prediction is used. The approximated matrix elements are replaced with the exact ones, but the Sudakov factors are kept to regularise the divergences. The matching combines the resummation with a fixed order, e.g. the parton shower with the NLO calculation. In this case, the limit for $1 \rightarrow 0$ jets is calculated with the Sudakov suppression. This is only applicable for a reliable fixed order calculation.

3.1.5 Hadronisation

Once the parton scale is below 1 GeV, no further shower development is applied. Due to the effect of confinement, the partons form final-state hadrons. This is part of the non-perturbative phase and thus phenomenological models are needed. Most used are the Lund string fragmentation [53] and the cluster hadronisation [54] model.

The cluster model groups partons to form colour-less clusters after forcing all final state gluons to split into quark-anti-quark pairs. The heaviest cluster can further split and decay into smaller clusters until the cluster masses are below 3 GeV.

In the string model, the confinement between the partons from the strong force is represented by a string between a quark and an antiquark. When the colour charges move apart, the string is stretched and the energy increases. If energetically favourable, the string breaks and a new quark-anti-quark pair is created. This is repeated until all energy is converted into quark-anti-quark pairs with short strings.

3.1.6 Underlying Event and Pile-Up

In addition to the hard process as described above, other physic processes can occur and are simulated.

The underlying event describes the soft interaction involving spectator partons from the colliding protons. This happens at low energies and thus phenomenological models are needed. As the cross-section for gluon-gluon scattering is large, multiple gluon scatterings per proton are likely. Soft scattering of partons is called multiple parton interaction. Furthermore, the colour connection with beam remnant is also simulated. Soft QCD interactions can lead to events with scattering of protons in the same bunch crossing as the hard process (in-time pile-up). For out-of-time pile-up, interactions in past bunch crossings are considered using the same physic description as detailed above.

These additional event types have to be predicted well. Therefore dedicated analyses (e.g. [55, 56]) are performed in order to tune parameters of dedicated models. In order to improve the simulation of the in-time pile-up, charged-particle distributions were measured in context of this dissertation and details are given in Section IV.

3.2 ATLAS Detector Simulation

The final output of the MC generators is a list of four-vectors of all stable particles. They are stored after the decay and hadronisation of all intermediate stable particles. This information is used for *particle level* studies.

In order to compare the MC information with the measured data, the *reconstruction level* is needed, which means the simulation of the detector. The GEANT 4 [57] software is used to simulate the interaction of particles with the detector. It converts energy deposits into electronic signals and takes into account both the geometry, material and the readout of the ATLAS detector [58].

4 Statistical Techniques

The analyses presented here use a variety of statistical techniques, such as the unfolding of a measurement in order to compare the results to theory predictions, hypothesis tests based on the profile likelihood technique to infer on models of new physics, as well as multivariate approaches to discriminate such a signal from the SM background. These techniques are explained in this section and referred to in the dedicated description of the analyses.

4.1 Unfolding

The measured data can be unfolded to particle level in order to remove detector effects. Particle level refers to the particles which interact with the detector. The unfolding provides the possibility to compare results between different experiments and at a later time to new theoretical predictions. For a proper comparison, the statistical and systematic uncertainties are propagated back to particle level as well. Simulation samples are used to correct for detector effects. As a first step, the different backgrounds are subtracted. The distributions of interest are divided in different bins, such that the measurement for bin i is given as x_i^{meas}.

In general, a response matrix A is defined. This matrix gives the probability A_{ij} that a simulated event from truth bin j is found in the reconstructed bin i. It therefore parametrises the detector effects that lead to migration effects and loss of efficiency. By unfolding the measurements, these detector effects are corrected for. The truth bin is defined using the generated particles. The expected number of simulated events in bin i can then be calculated from

$$x_i^{\text{reco}} = \sum_j A_{ij} \cdot x_j^{\text{truth}} \,. \tag{4.1}$$

The aim of the measurement is to estimate the x_j^{truth}, corresponding to the unfolded data. As the A_{ij} are determined from simulation, this can potentially lead to a strong bias towards the input model. This dependence is checked in detail in the analysis. To determine the unfolded data, the matrix A should be inverted. This is not always possible, as it can lead to large negative off-diagonal entries. To avoid the direct inversion, different methods are developed. In the presented analysis, the Bayesian unfolding procedure is used which follows the idea of d'Agostini [59].

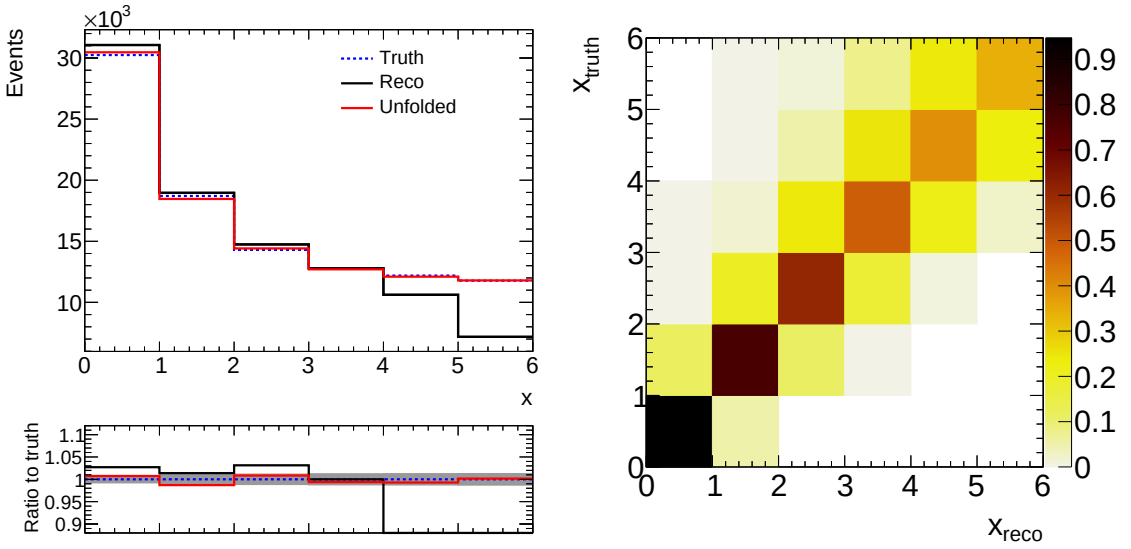

Figure 4.1: Generated, smeared and unfolded exponential distribution (left) and the corresponding response matrix (right).

$$x_j = x_j^{\text{truth}} \sum_i \frac{A_{ij}}{\varepsilon_j} \cdot \frac{x_i^{\text{meas}}}{x_i^{\text{reco}}} \,. \tag{4.2}$$

Here, ε_j is defined as $\varepsilon_j = \sum_i A_{ij}$. The idea is to minimise the model dependence by iterating this calculation. Therefore, in the second iteration the x_j^{truth} is replaced by the x_j which was calculated in the previous iteration. Additionally, x_i^{reco} is replaced by $\sum_j A_{ij} \cdot x_j$. The iteration is performed until the changes between x_j^{truth} and x_j are small. In Figure 4.1, this concept is illustrated with the example of an exponential distribution. The detector effects are simulated by a smearing of the distribution. As can be seen, the unfolding recovers the generated distribution within the uncertainties. For the following analysis, an improved method of this Bayesian unfolding is used including the correct treatment of the statistical uncertainties of the data events [60].

In the easiest case, the resolution of the measured data is smaller than the bin width of the distribution. In this case, any migration effects are small and the matrix A_{ij} is effectively diagonal. Thus, a bin-by-bin migration factor is sufficient. This factor can be calculated using MC information. The generated MC truth information from bin i is given as x_i^{truth} and the reconstructed MC information in the same bin is defined as x_i^{reco}. The ratio then gives the unfolding factor

$$f_i = \frac{x_i^{\text{truth}}}{x_i^{\text{reco}}} \,. \tag{4.3}$$

In order to calculate the corrected data with the bin-by-bin correction, the factor is multiplied with the measured data

$$x_i = f_i \cdot x_i^{\text{meas}} \,. \tag{4.4}$$

4.2 Hypothesis Testing and Profile Likelihood Fit

Statistical tests are performed in order to either discover or exclude a new physics model [61]. For this, two hypotheses are defined including the SM processes only or the SM processes plus a new signal process. The background-only hypothesis is called Null-Hypothesis, while the signal-plus-background hypothesis is called Test-Hypothesis. A more general approach defines the signal strength μ as a multiplicative factor on the signal cross-section. The cases $\mu = 0$ or $\mu = 1$ correspond to the Null- or Test-Hypothesis, respectively.

In order to give the probability of an observation to come from a given model, the likelihood function is defined. The expected number of events for a bin i is given as

$$E_i = \mu \cdot s_i + b_i \,, \tag{4.5}$$

where s_i and b_i are the expected signal and background events in bin i, respectively. The observed data events in this bin are n_i and the expectation by the model is compared to this number. Assuming a Poisson distribution for the data events, the likelihood for bin i can be expressed as

$$L_i(\mu) = \frac{(\mu \cdot s_i + b_i)^{n_i}}{n_i!} \cdot e^{-(\mu \cdot s_i + b_i)} \,. \tag{4.6}$$

In this equation, no uncertainties are taken into account. Systematic and MC statistical uncertainties are introduced with nuisance parameters (NPs), θ. The number of expected signal and background events depend on these NPs – $s_i(\theta)$ and $b_i(\theta)$. By maximising the likelihood when varying the NPs, the agreement between the measured data and the expectation improves.

The NPs are defined by their probability density function (pdf) $\rho(\theta)$ which includes information about their best estimate and the size of the uncertainty. Additional measurements are needed to determine the pdfs for each systematic individually. The pdf is then included into the likelihood as a prior on θ using different functional forms. A Gaussian pdf is considered for systematic uncertainties

$$\rho(\theta) = \frac{1}{\sqrt{2\pi}\sigma} \exp\left(-\frac{(\theta - \hat{\theta})^2}{2\sigma^2}\right) \tag{4.7}$$

with the measured value $\hat{\theta}$ and the given uncertainty σ. For statistical uncertainties, a gamma distribution is used. The event rate n in a region depends on the number of events N in MC by the relation $n = \alpha \cdot N$. The corresponding pdf can be defined as

$$\rho(n) = \frac{1}{\alpha} \frac{(n/\alpha)^N}{N!} e^{-n/\alpha} \,. \tag{4.8}$$

The description of the priors depends on the absolute values and the uncertainty of the NPs and the pre-fit values for each NP are needed to understand the fit result. To simplify this, the Gaussian NPs are redefined to have the centre at zero with a width of one. The transformation for a Gaussian nuisance parameter is

$$\theta' = \frac{\theta - \hat{\theta}}{\sigma} \,. \tag{4.9}$$

The transformed NPs enable an easy comparison for the pre- and post-fit values. Post-fit values close to zero with an uncertainty of one indicate that the data do not have enough statistical power to infer on the systematic effect. If, on the other hand, the statistical power is sufficient, the uncertainty may be reduced, and the best fit value can deviate from the initial assumption, inducing a so-called constraint or pull. If the modified MC is in better agreement with the observed data, the post-fit value is shifted away from zero. The post-fit values of the NPs are a good tool for understanding the fit behaviour.

After introducing the NPs and their pdfs, the likelihood changes to

$$L(\mu, \theta) = \prod_{i=1}^{N} \frac{(\mu \cdot s_i + b_i)_i^n}{n_i!} e^{-(\mu \cdot s_i + b_i)} \prod_{k=1}^{M} \rho(\theta_k) \, . \tag{4.10}$$

The global maximum when varying the signal strength and the NPs is $L(\hat{\mu}, \hat{\theta})$. For a fixed value of μ, the global maximum $L(\mu, \hat{\hat{\theta}}_\mu)$ is determined by varying only the NPs. Using these two values, the profile likelihood ratio is defined as

$$\lambda(\mu) = \frac{L(\mu, \hat{\hat{\theta}}_\mu)}{L(\hat{\mu}, \hat{\theta})} \, . \tag{4.11}$$

If a good agreement between the measured data and the signal hypothesis with a signal strength μ is observed, the likelihood ratio λ is close to one. Based on this ratio, the test statistic can be defined as $q_\mu = -2 \cdot \ln \lambda(\mu)$. The p-value corresponding to this test statistic can be computed, giving the probability that the observed data originate from the considered hypothesis.

$$p_\mu = \int_{q_{\mu,\mathrm{obs}}}^{\infty} f(q_\mu|\mu) dq_\mu \, , \tag{4.12}$$

where $q_{\mu,\mathrm{obs}}$ is the observed value of the test statistic in data and $f(q_\mu|\mu)$ is the pdf of q_μ assuming a specific μ. The analytic form of the pdf is known in the asymptotic regime, for large event counts. This procedure fits all NPs at the same time while taking their correlations into account.

The p_μ-value is determined in order to provide an estimate for the compatibility of the observed data with a given hypothesis and depends on the signal strength. The p_0 gives the probability that the data agree with the background-only hypothesis. Normally, this value is converted into the corresponding Gaussian significance Z. The convention defines that a new physics model can be excluded if the p_μ is below 5%, corresponding to a 95% confidence level (CL). In the case of $\mu = 1$, the nominal prediction is falsified. The 5% threshold corresponds to a significance of $Z = 1.64$. In the case of incompatibility with the background only hypothesis, evidence for new physics is defined for $p_0 < 1.3 \cdot 10^{-3}$ ($Z = 3$), and a discovery is achieved when $p_0 < 2.9 \cdot 10^{-7}$ ($Z = 5$).

The p_μ value is sensitive to statistical fluctuations and the approach can lead to exclusion, even when the analysis is not sensitive to the signal. In order to avoid this, the $\mathrm{CL_s}$ method [62] is introduced, which is commonly used at the LHC experiments.

$$\mathrm{CL_s} = \frac{p_\mu}{1 - p_0} \tag{4.13}$$

The motivation for this definition can be seen considering an example of a downward background fluctuation in an analysis. The p_μ would be small, even in case of a new physics model with a small

cross-section. On the other hand, the denominator $1 - p_0$ will also be small. In total, the CL_s value increases compared to p_μ and no exclusion will be placed on the new physics model. The 95% CL exclusion thus corresponds to a CL_s value smaller than 0.05 for the signal-plus-background hypothesis for the given signal strength.

The implementation of this procedure in the `HistFitter` framework [63] is used in this dissertation.

4.3 Boosted Decision Trees

Multivariate techniques are a powerful tool to separate signal from background processes by taking correlations between variables into account. In the so-called supervised learning approach, the classifier is *trained* by adjusting parameters of the techniques using a reference sample with known classification, e.g. from simulation. With this, discriminating information in the input variables is exploited in an automatised fashion. When evaluating the method on an independent dataset without a known classification, the previously learned relationship between the input variables is used to classify the events. For this dissertation, a boosted decision tree is used, based on the implementation in the `TMVA` [64] framework.

A decision tree is a binary tree-structured classifier. Starting at the root node, a sequence of binary splits is applied using discriminant variables. Each split results into two new subsets of training events and each of these go through the same algorithm for the next splitting until the final tree is built. The splitting is iterated until a minimum number of events remains in the final node. These events are then classified as S or B, depending on the amount of signal or background events in each node. At each node, the variable giving the best separation between signal and background events is used. Therefore the same variable can be used several times, and others might not be used at all. The separation criterion is defined using the `Gini Index`, which is the default method implemented in `TMVA`. The `Gini Index` is calculated as $p \cdot (1 - p)$ where the purity p of a node is given by the ratio of signal events to all events in that node. No performance differences to other criteria, e.g. the statistical significance $S/\sqrt{S+B}$, were found.

Statistical fluctuations in the training set can lead to unstable results. For example, in case of two similar powerful variables, a statistical fluctuation of the training set will lead to a preference of one of the variables. When such fluctuations affect the training, the learned relationships between the input variables cannot be generalised to an independent dataset and the performance of the classifier is reduced. This effect is called *overtraining*. To reduce this effect, more decision trees are trained and combined into a so-called forest. Each event is classified based on the classification performed from the majority of trees by taking the average of the individual decision trees. In the training of the individual classifiers, a random subset of events from the training set is used. In addition, a random subset of variables can be used for each tree. The final, combined classifier then relies less on statistical fluctuations and offers an improved separation performance compared to a single tree.

The concept of boosting is introduced in order to improve the training of the additional decision trees. With the boosting procedure, misclassified events are effectively weighted higher in order to improve the classification. Therefore the dependence on fluctuations is reduced further. The most common boosting procedure is the `Gradient Boost`. There, the weight of an event in the training

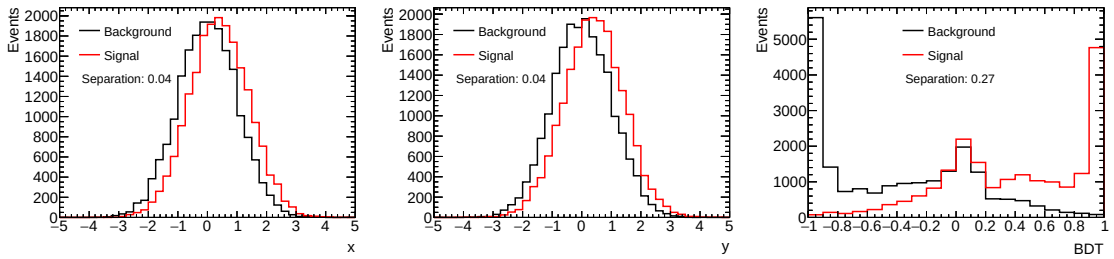

Figure 4.2: Gaussian distributed variable x and y for signal and background processes (left, middle) and the resulting BDT distribution (right). The separation for each individual distribution is indicated.

of an additional decision tree is derived from the gradient of the loss function, which encodes the difference between the derived and the true classification from the previous trained tree.

For a single tree and also the combined forest, the importance of each variable can be calculated. The variables are ranked counting the split occurrence for each variable in all trees. This is weighted by the separation gain achieved by the split and the number of events in the specific note.

Figure 4.2 illustrates the possible performance gain of using a multivariate classifier in comparison to one-dimensional distributions. Here, toy events are drawn randomly from a two-dimensional Gaussian distribution, with different correlation factors for signal and background. The individual distributions of x and y do not show a good separation between the two classes. The separation is here calculated as the integral of the squared differences between the distributions, normalised to their sum. A BDT is trained using these two variables, and the resulting classifier output shows a strongly improved separation power. While in this simple example, a transformation can be constructed by hand to improve the separation, the training of the BDT automatically learns the relationship between the variables. This behaviour generalises to more complex problems with unknown correlations.

The ATLAS Experiment at the Large Hadron Collider

One Ring to find them

J.R.R. Tolkien

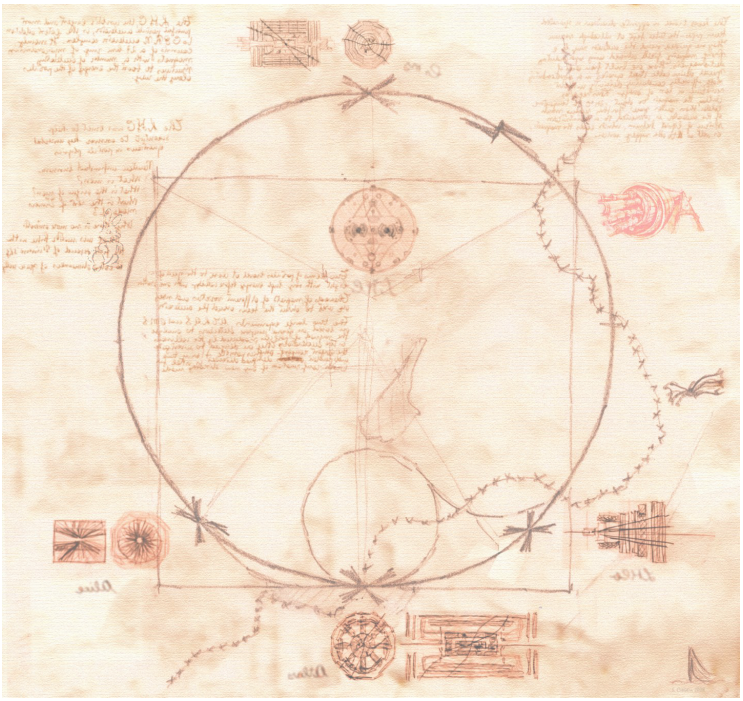

5 The Large Hadron Collider

The Large Hadron Collider (LHC) is a circular particle accelerator [65] in a 27 km long tunnel approximately 100 m below the surface at CERN. It is designed to collide protons at a centre-of-mass energy of 14 TeV and is thus the collider achieving the highest energy. In the years 2015 and 2016, the LHC was operated at a centre-of-mass energy of 13 TeV.

The particles are collided at different interaction points in the LHC tunnel, where detectors are installed in order to measure and analyse the products of the collisions. There are four large experiments at the LHC: ALICE [66], ATLAS [67], CMS [68] and LHCb [69]. ATLAS and CMS are both multi-purpose detectors with a similar and broad physics program. The LHCb experiment concentrates on *b*-hadron physics. For these three experiments, the LHC usually operates proton-proton (pp) collisions. The LHC can also collide lead ions, where the ALICE experiment concentrates on for heavy-ion studies.

In order to achieve the high centre-of-mass energy, the particles are accelerated in different steps, illustrated in Figure 5.1. As the first step, the protons are extracted from ionisation of hydrogen gas and are injected in a linear accelerator (LINAC2) and accelerated to an energy of 50 MeV. Afterwards, they are injected into a circular accelerator, the Proton Synchrotron Booster (BOOSTER), and accelerated to an energy of 1.4 GeV. A further energy increase up to 25 GeV is achieved in the

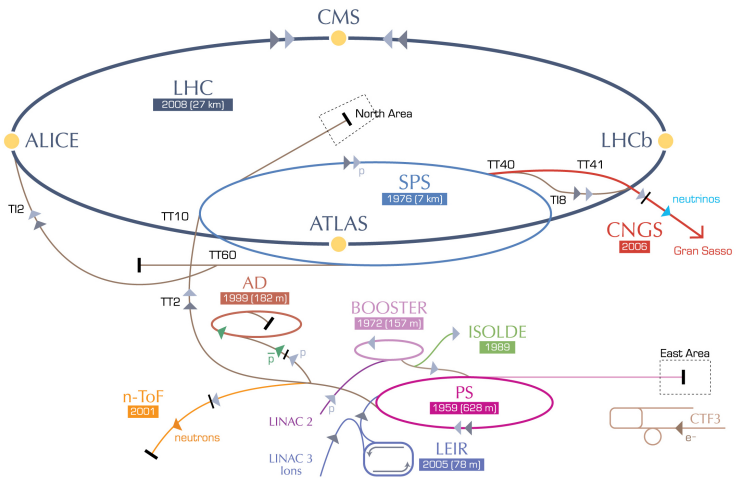

Figure 5.1: Schematic view of the CERN accelerator complex [70].

Table 5.1: Machine parameters of the LHC for 2015 and 2016 [71], compared to the design parameters [65].

Parameter	Design	2015	2016
Beam energy [TeV]	7	6.5	6.5
Bunch spacing [ns]	25	25	25
Beam focus β^* [cm]	55	80	40
Number of protons per bunch	1.15×10^{11}	1.15×10^{11}	1.15×10^{11}
Number of bunches per beam	2808	2244	2220
Peak luminosity [$\mathrm{cm}^{-2}\mathrm{s}^{-1}$]	1×10^{34}	0.5×10^{34}	1.4×10^{34}

second circular accelerator, the Proton Synchrotron (PS). After the Super Proton Synchrotron (SPS), the protons are accelerated to an energy of 450 GeV and can be injected into the LHC.

The LHC consists of two beam pipes each containing protons which are further accelerated. The protons go into opposite directions, so that they can be collided at the interaction points. In order to keep the particles on a circular path at an energy of 7 TeV for each beam, magnetic fields of 8.3 T are used. This is achieved by superconducting magnets cooled by superfluid Helium.

In addition to the high energy, the LHC also achieves a high luminosity, where the instantaneous luminosity is defined as

$$\mathcal{L} = \frac{n_b f_r n_1 n_2}{2\pi \Sigma_x \Sigma_y} \,. \tag{5.1}$$

The number of protons per bunch in beam 1 and beam 2 are given as n_1 and n_2 respectively, where f_r is the revolution frequency and n_b is the number of colliding bunch pairs. Σ_x and Σ_y are the horizontal and vertical convolved beam widths. Alternatively, the size of the beam can be parametrised by the β^* parameter, which describes the envelope of the beam at the interaction points. The design values for these and other LHC parameters as well as the achieved values are detailed in Table 5.1.

The event rate is defined as the product of the instantaneous luminosity with the cross-section.

$$\frac{dN}{dt} = \mathcal{L} \cdot \sigma \tag{5.2}$$

The integrated luminosity is the instantaneous luminosity integrated over the active accelerator time. Thus, the total number of produced events calculates to

$$N_{\mathrm{tot}} = \sigma \int \mathcal{L} dt \,. \tag{5.3}$$

The luminosity is measured with so-called van der Meer scans [72]. ATLAS has also dedicated sub-detectors measuring the delivered luminosity. The total delivered luminosity is shown in Figure 5.2 on the left-hand side separately for each year. For this dissertation, only the data at a centre-of-mass energy of 13 TeV are used, both from 2015 and 2016.

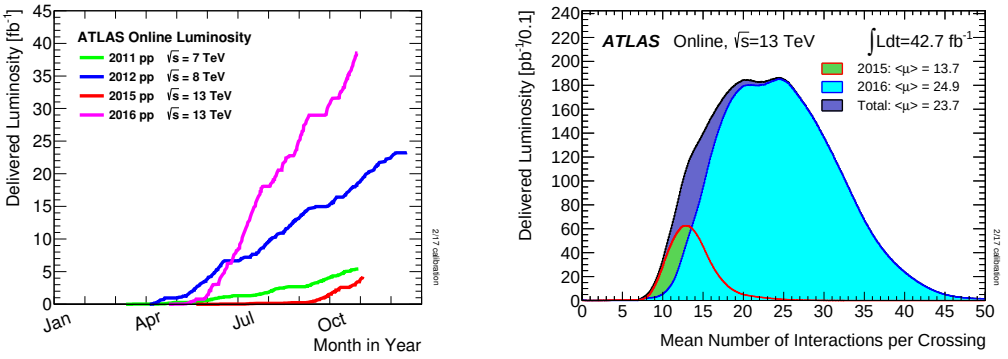

Figure 5.2: Delivered integrated luminosity versus time for all years with *pp* data taking (left) and the luminosity weighted distribution of the mean number of interactions per bunch crossing for 2015 and 2016 (right) [73, 74].

The high frequency and the high bunch density lead to several simultaneous events. These events are called pile-up and come either from additional interaction in the same bunch collision (in-time pile-up) or from traces stemming from an event in a different bunch crossing (out-of-time pile-up). This is measured as the mean number of interactions per bunch crossing $\langle\mu\rangle$ and is shown for the 2015 and 2016 data in Figure 5.2. The mean number of interaction was 13.7 in 2015 and 24.9 in 2016.

The ATLAS experiment recorded an integrated luminosity of 39.5 fb^{-1}in 2015 and 2016. The data-taking efficiency was 92% and the delivered luminosity is 42.7 fb^{-1}. Of the recorded dataset, more than 90% fulfil all data quality requirement, resulting into 36.1 fb^{-1}integrated luminosity for physics analysis.

6 The ATLAS Experiment

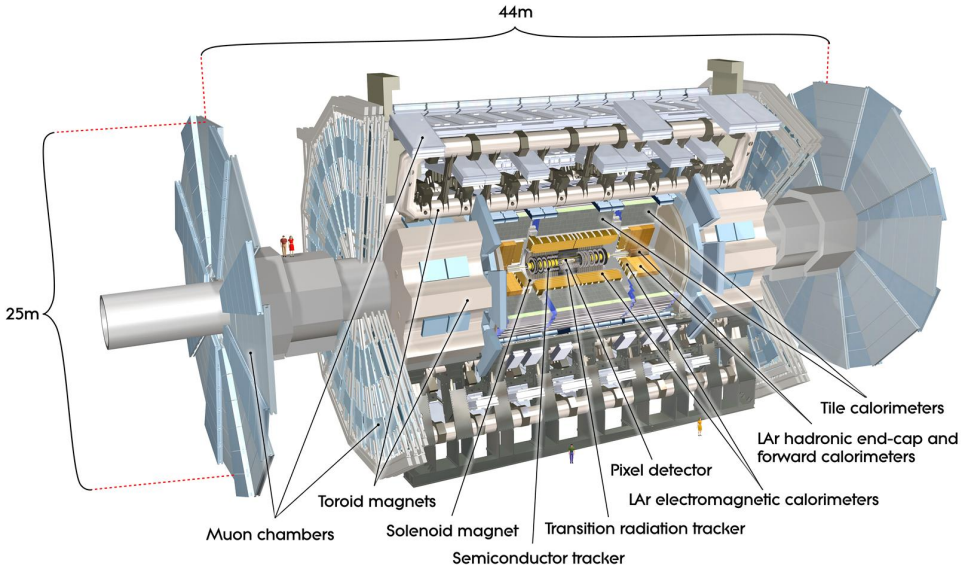

Figure 6.1: Overview of the ATLAS detector showing the different sub-systems and the magnet system [75].

ATLAS [67] is a general purpose detector which is 44 m long and has a diameter of 25 m and a weight of 7000 t. In order to be sensitive to different types of particles, different sub-systems are installed concentrically around each other. This layout ensures the coverage of nearly the full space around the interaction point and is illustrated in Figure 6.1.

All sub-systems consist of a barrel part with different layers installed at different radii. In addition, each sub-system consists of a disk or end-cap part with detecting layers perpendicular to the beam axis.

The innermost part is the Inner Detector (ID), which is installed in a solenoid magnetic field. This tracking detector is used to identify and measure the momenta of charged-particles and to identify the primary and secondary vertices. The calorimeters are installed around the Inner Detector and are used to identify and measure the energy of particles. Most types of particles are stopped in the calorimeters, except for muons and neutrinos. The outermost part is the muon spectrometer which

consists of a toroid magnet and the muon chambers. The muon spectrometer detects and measures the momenta of muons.

All sub-detectors are combined for ATLAS measurements and searches in order to get precise measurements of tracks as well as momenta, energy and electrical charge of the physics objects needed for the different analyses. The performance goals of the different sub-systems are given in Table 6.1. In this section, first the ATLAS coordinate system is introduced. Afterwards, the functionality of each sub-system is explained shortly, followed by an overview of the luminosity measurement and the trigger system.

Table 6.1: Performance goals of the ATLAS detector [67]. The units for the energy E and the transverse momentum p_{T} are in GeV.

Sub-detector	Resolution	Coverage
Inner Detector	$\sigma_{p_{\mathrm{T}}}/p_{\mathrm{T}} = 0.05\% \cdot p_{\mathrm{T}} \oplus 1\%$	$\lvert\eta\rvert < 2.5$
EM Calorimeter	$\sigma_E/E = 10\%/\sqrt{E} \oplus 0.7\%$	$\lvert\eta\rvert < 3.2$
Hadronic Calorimeter	$\sigma_E/E = 50\%/\sqrt{E} \oplus 3\%$	$\lvert\eta\rvert < 3.2$
Forward Had. Calorimeter	$\sigma_E/E = 100\%/\sqrt{E} \oplus 10\%$	$3.1 < \lvert\eta\rvert < 4.9$
Muon Spectrometer	$\sigma_{p_{\mathrm{T}}}/p_{\mathrm{T}} = 10\%$ at $p_{\mathrm{T}} = 1$ TeV	$\lvert\eta\rvert < 2.7$

6.1 ATLAS Coordinate System

ATLAS uses a right-handed Cartesian coordinate system with the origin at the nominal interaction point in the centre of the detector. The x-axis is defined from the interaction point towards the centre of the LHC ring, the y-axis goes upward and the z-axis is defined along the anti-clockwise beam direction. The azimuthal angle ϕ is measured around the beam axis with respect to the x-axis and the polar angle θ is measured with respect to the z-axis.

The momentum of the colliding protons along the z-axis is unknown, therefore it is useful to define the transverse component of variables of interest. These are boost-invariant along the z-axis. As the initial state has a transverse momentum of zero, the momentum conservation can also be applied.

$$p_{\mathrm{T}} = p \cdot \sin\theta = \sqrt{p_x^2 + p_y^2} \tag{6.1}$$

Another common variable is the rapidity, defined as

$$y = \frac{1}{2} \ln\left(\frac{E + p_z}{E - p_z}\right) . \tag{6.2}$$

For massless particles or particles with small masses compared to its energy, this is equivalent to the pseudorapidity

$$\eta = -\ln\left(\tan\left(\frac{\theta}{2}\right)\right) . \tag{6.3}$$

Differences in rapidity Δy are boost-invariant along the z-axis.

The distance between two particles can be defined in this coordinate system as

$$\Delta R = \sqrt{(\Delta\eta)^2 + (\Delta\phi)^2} \, . \tag{6.4}$$

6.2 Inner Detector

The Inner Detector consists of three different sub-systems [76, 77], the Pixel Detector, the Semi-conductor Tracker (SCT) and the Transition Radiation Tracker (TRT). The overview of these sub-systems is shown in Figure 6.2 on the left-hand side. This detector part is closest to the interaction point and is needed for the tracking of a large number of charged-particles, for the vertex reconstruction and for the measurement of track momenta in $|\eta| < 2.5$.

The Pixel Detector consists of four cylindrical layers in the barrel region and three discs in each end-cap region. For each charged-particle passing through the barrel region of this detector, typically four hits are measured. The newest part of the Pixel Detector is the IBL [80] (Innermost B Layer), which is the innermost layer with a radius of only 33 mm. In Figure 6.2, photon conversion candidate measurements are shown versus the reconstructed vertex radius. In this figure, measurements in the beam pipe, the IBL and the other Pixel layers are highlighted using different shades of blue. It is clearly visible that the IBL is next to the beam pipe and can therefore help to improve the measurement of the interaction point parameters, the vertexing and with this also the b-tagging. In total, the Pixel Detector measures with a precision of 10 μm in r-ϕ and 70-115 μm in the z-direction and consists of 86.6 million readout channels.

The IBL was installed during the Long Shutdown 1 in 2013 and 2014 and commissioned in early 2015. Due to the high rate of particles passing through the closest part of the detector, the readout

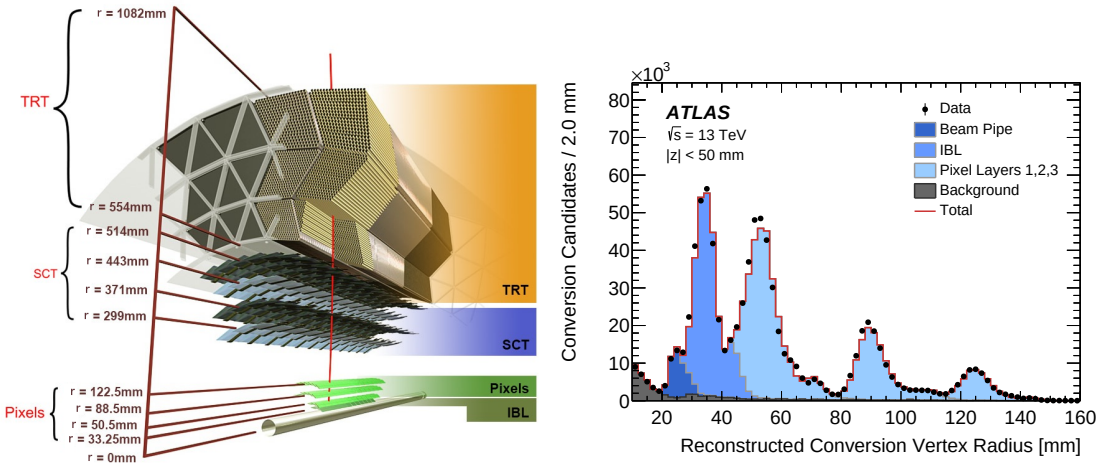

Figure 6.2: Overview of the ATLAS Inner Detector showing the different sub-systems [78]. Photon conversion candidates versus the reconstructed vertex radius highlighting the nearest Pixel layers to the beam pipe [79].

of the IBL detector has to be closely monitored to ensure a high data taking efficiency. Appendix A gives details on some developments for this monitoring.

The SCT Detector is the middle part of the Inner Detector and is a silicon microstrip detector. It consists of four layers in the barrel region and nine disks in the end-cap areas and covers the region of $|\eta| < 2.5$. As each layer is built as double layer, charged-particles cross at least eight strip sensors. The double layer is constructed such that both individual layers are mounted with a 40 mrad tilt angle in order to determine the z-coordinate position. This improves the resolution as the effective 3D information avoids ambiguities. The spatial resolution is 17 μm $\times$ 580 μm in the barrel and the end-cap region.

The outermost part of the Inner Detector is the TRT. It consists of 4 mm diameter gaseous straw tubes interleaved with transition material. The straw tubes are filled with a Xenon-based gas mixture. A charged-particle passing through these tubes ionises the gas and the resulting electrons drift to an anode wire inside the tube. Typically, 36 such hits are measured for one charged-particle. The TRT allows tracking in the region $|\eta| < 2$ with a precision of 130 μm per straw. The space between the tubes is filled with plastic material in order to generate the transition radiation. As the transition radiation depends on the particle mass, electrons can be separated from a charged pion which is useful for the electron identification.

6.3 Calorimeters

The calorimeter is installed around the Inner Detector and is used to identify electrons, photons and jets, and to measure their energy and direction. The general idea is that the primary particles hit an absorber and loose energy by bremsstrahlung or pair production in case of electromagnetic particles. Hadronic particles loose their energy by inelastic hadronic interaction. Both losses produce particle showers. Like the Inner Detector, it consists of a barrel part and symmetric end-caps. The electromagnetic barrel part is finely segmented to ensure a precise measurement of the electrons and photons. The hadronic and forward calorimeter are coarser segmented, but precise enough for jet kinematics and the missing transverse energy calculation.

The electromagnetic calorimeter (ECAL [81]) is a sampling calorimeter. Liquid argon is used as active material and lead plates as absorber. The liquid argon provides a high ionisation yield and shows an intrinsic linear behaviour with a resistance to radiation. The lead plates are arranged in an accordion shape and are orientated in radial direction. The barrel is designed for the region $|\eta| < 1.475$ and the end-caps7 for the region $1.375 < |\eta| < 3.2$.

The electromagnetic barrel consists of three longitudinal subsections. The first subsection has a thickness of 4.3 radiation lengths (X_0), which is the mean distance to reduce the energy of a high-energy electron by $1/e$. This layer measures the direction of the particles most precisely. It can measure the decay of a π^0 into two separated photons, which is important for the photon and electron identification. The second layer is 16 X_0 thick and is thus the largest part of the calorimeter. It is divided into separate towers and provides information of the position of the cluster. The first two layers are combined in order to find the production vertex of photons. The third layer is 3 X_0 thick and has a coarser granularity. It is used to estimate the amount of energy lost beyond the ECAL and to trigger events. In the central region, an additional pre-sampler layer is also present

which is used to estimate the energy loss from electrons or photons in the passive material of the solenoid.

The total thickness is 22-33 X_0 in the barrel and 24-38 X_0 in the end-cap region and therefore fully contains electrons and photons up to energies of a few TeV.

The hadronic calorimeter is an independent sampling calorimeter using different technologies and materials. The central region is the Tile Calorimeter (TileCal [82]) and covers the region of $|\eta| < 1.7$. As absorber, steel tiles are used and plastic scintillator as active material. It is segmented into three layers with a thickness of 1.5, 4.1 and 1.8 hadronic interaction lengths (λ, mean path length to reduce the energy of hadrons by $1/e$) in the barrel and 1.5, 2.6 and 3.3 λ for the extended barrel region. The readout is done with photomultiplier tubes. For the end-cap region, the passive material is copper and the active material is again liquid argon. It consists of two wheels with a finer granularity for the inner one. The forward calorimeter uses tungsten absorber and the thin gap is filled with liquid argon as active material. It covers the very forward region $3.1 < |\eta| < 4.9$. The sub-systems are arranged such that the overall coverage is ensured and thus the full shower can be measured. The full radius from 2.28 m to 4.25 m is covered, which correspond to around 10 interaction length.

6.4 Muon Spectrometer

Muons interact only minimally with all previously discussed sub-detectors as they produce nearly no bremsstrahlung when they cross matter. The Muon Spectrometer is more than 5 m away from the interaction point in order to measure the momentum of muons. It is a combination of the toroidal superconducting magnets, the muon chambers and an independent trigger system. There are four sub-detectors: Monitored Drift-Tubes (MDT), Cathode Strips Chambers (CSC), Resistive Plate Chambers (RPC) and Thin Gap Chambers (TGC). In the barrel region, the chambers are arranged in three cylindrical layers around the beam axis, where one layer is inside the magnet. The end-caps consist of three layers perpendicular to the beam axis.

The detection chambers MDT and CSC are both proportional chambers using an argon and carbon dioxide mixture and they produce radial electric fields at their wires. The MDT has a very good track reconstruction and a high reduction of fake tracks. It covers the area of $|\eta| < 2.7$ ($|\eta| < 2.0$ for the innermost layer). The CSC is a multi-wire proportional chamber and thus has a higher rate capability. The maximal drift time is 40 ns for the CSC and 700 ns for the MDT. The CSC is used at high $|\eta|$ in order to help confront the increased rates.

The triggering chambers RPC and TGC need to have a faster response than the previously discussed drift chambers. The RPC has a gas mixture of $C_2H_2F_4$ (94.7%), Iso-C_4H_{10} (5%), SF_6 (0.3%) between two resistive Bakelite plates. This gives a 1 ns time resolution and allows the discrimination between individual bunch crossings (the bunch spacing is 25 ns). It provides also the ϕ-coordinate for the track reconstruction, where the MDT only provides η-information. The TGC is also a multi-wire proportional chamber with a small wire-to-cathode distance to ensure a fast collecting time. It is installed in the end-cap wheels and has a similar time resolution as the RPC and is also used for triggering.

6.5 Magnets

Charged particle momenta can be measured based on their deflection in a magnetic field. For this, ATLAS uses four large superconducting magnets, a central solenoid and three toroids [83].

The central solenoid is around the Inner Detector and produces a magnetic field parallel to the beam axis, bending charged-particles in the ϕ-direction. At the interaction point, a magnetic field of 2 T is achieved which is constant in radial direction but decreases in z-direction due to the finite size of the solenoid.

The toroid is installed in combination with the muon system and deflects particles in the η-direction. The barrel toroid is installed centrally around the calorimeter with two additional end-caps. Each toroid consists of eight independent coils equally distributed. A magnetic field of 3.9 T and 4.1 T is achieved in the barrel and the end-cap regions, respectively. The toroids are constructed such that a large volume is covered while reducing the additional amount of material in order to improve the muon reconstruction. Less material means less multiple scattering, as charged-particles interact less with the atomic structure of the medium and can be measured more precisely.

6.6 Luminosity Measurement

The precision of measurements depends strongly on a precise determination of the integrated luminosity. The measurement of the luminosity follows the method described in Reference [84]. For the data recorded in 2015 and 2016, a total uncertainty of 3.2 percent was achieved.

Equation 5.1, defining the luminosity, can be rewritten as

$$\mathcal{L} = \frac{\mu_{\text{vis}} n_b f_r}{\sigma_{\text{vis}}}; \tag{6.5}$$

with f_r as collider revolution frequency, n_b the number of colliding bunches, and σ_{vis} as visible cross-section which is the total inelastic cross-section multiplied with the detector acceptance and efficiency. The visible interaction rate per bunch crossing μ_{vis} can be determined using dedicated luminosity detectors by e.g. simply counting bunch crossings. This simplest algorithm ignores any pile-up effects which are not negligible and thus more advanced algorithms are defined [85].

In order to determine the σ_{vis}, a calibration is needed for each luminosity detector using "van der Meer" scans [72]. For this, low-intensity LHC runs are performed where the beam separation is varied and the beam overlap profile is estimated. With this method, the absolute luminosity can be determined and when combining Equation 5.1 and Equation 6.5, the σ_{vis} can be calculated.

The ATLAS experiment uses dedicated luminosity detectors. LUCID (LUminosity measurements using Cherenkov Integrated Detector) is a cherenkov detector. BCM (Beam Conditions Monitor) is a diamond detector. Both are around the beam pipe with a distance of 17 m and 184 cm to the interaction point for LUCID and BCM, respectively. They have a good time resolution and can deliver the luminosity information per bunch crossing. BCM can also trigger on beam losses and induce a beam dump in order to protect the silicon detectors from damage of uncontrolled beams.

The resulting luminosity measurements are cross-checked with other measurements, e.g. by counting the primary vertices reconstructed in the Inner Detector or by using $Z \rightarrow \mu\mu$ measurements.

6.7 Trigger System

A trigger system was developed to select events for storage and analyses [86], as due to technical limitations not all events can be stored and reconstructed. Typically, interesting events occur with a much smaller cross-section than the more general processes, and can be identified by high momentum particles in the final state.

The trigger system consists first of a hardware trigger (L1 trigger) using coarse calorimeter and muon information for the trigger decision. The second trigger is software based (HLT). This trigger uses similar algorithms as the offline reconstruction and can build candidate objects including their position and energy, based on more detailed measurements of the full detector. These objects can be selected and only the events are kept where all trigger selection cuts are fulfilled.

The LHC collision frequency is 40 MHz. After the selection of the L1 trigger, the event rate is reduced to 100 kHz with a final reduction to around 1 kHz after the HLT trigger selection is applied.

6.7.1 Minimum Bias Trigger

For the minimum bias measurement, a dedicated high-efficiency trigger (MBTS) is needed which selects inelastic interaction events resulting in particle production in the detector. The trigger is designed to be efficient for events with only two charged-particles with $p_{\mathrm{T}} > 100$ MeV.

The plastic scintillation counters composing the system were replaced before the data taking of 2015. They are mounted at each end of the detector at $z = \pm 3.56$ m and segmented into two rings in pseudorapidity ($2.07 < |\eta| < 2.76$ and $2.76 < |\eta| < 3.86$). The plane is formed of an inner ring segmented into eight counters and an outer ring of four counters. Each counter is connected to a photomultiplier tube which provides fast readout capabilities. In order to trigger an event, one of the counters has to be above the threshold in a bunch-crossing. No further HLT selection is applied.

In order to investigate the beam-induced background, the same trigger selection is applied to beam crossings without any beam (empty) or only one present beam (unpaired). A dedicated control trigger is specified, which is seeded with a random trigger on filled bunches. It only requires a minimum of two reconstructed tracks.

6.8 Data Quality

A further reduction of the recorded events is done before any data analysis. Recorded events are only used when all needed sub-detectors fulfil certain quality requirements. This information is stored in a Good Run List (GRL) for each lumiblock, which is the time interval where the data-taking configuration for ATLAS is unchanged (in the order of one minute).

In the case of the search for Supersymmetry, the physics objects are reconstructed using all sub-detectors. Thus after fulfilling the trigger selection, the GRL removes further events where one or more sub-systems were not fully functional. Events are removed when they have noise burst in the calorimeters or data integrity problems.

Further data quality requirements are applied based on the reconstructed physics objects which are explained in Section 7. The primary vertex is defined as the vertex with the highest sum of squared transverse momenta of all associated tracks. It is required to have at least two associated tracks each with a $p_{\mathrm{T}} > 400\,\mathrm{MeV}$. Any event containing a jet after the overlap removal failing the loose jet cleaning recommendations is vetoed in order to reject events with badly measured jets.

These requirements are applied in order to ensure a good quality of the data and to avoid mis-measurements.

7 Event Reconstruction

For the two analyses presented in this dissertation, physics objects are identified and reconstructed using specialised algorithms. In this section, first the track reconstruction is detailed. For the minimum bias measurement, the tracking is performed for particles with a transverse momentum larger than 100 MeV. The default tracking as well as the needed changes for the low momentum tracking are explained.

For the search for Supersymmetry also leptons, jets and the missing transverse momentum are required as physics objects. The reconstruction of those objects, as well as the dedicated selection for this analysis are presented in the latter part of this section. For the further selection, physics objects are labelled as *baseline* or *signal* objects where the signal objects are a sub-set of the baseline ones. The baseline objects are used to classify the overlapping objects and to calculate the missing transverse momentum. Furthermore, baseline leptons (which include only electrons or muons) are used to veto events with more than one lepton. The signal objects fulfil tighter requirements and are used to construct the kinematic variables which are used for the event selection in the analysis. In the search for Supersymmetry, two different selections will be presented, which are called intermediate and diagonal signal region. If the object selection differs, the dedicated requirements are given.

7.1 Tracks and Primary Vertex

Tracks are reconstructed in order to identify charged-particles and measure their momentum. For this, the signals induced in the Inner Detector are fitted with trajectory models. The trajectories of charged-particles are bent by the solenoidal magnetic field in the Inner Detector. The curvature of the helix curve in the x-y-plane of the detector is inversely proportional to the momentum of the particle. The knowledge of the reconstructed trajectories allows the identification of interaction vertices and the reconstruction of decays of long-lived particles such as b-hadrons.

Pattern recognition algorithms are defined in order to find track candidates [87–89]. For this, track seeds are built from measurements in the Pixel or SCT detector, so-called silicon hits. Other hits near this seed are collected and judged by a simplified Kalman filtering and smoothing approach [90]. An ambiguity solving procedure is applied in order to remove track candidates with incorrectly assigned hits, e.g. shared hits by two track candidates. ATLAS uses an inside-out pattern algorithm, the track candidates as described above are further extrapolated to the TRT and the TRT measurement is included as well.

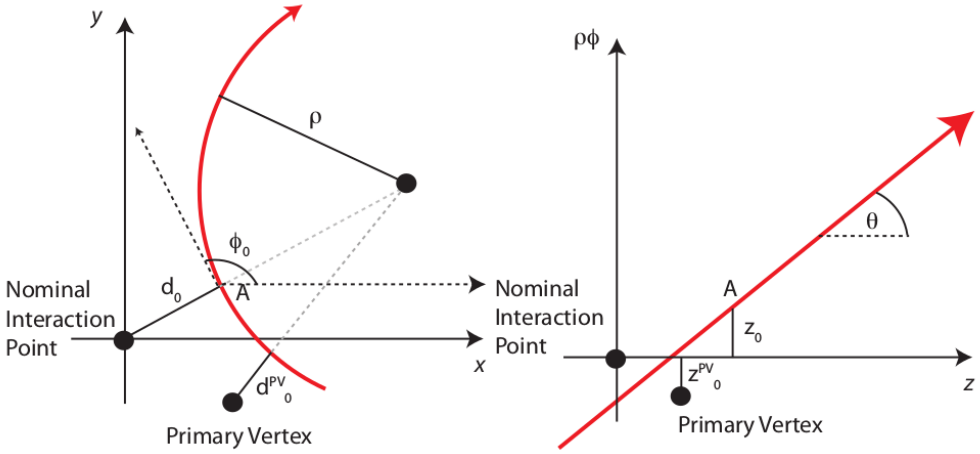

Figure 7.1: Illustration of the track parameters in the transverse plane (left) and the longitudinal plane (right) [87].

The track fitting is done with a χ^2 fit. Further quality requirements are needed for each track candidate. For the default tracking procedure, track candidates have to have a $p_T > 400$ MeV and at least six silicon hits. These track candidates are used in the search for top squarks. For the minimum bias measurement, the track momentum is lowered to $p_T > 100$ MeV and the number of silicon hits is reduced to five.

For each reconstructed track the impact parameters d_0 and z_0 are defined. They are the minimum distance to the centre of the detector in the transverse and the longitudinal direction, respectively. The angles ϕ and θ are the azimuthal and polar angle, and q/p is the charge over the momentum. Those parameters are illustrated in Figure 7.1.

The track reconstruction efficiency is above 90% in the central region and above 70% in the forward region. The impact parameter resolution is around 15 µm at $p_T > 30$ GeV for d_0 and around 60 µm at $p_T > 30$ GeV for z_0 [91, 92].

Multiple interactions can occur in one bunch crossing. For the further analyses, it is important to find the primary vertex, which is done with an adaptive vertex finding algorithm [93, 94]. The reconstructed track collection is used and the seed position for the first vertex is selected by calculating the mean of the z-coordinate of all tracks. The tracks and the seed vertex are combined in an iterative fit procedure in order to find the best vertex position. In each iteration, less compatible tracks are down-weighted and the vertex position is recomputed. After the determination of the vertex position, tracks incompatible with the vertex are removed and allowed to be used in the determination of another vertex. For each vertex at least two tracks are required. This procedure is repeated with the remaining tracks in the event.

The primary vertex is then the reconstructed vertex with the highest sum of squared track momenta. The impact parameters are often expressed with respect to the main primary vertex in the event and can be used to reject tracks which do not come from the primary event. Other vertices come from pile-up interactions. Secondary vertices are vertices which are not within the estimated beam spot region, which is the spatial region around the interaction point where the profile of the two beams overlap. These secondary vertices are used for b- and c-hadron identification.

7.2 Electrons

Electrons are reconstructed from energy clusters in the electromagnetic calorimeter which are associated with an Inner Detector track while vetoing any activity in the hadronic calorimeter [95]. In order to find a cluster seed, a sliding-window algorithm is used with 3×5 units of the middle layer granularity in η- and ϕ-direction. The cluster energy is required to be above 2.5 GeV. Tracks from the Inner Detector are extrapolated to the middle layer and are matched to the cluster seed. If more than one matching track is found, the cluster-track distance, the number of Pixel hits and the presence of a hit in the first silicon layer are taken into account. Furthermore, the associated track should be compatible with the primary vertex in order to reduce the background from photon conversions and secondary particles. A matched cluster is rebuilt using a larger window of 3×7 units in the barrel and 5×5 units in the end-cap region. If a seed cluster is not associated to a track, it is considered as a photon and not further considered for this analysis.

The electron four-momentum is built using the energy from the calorimeter measurement and the η- and ϕ-direction from the track. The final cluster is corrected to take into account energy losses in the material in front of the calorimeter and the fixed cluster size. Corrections are derived using MC studies in order to calibrate the electron energy [96].

For the identification of electron candidates, a multivariate likelihood-based method is used. This method shows only a small pile-up dependence, which is modelled well in simulation. The identification takes the cluster shape into account. Furthermore, the track quality requirements are checked to avoid association with other particles. For this, the quality of the cluster-track matching and especially TRT and IBL hit information are taken into account. A further track refitting corrects for bremsstrahlung emitted by an electron. Different operation points are discussed in Reference [95]: Loose, Medium and Tight. For this analysis, an additional operation point is used, called VeryLoose, to achieve a highly efficient selection.

A track-based isolation requirement is applied in this analysis in order to exclude electrons from semi-leptonic decays of heavy hadrons. The scalar sum of the transverse momentum of tracks with a distance of $\Delta R < \min(0.2, {}^{10\,\mathrm{GeV}}/_{E_\mathrm{T}})$ to the electron is used as a measure of the activity close-by the electron. Tracks associated to the electron are excluded.

The efficiency of the electron reconstruction, identification and isolation is measured in $Z \to ee$ and $J/\psi \to ee$ events using the tag and probe method. For this, one electron (tag) is selected using tight requirements. The other electron (probe) is selected considering the mass requirements to avoid any bias. The efficiency of the probe to pass the selection requirements is then measured. From these measurements, a correction for the simulation is determined via E_T and η dependent scale factors. The scale factors have a few percent precision at low E_T and below 1% uncertainty for high E_T. The scale and the resolution of the energy are calibrated using the same method.

The baseline requirement for the search for top squarks is the VeryLoose identification with an $E_\mathrm{T} > 5\,\mathrm{GeV}$ and $|\eta| < 2.47$. The transverse impact parameter of the signal electrons with respect to the reconstructed primary vertex has to be ${}^{|d_0|}/_{\sigma_{d_0}} < 5$, as well as a minimal distance from this point to the primary vertex along the beam direction is required ($|z_0 \cdot \sin\theta| < 0.5\,\mathrm{mm}$.). Additionally, signal electrons are required to be isolated with a surrounding activity of less than 6% of the electron E_T. A signal electron has to satisfy the Loose or the Tight likelihood identification for the

intermediate top squark masses and the diagonal region, respectively. Those electrons are called either loose or tight electrons. For loose electrons, only track-based information is used and the lepton isolation is therefore independent of the transverse momentum. This gives a 99% efficiency for signal electrons. The lepton isolation for tight electrons relies on both the track and calorimeter based information with a fixed cut on the isolation energy over the electron E_{T}. In general, the signal lepton momentum requirement is increased to $E_{\mathrm{T}} > 25\,\mathrm{GeV}$ and $E_{\mathrm{T}} > 27\,\mathrm{GeV}$ for the loose and tight electrons, respectively.

7.3 Muons

Muons are reconstructed from hits in the Inner Detector and the Muon Spectrometer [97]. For this, first the tracks are reconstructed in the Inner Detector as previously discussed. In the Muon Spectrometer, hit patterns are combined to segments in each muon chamber. These segments are fit together into tracks using a global χ^2 fit. Hits with large contributions to the χ^2 can be removed and additional hits can be added if they agree with the candidate trajectory. In order to combine the Inner Detector and the Muon Spectrometer measurement, four algorithms are defined:

- Combined Muons (CB): track reconstruction is performed in the Inner Detector and Muon Spectrometer separately. With the outside-in algorithm, the Muon Spectrometer tracks are extrapolated into the Inner Detector. Hits from the Muon Spectrometer are added or removed in order to improve the fit quality.
- Segment-tagged Muons (ST): a track in the Inner Detector is extrapolated to the Muon Spectrometer. If it can be associated with at least one track segment in the MDT or CSC chambers, the track and the segment are combined as muon candidate. This is useful for low p_{T} muons or muons crossing only one layer of the Muon Spectrometer in regions with a low coverage.
- Calorimeter-tagged Muons (CT): reconstruct a muon candidate from an Inner Detector track and a calorimeter measurement compatible with a minimally ionising particle. This is useful in the central part $|\eta| < 0.1$ and the momentum range $15 < p_{\mathrm{T}} < 100\,\mathrm{GeV}$. This reconstruction has the lowest purity, but it recovers the acceptance in the region with low sensitivity of the Muon Spectrometer.
- Extrapolated Muons (ME): reconstruct a muon candidate in the forward region $2.5 < |\eta| < 2.7$ which is not covered by the Inner Detector. The Muon Spectrometer track has to be compatible with the interaction point.

In order to avoid any overlap of muon candidates with the same Inner Detector track, preferably the CB, then ST and last CT muons are used. The overlap with the ME muons is removed by selecting the track with the better fit quality and the larger number of hits.

For the identification of muon candidates, at least one Pixel hit, at least five SCT hits and less than three Pixel or SCT holes are required. If a hit were expected in the Pixel or SCT detector, but it is not measured, it is called hole. In addition, at least 10% of the originally assigned TRT hits have to be included in the final fit. The Medium identification is the default selection in order to minimise the systematic uncertainties. Muon tracks reconstructed using only the algorithms for CB and ME

muons are used. The Loose identification maximises the reconstruction efficiency while providing good quality muons. The same muons as for the Medium selection are used, and CT and ST muons are added for the region $|\eta| < 0.1$.

The muon isolation is also track-based and used to separate prompt muons from the hard interaction and muons from different decay chains. The scalar sum of the track p_{T} in a cone $\Delta R = \min(0.3, {}^{10\,\mathrm{GeV}}/_{p_{\mathrm{T}}^{\mu}})$ excluding the muon track itself has to be less than 6% of the muon p_{T}.

The reconstruction, identification and isolation efficiencies are again measured using the tag and probe method with $Z \rightarrow \mu\mu$ and $J/\psi \rightarrow \mu\mu$ events. The scale factors for the muon scale and resolution are estimated with the same method and measured in dependence of p_{T} and η.

The baseline requirement for muons in the search for top squarks is the Loose identification with a a $p_{\mathrm{T}} > 4\,\mathrm{GeV}$ and $|\eta| < 2.7$. A signal muon has to pass the baseline muon selection, and to fulfil $|z_0 \cdot \sin\theta| < 0.5\,\mathrm{mm}$, $\frac{|d_0|}{\sigma_{d_0}} < 3$, and the Medium identification. The signal p_{T} threshold is increased to 25 GeV and 27 GeV for the intermediate top squarks search and the diagonal region, respectively.

7.4 Jets

Quarks and gluons from the hard interaction are not measured directly in the detector due to confinement. They hadronise into a collimated group of particles, so-called jets. The reconstructed physics objects are calibrated to be as close to the initial parton as possible. For the reconstruction, different algorithms are defined depending mostly on the types of input. Jets built from truth stable particles from simulation are named truth or particle jets.

For the reconstruction of the jets, the three dimensional clusters of energy deposits in the calorimeter are considered [98]. For this, jet seeds are defined as calorimeter measurements with a significant signal-to-noise ratio. Measurement noise stems from electronic noise or pile-up. This needs a high granular calorimeter. For seeds, the ratio $|E_{\mathrm{cell}}^{\mathrm{EM}}|/\sigma_{\mathrm{noise}}^{\mathrm{EM}}$ has to exceed a value of four. The $E_{\mathrm{cell}}^{\mathrm{EM}}$ is measured on electromagnetic (EM) scale which reconstructs the energy deposit of electrons and photons correctly, but does not include any corrections for signal loss of hadrons. The $\sigma_{\mathrm{noise}}^{\mathrm{EM}}$ is the quadratic sum of the electronic noise and the noise from pile-up events. All neighbouring cells are added to the cluster when $|E_{\mathrm{cell}}^{\mathrm{EM}}|/\sigma_{\mathrm{noise}}^{\mathrm{EM}} \geq 2$. Further cells with $|E_{\mathrm{cell}}^{\mathrm{EM}}|/\sigma_{\mathrm{noise}}^{\mathrm{EM}} \geq 0$ are added to ensure that the tails of the showers are not discarded. Using this approach, the shower development of a single particle interacting with the calorimeter can be followed. Topo-clusters with multiple local maxima are split.

In order to define the reconstructed jets, a jet-finding algorithm is needed. This algorithm decides which clusters are aggregated into an individual jet. The sequential recombination algorithm anti-k_t [99] is used, as it is infrared and collinear safe, meaning that neither soft emissions at high angles nor hard, collinear emissions alter the jets in an event. This combination gives circular jets in the η-ϕ-plane. For all inputs, the effective distance is calculated

$$d_{ij} = \min\left(\frac{1}{k_{Ti}^2}, \frac{1}{k_{Tj}^2}\right) \cdot \frac{\Delta R_{ij}^2}{R^2}\,, \tag{7.1}$$

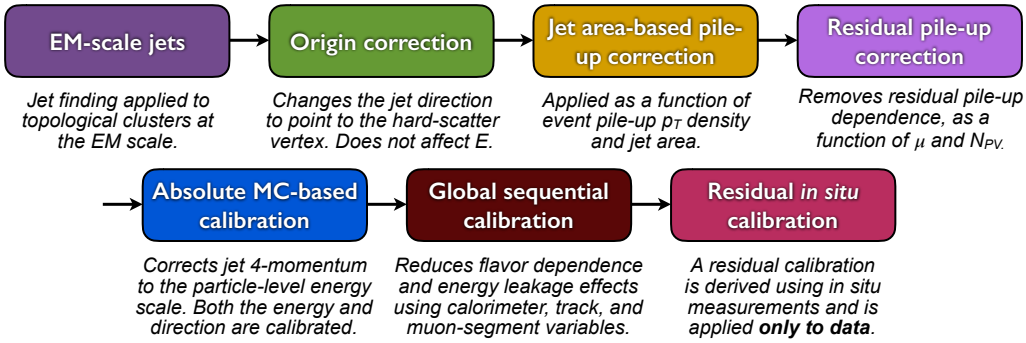

Figure 7.2: Calibration stages for the reconstructed jets [100].

where the parameter R corresponds approximately to the size of the jet, k_{Ti} is the transverse momentum of the input i, and ΔR_{ij} is the distance between the inputs i and j. The effective distance between the input i and the beam can be determined similarly

$$d_{iB} = \frac{1}{k_{Ti}^2} \,. \tag{7.2}$$

In the algorithm, first the smallest distance is searched for, which corresponds to the most energetic particles. If the distance between the inputs i and j is smaller than between i and the beam, the two inputs are combined to a pseudo-jet, which is added to the list of inputs. This is iterated until the distance between the input and the beam is smaller. Then the input is the final jet and will be removed from the list of possible inputs. The procedure is repeated until all constituents are assigned to a jet. The four-momentum of a jet is then directly defined as the four-momentum sum of its constituent clusters.

This algorithm prefers to cluster hard particles and jets grow circular around the seed cluster as the soft particles do not influence the jet area. The radius $R = 0.4$ is used for the presented top squark search.

As the jets are reconstructed at the EM scale, a calibration is needed to correctly measure the energy for the particles produced in a hadronic shower [100]. The corrections reduce the impact of pile-up contamination and recover the energy of the particle jets on average. Different calibration stages are performed and are illustrated in Figure 7.2. The calibration restores the jet energy scale to that of truth jets reconstructed at the particle jets.

The first correction is the *Origin correction* where the jet direction is corrected. A reconstructed jet points towards the centre of the ATLAS detector. After the correction, the jet points towards the primary vertex. This improves the angular resolution and has no effect on the jet energy.

Pile-up can distort the measured jet energy and thus two pile-up corrections are applied to reduce this effect. The *area-based correction* removes the per-event pile-up contribution of each jet according to its area. The pile-up contribution is calculated from the median transverse momentum density ρ in the η-ϕ-plane in order to reduce the bias from hard-scatter jets. The momentum density calculation is based on k_t clustered jets and is calculated as p_T/A, where the area A of the jet is calculated using ghost association. After this correction, there can still be some remaining dependence of the reconstructed jet momentum on the amount of pile-up. For this, an additional *residual correction*

is applied which is sensitive to in-time pile-up, N_{PV} and out-of-time pile-up, μ. The dependence to the two pile-up contributions (called α and β) is assumed to be linear and independent of each other, and is fitted in a combined likelihood approach. The new transverse momentum of the jet after these pile-up corrections changes to

$$p_{\mathrm{T}}^{\mathrm{corr}} = p_{\mathrm{T}}^{\mathrm{reco}} - \rho \cdot A - \alpha \cdot (N_{\mathrm{P\,V}} - 1) - \beta \cdot < \mu > \ . \tag{7.3}$$

Jets are further calibrated in order to correct for detector effects due to mis-measurements of the deposited energy, energy lost in inactive regions, or energy deposits of particles not clustered into the reconstructed jet. Particles are matched to jets with a $\Delta R < 0.3$ in order to calculate the energy ratio from the reconstructed jets and the particles jets with the jet response $R = {}^{E_{\mathrm{jet}}}/_{E_{\mathrm{particle\ jet}}}$ which is fully based on simulation. First, the absolute jet energy scale and η calibration is performed and corrects the jet four-momentum to particle-level scale and accounts for biases in the η reconstruction. Furthermore, the residual dependence of the jet energy scale on the longitudinal and transverse direction is corrected for. The average particle composition and shower shape depend on the initiating particles, e.g. quark and gluon initiated jets. In addition, the *punch-through* effect is corrected for, which describes jets not fully contained in the calorimeter. Several sensitive variables are found and are corrected for separately. The order of the corrections and the correlations between these observables are found to have a negligible influence on the final calibration. Five corrections are performed with the variables being the fraction of energy in the first layer of hadronic Tile calorimeter, the fraction of energy in the last layer of the electromagnetic calorimeter, the number of tracks associated to the jet, the momentum weighted distance of the associated tracks to the jet axis and the number of track segments in the MS associated to the track. A p_{T} and η dependent correction is derived for each observable. The correction factors are scaled such that the average energy of the jets is not changed.

The last correction is an *in-situ* calibration for data where the differences between data and simulation are considered. The transverse momentum balance between a jet and a well-measured object, e.g. a photon, Z boson or other jets is exploited. For this, Z+jets, γ+jets and multi-jet events are used. The latter method is used to correct high momentum jets based on multiple low momentum jets which are corrected with the two former approaches. The correction is applied to data in order to restore the energy of reconstructed jets. For forward jets, the η-intercalibration technique is used where the momentum balance between jets in different η regions is exploited using di-jet events. This can be done, as the central jets are more precisely measured. All these calibration effects are taken into account and propagated to the jet energy scale and jet energy resolution uncertainty.

Background to the jet reconstruction can arise from problems in the calorimeter hardware, LHC beam-gas interactions or showers induced by cosmic rays. Therefore, quality criteria are needed to find the jets from the hard-interaction. The shape of an electric signal from each calorimeter cell is compared to a reference and if significant deviations are found, the jet is rejected. The energy deposit in the ECAL has to be between 5% and 95% in order to reduce noise effects from the ECAL and from non-collision backgrounds. In the end-cap calorimeter, larger noise is expected and thus the fraction of the jet energy there should be smaller than 50%. Furthermore, the jet energy fraction of a jet in one single layer should be smaller than 99%.

Pile-up jets are hard QCD jets from a pile-up vertex. The jet vertex tagger is defined to remove these pile-up jets [101]. As input, it uses the jet vertex fraction which is calculated as the ratio of the scalar sum of the momentum of matched tracks originating from the primary vertex to the scalar sum of the momentum of all matched tracks in the jet. This variable is limited for higher luminosity

conditions as it depends on the number of vertices and tracks. To correct for the dependence on the number of primary vertices, a modified track-to-vertex association is used. In a first step, the tracks are assigned to the vertices as also done for the jet vertex fraction, but in a second step, tracks with $|\Delta z| < 3$ mm to the hard-scatter vertex are added to the hard-scatter vertex. Furthermore, the R_{pT} is defined as scalar sum of the momentum of the tracks associated with the jet and originating from the hard-scatter vertex divided by the fully calibrated jet momentum including the pile-up subtraction. A two dimensional likelihood in the R_{pT} and the corrected jet vertex fraction defines the *jet vertex tagger*.

Baseline jets have to have a $p_{\mathrm{T}} > 20$ GeV. For signal jets, the cut is tightened to $p_{\mathrm{T}} > 25$ GeV. In addition, baseline jets have to have $|\eta| < 4.7$ which is also tightened for signal jets to $|\eta| < 2.5$. Signal jets with a $p_{\mathrm{T}} < 60$ GeV and $|\eta| < 2.5$ need also to satisfy track-based criteria to reject jets originating from pile-up requiring the jet vertex tagger variable to be below 0.59. In order to reject events with badly measured jets, any event is vetoed that contains a jet which fails the loose jet cleaning requirements after the later explained overlap removal.

7.5 Flavour Tagging

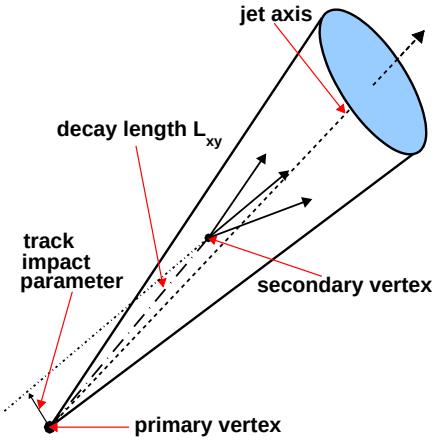

Figure 7.3: Illustration of the decay of a b-hadron. The most relevant variables used for b-tagging are illustrated [102].

For the analysis, it is important to identify jets resulting from the fragmentation of b-quarks, called b-tagging [103, 104]. The b-hadrons are long-living particles with a mean lifetime of $\tau \simeq 1.5$ ps and their decay length in the detector reference frame is $L_{xy} = \gamma\beta c\tau = 6.4$ mm for a transverse momentum of 70 GeV. They decay away from the production vertex and their decay can be resolved in a secondary vertex. This is illustrated in Figure 7.3 using the standard naming scheme.

Tracks are associated to a jet in a jet p_{T} dependent distance with smaller cones for high momentum jets. Important for the further algorithms are the decay length, which is the distance to the primary

vertex, the mass of all particles associated to the secondary vertex (at least 5 GeV as neutral particles are not included) and the impact parameter of each track in the jet.

The final *b*-tagging algorithm is based on several input algorithms. The first inputs come from the IP2D and IP3D algorithms where a likelihood ratio is built to find a discriminant based on the impact parameters. The IP2D uses only the d_0 significance, while IP3D uses also the z_0 significance. The latter one is less robust against pile-up effects. A second algorithm is the SV1, where the secondary vertex is reconstructed and another likelihood ratio is built. The input is the decay length divided by its uncertainty to reduce the effect of poorly measured vertices, the invariant mass, the ratio of the sum of energies of the tracks in the vertex to the sum of the energies of all tracks in the jet, and the number of two-track vertices. The JetFitter algorithm tries to reconstruct the decay chain inside the jet and exploits topological structures of *b*- and *c*-hadron decays inside the jet. With a combined Kalman filter, a common flight path is reconstructed. This can even be done for vertices with a single charged-particle. Important for this algorithm are the number of vertices and the number of tracks at the vertices. These algorithms are then combined in a multivariate *b*-tagging algorithm in order to discriminate *b*-jets from light and *c*-jets. The training is based on $t\bar{t}$ events using a variable fraction of *c*-jets (e.g. 10% for MV2c10 in this analysis). The p_{T} and η distributions are included into the training, but reweighted to match those of the light-jet distribution to not train on the kinematic differences.

The performance of a *b*-tagging algorithm is given by the efficiency of a correct identification of a real *b*-quark jet compared to the mis-tagging of a *c*-quark or light-flavour parton. The chosen working point of the *b*-tagging algorithm in this analysis corresponds to a 77% *b*-tagging efficiency. The rejection rate for light and *c*-jets is given by the inverse of the misidentification efficiency and results into a rejection of 134 for light jets and 6 for *c*-jets.

For each working point, the efficiency is calibrated to correct for mis-modelling in the input variables in the *b*-tagging algorithm. The efficiency for tagging jets in a sample enriched in *b*, *c* or light jets is measured [105–107]. Scale factors are estimated from the differences between the efficiency in data and MC in various p_{T} bins.

7.6 Hadronically Decaying τ Leptons

The τ lepton decays into a τ neutrino and one or more charged hadrons with a branching ratio of 65%. The most common decay mode is with one charged hadron (one prong), followed by three charged hadrons (three prong). The τ reconstruction is seeded by jet candidates with a transverse momentum of 10 GeV which are within the acceptance of the Inner Detector with $|\eta| < 2.5$ [108, 109]. For the reconstruction, the τ lepton production vertex is selected in order to reduce effects from pile-up. For this, all tracks in the $\Delta R < 0.2$ region of the seed are used.

In order to identify τ leptons, a BDT was trained to reject the jet background. The BDT is based on variables sensitive to the decay topology, features of the associated tracks and energy fractions. A dedicated BDT is trained for the one and three prong candidates. The reconstruction efficiency for one (three) prong τ candidates is 60% (50%). The calibration is used to remove any effects from pile-up, decay products not reaching the calorimeter, or too small energy deposit to create a jet seed.

The hadronically decaying τ candidates are required to have one or three associated tracks and a total electrical charge which is opposite to that of the in the analysis required signal electron or muon. Furthermore, the τ candidate has to have a $p_{\mathrm{T}} > 20\,\mathrm{GeV}$ and $|\eta| < 2.5$.

7.7 Missing Transverse Momentum

Particles such as neutrinos or neutral weakly-interacting particles predicted in BSM theories escape the ATLAS detector undetected. The momentum in the plane transverse to the beam axis should sum to zero, any imbalance stemming from these weakly-interacting particles is called *missing transverse momentum* $E_{\mathrm{T}}^{\mathrm{miss}}$ [110, 111]

$$E_{\mathrm{T}}^{\mathrm{miss}} = \sqrt{((E_x^{\mathrm{miss}})^2 + (E_y^{\mathrm{miss}})^2)}\,. \tag{7.4}$$

The missing transverse momentum calculation is based on the previously calibrated physics objects

$$E_{x(y)}^{\mathrm{miss}} = E_{x(y)}^{\mathrm{miss},e} + E_{x(y)}^{\mathrm{miss,jets}} + E_{x(y)}^{\mathrm{miss},\mu} + E_{x(y)}^{\mathrm{miss,soft}}\,. \tag{7.5}$$

The calibrated objects, as electrons (e), jets and muons (μ), are used to calculate the negative sum of the calibrated transverse momenta. Photons or hadronically decaying τ candidates enter either as jets, electrons or via the soft-term.

The soft-term in the equation is a track-based soft-term. Only tracks associated to the identified hard scatter vertex are used to the track-based soft term which makes it robust against pile-up effects. Tracks which are not associated to any calibrated object are used, if the distance to the next electron or photon (τ-lepton) is $\Delta R > 0.05$ ($\Delta R > 0.2$). Tracks which can be ghost associated to a jet are removed. The $E_{\mathrm{T}}^{\mathrm{miss}}$ scale and resolution is measured in $Z \to \mu\mu$ events.

7.8 Overlap Removal

Reconstructing all objects with the procedures detailed above can lead to detector signatures labelled as more than one object. To avoid this ambiguity, an overlap removal is applied which is optimised specific for the analysis presented in [5]. The following ordering and methods are used for the overlap removal using the previously defined baseline objects:

- Electron/muon: if an electron and a muon overlap within $\Delta R < 0.01$, the muon is removed when it is a CT muon, otherwise the electron is removed.
- Electron/jet: if a not b-tagged jet is found within $\Delta R < 0.2$ to an electron, the object is selected as an electron.
- Muon/jet: if a muon overlaps with a jet within $\Delta R < 0.4$, the jet is removed, if it is not b-tagged, and it has less than three associated tracks with $p_{\mathrm{T}} > 500\,\mathrm{MeV}$ or if $p_{\mathrm{T}}^{\mu}/p_{\mathrm{T}}^{j} > 0.7$; otherwise both candidates are kept for the further steps.

- Jet/lepton: if a jet overlaps with a lepton within $\Delta R < \min(0.4, 0.04 + \frac{10}{p_{\mathrm{T}}^{\ell}/\mathrm{GeV}})$, the lepton is removed.
- Electron/τ: if an electron overlaps with a hadronically decaying τ candidate within $\Delta R < 0.1$, the τ candidate is removed.

If the listed requirements are not fulfilled, both objects are kept for the further analysis.

Charged-particle Measurements

There's always another secret.

Brandon Sanderson

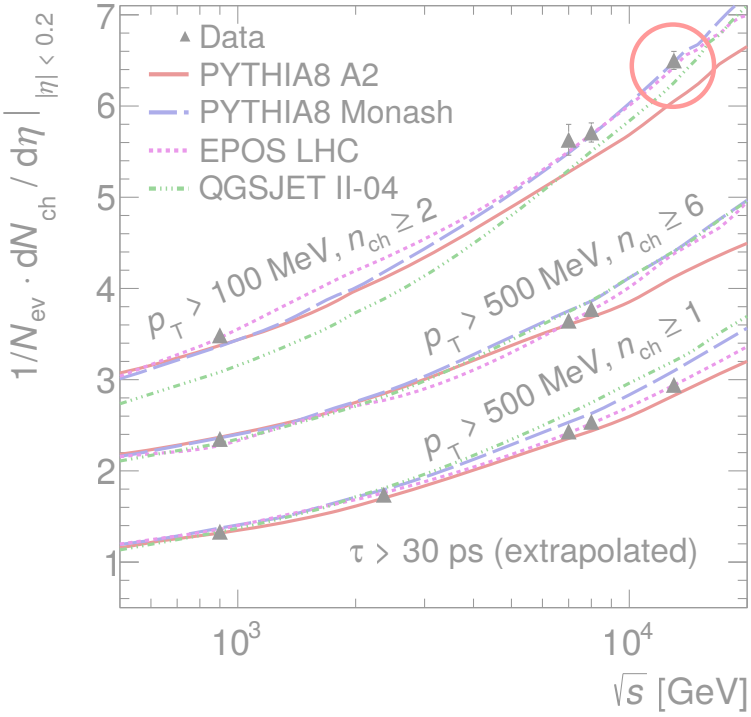

8 Introduction

Measurements of charged-particle distributions in pp collisions probe the strong interaction in the low-momentum transfer, non-perturbative region of quantum chromodynamics (QCD). In this region, charged-particle interactions are described by QCD-inspired models implemented in Monte Carlo event generators. Measurements are used to constrain the free parameters of these models. An accurate description of low-energy strong interaction processes is essential for simulating single pp interactions and the effects of multiple pp interactions in the same bunch crossing at high instantaneous luminosity in hadron colliders. Charged-particle distributions have been measured in hadronic collisions at various centre-of-mass energies [112–121].

The results shown here are published in Reference [4]. This analysis uses the same data set and Monte Carlo samples, as well as a similar analysis strategy as described in a previous measurement where charged-particles with a transverse momentum above 500 MeV were used [2]. The presented analysis extends the measurement to the low–p_{T} regime of $p_{\mathrm{T}} > 100\,\mathrm{MeV}$. Reducing this kinematic cut nearly doubles the overall number of particles in the kinematic acceptance. On the other hand, the measurements are rendered more difficult as they are more sensitive to multiple scattering and imprecise knowledge of the material in the detector. Measurements in the low-momentum regime provide important information for the description of the strong interaction in the low-momentum-transfer, non-perturbative region of QCD and thus a better discriminant between the different models.

These measurements use tracks from primary charged-particles, corrected for detector effects to the particle level, and are presented as inclusive distributions in a fiducial phase-space region. Primary charged-particles are defined as charged-particles with a mean lifetime $\tau > 300\,\mathrm{ps}$, either directly produced in pp interactions or from subsequent decays of directly produced particles with $\tau < 30\,\mathrm{ps}$; particles produced from subsequent decays of particles with $\tau > 30\,\mathrm{ps}$, denoted secondary particles, are excluded. Charged particles with a mean lifetime of $30 < \tau < 300\,\mathrm{ps}$ are charged strange baryons and have been treated as background for the present analysis due to their low reconstruction efficiency. All primary charged particles are required to have a momentum component transverse to the beam direction $p_{\mathrm{T}} > 100\,\mathrm{MeV}$ and absolute pseudorapidity $|\eta| < 2.5$ to be within the geometrical acceptance of the tracking detector. Each event is required to have at least two primary charged-particles. The following observables are measured

$$\frac{1}{N_{\mathrm{ev}}} \cdot \frac{\mathrm{d}N_{\mathrm{ch}}}{\mathrm{d}\eta}, \quad \frac{1}{N_{\mathrm{ev}}} \cdot \frac{1}{2\pi p_{\mathrm{T}}} \cdot \frac{\mathrm{d}^2 N_{\mathrm{ch}}}{\mathrm{d}\eta \mathrm{d}p_{\mathrm{T}}}, \quad \frac{1}{N_{\mathrm{ev}}} \cdot \frac{\mathrm{d}N_{\mathrm{ev}}}{\mathrm{d}n_{\mathrm{ch}}} \quad \text{and} \quad \langle p_{\mathrm{T}} \rangle \text{ vs. } n_{\mathrm{ch}} \,.$$

Here n_{ch} is the number of primary charged-particles within the kinematic acceptance in an event, N_{ev} is the number of events with $n_{\mathrm{ch}} \geq 2$, and N_{ch} is the total number of primary charged-particles in the kinematic acceptance.

These observables are measured and the measured data are compared to the various MC models and between different measurements, e.g. measurements from other experiments. For this, the measured data have to be transformed back to particle level such that the detector effects are removed from the measurement. Therefore, the efficiency of the various reconstruction algorithms and selections is taken into account as corrections factors. Furthermore, an unfolding of the corrected data is performed to transform the data to particle level. These unfolded data are then used for the different comparisons.

9 Event Selection

9.1 Data and Monte Carlo Samples

For this analysis, data from pp collisions at a centre-of-mass energy of $\sqrt{s} = 13\,\text{TeV}$ recorded by the ATLAS experiment in 2015 are used. The data were recorded during special fills with low beam currents and reduced focusing to give a mean number of interactions per bunch crossing of $\langle\mu\rangle$=0.005. The data amount to an integrated luminosity of 151 μb^{-1}. Events from colliding proton bunches were selected using a trigger which required one or more Minimum Bias Trigger Scintillator (MBTS) counters above threshold on either side of the detector.

Several generators are used to compare their prediction with the measured unfolded data. Both the PYTHIA 8 [122] and EPOS [123] generators model the effect of colour coherence, which is important in dense parton environments and effectively reduces the number of particles produced in pp interactions. In PYTHIA, the simulation is split into non-diffractive and diffractive processes, the former dominated by t-channel gluon exchange, and the latter described by a pomeron-based approach [124]. The main contribution is from non-diffractive (ND) events with around 80%, single (SD) and double diffractive (DD) events contribute around 10% each. In contrast, EPOS implements a parton-based Gribov–Regge [125] theory, an effective field theory describing both hard and soft scattering at the same time. QGSJET-II [126] is based upon the Reggeon field theory framework [127].

Different parameter settings in the models are used in the simulation to reproduce existing experimental data and are referred to as tunes. For PYTHIA 8, the ATLAS minimum-bias A2 [128] tune is used, which is based on the MSTW2008LO PDF [129] and provides a good description of minimum bias events and of the transverse energy flow data. In addition, the Monash [130] tune is used instead of the dedicated ATLAS tune. It is based on the NNPDF23LO PDF [131]. For EPOS and QGSJET-II a LHC tune is provided by the respective authors.

A reweighting is applied in order to correct for the beamspot position in z, which differs between simulation and data. This reweighting is required as the efficiencies depend on the beamspot distribution.

Table 9.1 shows the list of used MC models. The first two are used for determining the different efficiencies and for analysing the unfolding method. All MC models are used to compare their predictions to the unfolded data distributions.

Table 9.1: Details of the MC models used. The tunes use data from different experiments to constraint different processes, but only the data with the largest contribution on each specific tune are shown. Here LHC indicates data taken at $\sqrt{s}$=7 TeV, although $\sqrt{s}$=900 GeV data were also included in ATLAS tunes. Some tunes are focused on describing the minimum bias (MB) distributions better, while the rest are tuned to describe the underlying events (UE) distributions.

Generator	Version	Tune	PDF	Focus	Data	From
PYTHIA 8	8.185	A2	MSTW2008LO	MB	LHC	ATLAS
EPOS	3.4	LHC	-	MB	LHC	Authors
PYTHIA 8	8.186	Monash	NNPDF23L0	MB/UE	LHC	Authors
QGSJET-II	II-04	LHC	-	MB	LHC	Authors

9.2 Event Selection

Events are selected from colliding proton bunches when one or more MBTS counters are above the threshold. Each event is required to contain a primary vertex, reconstructed from at least two tracks with a minimum transverse momentum of 100 MeV. To reduce contamination from events with more than one interaction in a bunch crossing, events with a second vertex containing four or more tracks are removed. There can be additional background either stemming from detector noise, cosmic particles passing the detector, or from proton losses in the LHC. Those proton losses can be generated by interactions with residual gas in the beam pipe or by beam cleaning losses. Those backgrounds are called non-collision background events. The contributions from non-collision background events and the fraction of events where two interactions are reconstructed as a single vertex have been studied in data and are found to be negligible.

The track candidates are reconstructed as detailed in Section 7.1 with the special configuration for the low-momentum tracks. Details of the performance of the track reconstruction in the 13 TeV data and its simulation can be found in Reference [6]. Figure 9.1 shows the comparison between data and simulation in the distribution of the number of Pixel hits associated with a track for the low-momentum region. Data and simulation agree reasonably well given the known imperfections in the simulation of inactive Pixel modules. These differences are taken into account in the systematic uncertainty in the tracking efficiency by comparing the efficiency of the Pixel hit requirements in data and simulation after applying all other track selection requirements.

Events are required to contain at least two selected tracks satisfying the following criteria: $p_{\mathrm{T}} > 100$ MeV and $|\eta| < 2.5$; at least one Pixel hit and an innermost Pixel-layer hit if expected. A hit is expected if the extrapolated track crosses a known active region of a Pixel module. If an innermost Pixel-layer hit is not expected, a next-to-innermost Pixel-layer hit is required if expected. Furthermore, the tracks are required to have at least two, four or six SCT hits for $p_{\mathrm{T}} < 300$ MeV, < 400 MeV or > 400 MeV respectively, in order to account for the dependence of the track length on p_{T}; $|d_0^{\mathrm{BL}}| < 1.5$ mm, where the transverse impact parameter d_0^{BL} is calculated with respect to the measured beam line (BL); and $|z_0^{\mathrm{BL}} \cdot \sin\theta| < 1.5$ mm, where z_0^{BL} is the difference between the longitudinal position of the track along the beam line at the point where d_0^{BL} is measured and the

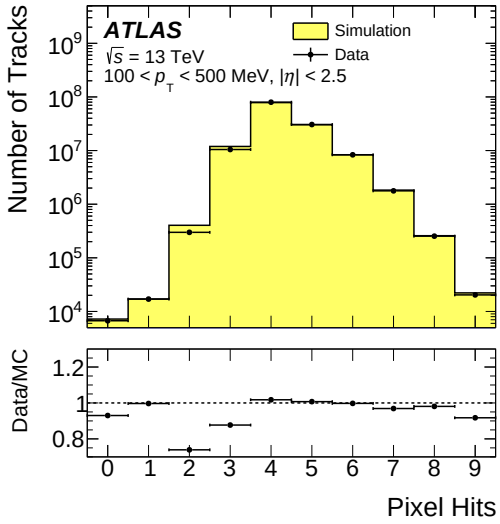

Figure 9.1: Comparison between data and PYTHIA A2 simulation for the distribution of the number of Pixel hits associated with a track. The distribution is shown before the requirement on the number of Pixel hits is applied, for tracks with $100 < p_{\mathrm{T}} < 500\,\mathrm{MeV}$ and $|\eta| < 2.5$. The error bars on the points are the statistical uncertainties of the data. The lower panel shows the ratio of data to the MC prediction [4].

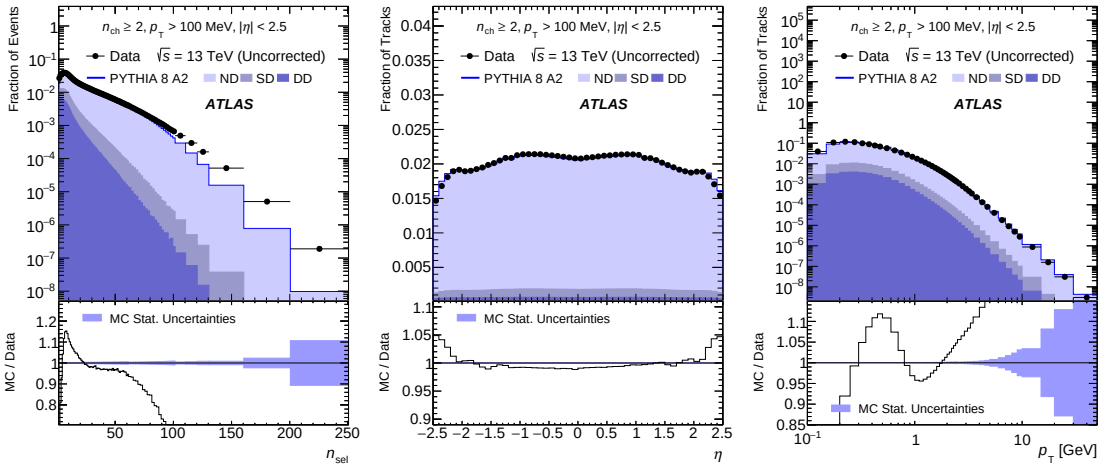

Figure 9.2: Raw distributions of the fraction of events versus the number of selected tracks n_{sel} (left) and of the fraction of tracks versus η (middle) and p_{T} (right). The MC distributions are split into single diffractive (SD), non-diffractive (ND) and double diffractive (DD) events. The lower panel shows the ratio of the MC prediction to data.

longitudinal position of the primary vertex and θ is the polar angle of the track. High-momentum tracks with mismeasured p_{T} are removed by requiring the track-fit χ^2 probability to be larger than 0.01 for tracks with $p_{\mathrm{T}} > 10\,\mathrm{GeV}$. In total 9.3×10^6 events pass the selection, containing a total of 3.2×10^8 selected tracks. The raw distributions after this selection of three variables of interest are shown in Figure 9.2. The observed differences between data and the MC prediction will be corrected for including different selection efficiencies and corrections for detector effects.

9.3 Background Estimation

Fake tracks (tracks formed by a random combination of hits), strange baryons and secondary particles contribute to the tracks from primary particles as background. The different contributions are subtracted from the number of reconstructed tracks before correcting for any detector effects. The contribution of fake tracks is estimated from simulation and is at most 1% for all p_{T} and η intervals with a relative uncertainty of ±50% determined from dedicated comparisons of data with simulation.

Charged strange baryons with a mean lifetime $30 < \tau < 300\,\mathrm{ps}$ are treated as background, because these particles and their decay products have a very low reconstruction efficiency. Corresponding to their lifetime, the mean flight length is $c\tau = 9-90\,\mathrm{mm}$ which means the strange baryons decay in the Pixel detector. The best description of the strange baryon contribution was checked by comparing different MC predictions to data and is expected to come from EPOS [132]. Therefore EPOS was used to estimate the contribution to be below 0.01% on average, with the fraction increasing with track p_{T} to be $(3 \pm 1)\%$ for $p_{\mathrm{T}} > 20\,\mathrm{GeV}$ (see Reference [2]). The fraction is much smaller at low transverse momentum due to the extremely low track reconstruction efficiency.

In order to estimate the contribution from secondary particles, a template fit to the distribution of the track transverse impact parameter d_0^{BL} is performed. As secondary particles are produced in the subsequent decay of directly produced particles, their distance to the primary vertex is generally larger compared to the primary particles. The templates for primary and secondary particles are calculated from PYTHIA 8 A2 simulation. For this, all selection requirements except that on the transverse impact parameter are applied. The fit is then performed in nine p_{T} intervals, each of 50 MeV width, in the region $4 < |d_0^{\mathrm{BL}}| < 9.5\,\mathrm{mm}$. Separate templates are used for electron and non-electron secondary particles in the region $p_{\mathrm{T}} < 500\,\mathrm{MeV}$ as the shape of the transverse impact parameter differs. The radial location defines where the secondary particles were produced and is reflected in d_0^{BL}. Those differences in the radial distribution are caused by the different processes for conversion and hadronic interaction and electrons are more often produced from conversions in the beampipe. Furthermore, the fraction of electrons increases as p_{T} decreases. The rate of secondary tracks is the sum of the contributions from electrons and non-electrons and is measured with the template fit. For the fit, the contribution of fake tracks and strange baryons has to be taken into account. Their background normalisation is determined from the prediction of the simulation. The fitted distribution for $100 < p_{\mathrm{T}} < 150\,\mathrm{MeV}$ is shown in Figure 9.3. For this p_{T} interval, the fraction of secondary tracks within the region $|d_0^{\mathrm{BL}}| < 1.5\,\mathrm{mm}$ is measured to be $(3.6 \pm 0.7)\%$, equally distributed between electrons and non-electrons. For tracks with $p_{\mathrm{T}} > 500\,\mathrm{MeV}$, the fraction of secondary particles is measured to be $(2.3 \pm 0.6)\%$; these are mostly non-electron secondary particles. The uncertainties are evaluated by estimating the interpolation from the fit region to

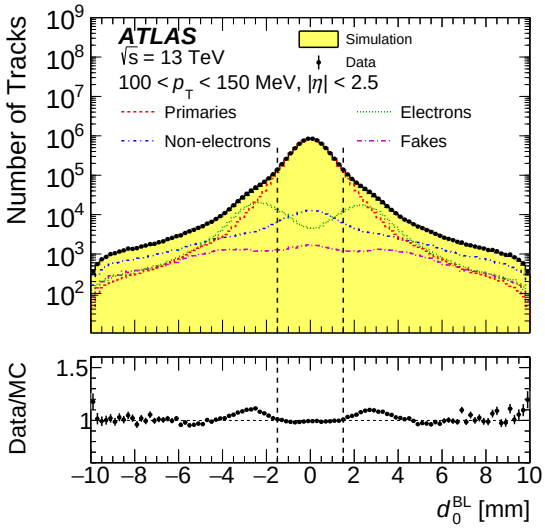

Figure 9.3: Comparison between data and PYTHIA 8 A2 simulation for the transverse impact parameter d_0^{BL} distribution. The d_0^{BL} distribution is shown for $100 < p_{\mathrm{T}} < 150\,\mathrm{MeV}$ without applying the cut on the transverse impact parameter. The position where the cut is applied is shown as dashed black lines at ±1.5 mm. The simulated d_0^{BL} distribution is normalised to the number of tracks in data and the separate contributions from primary, fake, electron and non-electron tracks are shown as lines using various combinations of dots and dashes. The secondary particles are scaled by the fitted fractions as described in the text. The error bars on the points are the statistical uncertainties of the data. The lower panel shows the ratio of data to the MC prediction [4].

$|d_0^{\mathrm{BL}}| < 1.5$ for different generators, changing the total fit range and checking the η dependence of the fraction of tracks originating from secondary particles. The systematic uncertainties arising from imperfect knowledge of the passive material in the detector are also included; these are estimated using the same material variations as used in the estimation of the uncertainty in the track reconstruction efficiency, described in Section 9.5.

Furthermore, the fraction of reconstructed selected tracks originating from particles outside the kinematic range is estimated from PYTHIA 8 A2. For this, the migrations across the p_{T} and η acceptance boundaries are studied separately. This fraction is largest at low p_{T} and high $|\eta|$. To evaluate the systematic uncertainty, the change in total migration between different generators or samples with varying amount of material is calculated. At $p_{\mathrm{T}} = 100\,\mathrm{MeV}$ and $|\eta| = 2.5$, 11% of these particles enter the kinematic range and the corresponding uncertainty is found to be ±4.5%.

9.4 Trigger and Vertex Reconstruction Efficiency

The trigger efficiency $\varepsilon_{\mathrm{trig}}$ is measured in a data sample recorded with a control trigger. This trigger selects events randomly at the first trigger level, requiring only that there are colliding beams in the ATLAS detector, and is uncorrelated to the trigger used for the event selection. Those events are further filtered to require at least one reconstructed track. The ratio of events that are accepted by both the control and the MBTS trigger to all events accepted by the control trigger gives the trigger

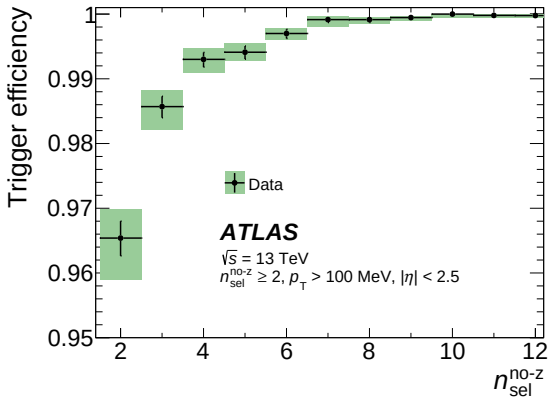

Figure 9.4: The trigger efficiency $\varepsilon_{\text{trig}}$ as a function of the number of selected tracks with $p_{\text{T}} > 100\,\text{MeV}$ and $|\eta| < 2.5$ without the cut on the longitudinal impact parameter applied, $n_{\text{sel}}^{\text{no-z}}$. The statistical uncertainties are shown as black vertical bars, the quadratic sum of statistical and systematic uncertainties as green shaded areas [4].

efficiency

$$\varepsilon_{\text{trig}}(n_{\text{sel}}^{\text{no-z}}) = \frac{N(\text{MBTS triggered} \cap \text{control triggered})}{N(\text{control triggered})} \,. \tag{9.1}$$

This ratio is calculated as function of the number of selected tracks $n_{\text{sel}}^{\text{no-z}}$. For events where only one reconstructed track is found, the vertex reconstruction cannot be performed. Therefore those tracks do not have to pass the vertex requirements, thus the requirement on the longitudinal impact parameter is removed. The trigger efficiency is shown in Figure 9.4, it increases from $96.5^{+0.4}_{-0.7}$ % for events with $n_{\text{sel}}^{\text{no-z}} = 2$, to $(99.3 \pm 0.2)\%$ for events with $n_{\text{sel}}^{\text{no-z}} \geq 4$. Those uncertainties include statistical and systematic uncertainties. Differences between the trigger efficiencies measured on the two sides of the detector and the impact of beam-induced background are considered as systematic uncertainties. The beam-induced background is determined in events recorded when only one beam was present at the interaction point.

The ratio of the number of triggered events with a reconstructed vertex to the total number of all triggered events is used as the vertex reconstruction efficiency

$$\varepsilon_{\text{vtx}}(n_{\text{sel}}^{\text{no-z}}) = \frac{N(\text{MBTS triggered} \cap n_{\text{vtx}} = 1)}{N(\text{MBTS triggered})} \,. \tag{9.2}$$

The vertex efficiency is shown in Figure 9.5 and is measured as a function of $n_{\text{sel}}^{\text{no-z}}$. It is approximately 87% for events with $n_{\text{sel}}^{\text{no-z}} = 2$ and rapidly rises to 100% for events with $n_{\text{sel}}^{\text{no-z}} > 4$. Due to the comparably low efficiency for events with $n_{\text{sel}}^{\text{no-z}} = 2$, the efficiency is also parametrised as a function of the difference between the longitudinal impact parameter of the two tracks (Δz_{tracks}). This efficiency decreases roughly linearly from 91% at $\Delta z_{\text{tracks}} = 0\,\text{mm}$ to 32% at $\Delta z_{\text{tracks}} = 10\,\text{mm}$. The systematic uncertainty is estimated from the difference between the vertex reconstruction efficiency measured before and after beam-background removal and found to be negligible.

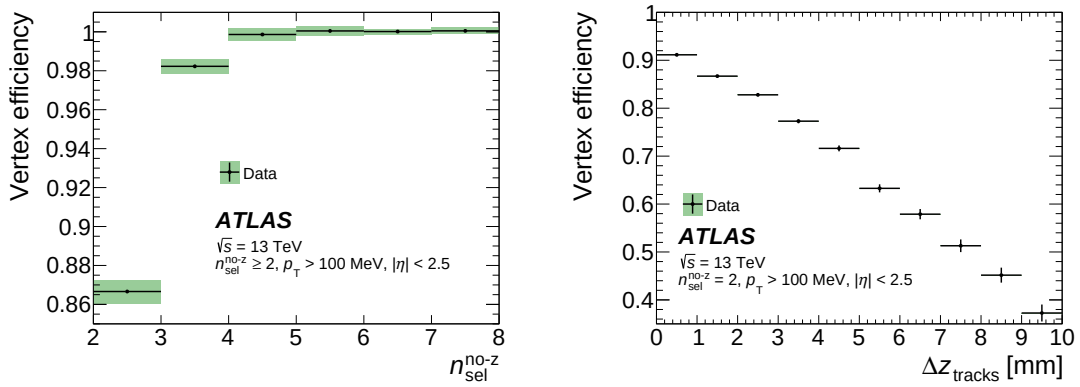

Figure 9.5: The vertex reconstruction efficiency ε_{vtx} as a function of the number of selected tracks with $p_{\text{T}} > 100\,\text{MeV}$ and $|\eta| < 2.5$ without the cut on the longitudinal parameter applied, $n_{\text{sel}}^{\text{no-z}}$ (left). For events with exactly two tracks, the vertex efficiency is considered as a function of the difference in longitudinal impact parameters between these two tracks Δz_{tracks} (right). The statistical uncertainties are shown as black vertical bars, the quadratic sum of statistical and systematic uncertainties as green shaded areas [4].

9.5 Track Reconstruction Efficiency

The primary-track reconstruction efficiency ε_{trk} is determined from simulation. The efficiency is parametrised in two-dimensional bins of p_{T} and η, and is defined as

$$\varepsilon_{\text{trk}}(p_{\text{T}}, \eta) = \frac{N_{\text{rec}}^{\text{matched}}(p_{\text{T}}, \eta)}{N_{\text{gen}}(p_{\text{T}}, \eta)},$$

where p_{T} and η are generated particle properties, $N_{\text{rec}}^{\text{matched}}(p_{\text{T}}, \eta)$ is the number of reconstructed tracks matched to generated primary charged-particles and $N_{\text{gen}}(p_{\text{T}}, \eta)$ is the number of generated primary charged-particles in that kinematic region. If the weighted fraction of track hits originating from a particle exceeds 50%, a track is matched to this generated particle. For $100 < p_{\text{T}} < 125\,\text{MeV}$ and integrated over η, the primary-track reconstruction efficiency is 27.5%. The efficiency increases strongly with increasing p_{T}. Tracks with a $p_{\text{T}} > 1\,\text{GeV}$ ($p_{\text{T}} > 10\,\text{GeV}$) have a track reconstruction efficiency of 80% (>85%) integrated over η.

Different sources contribute to the systematic uncertainties in the track reconstruction efficiency, where the dominant uncertainty comes from imprecise knowledge of the passive material in the detector. The passive material can lead to multiple scattering and energy loss due to the interaction with the material. This influences the track direction and thus the track reconstruction. To estimate this uncertainty, the tracking efficiency is evaluated using dedicated simulated samples with varied detector material. The total uncertainty in the track reconstruction efficiency due to the amount of material is calculated as the linear sum of the contributions of 5% additional material in the entire inner detector, 10% additional material in the IBL and 50% additional material in the Pixel services region at $|\eta| > 1.5$. Those uncertainties are treated as fully correlated. The sizes of these variations were estimated already for previous analyses from studies of the rate of photon conversions, of

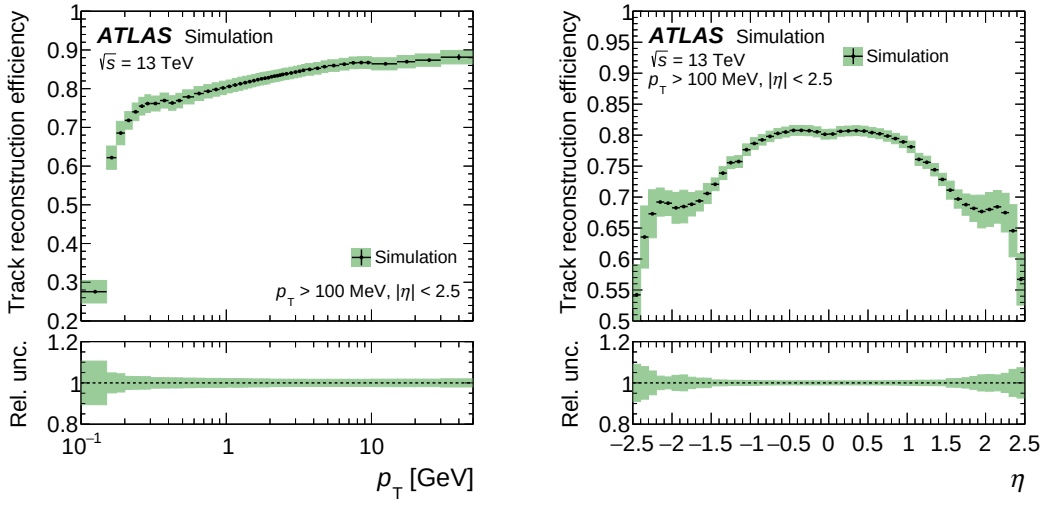

Figure 9.6: Track reconstruction efficiency ε_{trk} as a function of transverse momentum p_{T} (left) and of pseudorapidity η (right) for selected tracks with $p_{\text{T}} > 100\,\text{MeV}$ and $|\eta| < 2.5$ as predicted by PYTHIA 8 A2 simulation. The statistical uncertainties are shown as vertical bars, the sum in quadrature of statistical and systematic uncertainties as shaded areas [4].

hadronic interactions, and of tracks lost due to interactions in the Pixel services [133, 134]. The resulting uncertainty in the track reconstruction efficiency is 1% at low $|\eta|$ and high p_{T} and up to 10% for higher $|\eta|$ or for lower p_{T}. Another systematic uncertainty is the uncertainty from the track selection requirements. This is studied by calculating and comparing the efficiency of each requirement both in data and simulation. This results in an uncertainty of 0.5% for all p_{T} and η bins. The total systematic uncertainty in the track reconstruction efficiency is obtained by adding up those effects in quadrature. The track reconstruction efficiency is shown as a function of p_{T} and η in Figure 9.6, including all systematic uncertainties. The shown track reconstruction efficiency is derived from PYTHIA 8 A2 simulation. This efficiency was also calculated using the predictions from EPOS and PYTHIA 8 MONASH, and equal results were obtained compared to the default using PYTHIA 8 A2. Therefore it is sufficient to use only the track reconstruction efficiency derived with PYTHIA 8 A2 for the analysis.

10 Correction Procedure

10.1 Detailed Unfolding Procedure

The data is corrected to obtain inclusive spectra for charged primary particles satisfying the particle-level phase-space requirement. Before the actual unfolding is performed as introduced in Section 4.1, the background is subtracted and inefficiencies are considered. The inefficiencies can be determined by using the inverse of the efficiencies described above.

The event-wise efficiencies as the trigger selection ($\varepsilon_{\text{trig}}$) and vertex reconstruction (ε_{vtx}) are included as event-by-event weight

$$w_{\text{ev}}(n_{\text{sel}}^{\text{no-z}}, \Delta z_{\text{tracks}}) = \frac{1}{\varepsilon_{\text{trig}}(n_{\text{sel}}^{\text{no-z}})} \cdot \frac{1}{\varepsilon_{\text{vtx}}(n_{\text{sel}}^{\text{no-z}}, \Delta z_{\text{tracks}})} \,. \tag{10.1}$$

The track-wise corrections are used as track-by-track weight as in the case of the track reconstruction (ε_{trk}). Furthermore, the described relevant backgrounds are subtracted. This is done, by removing the fraction of non-primary particles (f_{nonp}), of fake tracks (f_{fake}), of strange baryons (f_{sb}) and of particles outside the kinematic range (f_{okr})

$$w_{\text{trk}}(p_{\text{T}}, \eta) = \frac{1}{\varepsilon_{\text{trk}}(p_{\text{T}}, \eta)} \cdot (1 - f_{\text{nonp}}(p_{\text{T}}, \eta) - f_{\text{okr}}(p_{\text{T}}, \eta) - f_{\text{sb}}(p_{\text{T}}, \eta) - f_{\text{fake}}(p_{\text{T}}, \eta)) \,. \tag{10.2}$$

After subtracting the background and applying the inefficiencies, the multiplicity distribution is expressed in terms of number of selected charged primary particles n_{ch} instead of the number of selected charged tracks n_{sel}. Bayes theorem gives the probability relation

$$P(n_{\text{ch}}) \cdot P(n_{\text{sel}}|n_{\text{ch}}) = P(n_{\text{ch}}|n_{\text{sel}}) \cdot P(n_{\text{sel}}) \,; \tag{10.3}$$

integrating over n_{sel} gives the distribution of primary particles

$$N_{\text{ev}}(n_{\text{ch}}) = \sum_{n_{\text{sel}} \geq 0} P(n_{\text{ch}}|n_{\text{sel}}) \cdot N_{\text{ev}}(n_{\text{sel}}) = \frac{1}{\varepsilon^{\text{miss}}(n_{\text{ch}})} \sum_{n_{\text{sel}} \geq 2} P(n_{\text{ch}}|n_{\text{sel}}) \cdot N_{\text{ev}}(n_{\text{sel}}) \,, \tag{10.4}$$

where the miss-factor $\varepsilon^{\text{miss}}(n_{\text{ch}})$ is defined as

$$\varepsilon^{\text{miss}}(n_{\text{ch}}) = \frac{1}{1 - (1 - \bar{\varepsilon}_{\text{trk}})^{n_{\text{ch}}} - n_{\text{ch}} \cdot \bar{\varepsilon}_{\text{trk}} \cdot (1 - \bar{\varepsilon}_{\text{trk}})^{(n_{\text{ch}}-1)}} \,. \tag{10.5}$$

Table 10.1: Mean track reconstruction efficiency in the first n_{sel} bin for the different samples. The track reconstruction efficiency is used in order to calculate the miss-factor for the out-of-phase-space correction (see Equation 10.5).

Sample	Mean efficiency
Data	0.72
PYTHIA 8 A2	0.71
EPOS	0.73

This correction accounts for the events which are lost due to the track reconstruction efficiency but would pass the particle level phase-space cuts. This can happen for events with $n_{\mathrm{ch}} \geq 2$ but $n_{\mathrm{sel}} = 0$ or 1. The $\bar{\varepsilon}_{\mathrm{trk}}$ in this correction is the mean track reconstruction efficiency in the first n_{sel} bin. In table 10.1, the mean track reconstruction efficiencies are listed for the different samples. For each of these samples, the corresponding mean track reconstruction efficiency is used in order to calculate the correction factor $\varepsilon^{\mathrm{miss}}$. This calculation is done for the nominal distribution as well as for the systematic uncertainties. The full correction is most significant in the first n_{ch} bin and is significantly smaller for higher values of n_{ch}.

The conditional probability $P(n_{\mathrm{ch}}|n_{\mathrm{sel}})$ needed in Equation 10.4 is unknown. It is estimated from the MC prediction using the Bayesian unfolding procedure

$$P(n_{\mathrm{ch}}|n_{\mathrm{sel}})^{r+1} = P(n_{\mathrm{sel}}|n_{\mathrm{ch}}) \frac{N^r_{\mathrm{ev}}(n_{\mathrm{ch}})}{N^r_{\mathrm{ev}}(n_{\mathrm{sel}})} \tag{10.6}$$

for the r-th iteration, where $P(n_{\mathrm{sel}}|n_{\mathrm{ch}})$ is the resolution function and $N^r_{\mathrm{ev}}(n_{\mathrm{ch}})$ and $N^r_{\mathrm{ev}}(n_{\mathrm{sel}})$ are the distributions of primary particles and of selected tracks, respectively. When $r = 0$, those are given by the MC prior estimate. The resolution function $P(n_{\mathrm{sel}}|n_{\mathrm{ch}})$ is a matrix. This matrix is calculated from MC simulation assuming that the resolution in data is not too different. In order to keep the statistical uncertainties form the matrix small, samples filtered on the multiplicity are used with the thresholds $n_{\mathrm{ch}} > 120, 160, 200$. The resulting matrix is mostly populated along the diagonal.

Correction to the Individual Distributions

In order to obtain the n_{ch} distribution, the correction factors from the trigger, vertex and track reconstruction efficiency as well as from the $\varepsilon^{\mathrm{miss}}$ factor are applied to the n_{sel} distribution. Afterwards the described unfolding procedure is performed. The total number of events N_{ev} is defined as integral over the final (corrected and unfolded) n_{ch} distribution. For the phase-space with a transverse momentum $\geq 100\,\mathrm{MeV}$ and $n_{\mathrm{ch}} \geq 2$, the total number of events after unfolding is $N_{\mathrm{ev}} = 9.5 \cdot 10^6$ with a relative uncertainty of 0.5%.

For the p_{T} distribution, the corrections from the trigger, vertex and track reconstruction efficiency are applied as event- and track-wise weights. Afterwards, the distribution is unfolded using the explained procedure.

For the η distribution, only the event- and track-wise weights are applied. The η distribution is normalised by the previously estimated N_{ev}. The resolution for this observable is smaller than the bin width ($\Delta\eta = 0.1$) and only the bin-by-bin correction is considered. The mean particle

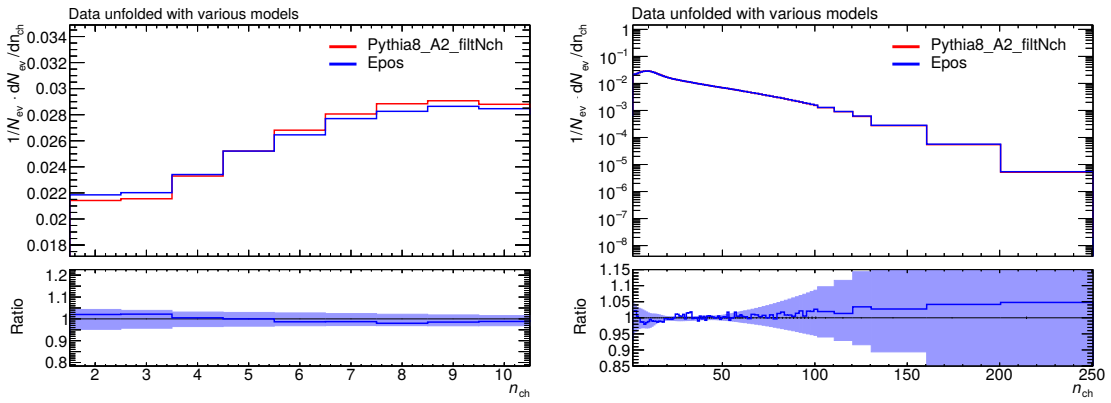

Figure 10.1: Comparison of the unfolded data using the PYTHIA 8 A2 and EPOS generator as input for the matrix calculation. This is shown for the n_{ch} distribution with a zoom in the low region (left) and over the full range (right). The lower panel shows the ratio between the two unfolded distributions with the statistical uncertainty shown in the error band.

density at $\eta = 0$ is calculated by taking the average over four bins at the centre of the η distribution, corresponding to an average of $\Delta\eta = 0.4$.

To obtain $\langle p_T \rangle$ versus n_{ch}, the correction and unfolding is done separately for the two components $\sum_i p_T$ versus n_{ch} and $\sum_i 1$ versus n_{ch}. For the individual unfolding of both distributions, the same correction and unfolding procedure is applied as for the n_{ch} distribution. To finally get the $\langle p_T \rangle$ versus n_{ch} distribution, the ratio of the two components is taken.

As the resolution matrix is calculated from MC simulation, there can be a bias to this simulation. In Figure 10.1, one can see the n_{ch} data distribution unfolded using the PYTHIA 8 A2 and the EPOS generators as input for the matrix calculation. For low n_{ch}, both unfolded distributions agree, but for higher n_{ch} some differences can be seen which are well covered by the statistical uncertainty. Thus, the dependence on the generator is only small for this analysis and no large bias to the simulation can be seen for the unfolding. For the unfolding of the data, the matrix is calculated using the PYTHIA 8 A2 generator.

10.2 Closure Tests

Before unfolding the data for the different distributions, so-called closure tests were performed. For these tests the unfolded distribution is compared to the MC particle information. For this, the resolution matrix and the distribution as well as the MC particle information are used from the same generator. When the unfolded distribution and the particle distribution agree, a closure is observed. In the following closure tests, the effect of combining different MC generator predictions is also considered. Those tests verify the general unfolding procedure and estimate the potential bias introduced by the unfolding. A systematic uncertainty in the method is derived, based on the difference between the generated and the unfolded distributions.

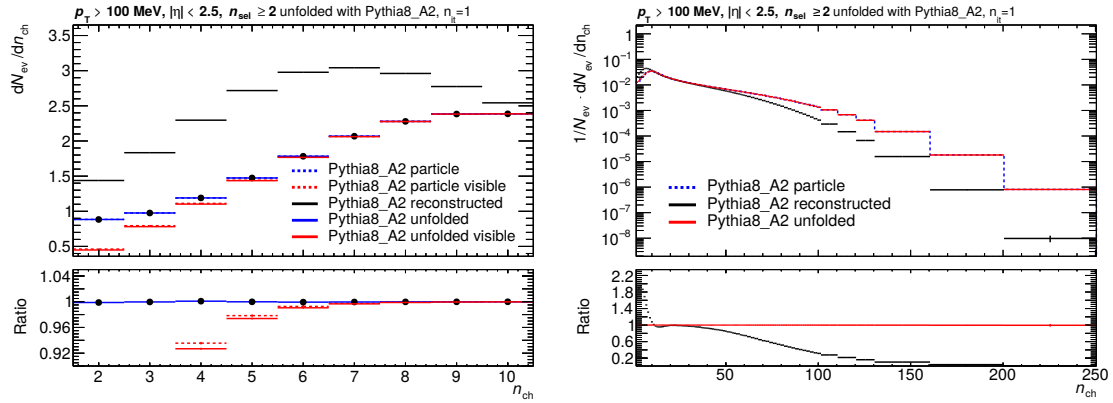

Figure 10.2: Closure test for the n_{ch} distribution using the PYTHIA 8 A2 generator for the input distribution and the construction of the unfolding matrix. The label "visible" is used for the subset of events with $n_{\mathrm{sel}} \geq 2$ that do not migrate outside the detector phase-space. The bottom panel shows the ratio to the particle level. The closure test is shown for a zoom to low multiplicities (left) and for the full range (right).

As a first test, the n_{ch} distribution on particle level predicted from PYTHIA 8 A2 is compared to the unfolded distribution using PYTHIA 8 A2 as input for the matrix calculation. By construction, those two distributions should agree. This is shown for the n_{ch} distribution in Figure 10.2. The ratio between the unfolded and the particle distribution is flat at one (blue line in ratio panel on the left-hand side and red line on the right-hand side). In the figure, the unfolded and particle distributions are also shown for events with $n_{\mathrm{sel}} \geq 2$ which do not migrate outside the detector phase-space. The unfolded and particle distributions are labelled "visible" and correspond to the distributions without applying the correction factor $\varepsilon^{\mathrm{miss}}$ (see Equation 10.5). These distributions are also very similar (two red lines) verifying the matrix-based step. In the ratio, one can see that the blue and the red curves do not agree for $n_{\mathrm{ch}} < 6$. The correction factor was introduced to account for events which are lost due to the track reconstruction efficiency but would pass the particle level phase-space cuts, which is mostly relevant for the low n_{ch} bins.

As additional closure tests, the unfolded distribution is compared when unfolding the prediction from the EPOS generator but using the matrix calculated with the PYTHIA 8 A2 generator. The results are shown in Figure 10.3 for the n_{ch} distribution. The same labelling is used as for the previous plot. In the left-hand plot, one can see differences in the first n_{ch} bin, as the ratio between the unfolded and the particle distributions differ by 3.5%. For higher values of n_{ch}, the ratio is at one, so a good agreement can be observed when unfolding the EPOS prediction from the PYTHIA 8 A2 matrix. On the right-hand side, the unfolded distributions for this setup are shown for an increasing number of iterations. As one can see, the agreement between the particle and the unfolded distributions increase with increasing iterations. The differences between the last two shown iterations are already small, thus for this setup five iterations were chosen.

Similar closure studies were also performed for the other distributions. In Figure 10.4, the η distribution is shown using the PYTHIA 8 A2 and EPOS generator as input distribution and applying the different correction factors and the bin-by-bin correction. The ratio shows the agreement between the particle and the corrected distribution. In the very first and the very last bin, a deviation of ~1% can be observed. Other deviations over the full η range are smaller than 0.4%.

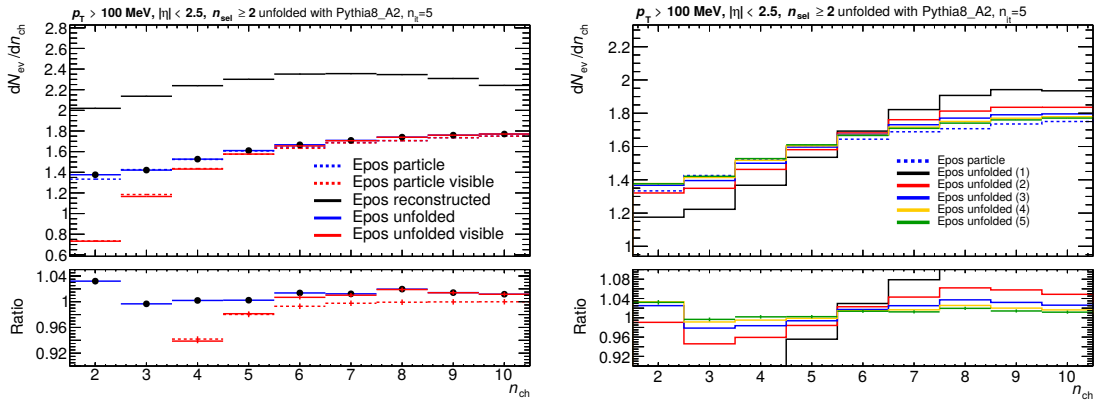

Figure 10.3: Closure test for the n_{ch} distribution (left). The particle and unfolded distributions for an increasing number of iterations (right). For both plots the EPOS generator was used for the input distribution and the PYTHIA 8 A2 generator for the construction of the unfolding matrix. The bottom panel shows the ratio to the particle level.

Figure 10.5 shows the closure tests for the p_{T} distribution using the PYTHIA 8 A2 (left) and EPOS (right) generator. For both cases, the PYTHIA 8 A2 generator was used to calculate the resolution matrix and the track weights. Comparing the generated (particle) to the unfolded distribution shows a very good agreement for both generators.

The closure test for $\langle p_{\mathrm{T}} \rangle$ versus n_{ch} is performed on the distribution itself as well as on the two individual input distributions. This is shown in Figure 10.6 using the PYTHIA 8 A2 generator for the input distribution and the resolution matrix. All three distributions show some disagreement between the generated and the unfolded distribution in the low n_{ch} region. The unfolding works well for $n_{\mathrm{ch}} > 15$ where the ratio is consistent with one.

Additional plots for these closure tests can be found in Appendix B.1 showing other combinations of generator inputs. All observed differences are taken into account for the analysis and are considered as the systematic uncertainty in the unfolding method. For n_{ch}, the general difference is around 3% in the first bin and smaller for the neighbouring bins. The non-closure for n_{ch} can be given as 4%,2%,2%,2% for $n_{\mathrm{ch}} = 2, 3, 4, 5$ respectively. For the η distribution, an overall non-closure of 0.4% is used. The very first and very last bin show larger differences up to 1%. The low p_{T} shows a good agreement between the generated and the unfolded distribution below 1%. The differences increase for increasing p_{T}, but stay below 3% for $p_{\mathrm{T}} > 10\,\mathrm{GeV}$. The ratio between the generated and the unfolded distribution for $\langle p_{\mathrm{T}} \rangle$ versus n_{ch} is nearly flat at one for high n_{ch} values. The differences are below 0.5%. For $n_{\mathrm{ch}} < 15$, a difference of 2% is observed.

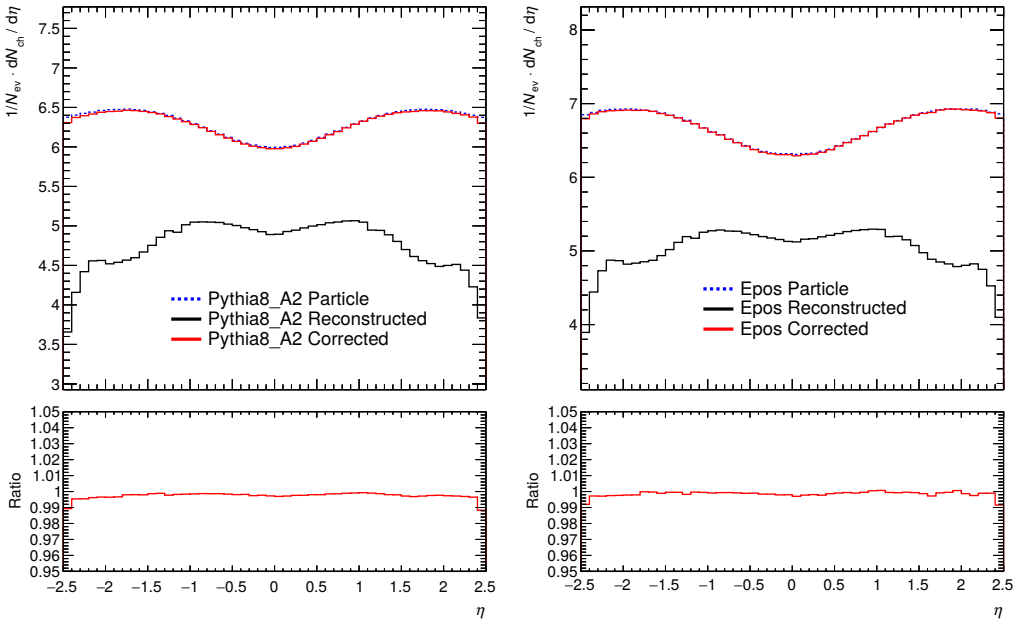

Figure 10.4: Closure test for the η distribution using the PYTHIA 8 A2 (left) and EPOS (right) generator for the input distribution. The bottom panel shows the ratio to the particle level.

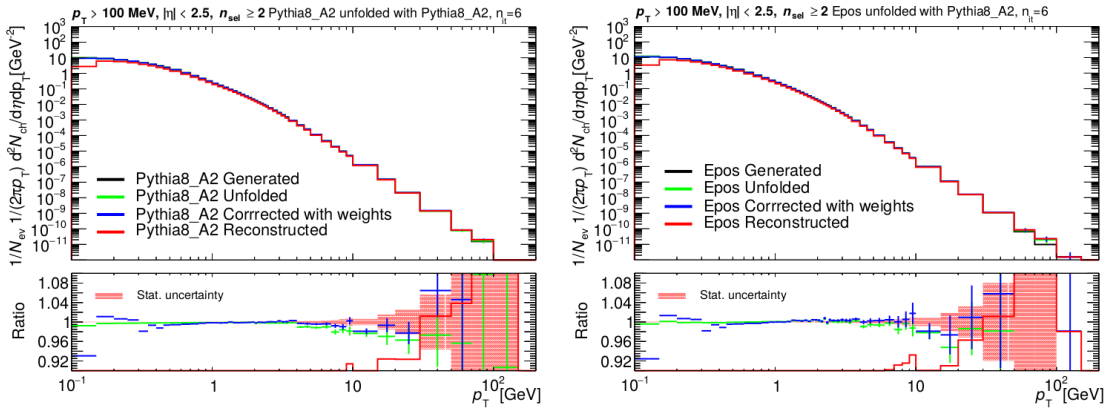

Figure 10.5: Closure test for the p_{T} distribution using the PYTHIA 8 A2 (left) and EPOS (right) generator for the distribution. The input matrix and the track wise corrections are derived from PYTHIA 8 A2 in both cases. The bottom panel shows the ratio to the generated level.

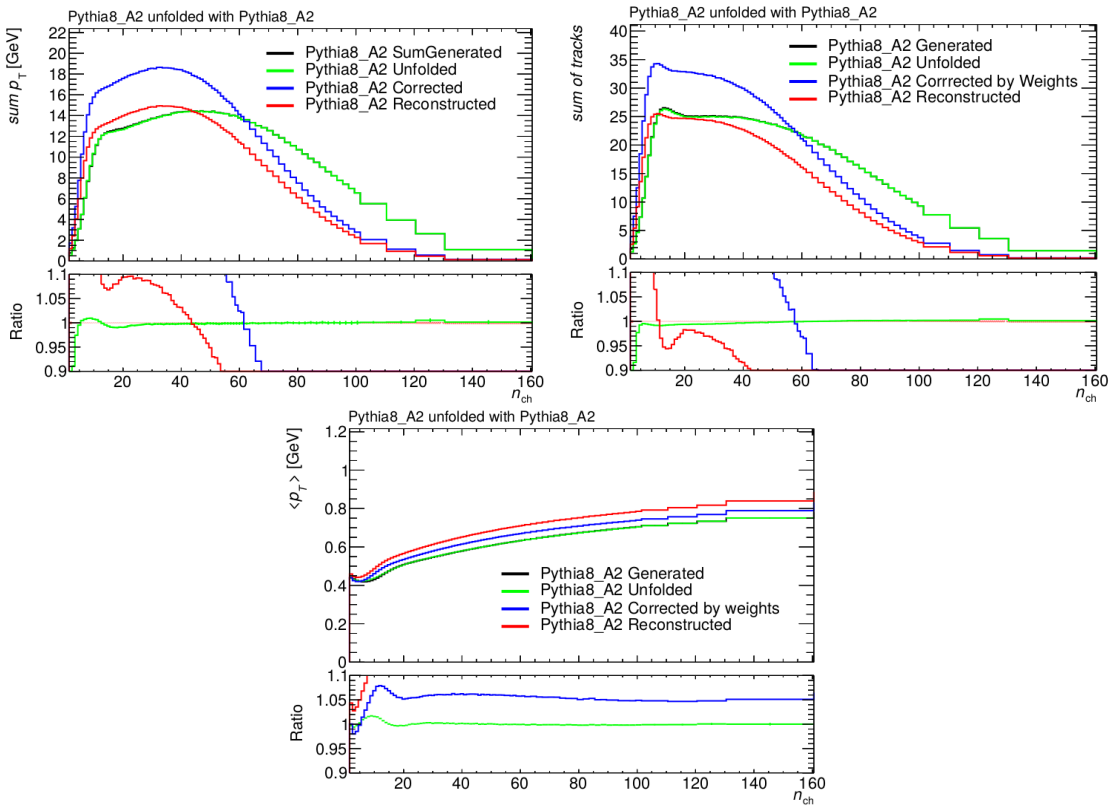

Figure 10.6: Closure test for $\sum_{\text{tracks}} p_{\text{T}}$ versus n_{ch} (left top) and $\sum_{\text{tracks}} 1$ versus n_{ch} (right top) as well as for $\langle p_{\text{T}} \rangle$ versus n_{ch} (bottom) using the PYTHIA 8 A2 generator for the input distribution and the resolution matrix. The bottom panel shows the ratio to the generated level.

10.3 Systematic Uncertainties

The systematic uncertainties are obtained by using modified input distributions. The unfolding procedure is applied to those and compared to the results using the nominal input distribution. For this, the matrix and the correction factors are not changed.

Systematic uncertainties arising from the material are considered. Those incorporate uncertainties due to the modelling of the material as well as the uncertainty obtained in N-1 tests of the track reconstruction efficiency when removing individual selection cuts. The following sources of uncertainties are also considered: The statistical uncertainty of the track reconstruction efficiency, the fraction of non-primary tracks and badly measured tracks which are not removed by the χ^2 cut, the uncertainty due to the out-of-phase-space correction, and the uncertainty related to the removal of strange baryons. The systematic uncertainties from the vertex and trigger efficiency are negligible compared to those from the track reconstruction efficiency and are not considered further in the analysis.

There are additional uncertainties, which are only significant for individual distributions and can be neglected for others. The correction factor $\varepsilon^{\text{miss}}$ is only relevant for the first bins of the n_{ch} distribution and thus the statistical uncertainty in this factor is only taken into account for the n_{ch} distribution. The corrections in the alignment are relevant for the transverse momentum of the tracks and is therefore taken into account for the p_{T} distribution. The statistical uncertainty in the resolution matrix is propagated for both the n_{ch} and the p_{T} distribution.

The differences between data and the MC prediction in the p_{T}-spectrum are also considered as a systematic uncertainty. For this, the average track reconstruction efficiency is calculated as function of n_{sel} for all tracks and compared between data and the prediction from the EPOS and PYTHIA 8 A2 generators. The differences arise from the differences in the p_{T} and η of the tracks. The prediction from EPOS is located between the measured data and the PYTHIA 8 A2 prediction for the full

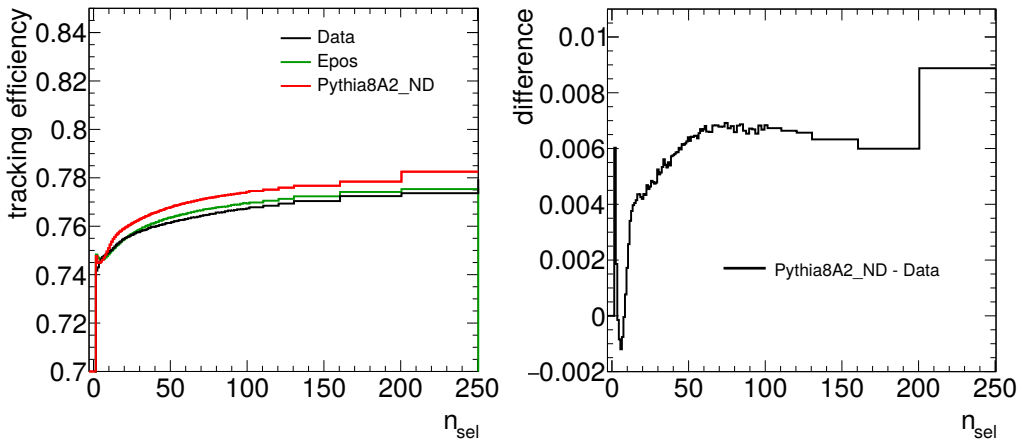

Figure 10.7: The average track reconstruction efficiency as function of n_{sel} for data and the EPOS and PYTHIA 8 A2 generator (left). The difference of the average track reconstruction efficiency between data and PYTHIA 8 A2 (right).

distribution as can be seen in Figure 10.7. Therefore, the difference between data and the prediction from PYTHIA 8 A2 is calculated and the absolute difference is taken as a systematic uncertainty. This difference can be seen on the right-hand side of Figure 10.7, it goes up to 1% for large multiplicities. The systematic uncertainty is applied for the n_{ch} distribution and for $\langle p_{\mathrm{T}} \rangle$ versus n_{ch}.

As described above, the non-closure of the unfolding procedure is taken into account as a systematic uncertainty in the method itself. These uncertainties are determined for each distribution separately. Table 10.2 gives a summary of all systematic uncertainties. As size of the systematic uncertainty, the maximum value observed in at least one bin of at least one distribution is given. The effect of e.g. badly measured tracks is only relevant for the p_{T} distribution, but very small for all other distributions. Overall, the uncertainties on the material and the secondaries have the largest effects for all distributions for this analysis.

In Figure 10.8, the breakdown of the systematic uncertainties is shown for the n_{ch} distribution. Both the unfolded data (labelled "Nominal") and all the different up and down variations are shown. The PYTHIA 8 A2 generator is used to determine the resolution matrix. It is clearly visible, that the effect of the material uncertainty shows the largest differences. The second leading systematic uncertainty arises from the secondaries, where especially the low momentum tracks are sensitive to. On the right-hand side of Figure 10.8, the total uncertainty as well as the contribution of the statistical uncertainty in the resolution matrix are shown. The uncertainty band is not symmetric, as the effect on the shape of the n_{ch} distribution varies for the up and down variations. This effect is strongest for the material uncertainty, as more material leads to a smaller track reconstruction efficiency, and thus less charged-particles, and vice versa. For the material, the up (down) variation is 0.82 (1.38) for the last shown bin.

Figure 10.9 shows the breakdown and the full uncertainty for the η distribution. Especially for this distribution, the main uncertainty arises from the imperfect knowledge of the material in the detector. The large uncertainty at high $|\eta|$ comes mainly from the uncertainty in the Pixel service region.

The breakdown of the systematic uncertainties is shown for the p_{T} distribution in Figure 10.10 on the left-hand side. The right-hand side shows the unfolded distribution with the systematic and the

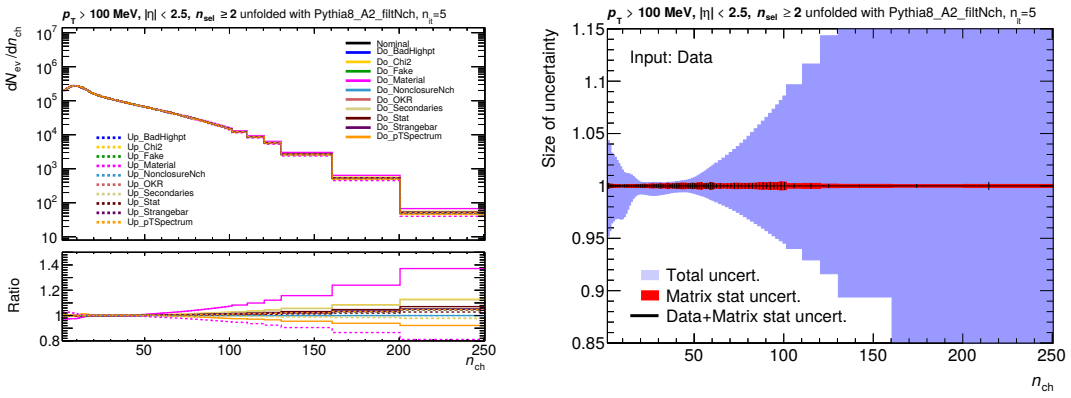

Figure 10.8: Breakdown of all systematic uncertainties for the n_{ch} distribution (left). Total uncertainty and the contribution from the statistical uncertainty from the resolution matrix as function of n_{ch} (right).

Table 10.2: List of all systematic uncertainties. As size the maximum value observed in at least one bin for at least one distribution is given, even if it is much smaller for the other distributions or for most of the bins.

Distribution	Systematic uncertainty	Max. value
all	material	10%
all	secondaries	5%
all	strange baryons	2%
all	badly measured tracks	7%
all	out-of-kinematic-range	0.5%
n_{ch}	propagation of stat uncert. on matrix	<1%
p_T	propagation of stat uncert. on matrix	4% for p_T <10 GeV
		<30% for p_T <14 GeV
		>40% for p_T >14 GeV
n_{ch}, $\langle p_T \rangle$	p_T spectrum	<1%
	Non-closures	
n_{ch}	4%,2%,2%,2% in n_{ch} =2,3,4,5	
η	0.4% for the full range, 1% for the first and last bin	
p_T	1% for p_T ≤10 GeV, 3% for p_T >10 GeV	
$\langle p_T \rangle$	2% in n_{ch} ≤15 and 0.5% everywhere	

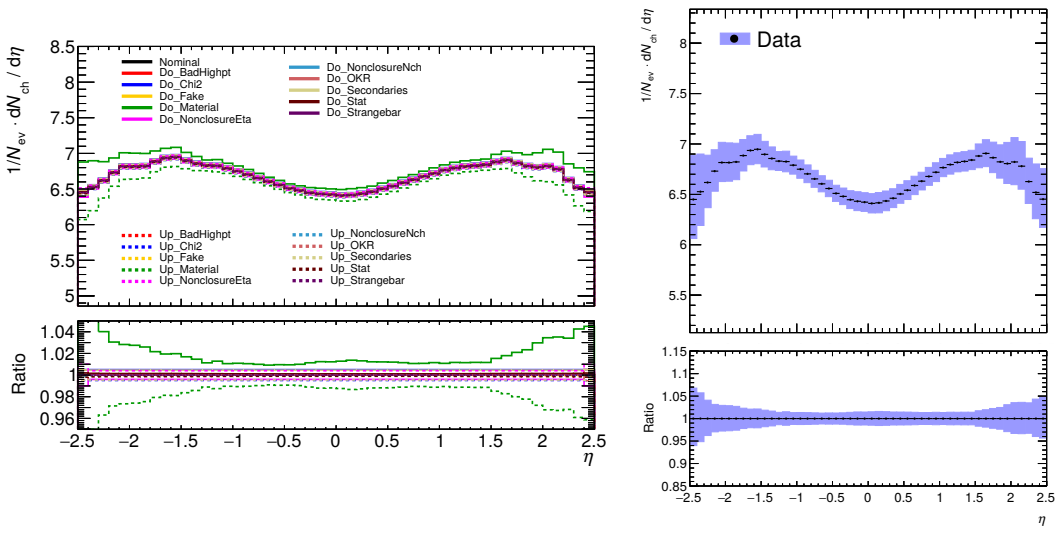

Figure 10.9: Breakdown of all systematic uncertainties for the η distribution (left). The corrected data with the total systematic uncertainty (right).

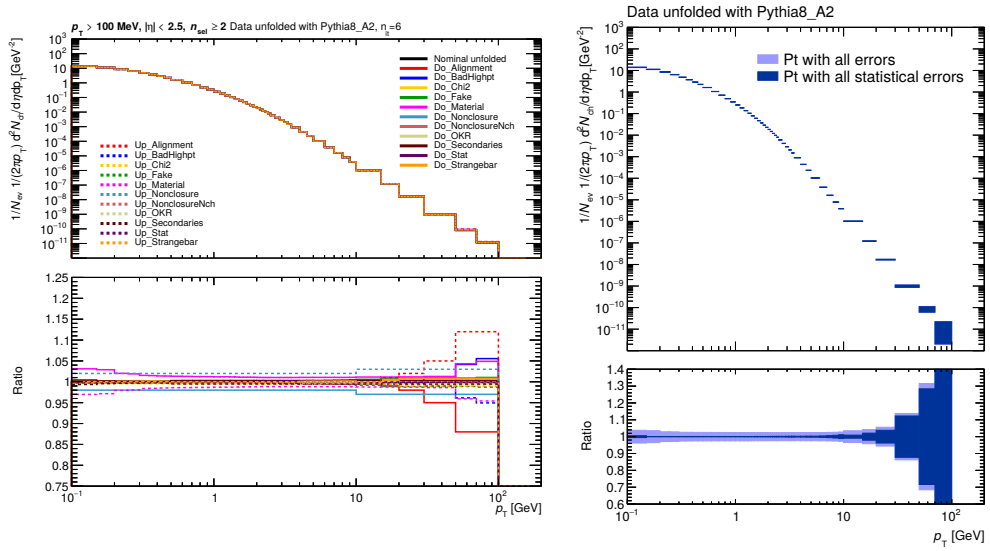

Figure 10.10: Breakdown of all systematic uncertainties for the p_T distribution (left). The corrected data with the total and only the statistical uncertainties (right).

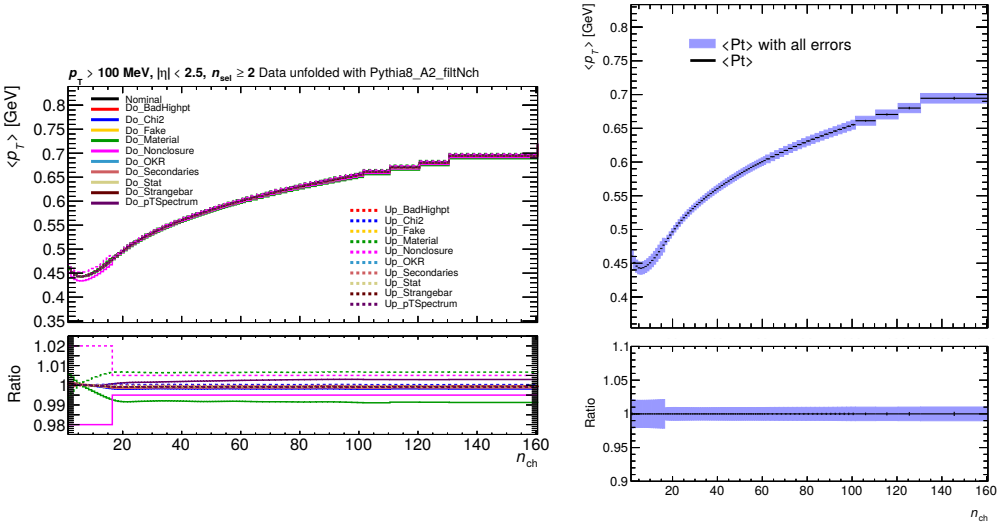

Figure 10.11: Breakdown of all systematic uncertainties for the $\langle p_T \rangle$ versus n_{ch} measurement (left). The corrected data with the total uncertainty (right).

statistical uncertainties combined. For the low momentum region, the imperfect knowledge of the material is again the most dominant systematic uncertainty. For high transverse momentum, the total uncertainty is mostly caused by the statistical uncertainty.

The systematic breakdown and the total uncertainty for the measurement of $\langle p_{\mathrm{T}} \rangle$ versus n_{ch} is shown in Figure 10.11. As previously discussed, for this measurement, first the individual components $\sum_i p_{\mathrm{T}}$ versus n_{ch} and $\sum_i 1$ versus n_{ch} are corrected and unfolded, which includes the individual consideration of the systematic uncertainties. For the final result, the ratio of those two distributions is considered, which leads to a cancellation of many of the systematic uncertainties. This can be seen in the breakdown for the $\langle p_{\mathrm{T}} \rangle$ versus n_{ch} measurement where the dominant uncertainty comes from the observed non-closure. Overall, this measurement is very precise and has, due to the non-closure, a total uncertainty of 2% in the first bin and less than 1% over the full range.

11 Results and Outlook

11.1 Results

The corrected and unfolded data distributions are compared to several MC predictions. Those are produced using a Rivet [135] routine for PYTHIA 8 A2, PYTHIA 8 MONASH, EPOS and QGSJET-II. In Figure 11.1, the unfolded data distributions and the different MC predictions are shown. As previously discussed, strange baryons are excluded from the primary particle definition for those plots. Similar plots are provided in Appendix B.1, where the strange baryons are included and additional plots are presented as comparison to other generators.

The general agreement for the η distribution between the unfolded data and the different MC predictions is good especially in the region $|\eta| < 1.5$. The prediction from the PYTHIA 8 A2 generator forecasts a similar shape, but lies below the data. For both the p_{T} and the n_{ch} distributions, the various MC predictions do not match the data well. Best agreement between the unfolded data and the MC prediction is visible for EPOS. Similar agreement between the prediction from EPOS and the unfolded data can be seen for the $\langle p_{\mathrm{T}} \rangle$ distribution. The agreement for PYTHIA 8 A2 and PYTHIA 8 MONASH gets worse for increasing multiplicities. The description from QGSJET-II is very poor as it predicts a mostly flat distribution.

In order to compare the mean particle density with other and previous ATLAS measurements, the contribution of the strange baryons have to be included into the definition for the primary particles. For this, an extrapolation factor was derived where the central value was calculated using the EPOS generator. The systematic uncertainty is taken as the difference between EPOS and PYTHIA 8 A2, due to the largest difference having been observed between those two generators. The extrapolation factor calculates to 1.0121 ± 0.0035. This results to a mean particle density of

$$\frac{1}{N_{\mathrm{ev}}} \cdot \left.\frac{dn_{\mathrm{ch}}}{d\eta}\right|_{\eta=0} = 6.500 \pm 0.002(\mathrm{stat.}) \pm 0.099(\mathrm{syst.}) \,. \tag{11.1}$$

Figure 11.2 shows the mean particle density including all previous ATLAS measurements [2, 112, 113]. The shown uncertainty includes the statistical and systematic uncertainties for the measured density as well as for the extrapolation factor, added in quadrature. The predictions for this analysis from QGSJET-II, PYTHIA 8 MONASH and EPOS match well, irrespective of the description problems observed in the unfolded distributions. Using the measurement with the lower momentum

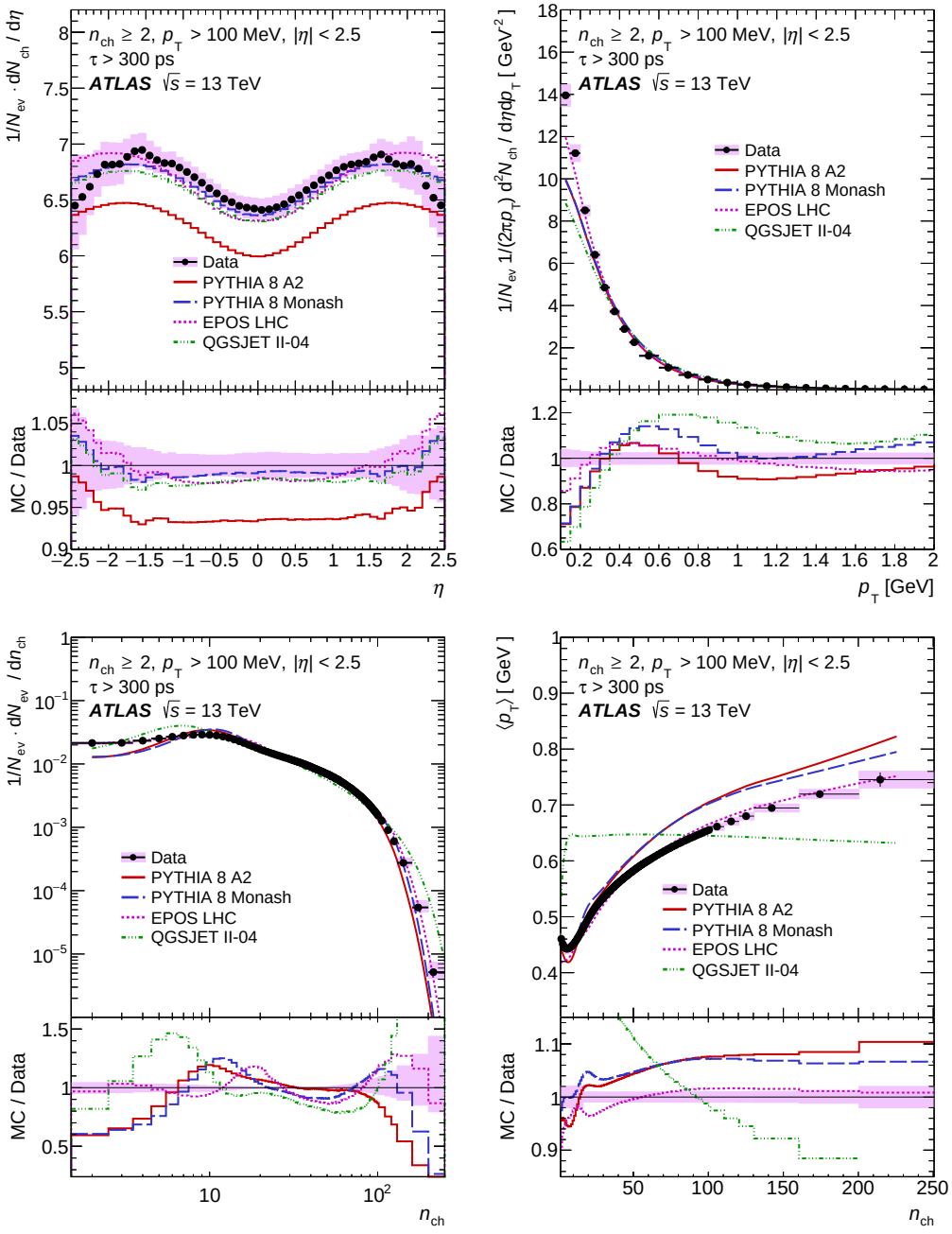

Figure 11.1: Primary charged-particle multiplicities as a function of pseudorapidity η (top left) and transverse momentum p_T (top right), the primary charged-particle multiplicity n_{ch} (bottom left) and the mean transverse momentum $\langle p_T \rangle$ (bottom right). The black dots represent the data and the coloured curves the different MC predictions. The vertical bars represent the statistical uncertainty, while the shaded areas show statistical and systematic uncertainties added in quadrature. The lower panel in each figure shows the ratio of the MC prediction to data.

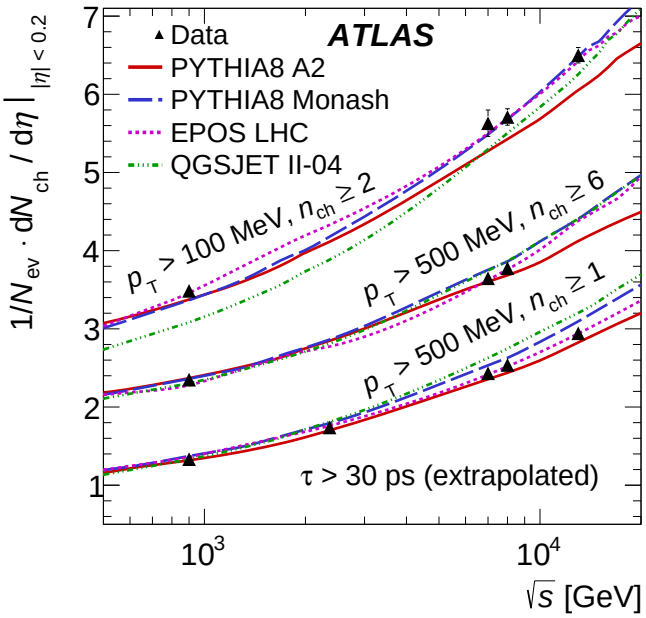

Figure 11.2: Summary plot of mean particle density at $\eta = 0$ including several ATLAS measurements for different phase-spaces and at different centre-of-mass energies [2, 112, 113]. The 13 TeV results have been extrapolated to include strange baryons. The data are shown as black triangle with vertical error bars representing the total uncertainty. They are compared to various MC predictions which are shown as coloured lines.

charged-particles, the low-momentum-transfer, non-perturbative region of QCD is tested in more detail than with the higher momentum charged-particles. Thus, comparing those results helps to better discriminate between the models. Overall, the agreement for PYTHIA 8 A2 seems to be worse compared to the previous ATLAS results at 13 TeV requiring charged-particles with a $p_T > 500$ MeV. On the other hand, the QGSJET-II description seems to be adequate for charged-particles with a $p_T > 100$ MeV, where larger differences were observed for charged-particles with a $p_T > 500$ MeV.

11.2 Summary and Comparison

Primary charged-particle multiplicity measurements with the ATLAS detector are presented for events with at least two primary charged-particles with $p_T > 100$ MeV and $|\eta| < 2.5$. Amongst the models considered, EPOS has the best overall description and both PYTHIA tunes provide an overall reasonable description. The presented results are compared to previous ATLAS measurements as well as to the latest CMS and ALICE measurements mainly comparing the mean particle density results without a detailed explanation of the different analysis methods.

From ATLAS, a previous measurement at $\sqrt{s} = 13$ TeV uses the same data set as the presented analysis, but selecting at least one charged-particle with $p_T > 500$ MeV [2]. A similar analysis strategy is used for both 13 TeV measurements, leading to very similar non-closure uncertainties.

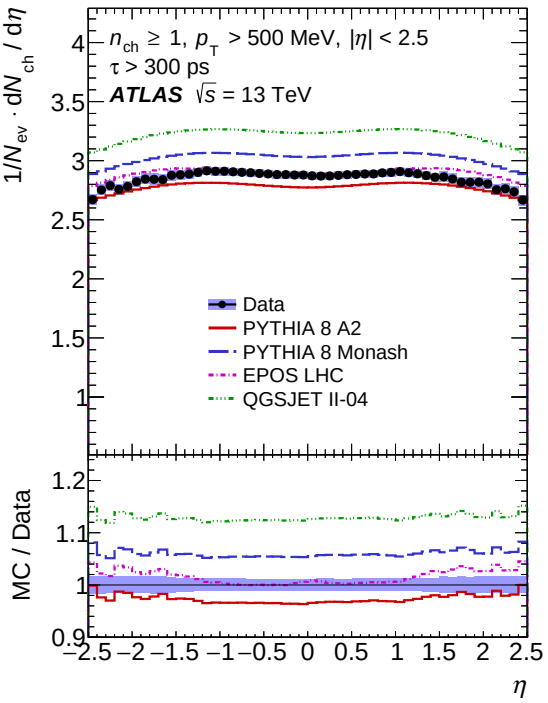

Figure 11.3: Primary charged-particle multiplicities as a function of pseudorapidity η. The black dots represent the data and the coloured curves the different MC predictions. The vertical bars represent the statistical uncertainty, while the shaded area show statistical and systematic uncertainties added in quadrature. The lower panel shows the ratio of the MC prediction to data [2].

Overall, the systematic uncertainties have a similar size, only the uncertainty in the material is larger for the presented analysis as the low p_T tracks are more sensitive to the material.

In Figure 11.3, the pseudo-rapidity distribution is shown for the 500 MeV selection. The charged-particle multiplicity in the central $|\eta|$ region is half of that in the analysis presented here. Overall, the distribution is flat and does not show the increased number of events for $|\eta| \simeq 1.5$. The relationship between the rapidity and the pseudo-rapidity can be approximated as

$$\eta \simeq y + \frac{\cos\theta}{2}\left(\frac{m}{p_T}\right)^2 . \tag{11.2}$$

Both rapidity definitions agree for massless particles or at high transverse momentum. The presented analysis goes down towards lower momentum tracks and thus the mass dependence is increased with respect to the 500 MeV analysis. Following Equation 11.2, a shift away from zero is expected, which leads to the aforementioned structure in the η distribution.

The same phase-space as presented has already been studied at $\sqrt{s} = 8$ TeV at ATLAS [113]. A similar analysis procedure has been used but applied to various phase-spaces. The mean particle density for events with at least two charged-particles with $p_T > 100$ MeV calculates at 8 TeV to

$$\frac{1}{N_{ev}} \cdot \left.\frac{dn_{ch}}{d\eta}\right|_{\eta \leq 0.2} = 5.71 \pm 0.11 . \tag{11.3}$$

This value is lower than the measured mean particle density from the presented 13 TeV measurement (see Equation 11.2), but agrees considering the dependence on the centre-of-mass energy which is also shown in Figure 10.5. The uncertainty has a similar size, as for both analyses the main uncertainty arises from the imperfect knowledge of the material. To reduce the material uncertainty at 8 TeV, detailed studies were performed. The findings of these studies were also adapted for the presented analysis, which helps to reduce the uncertainties for both analyses in the same way. For the presented analysis, the material uncertainties in the high η region are larger compared to the 8 TeV results as it is dominated by the uncertainty arising from the Pixel services which were newly installed during the long shutdown. The slightly smaller uncertainty in the mean particle density, compared to the 8 TeV analysis, originates from the improved track reconstruction due to the IBL detector and thus lower uncertainties in the track reconstruction efficiency.

The latest results from CMS [114] are measured at 13 TeV without a magnetic field. In this analysis, two different reconstruction methods are used. The first method is the tracklet method which uses hit pairs, the second one uses tracks where the tracks are reconstructed from hit triplets. The latter one has overall less background and a better η resolution. For the final result, both methods are combined to get a more robust result. The uncertainties between the methods are considered correlated. The CMS measurements are corrected to inelastic pp collisions. In comparison, the results presented here do not include such a correction, but are defined via particle level phase-space cuts, and are therefore more model independent [136].

CMS measured a mean particle density of

$$\frac{1}{N_{\text{ev}}} \cdot \frac{dn_{\text{ch}}}{d\eta}\bigg|_{\eta \leq 0.5} = 5.49 \pm 0.01(\text{stat.}) \pm 0.17(\text{syst.}) \,. \tag{11.4}$$

The phase-space is not identical to the presented one, but a coarse comparison shows that the overall uncertainty is smaller than the one from CMS. Without the magnetic field, no p_{T} measurement was possible for CMS. Without the magnetic bending, the track reconstruction is more complicated and therefore the uncertainty increases.

The mean particle density was also measured by ALICE [137] for events with at least one charged-particle to

$$\frac{1}{N_{\text{ev}}} \cdot \frac{dn_{\text{ch}}}{d\eta}\bigg|_{\eta \leq 0.5} = 5.31 \pm 0.18 \,. \tag{11.5}$$

For this measurement, tracklets are reconstructed using the positions of the primary vertex and two hits. Overall, the uncertainty is larger than in the presented analysis. The largest systematic uncertainty arises from the normalisation, the detector acceptance and efficiencies and the material. For the low momentum tracklets, the strange hadron content becomes larger and leads also to larger uncertainties.

In conclusion, the various measurements give similar results considering the different η-ranges used to define the mean particle density and the slightly different selections. The systematic uncertainties are lower for the presented and the previous ATLAS measurements compared to CMS and ALICE.

Search for Supersymmetry

Once we accept our limits, we go beyond them.

Albert Einstein

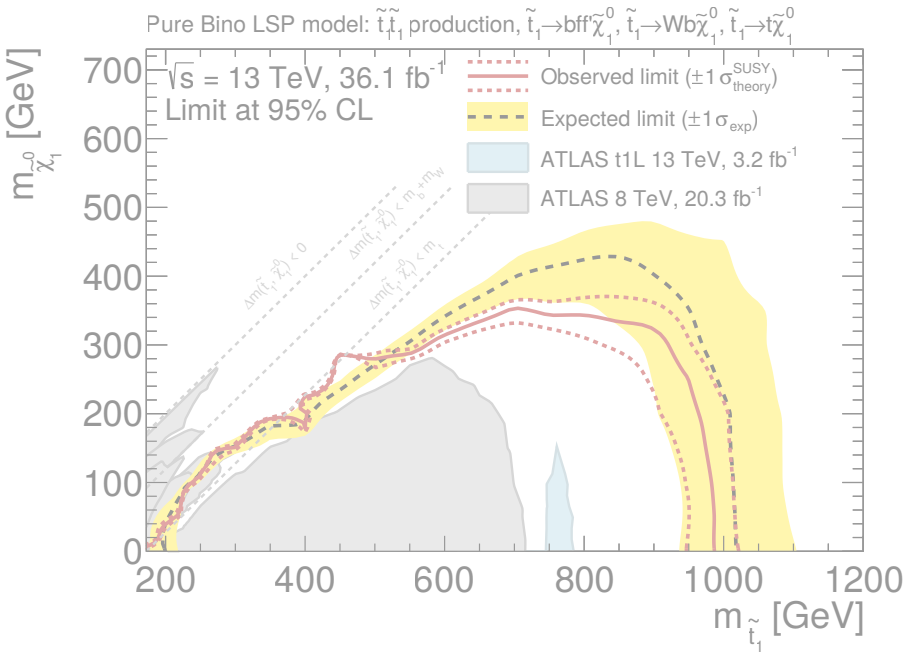

12 Introduction

12.1 Simplified Supersymmetric Model

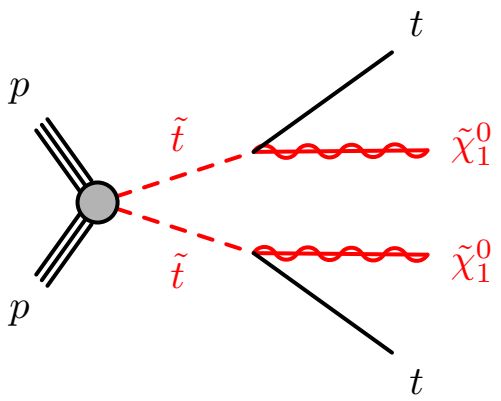

Figure 12.1: The diagram illustrates the top squark decay into a top quark and the lightest neutralino. The sparticles are shown as red lines. The direct top squark production begins with a squark-anti-squark pair, but for simplicity, no charge-conjugate symbols are shown [5].

In Section 2, Supersymmetry and corresponding models were introduced as possible extension to the Standard Model. For the following analysis, the bino LSP scenario is considered (see Section 2.2). Only the top squark and the neutralino are considered to be light, all other particles are assumed to be heavy and well decoupled. Different decays are possible according to the mass splitting between the top squark and the neutralino. The main decay scenario considered in this dissertation is the decay of a top squark to a top quark and a neutralino which is illustrated in Figure 12.1. If the mass difference of the top squark and the neutralino is less than the top quark mass, the top squark can also decay into a bottom quark, a W boson and a neutralino via a so-called three-body decay. The sensitivity towards this decay is tested.

Several distinct regions of parameter spaces are considered in the analysis presented in the published paper [5], two of these are presented in the following. The so-called tN_med region is sensitive to the intermediate to high top squark masses (500 – 900 GeV) and a large range of neutralino masses (0 – 300 GeV). The other parameter space targets the compressed region where the top squark mass

is similar to the sum of the neutralino mass and the top quark mass for light top squark masses (190 – 300 GeV). This parameter space is challenging as the behaviour of the signal is similar to the main SM background. This region is called *diagonal* region.

The kinematics of the signal depends strongly on the mass difference of the top squark and the neutralino. In the scenario targeted by the tN_med region, the high $E_{\mathrm{T}}^{\mathrm{miss}}$ from the signal drives the selection strategy, while in the diagonal region a different approach is needed. The signal there strongly resembles the background, motivating the use of multivariate techniques to gain sensitivity.

12.2 Basic Strategy

The basic strategy of the analysis is to define a so-called signal region (SR). For this, a selection strategy is developed to define a region with a large signal and a small background contribution. The dedicated procedure to define such a signal region depends on the parameter space of interest and is described in the corresponding section.

Once this signal region is defined, the contribution of the main background processes in this phase-space has to be determined. For the leading backgrounds, so-called control regions (CRs) are defined. For each large background, such a region is defined where the corresponding background process is enhanced. To stay in a kinematic similar parameter space as the signal region, only some selection cuts differ compared to the signal region.

The normalisation extracted in the control regions is extrapolated to the signal region. The extrapolation is also validated in validation regions. As the control regions, the validation regions should be dominated by the dedicated background process and stay kinematically as similar as possible to the signal region. Details for these procedures are explained in the dedicated sections.

After the validation of the background estimates, the expected and observed events in the signal region can be checked. The extraction of the background normalisation and the test for a possible signal contribution is done simultaneously in a maximum likelihood fit, as introduced in Section 4.2.

13 Common Analysis Strategy

In the following, two analyses are presented which are part of the published ATLAS results [5]. The optimisation of the tN_med signal region is based on the studies for previous publications [1]. A single bin signal region is defined and additionally a shape fit is performed in order to increase the exclusion potential. The second signal region targets the diagonal region where the signal and the background have very similar kinematics. In order to be sensitive to the signal, a BDT is used to differentiate between signal and background. The full shape information of the BDT output is used in the analysis, to maximise the sensitivity.

The optimisation of both signal regions is done differently and will be explained in detail in the later sections. Common for both regions is the same final state requiring at least one lepton and four jets. The branching ratio for the semi-leptonic decay is smaller than for the pure hadronic decay, but the charged lepton selection in the final state strongly reduces the QCD multijet background. Due to the same final state for both signal region, the same data and Monte Carlo samples are used, the sources of systematic uncertainties are similar, a comparable preselection is applied and similar variables are useful to separate the signal and the various background processes. Those common aspects are explained for both regions combined before the details of each region are given.

13.1 Data and Simulated Samples

The analysis is based on the dataset recorded 2015 and 2016 with the ATLAS detector at a centre-of-mass energy of $\sqrt{s} = 13\,\text{TeV}$. After beam, detector and data quality requirements are applied, the total integrated luminosity calculates to $36.1\,\text{fb}^{-1}$ with an uncertainty of 3.2% [85].

In order to describe the different SM background processes and to model the signal processes, MC simulated events are produced. For this, different generators, PDFs and cross-section calculations are used which are given in Table 13.1. The dominant background $t\bar{t}$ is generated with Powheg-Box v2 [138] at NLO using the CT10 PDF [139] and pythia 6 [140] for the parton shower and the hadronisation. As underlying event tune P2012 [141] is applied. The cross-section calculations are based on NNLO+NNLL [142–147]. The top quark mass for all simulations is set to a value of 172.5 GeV. The same settings are used to produce the single top process where s- and Wt-channels are included and for the Wt process, the diagram removal scheme (DR) [148] is applied. The cross-section calculation is also based on NNLO+NNLL [149, 150]. The t-channel is generated with Powheg-Box v1 using the same PDF set and parton shower as used for the $t\bar{t}$ process.

Table 13.1: Overview of the production of the nominal simulated samples.

Process	MC generator	PDF	PS/had.	Cross-section
$t\bar{t}$	Powheg-Box v2	CT10	pythia 6	NNLO+NNLL
Single-top				
t	Powheg-Box v1	CT10	pythia 6	NNLO+NNLL
s, Wt	Powheg-Box v2	CT10	pythia 6	NNLO+NNLL
W/Z+jets	Sherpa 2.2.0	NNPDF3.0	Sherpa	NNLO
Diboson	Sherpa 2.1.1-2.2.1	CT10/NNPDF3.0	Sherpa	NLO
$t\bar{t}+V$	MG5_aMC@NLO 2.3.3	NNPDF3.0	pythia 8	NLO

The cross-section calculation are based on NNLO+NNLL [151]. For modelling comparisons and the evaluation of systematic uncertainties in the $t\bar{t}$ and single top prediction, similar samples are produced with MG5_aMC@NLO interfaced to Herwig++ and Powheg+Herwig++ [152, 153]. As part of the Wt theoretical modelling uncertainty, the effects between the singly and doubly resonant process are considered. For this, additional samples for $WWbb$, Wt and $t\bar{t}$ are generated at LO with MG5_aMC@NLO interfaced to pythia 8.

Sherpa 2.2.0 [154] is used as generator for W and Z+jets events, where also the parton shower and hadronisation is applied by Sherpa using the default underlying event tune. The NNPDF3.0 [155] PDF as well as NNLO [156] cross-section calculations are used. The diboson generation is done using Sherpa 2.2.1 with the CT10 PDF and NLO cross-section calculation. For the $t\bar{t}+W/Z$ generation, MG5_aMC@NLO 2.3.3 [157] is used at NLO, combined with the parton showering and hadronisation from pythia 8 [122], as well as the A14 [158] tune and the NNPDF3.0. The cross-section is calculated at NLO [157].

The signal samples are generated at LO with MG5_aMC@NLO, including up to two extra partons and interfaced to pythia 8 for parton showering and hadronisation. The cross-section is calculated at NLO+NLL [38] and NNPDF2.3 [131] PDF. For the $\tilde{t}_1 \rightarrow t + \tilde{\chi}_1^0$ samples, the top squark is decayed in pythia 8 using phase-space considerations instead of the full matrix element. Thus the decay products do not preserve the spin information and a polarisation reweighting is needed [159]. For the $\tilde{t}_1 \rightarrow bW\tilde{\chi}_1^0$ and $\tilde{t}_1 \rightarrow bff'\tilde{\chi}_1^0$ samples, the decay is done in MadSpin [160] interfaced to pythia 8. Without calculating the full matrix element, this gives a good description of the kinematic distributions such as the mass of the bW system. For those samples, the top squark is assumed to be composed mainly of $\tilde{t}_R$ which is consistent with the pure bino LSP scenarios.

Samples produced with MG5_aMC@NLO and Powheg use EvtGen v1.2.0 [161] for the modelling of b hadron decays. The signal samples are processed with a fast simulation while all background samples are processed with the full simulation of the ATLAS detector [58]. The effect of multiple pp interactions in the same or a nearby bunch crossing is incorporated by varying the number of minimum-bias interactions overlaid on the hard-scattering event using the pythia 8 A2 prediction. The number of interactions per bunch crossing is reweighted in the simulation to match the distribution in data.

13.2 Preselection

After the general object reconstruction and selection as detailed in Section 7, a basic preselection is applied. Events surviving this preselection are then used to optimise and define the signal region.

The basic preselection is similar for the two regions, as they both target the semi-leptonic decay of the top-squark anti-top-squark pair. Thus, exactly one lepton (electron or muon), at least one b-jet and at least four jets are required. A veto on events with a second baseline lepton reduces the contribution from dileptonic $t\bar{t}$ production. The largest backgrounds after this selection are events from $t\bar{t}$ and W+jets processes. Any background process with mis-measured jets can be reduced with additional cuts on the angular distance between the first two leading jets and the missing transverse energy ($|\Delta\phi(j_{1,2}, E_{\mathrm{T}}^{\mathrm{miss}})| > 0.4$). This cut reduces largely the contribution from QCD multijet events. A QCD estimate was performed for Reference [5] and the contribution from multijet events was found to be negligible with a much looser selection. Furthermore, the angular cut improves the resolution of the m_{T} variable which is defined as

$$m_{\mathrm{T}} = \sqrt{2 \cdot p_{\mathrm{T}}^{\ell} \cdot E_{\mathrm{T}}^{\mathrm{miss}} \cdot (1 - \cos\Delta\phi(\ell, E_{\mathrm{T}}^{\mathrm{miss}}))}\,. \tag{13.1}$$

Here $\Delta\phi$ is the azimuthal angle between the lepton and the direction of the missing transverse energy. The resulting m_{T} distribution is shown in Figure 13.1 for the two leading background processes – $t\bar{t}$ and W+jets. Additionally, a benchmark for the diagonal ($m(\tilde{t}_1, \tilde{\chi}_1^0) = (250, 62)$ GeV) and for the tN_med ($m(\tilde{t}_1, \tilde{\chi}_1^0) = 600, 300)$ GeV) signal region is shown. For SM decays including a W boson decay, this is equivalent to the transverse W boson mass and the distribution tends to values below the W boson mass apart from resolution effects. Due to the additional transverse energy from the neutralinos in the top squark pair decay, the m_{T} reaches higher values for the two benchmark signals with a larger effect for the tN_med benchmark sample where the neutralino momentum is expected to be larger. When applying the preselection cut at 120 GeV, the largest part of the W+jets background is already removed and is therefore not included in the further plots. The dominant

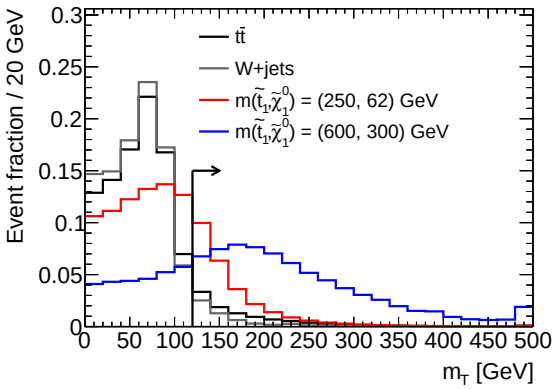

Figure 13.1: m_{T} distribution for the two dominant backgrounds– $t\bar{t}$ and W+jets – and a benchmark signal for the diagonal and the tN_med signal region after requiring $= 1\ell$, $\geq 1b$-jet, ≥ 4 jets, $E_{\mathrm{T}}^{\mathrm{miss}} >$ 120 GeV and $|\Delta\phi(j_{1,2}, E_{\mathrm{T}}^{\mathrm{miss}})| > 0.4$. The black line illustrates the position of the m_{T} preselection cut. The distributions are normalised to unit area in order to show the shape differences.

background after applying the preselection cut stems from dileptonic $t\bar{t}$ events where one lepton is outside the detector acceptance or a hadronically decaying τ lepton.

The semi-leptonic and dileptonic $t\bar{t}$ processes behave very differently. The dileptonic $t\bar{t}$ process easily survives the m_{T} requirement, but to enter the selection two extra jets are required. In order to take any differences into account, the $t\bar{t}$ process is split in the full analysis into the two separate components – dileptonic ($t\bar{t}$ 2L) and semi-leptonic ($t\bar{t}$ 1L) $t\bar{t}$.

The stransverse mass m_{T2} [162] variable targets decays with invisible decay products inside, assuming a decay topology with two branches a and b. For a branch i (with $i = a, b$), the sum of the four vectors of the measured momenta are labelled as $p_i = (E_i, \vec{p}_{\mathrm{T}i}, p_{zi})$ and the sum of the four vectors of the unmeasured momenta as $q_i = (F_i, \vec{q}_{\mathrm{T}i}, q_{zi})$. Using the mass relations $m^2_{p_i} = E_i^2 - \vec{p}_i^{\,2}$ and $m^2_{q_i} = F_i^2 - \vec{q}_i^{\,2}$, the general transverse mass for branch i can be defined as

$$m^2_{\mathrm{T}i} = \left(\sqrt{p^2_{\mathrm{T}i} + m^2_{p_i}} + \sqrt{q^2_{\mathrm{T}i} + m^2_{q_i}}\right)^2 - (\vec{p}_{\mathrm{T}i} + \vec{q}_{\mathrm{T}i})^2 \,. \tag{13.2}$$

To generalise this, m_{T2} is defined as minimisation of the missing transverse energy between $\vec{q}_{\mathrm{T}a}$ and $\vec{q}_{\mathrm{T}b}$ while maximising $m_{\mathrm{T}a}$ or $m_{\mathrm{T}b}$

$$m_{T2} = \min_{\vec{q}_{\mathrm{T}a} + \vec{q}_{\mathrm{T}b} = \vec{E}^{\mathrm{miss}}_{\mathrm{T}}} \{\max(m_{\mathrm{T}a}, m_{\mathrm{T}b})\} \,. \tag{13.3}$$

There are different variants of this variable which only differ in the measured particles, the assumed unmeasured particles and the choices for the input masses m_{qa} and m_{qb}.

Dileptonic $t\bar{t}$ events where one of the two leptons decays via a hadronically decaying τ are further suppressed using the stransverse mass variable m^{τ}_{T2}. As measured particles, the τ candidate is assigned to branch a and the charged lepton to branch b. This means, the unmeasured particles in branch a are the two neutrinos associated with the W and τ decay, and the neutrino associated with the charged lepton is assigned to branch b. Therefore the input masses are chosen as $m_{qa} = m_{qb} = m_{\nu} = 0\,\mathrm{GeV}$. This is illustrated in Figure 13.2 on the left-hand side. With these assumptions the

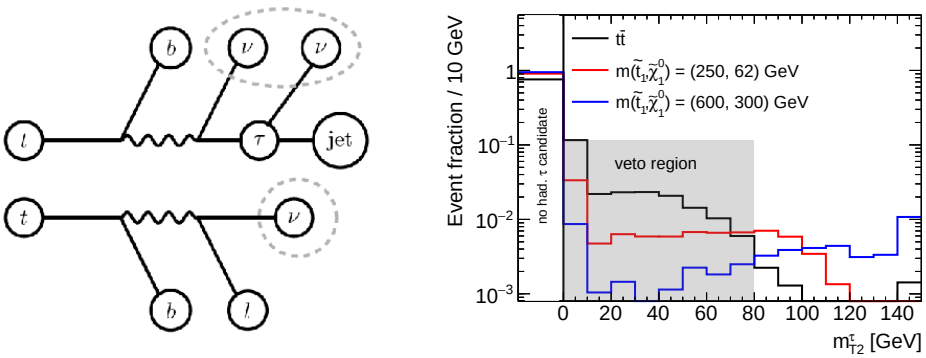

Figure 13.2: Illustration of the m^{τ}_{T2} reconstruction (left) and the resulting distribution (right) for the leading background process $t\bar{t}$ and a benchmark signal for the diagonal and the tN_med signal region after requiring = 1ℓ, $\geq 1b$-jet, ≥ 4 jets, $E^{\mathrm{miss}}_{\mathrm{T}} > 120\,\mathrm{GeV}$, $|\Delta\phi(j_{1,2}, E^{\mathrm{miss}}_{\mathrm{T}})| > 0.4$ and $m_{\mathrm{T}} > 120\,\mathrm{GeV}$. The coloured box (veto region) illustrates the region which is cut out.

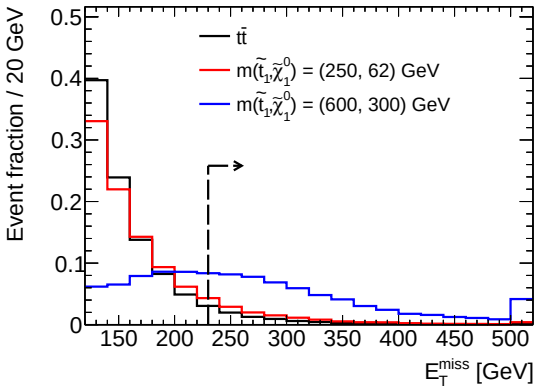

Figure 13.3: $E_{\mathrm{T}}^{\mathrm{miss}}$ distribution for the leading background process $t\bar{t}$ and a benchmark signal for the diagonal and the tN_med signal region after requiring = 1ℓ, $\geq 1b$-jet, ≥ 4 jets, $E_{\mathrm{T}}^{\mathrm{miss}} > 120\,\mathrm{GeV}$, $|\Delta\phi(j_{1,2}, E_{\mathrm{T}}^{\mathrm{miss}})| > 0.4$, $m_{\mathrm{T}} > 120\,\mathrm{GeV}$ as well as the m_{T2}^{τ} veto. The dashed black line illustrates the increased position of the $E_{\mathrm{T}}^{\mathrm{miss}}$ cut for the tN_med preselection. The distributions are normalised to unit area in order to show the shape differences.

m_{T2}^{τ} variable can be calculated. For the SM background processes, the endpoint of this variable is around the W boson mass, where the signal tends towards higher values as the $E_{\mathrm{T}}^{\mathrm{miss}}$ spectrum and the jets are harder. This effect is stronger for the tN_med benchmark signal as the differences between the signal and the background increase with increasing top squark and neutralino mass difference. In case of a hadronically decaying τ candidate, the event is vetoed when $m_{T2}^{\tau} < 80\,\mathrm{GeV}$. An event will be kept, if no hadronically decaying τ candidate is found. The full m_{T2}^{τ} distribution is shown in Figure 13.2 where the coloured area indicates the removed events (veto region).

The $E_{\mathrm{T}}^{\mathrm{miss}}$ distribution is shown in Figure 13.3 after applying the looser preselection requirement of 120 GeV. The SM background processes as e.g. $t\bar{t}$ have only a small amount of $E_{\mathrm{T}}^{\mathrm{miss}}$. The signal kinematic for the diagonal benchmark sample is very similar, as no additional $E_{\mathrm{T}}^{\mathrm{miss}}$ can be produced in the compressed region and thus no tighter cut is applied. The $E_{\mathrm{T}}^{\mathrm{miss}}$ increases when the mass difference between the top squark and the neutralino increases and thus the neutralinos have a larger momentum. As they cannot be measured in the detector, this results into larger $E_{\mathrm{T}}^{\mathrm{miss}}$ as visible for the tN_med signal benchmark. For the tN_med region an increased $E_{\mathrm{T}}^{\mathrm{miss}}$ cut is used in the preselection at 230 GeV which is shown as dashed line in the plot. Using this tighter preselection reduces a large amount of the background contribution for this signal region.

In Table 13.2, the exact preselection requirements are given for both the diagonal and the tN_med signal region. Due to the $E_{\mathrm{T}}^{\mathrm{miss}}$ requirement, the preselection for the diagonal region is looser.

The tN_med signal region requires a $E_{\mathrm{T}}^{\mathrm{miss}}$ cut of 230 GeV and therefore the $E_{\mathrm{T}}^{\mathrm{miss}}$ trigger is applied. The trigger efficiency is shown for data and $t\bar{t}$ events on the left-hand side of Figure 13.4 and is larger than 95% for the given $E_{\mathrm{T}}^{\mathrm{miss}}$ selection. The data and $t\bar{t}$ simulation agree well for all events with $E_{\mathrm{T}}^{\mathrm{miss}} > 230\,\mathrm{GeV}$ which verifies a good modelling of the trigger turn-on.

For events with $E_{\mathrm{T}}^{\mathrm{miss}} < 230\,\mathrm{GeV}$, the trigger efficiency gets low and differences between data and $t\bar{t}$ events show up. Thus the $E_{\mathrm{T}}^{\mathrm{miss}}$ trigger alone is not sufficient for the diagonal preselection. For this preselection, a combination of the $E_{\mathrm{T}}^{\mathrm{miss}}$ trigger and the single lepton triggers is used. The $E_{\mathrm{T}}^{\mathrm{miss}}$ trigger is used for events with $E_{\mathrm{T}}^{\mathrm{miss}} > 230\,\mathrm{GeV}$ and the single lepton triggers are used for the events with a lower $E_{\mathrm{T}}^{\mathrm{miss}}$ value. The single lepton triggers are 90% (80%) efficient for electrons (muons).

Table 13.2: Preselection requirements applied before the signal region is optimised for the diagonal phase-space and the region targeting intermediate top squark masses (tN_med).

Selection	Diagonal	tN_med	Comment
Trigger	$E_{\mathrm{T}}^{\mathrm{miss}}$ or lepton	$E_{\mathrm{T}}^{\mathrm{miss}}$	$E_{\mathrm{T}}^{\mathrm{miss}}$ trigger when $E_{\mathrm{T}}^{\mathrm{miss}} > 230\,\mathrm{GeV}$
Jet cleaning	yes	yes	veto jets failing the loose cleaning criteria
Signal lepton	$= 1$	$= 1$	no additional baseline lepton
Signal jets	≥ 4	≥ 4	
b-jet	≥ 1	≥ 1	
$\lvert\Delta\phi(j_{1,2}, E_{\mathrm{T}}^{\mathrm{miss}})\rvert$	> 0.4	> 0.4	reduces events with mis-measured jets
m_{T2}^{τ}	$> 80\,\mathrm{GeV}$	$> 80\,\mathrm{GeV}$	remove events with had. τ candidates
m_{T}	$> 120\,\mathrm{GeV}$	$> 120\,\mathrm{GeV}$	
$E_{\mathrm{T}}^{\mathrm{miss}}$	$> 120\,\mathrm{GeV}$	$> 230\,\mathrm{GeV}$	

In Figure 13.4, the $E_{\mathrm{T}}^{\mathrm{miss}}$ distribution is shown when using the combination of single lepton and $E_{\mathrm{T}}^{\mathrm{miss}}$ trigger as described above and using only the lepton trigger for $t\bar{t}$ events. Adding the $E_{\mathrm{T}}^{\mathrm{miss}}$ trigger increases the amount of events for the $E_{\mathrm{T}}^{\mathrm{miss}}$ tail by 20%.

In Figure 13.5, the contribution of the different background components is shown for both preselections. The leading background process is dileptonic $t\bar{t}$. The next leading background for the diagonal preselection is semi-leptonic $t\bar{t}$, followed by W+jets. Due to the higher $E_{\mathrm{T}}^{\mathrm{miss}}$ requirement for the tN_med preselection, more semi-leptonic $t\bar{t}$ is removed as only one neutrino contributes to the $E_{\mathrm{T}}^{\mathrm{miss}}$ (compared to two neutrinos in the dileptonic $t\bar{t}$ case). Therefore the W+jets contribution is slightly larger for this preselection compared to semi-leptonic $t\bar{t}$. Smaller backgrounds which are taken into account in the analysis are single top (dominated by dileptonic Wt channel), $t\bar{t}+V$ and diboson processes.

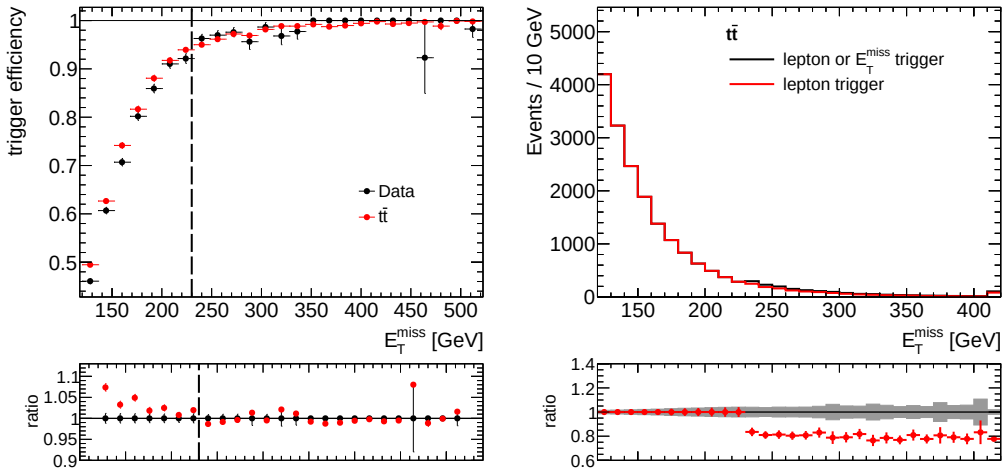

Figure 13.4: Trigger efficiency versus $E_{\mathrm{T}}^{\mathrm{miss}}$ for data and $t\bar{t}$ simulation. The preselection cut for tN_med is indicated as black dashed line (left). $E_{\mathrm{T}}^{\mathrm{miss}}$ distribution using the combination of single lepton or $E_{\mathrm{T}}^{\mathrm{miss}}$ trigger and using only the single lepton trigger (right).

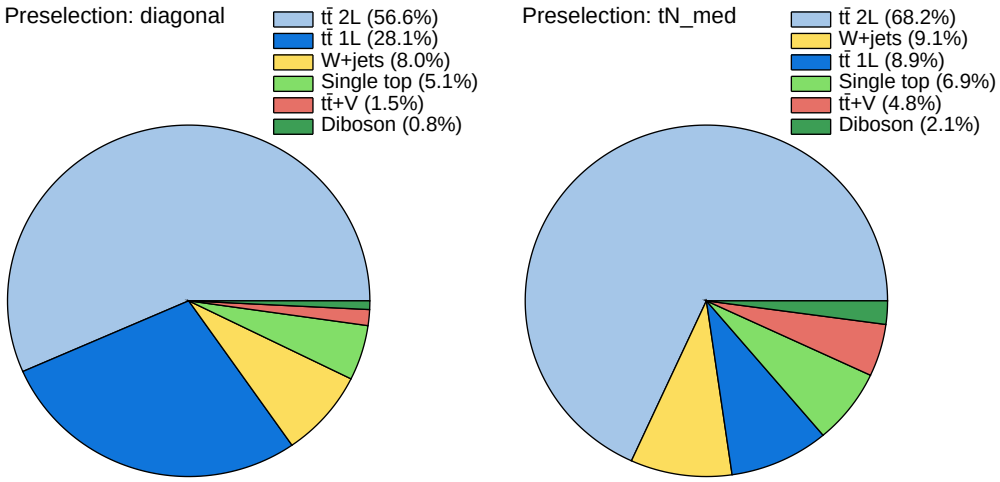

Figure 13.5: Contribution of the various background components after the diagonal (left) and the tN_med (right) preselection.

13.3 Variables Separating between Signal and Background

In the following, further variables are presented which are used either for the tN_med or the diagonal signal region. All those variables are shown as shape comparison plots after applying the looser preselection as needed for the diagonal region. The leading background process $t\bar{t}$ and two benchmark signals are shown. The benchmark signal for the compressed phase-space has a top squark mass of 250 GeV and a neutralino mass of 62 GeV such that is located near the diagonal boundary. The tN_med benchmark signal has a higher top squark mass with 600 GeV and also a higher neutralino mass with 300 GeV, this signal sample is at the border of the previous exclusion limits [163].

The am_{T2} variable is an asymmetric m_{T2} variant similar to the above described m_{T2}^{τ}. In this case dileptonic events are targeted where one lepton is not reconstructed. As measured particles, one b-jet is assigned to branch a and the second b-jet as well as the charged lepton are assigned to branch b. As only one b-jet is required in the preselection, the b-jets are identified based on the highest b-tagging weights. As the b-tagged jets can thus be assigned in two different ways, both variations are calculated and the minimum is kept for the final variable. The unmeasured particle in branch a is the W boson which decays leptonically but the charged lepton is not identified as lepton. For branch b, the unmeasured particle is the neutrino associated to the measured charged lepton. Thus the input masses are chosen as $m_{qa} = m_W = 80\,\text{GeV}$ and $m_{qb} = m_\nu = 0\,\text{GeV}$. An illustration of this and the corresponding distribution are shown in Figure 13.6. For dileptonic $t\bar{t}$ events where one lepton is lost, this variable is bound from above by the top quark mass. For most of those events the average value is lower at around 140 GeV. A similar shape can be observed for the diagonal benchmark sample, as the mass difference between the top squark, the neutralino and the top quark is small and thus the momenta of the neutralino is small. Therefore, this variable does not help to separate the samples near the diagonal boundary from the $t\bar{t}$ process. Going towards higher top squark masses, higher values for the am_{T2} are observed as the larger momentum of

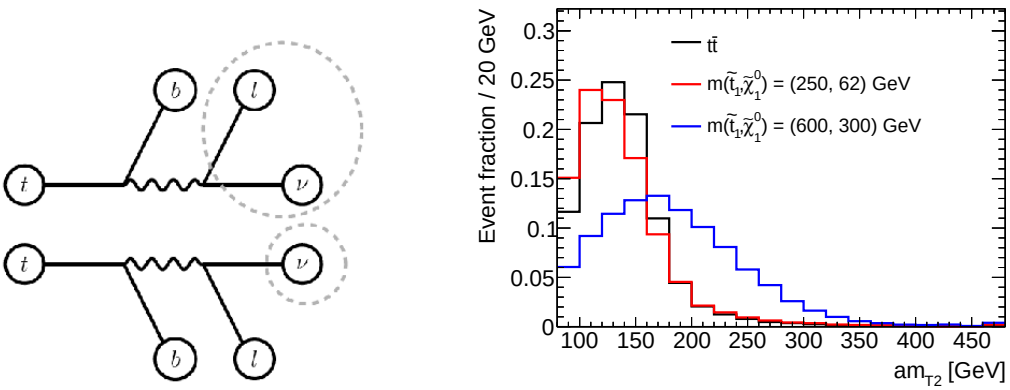

Figure 13.6: Illustration of the am_{T2} reconstruction (left) and the resulting distribution (right) for the leading background process $t\bar{t}$ and a benchmark signal for the diagonal and the tN_med signal region after applying all preselection requirements. The distribution is normalised to unit area in order to show the shape differences.

the neutralinos contributes to the $E_{\mathrm{T}}^{\mathrm{miss}}$ and thus to the individual masses $m_{\mathrm{T}i}$. This shows a good separation potential using the am_{T2} variable for the tN_med signal region.

Another variable used, is the angular distance between the b-jet and the lepton. The variable is called $\Delta R(b, \ell)$ and is shown in Figure 13.7. The b-tagged jet can either be from the same top quark as the lepton, which would lead to smaller values of $\Delta R(b, \ell)$. If the b-tagged jet comes from the hadronically decaying top quark, the $\Delta R(b, \ell)$ value will be larger. Thus a two peak structure can be seen for the $t\bar{t}$ process and the benchmark signal for the compressed phase-space. The tN_med benchmark signal tends toward lower values. As the $t\bar{t}$ system is boosted against the neutralinos, the b-tagged jet is nearer to the lepton independent from which top quark both stem.

The $H_{\mathrm{T,sig}}^{\mathrm{miss}}$ is the negative vectorial sum of the momenta of the signal jets and the lepton and defined as

$$H_{\mathrm{T,sig}}^{\mathrm{miss}} = \frac{|\vec{H}_{\mathrm{T}}^{\mathrm{miss}}| - M}{\sigma_{|\vec{H}_{\mathrm{T}}^{\mathrm{miss}}|}}, \tag{13.4}$$

where the $\sigma_{|\vec{H}_{\mathrm{T}}^{\mathrm{miss}}|}$ is the corresponding resolution. The jet momenta are smeared 1000 times for each event according the corresponding jet energy resolution. The $\vec{H}_{\mathrm{T}}^{\mathrm{miss}}$ is recalculated and the $\sigma_{|\vec{H}_{\mathrm{T}}^{\mathrm{miss}}|}$ is then defined as the RMS of the $\vec{H}_{\mathrm{T}}^{\mathrm{miss}}$ distribution from those smeared jets. The lepton is assumed to be well measured and thus the corresponding uncertainty is not considered. The M is an offset parameter which is taken to be 100 GeV which is a characteristic scale of background processes and was optimised for previous publications [164]. The $H_{\mathrm{T,sig}}^{\mathrm{miss}}$ is thus the significance of the excess of $\vec{H}_{\mathrm{T}}^{\mathrm{miss}}$ above the background expectation. This variable helps to reject backgrounds with $E_{\mathrm{T}}^{\mathrm{miss}}$ due to mis-measured jets. In Figure 13.7, the $H_{\mathrm{T,sig}}^{\mathrm{miss}}$ distribution is shown where a similar shape can be seen for the background and the compressed benchmark signal. The tN_med benchmark tends towards higher values as the neutralinos have a stronger boost in the process and thus the momenta of the lepton and jets are larger.

The leading background comes from dileptonic $t\bar{t}$ events. These events do not have a hadronically decaying top quark, while such a top quark is expected for the signal processes. Thus, reconstructing the hadronically decaying top quark further reduces the dileptonic $t\bar{t}$ process. Two different methods

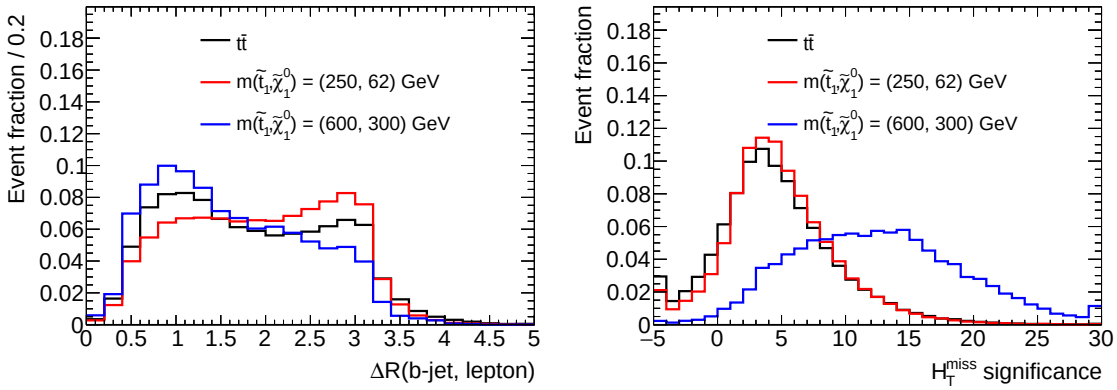

Figure 13.7: $\Delta R(b, \ell)$ (left) and $H_{\mathrm{T,sig}}^{\mathrm{miss}}$ (right) distribution shown for the leading background process $t\bar{t}$ and a benchmark signal for the diagonal and the tN_med signal region after applying all preselection requirements. The distributions are normalised to unit area in order to show the shape differences.

are used for the two signal regions. The reconstructed top quark mass is shown in Figure 13.8 for the $t\bar{t}$ background and both signal benchmarks. For the left-hand side plot, a reclustering technique is used while a χ^2 method is applied for the right-hand side plot. With both techniques, the hadronic top quark decay is reconstructed at a mass of 175 GeV.

The recursive reclustering is based on the usual small radius jets as described previously in the object reconstruction in Section 7. Those jets are clustered together into a large jet using the anti-k_t algorithm with a radius parameter of $R = 3.0$. Using an iterative procedure, this radius is reduced to a radius which approximately matches the p_{T}: $R(p_{\mathrm{T}}) = 2 \cdot m_{\mathrm{top}}/p_{\mathrm{T}}$. If a large fraction of p_{T} loss is observed during the shrinking process, the large radius jet is discarded as a potential candidate. When more than one top quark candidate is found with this procedure, the one with a mass closest to the top quark mass is used. Applying an additional mass cut for the top candidate can therefore help to reduce events with no true hadronically decaying top quark inside. In the shown distribution, the $t\bar{t}$ process includes both semi-leptonic and dileptonic $t\bar{t}$ events leading to a mass peak around the top quark mass produced from the semi-leptonic events.

The other reconstruction method uses a χ^2 minimisation in order to select the three jets which are most compatible with a hadronically decaying top quark. This is done by minimising

$$\chi^2 = \frac{(m_{j_1,j_2,b_i} - m_t)^2}{\sigma^2_{m_{j_1,j_2,b_i}}} + \frac{(m_{j_1,j_2} - m_W)^2}{\sigma^2_{m_{j_1,j_2}}} \tag{13.5}$$

where $i = 1, 2$. As previously, the two jets with the highest b-tagging weight are considered as the b-jets. The two jets j_1, j_2 are the jets with the highest p_{T} excluding b_1 and b_2. The resolution parameters are defined as

$$\sigma^2_{m_{j_1,j_2,b_i}} = m^2_{j_1,j_2,b_i} \cdot (r^2_{j_1} + r^2_{j_2} + r^2_{b_i}) \tag{13.6}$$

$$\sigma_{m^2_{j_1,j_2}} = m^2_{j_1,j_2} \cdot (r^2_{j_1} + r^2_{j_2}) \tag{13.7}$$

where r_x is the fractional jet energy uncertainty of the p_{T} for jet x determined in dedicated studies [5]. The mass combining these three jets as top quark is shown in Figure 13.8 on the right-hand side and

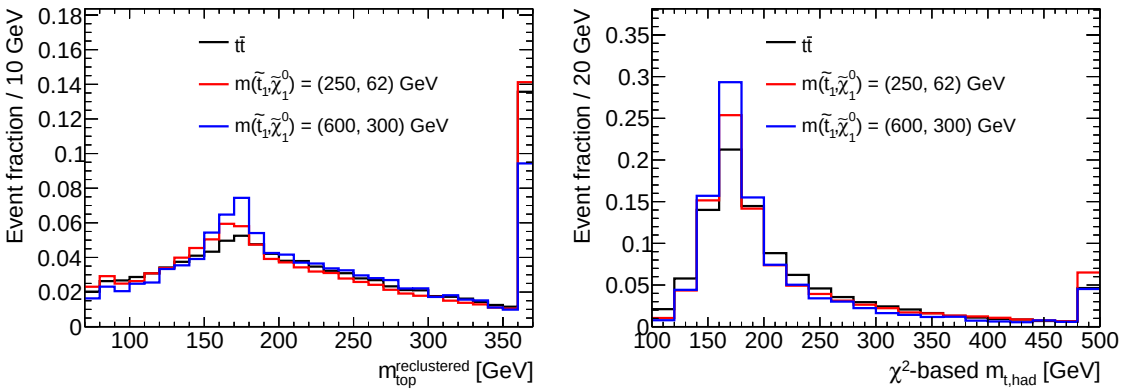

Figure 13.8: Mass distribution of the reclustered hadronic top candidate (left) and using the χ^2 method (right) shown for the leading background process $t\bar{t}$ and a benchmark signal for the diagonal and the tN_med signal region after applying all preselection requirements. The distributions are normalised to unit area in order to show the shape differences.

is referred to as χ^2-based $m_{\mathrm{t,had}}$. Using the χ^2 minimisation, in most of the events, a combination compatible with the top quark mass is calculated. The leptonically decaying top quark can then be reconstructed by combining the lepton with the remaining b-tagged jet, or the highest p_{T} jet (in case the event has exactly one b-tagged jet which was already used for the hadronically decaying top quark).

In Figure 13.9, the hadronic top p_{T} is shown using MC generator information (selecting the true hadronic top). The transverse momentum of the hadronic top quark is strongly related to the mass difference of the top squark and the neutralino. Larger mass differences result in a larger transverse momentum, which can be seen in the comparison between the diagonal and the tN_med benchmark signal: the diagonal signal tends toward lower p_{T} values. On the right-hand side, the efficiency for both top quark reconstruction methods is shown. The reconstruction efficiency for the χ^2 method is estimated using the jets which are matched to the partons with a minimal radial distance of

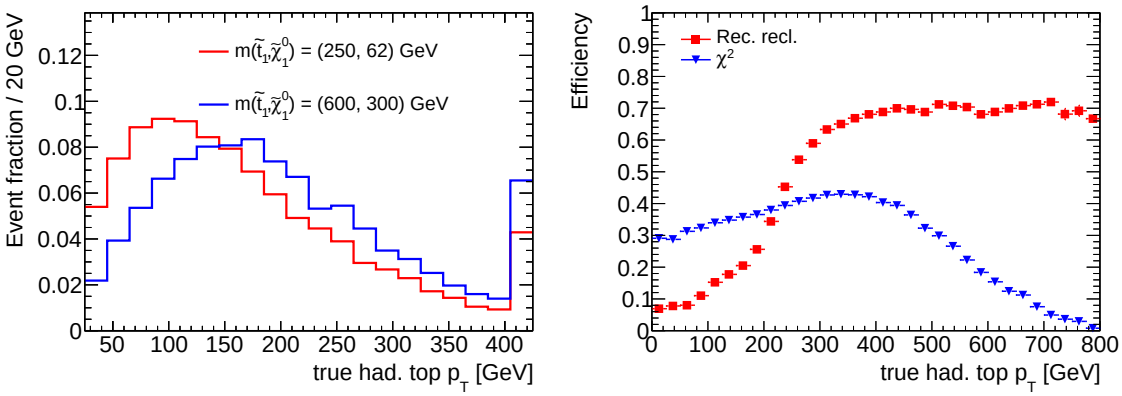

Figure 13.9: Transverse momentum distribution of the true hadronic top quark for $t\bar{t}$ and a benchmark signal for the diagonal and the tN_med signal region (left). The efficiency to reconstruct the hadronically decaying top quark for the χ^2 method and the recursive reclustering (right).

$\Delta R < 0.4$. For the efficiency of the recursive reclustering, the top candidates are matched to a true top quark with a minimal radial distance smaller than the radius of the candidate. Furthermore, the partons are matched to the candidate and no other matches have to be found to reconstruct exactly the hadronic decay. In addition, the top quark mass has to be in the mass window of $m_{\text{top}} \in (150, 200)$. Comparing the two efficiencies versus the true hadronic top quark p_{T} shows that the recursive reclustering is better for higher p_{T} values. But for lower values around $p_{\text{T}} = 100\,\text{GeV}$, the χ^2 method has a higher efficiency. A high efficient top tagging approach is desirable as it can be used to build signal-depleted region by vetoing. For the diagonal benchmark with an overall smaller true hadronic top p_{T}, the χ^2 method is preferred, whereas for the tN_med benchmark the recursive reclustering is used. In cases where also the leptonic top reconstruction is needed, the χ^2 method is used for this reconstruction even for the tN_med signal region.

In the following, additional variables are presented which are based on the χ^2 reconstruction method as these variables use the reconstructed hadronically and leptonically decaying top quark as input for the calculation.

One of these variables is the perpendicular component of the missing transverse energy to the leptonically decaying top quark – $E_{T,\perp}^{\text{miss}}$. For this, both the $E_{\text{T}}^{\text{miss}}$ and the leptonically decaying top

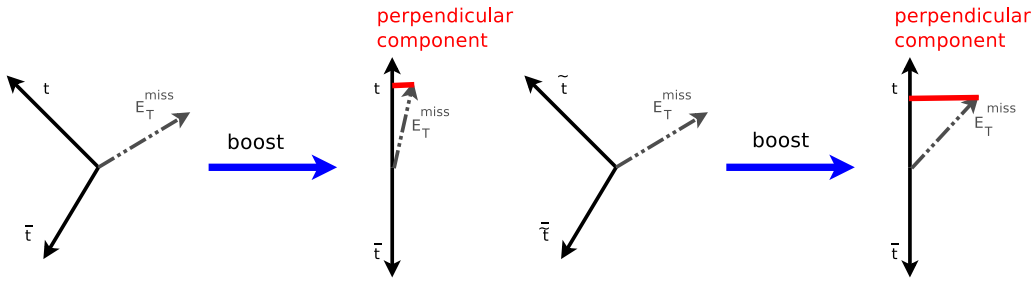

Figure 13.10: Schematic for the $E_{T,\perp}^{\text{miss}}$. For backgrounds, the neutrino is collinear to the $E_{\text{T}}^{\text{miss}}$ and thus a small perpendicular component is expected (left). For top squark decays, the neutralinos contribute to the $E_{\text{T}}^{\text{miss}}$ and thus the collinearity is not given and higher values are expected (right) [165].

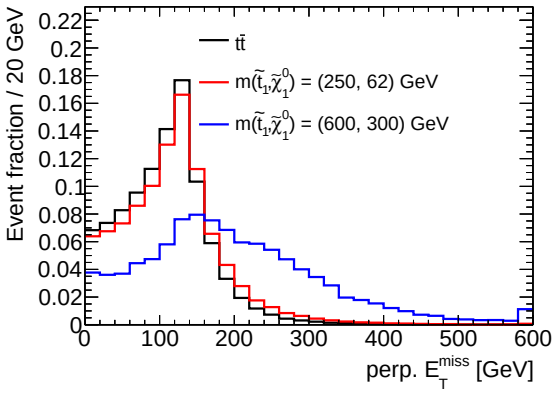

Figure 13.11: $E_{T,\perp}^{\text{miss}}$ distribution shown for the leading background process $t\bar{t}$ and a benchmark signal for the diagonal and the tN_med signal region after applying all preselection requirements. The distributions are normalised to unit area in order to show the shape differences.

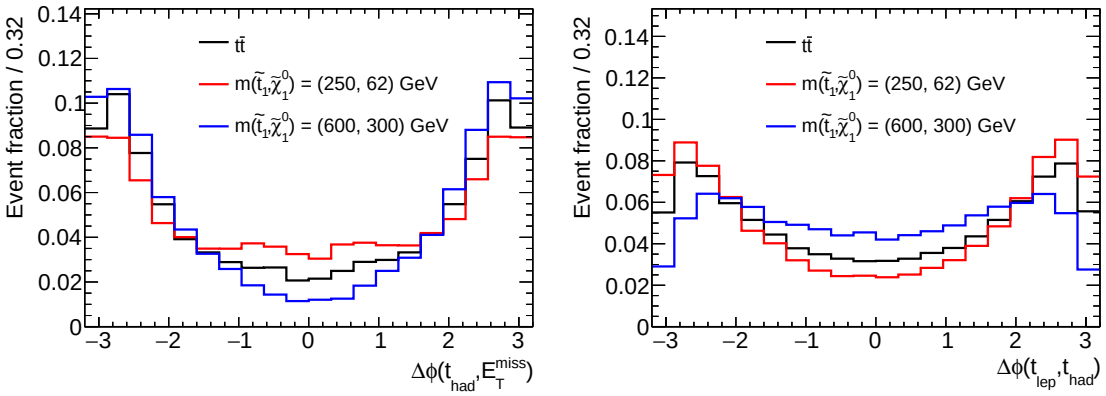

Figure 13.12: Angular distribution between the hadronic top and the $E_{\mathrm{T}}^{\mathrm{miss}}$ (left) and between both top quarks (right) using the χ^2 method for the reconstruction shown for the leading background process $t\bar{t}$ and a benchmark signal for the diagonal and the tN_med signal region after applying all preselection requirements. The distributions are normalised to unit area in order to show the shape differences.

quark are boosted into the $t\bar{t}$ rest frame. For the following calculation only the x- and y-components of the four-vectors are considered. Thus, the magnitude of the perpendicular component can be defined. This is illustrated in Figure 13.10 and the corresponding distribution is shown in Figure 13.11. For the $t\bar{t}$ background, the neutrino is mostly collinear to the leptonically decaying top quark and thus only small values are observed. For the signal, the neutralinos contribute to the missing transverse energy and this distorts the collinearity from the leptonically decaying top quark and the $E_{\mathrm{T}}^{\mathrm{miss}}$. For increasing mass difference between the top squark and the neutralino, the $E_{T,\perp}^{\mathrm{miss}}$ increases. This is visible in the plot, where the $t\bar{t}$ background as well as the signal with low neutralino masses are very similar at values around 120 GeV. For higher mass differences, as for the tN_med benchmark, higher values are observed and a good separation potential can be seen.

Further input variables are angles between the reconstructed hadronically decaying top quark (based on the χ^2 method) and either the $E_{\mathrm{T}}^{\mathrm{miss}}$ or the reconstructed leptonically decaying top quark. The corresponding distributions are shown in Figure 13.12. Overall, only small shape differences are visible as the angle between the decay products changes slightly in the various decays. These differences are not sufficient to use in a cut-based analysis, but can improve the separation in an analysis based on a BDT as it is described later.

13.4 Systematic Uncertainties

Besides the statistical uncertainty coming from the finite number of events in the sample, the signal and background estimation is also affected by systematic uncertainties. Sources of systematic uncertainties are the finite precision of the calibration of the reconstructed objects, the inaccuracies in signal and background modelling and the non-perfect description of the experimental conditions, for example luminosity or pile-up. The sources of the systematic uncertainties are similar for both regions and these common aspects are detailed below. The effects and the estimation of

the systematic uncertainties are different for both signal region and thus the exact handling and additional information are given in the dedicated sections.

13.4.1 Experimental Systematic Uncertainties

The dominant experimental uncertainty arises from the imperfect knowledge of the jet energy scale (JES) and the jet energy resolution (JER) [166, 167]. The jet energy resolution affects the endpoint of the m_{T} distribution and thus influences the efficiency of the m_{T} requirement. For the JES uncertainties, a reduced set of uncertainties is used, which includes three jet energy scale components and one uncertainty for the η-intercalibration. It is designed to reduce the computing time without loosing too many correlation information of the uncertainty [7]. This reduced set is tested and found to be sufficient for this analysis. Further uncertainties arise from the modelling of the b-tagging efficiencies and the mis-tag rates [105, 168].

Smaller sources of the experimental uncertainties are the modelling of the lepton energy scale and energy resolution, the contribution of the $E_{\mathrm{T}}^{\mathrm{miss}}$ soft term, the reconstruction and identification efficiencies as well as the trigger efficiency, the modelling of pile-up and the uncertainty in the integrated luminosity.

13.4.2 Theoretical Systematic Uncertainties

The theoretical systematic uncertainties arise from the imperfect modelling of the processes in MC generators. They are determined by varying the MC generator parameters, such as the renormalisation and factorisation scales, and the merging parameters. In order to assess the influence of the MC generator implementation, the prediction of different MC generators are compared. Further uncertainties arise from the uncertainty in the total cross-section of the predicted backgrounds. As the yields of the dominant backgrounds are determined in dedicated control regions, uncertainties in those processes only affect the extrapolation from the control into the signal region (and amongst the various control regions). Thus for those processes, no cross-section uncertainty is considered.

Considered theoretical systematic uncertainties for $t\bar{t}$ and single top are uncertainties due to the choice of the MC event generator, hadronisation and fragmentation modelling, the amount of initial and final state radiation [169]. The MC generator uncertainty is estimated comparing the events generated with Powheg-Box and Herwig++ v2.7.1 with either MG5_aMC@NLO v2.2.3 and Herwig++ v2.7.1 (NLO) or Sherpa v2.2. To estimate the effect of fragmentation and hadronisation, events are compared which are generated with Powheg-Box and hadronised with either pythia 6 or Herwig++. The size of the initial and final state radiation is estimated by comparing events generated with Powheg-Box +pythia 6 using different parton-shower radiation, NLO radiation, as well as modified factorisation and renormalisation scales where the scales are each varied by a factor of either 0.5 or 2. For the diagonal region, no dedicated control region is built for the single top background and the total cross-section uncertainty for this process is 5.3% [149], derived from the uncertainty in PDF effects and the scales.

Interference effects between $t\bar{t}$ and single top Wt processes are taken into account by using a sample with inclusive $WWbb$ events generated with MG5_aMC@NLO v2.2.3 (LO) which are compared to the sum of the $t\bar{t}$ and Wt events [169].

For W+jets, the generator comparison is performed using SHERPA with MG5_aMC@NLO v2.2.3 and PYTHIA 8 (NLO). Additionally, variations are estimated for the renormalisation, factorisation and resummation scale, and the matching scheme related to the matrix elements and the parton showers.

The modelling uncertainty of the $t\bar{t} + Z$ is estimated using independent variations for the renormalisation and factorisation scales as well as PDF variations. The generator uncertainty is performed comparing events generated with MG5_aMC@NLO v2.2.3 and PYTHIA 8 (NLO) and SHERPA v2.2. For the diagonal region, no dedicated control region is built for this background and therefore the uncertainty in the total cross-section of 13% [157] affects the estimate.

For the diboson background, also the renormalisation, factorisation and resummation scale are varied and taken into account as uncertainty. As no control region is defined for this background, the uncertainty in the cross-section is taken into account and used as uncertainty. This uncertainty in the total cross-section is 6% [170].

For the signal samples, the effect of the cross-section uncertainty is calculated using the envelop of different cross-section predictions varying the different PDF sets, the factorisation and renormalisation scales [38].

14 Intermediate Top Squark Masses

The first analysis presented is the tN_med region targeting intermediate top squark masses and a wide range of neutralino masses. This region is optimised as a cut-and-count signal region using the same optimisation procedure as the other cut-and-count regions in the corresponding publication [5]. The algorithm was developed as part of this dissertation and already applied for signal regions in previous publications [1].

Figure 14.1 shows previous limits from the different ATLAS searches at $\sqrt{s} = 8$ and 13 TeV. The benchmark point for the presented analysis is chosen to be at the border of the previous exclusion with a top squark mass of 600 GeV and a neutralino mass of 300 GeV aiming at intermediate top squark masses.

In this chapter, first the algorithm used for the optimisation is presented and afterwards the details of the tN_med signal region are given. The dominant backgrounds are normalised using a data-driven technique. The exact procedure for the determination and its validation is explained. The compatibility of the background estimate in the signal region with the data is tested in a simultaneous fit, determining also an optional signal contribution.

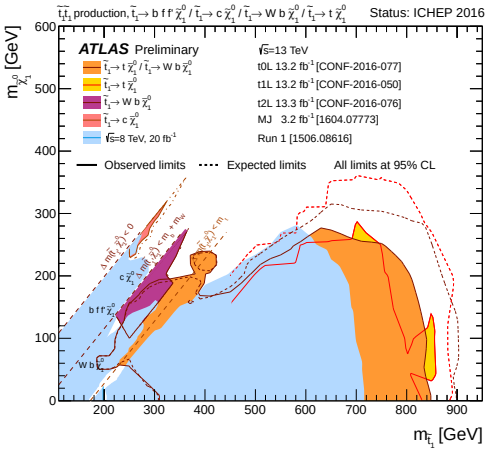

Figure 14.1: Summary of the dedicated ATLAS searches for top squark pair production based on data taken at $\sqrt{s} = 8$ and 13 TeV [163]. Exclusion limits at 95% CLs are shown. The dashed and solid lines show the expected and observed limits, respectively, including all uncertainties except the theoretical signal cross-section uncertainty.

14.1 Optimisation Algorithm

The signal region is defined by requirements on various variables which can separate between the signal and the background processes. These variables can be correlated and thus a simple scan for each variable is not sufficient. It is no option to simply test many combinations as the amount of combinations increases strongly with each new variable. Therefore, an algorithm is defined which finds the optimal set of variables and the exact requirements.

The optimisation is done for a signal process and given background processes after applying a preselection. The algorithm is performed iterative. First of all, for each input variable an optimal cut is searched. This means the cut position, where the expected significance is the largest.[1] The variables are then ranked by the largest significances after these cuts. For the best ranked variable the cut is applied. Afterwards, all variables are ranked again and the next cut is applied, resulting into tighter cuts for each iteration. This is iterated until the change in significance when applying the next cut is lower than one percent.

With this procedure, the first cuts are very tight as no correlations between the variables are taken into account and the cuts cannot be relaxed anymore. Therefore the algorithm is improved by introducing a so-called damping function which limits the minimal background efficiency. With this function, the first cuts are looser than the optimal cut position. The efficiency threshold is determined by the damping function depending on the number of iterations, and no background restriction is applied at a high number of iterations. For each ranking all variables are checked, so basically a tighter cut at the variable from the previous iteration can be applied if no other variable is preferred due to some correlations.

The performance of this damping function was studied with a simplified case. For this, random distributions for a signal and background were produced. Both are produced as 2D Gaussian with the same correlation factor. The cut values and the resulting significances were optimised without any damping function and with a linear and an exponential damping function. Without any damping function, a tight cut is applied on the y variable. In the second iteration, no further cut for the y variable is needed, but the overall significance improves when applying a requirement on the x variable. No further iteration is needed in this case. When using the damping function, the cuts are chosen looser. The cut value increases slightly over the iterations in a similar way for both variables. The number of iterations needed increased in this example to six.

The results are summarised in Figure 14.2. The distributions are shown as well as the different cut values when using no damping function or the linear or exponential damping function. When using a damping function, the cuts used are set more reasonable as they get more symmetric. Without the damping, the first cut was chosen too tight and thus the overall result is worse. This can also be seen in the given significances in the plot, where a value of $5.6\,\sigma$ was calculated when using the algorithm without any damping. With a damping function, the significance increases to around $30\,\sigma$. The best expected significance was achieved in this case with the exponential damping function where also the most symmetric cuts are observed.

[1] The considered significance is calculated using a function provided by the `ROOT` framework – `RooStats::NumberCountingUtils::BinomialExpZ`, which is based on Poisson statistics. This function takes a flat background uncertainty into account. The result of this calculation is conservative compared to the same calculation from `HistFitter`, but much faster and thus a good estimate for an expected significance.

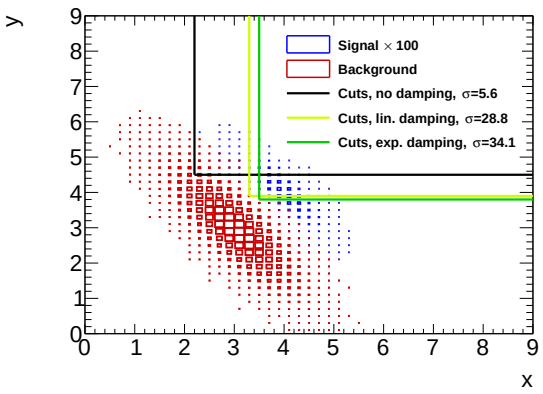

Figure 14.2: Toy signal and background distribution, generated as a 2D Gaussian with the same correlation factor but with different mean values. The signal is scaled by a factor of 100 to be visible. The different cuts and the corresponding significances are shown without damping and for a linear and exponential damping function.

Using this procedure, the first cuts are less powerful and therefore less prone to statistical fluctuations, and the correlations between variables are taken into account. Therefore, the damping function helps to get more reasonable cuts and a better significance. More iteration are needed, when introducing the damping functions, but as the algorithm works fast, this is not a problem. For the optimisation of the tN_med signal region, the exponential damping function is used.

14.2 tN_med Signal Region

The optimisation of the tN_med signal region is performed for one benchmark signal with a top squark mass of 600 GeV and a neutralino mass of 300 GeV after applying the preselection cuts from Table 13.2. The $t\bar{t}$, $t\bar{t}+V$, W+jets, single top and diboson background processes are taken into account in the optimisation. For all backgrounds, a flat uncertainty of 30% is included. The tN_med signal region targets medium top squark masses and a wide range of neutralino masses. The variables discussed in Section 13.3 are used as input variables when a good separation for the tN_med benchmark was observed. All those variables show a good agreement between the data and the SM prediction after the preselection (see Appendix C.1). The exact signal region cuts determined from the optimisation algorithm are given in Table 14.1.

As discussed previously, for the tN_med region the recursive reclustering algorithm is used for the top reconstruction. From this reconstruction, a hadronic top candidate is required with a mass of at least 150 GeV in order to remove events with badly reconstructed top quarks. The am_{T2} requirement sets a threshold at the top quark mass, reducing the $t\bar{t}$ background. The m_{T} requirement is well above the W boson mass. The W+jets background is further reduced by requiring at least one b-tagged jet. In addition, high requirements are placed on the $E_{\mathrm{T}}^{\mathrm{miss}}$ and the $H_{\mathrm{T,sig}}^{\mathrm{miss}}$. In order to reduce the backgrounds further, a $E_{T,\perp}^{\mathrm{miss}}$ cut is applied as well.

In Table 14.2 and Figure 14.3, the pre-fit expected events and the contribution of the different background processes can be seen. The main background process stems from dileptonic $t\bar{t}$ events,

Table 14.1: Overview of the event selections defining the tN_med signal region. The tN_med preselection as defined in Table 13.2 is applied.

	tN_med
Leading jet p_{T}	$> 60\,\mathrm{GeV}$
Second jet p_{T}	$> 50\,\mathrm{GeV}$
Third jet p_{T}	$> 40\,\mathrm{GeV}$
Fourth jet p_{T}	$> 40\,\mathrm{GeV}$
$E_{\mathrm{T}}^{\mathrm{miss}}$	$> 250\,\mathrm{GeV}$
$E_{T,\perp}^{\mathrm{miss}}$	$> 230\,\mathrm{GeV}$
m_{T}	$> 160\,\mathrm{GeV}$
$H_{\mathrm{T,sig}}^{\mathrm{miss}}$	> 14
Mass of the top candidate	$> 150\,\mathrm{GeV}$
am_{T2}	$> 175\,\mathrm{GeV}$
Number of b-tags @ 77%	≥ 1
$\Delta R(b, \ell)$	< 2

followed by the $t\bar{t} + V$ process when applying all tN_med signal region cuts. The $t\bar{t} + Z(\rightarrow \nu\nu)$ background is an irreducible background and becomes relevant especially at high $E_{\mathrm{T}}^{\mathrm{miss}}$. W+jets, single top and diboson processes contribute less, and the semi-leptonic $t\bar{t}$ is nearly negligible after applying these cuts. The exact cut efficiencies are presented for the benchmark signal and the dominant backgrounds – $t\bar{t}$, $t\bar{t} + V$ and W+jets – in Table 14.3. Most of the individual cuts are more than 60% efficient for the benchmark signal, resulting in a total efficiency of 1%. The efficiencies for the background processes are mostly lower, especially applying the $E_{\mathrm{T}}^{\mathrm{miss}}$ and m_{T} cut reduces the background events strongly.

Table 14.2: Pre-fit expected events in tN_med for 36.1 fb^{-1}. Only the statistical uncertainty of the MC samples is given.

tN_med	Electron	Muon	Total
$t\bar{t}$ 2L	5.8 ± 0.6	6.8 ± 0.6	12.6 ± 0.8
$t\bar{t}$ 1L	0.1 ± 0.1	0.1 ± 0.1	0.2 ± 0.1
Single top	1.4 ± 0.2	1.5 ± 0.3	2.9 ± 0.4
W+jets	2.3 ± 0.3	2.7 ± 0.4	5.0 ± 0.5
Diboson	1.2 ± 0.3	0.9 ± 0.1	2.08 ± 0.3
$t\bar{t}$+V	5.9 ± 0.4	6.6 ± 0.4	12.5 ± 0.6
Total SM	16.7 ± 0.8	18.6 ± 0.9	35.3 ± 1.2
Signal	15.1 ± 0.8	17.4 ± 0.9	32.5 ± 1.2

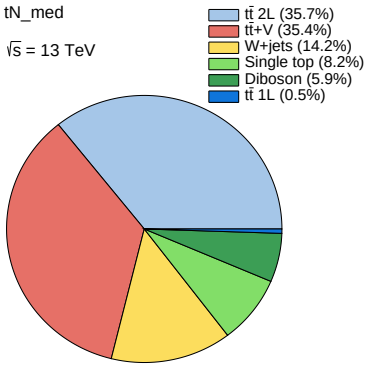

Figure 14.3: Breakdown of the individual SM contributions in the signal region.

Table 14.3: Cut efficiency for all preselection and signal region requirements for the benchmark signal and the dominant backgrounds – $t\bar{t}$, $t\bar{t}+V$ and W+jets. The $t\bar{t}$ and W+jets processes only contain events with at least one lepton, while for the signal and for $t\bar{t}+V$ also pure hadronic decays are included.

Cut	Signal	$t\bar{t}$	$t\bar{t}+V$	W+jets
Event cleaning	99 %	97 %	99 %	100 %
≥ 1 baseline lepton	62 %	91 %	79 %	98 %
≥ 1 signal lepton	67 %	83 %	77 %	91 %
== 1 signal lepton	91 %	91 %	87 %	100 %
== 1 baseline lepton	83 %	82 %	78 %	96 %
$E_{\mathrm{T}}^{\mathrm{miss}}$ trigger	92 %	70 %	78 %	73 %
≥ 4 jets	90 %	97 %	97 %	81 %
$E_{\mathrm{T}}^{\mathrm{miss}} > 230\,\mathrm{GeV}$	53 %	9 %	20 %	13 %
$\lvert\Delta\phi(j_{1,2}, E_{\mathrm{T}}^{\mathrm{miss}})\rvert > 0.4$	95 %	85 %	87 %	91 %
$m_{\mathrm{T}} > 120\,\mathrm{GeV}$	77 %	9 %	36 %	3 %
≥ 1 b-jet	92 %	90 %	91 %	18 %
$m_{T2}^{\tau} > 80\,\mathrm{GeV}$	98 %	80 %	94 %	99 %
Jet $p_{\mathrm{T}} > 60, 50, 40, 40\,\mathrm{GeV}$	93 %	84 %	91 %	75 %
top candidate mass $> 150\,\mathrm{GeV}$	68 %	50 %	67 %	51 %
$am_{T2} > 175\,\mathrm{GeV}$	67 %	25 %	70 %	82 %
$E_{T,\perp}^{\mathrm{miss}} > 230\,\mathrm{GeV}$	64 %	37 %	60 %	48 %
$E_{\mathrm{T}}^{\mathrm{miss}} > 250\,\mathrm{GeV}$	91 %	81 %	92 %	81 %
$m_{\mathrm{T}} > 160\,\mathrm{GeV}$	89 %	70 %	90 %	76 %
$H_{\mathrm{T,sig}}^{\mathrm{miss}} > 14$	82 %	64 %	80 %	66 %
$\Delta R(b, \ell) < 2$	94 %	90 %	90 %	77 %
Total efficiency	1 %	2×10^{-4} %	0.07 %	1.6×10^{-6} %

There are minor backgrounds as Z+jets, tZ, tWZ and $t\bar{t}+WW$ which contribute in total with 0.67 ± 0.21 events where 78% of these event come from Z+jets processes. The previously discussed background processes sum up to 35.3 ± 1.2 expected events and thus the contribution of the minor backgrounds is neglected for the full analysis.

The importance of each variable is visualised in the N-1 plots which are presented for all variables used to define the signal region. In those plots, all signal region cuts are applied except the one on the shown distribution. The place and the direction of the signal region cut is shown with a blue line. In Figure 14.4, the $E_{\mathrm{T}}^{\mathrm{miss}}$ and m_{T} distribution are shown, applying marginally increased cuts compared to the preselection. The $H_{\mathrm{T,sig}}^{\mathrm{miss}}$, am_{T2}, $m_{\mathrm{top}}^{\mathrm{reclustered}}$, $E_{T,\perp}^{\mathrm{miss}}$ and $\Delta R(b, \ell)$ distribution are shown in Figure 14.5, Figure 14.6 and Figure 14.7. In all those distribution, it is clearly visible that the selected cuts increase the significance as the majority of the signal is kept. All distributions show that a large background contribution is rejected especially large parts of the dileptonic $t\bar{t}$ background which is still the dominant background process.

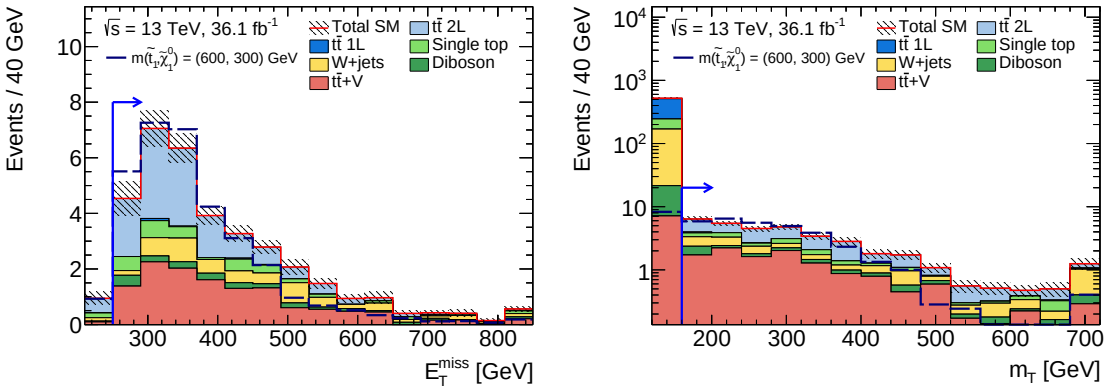

Figure 14.4: Distribution of the $E_{\mathrm{T}}^{\mathrm{miss}}$ and the m_{T} after applying all tN_med cuts, except the one on the displayed distribution. The background processes are added together and the signal benchmark is overlaid. The cut position and direction is shown as blue line.

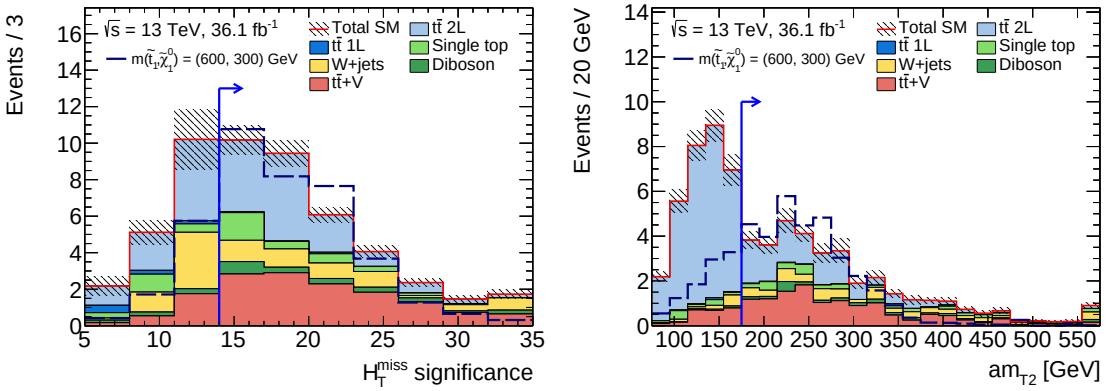

Figure 14.5: Distribution of the $H_{\mathrm{T,sig}}^{\mathrm{miss}}$ and the am_{T2} after applying all tN_med cuts, except the one on the displayed distribution. The background processes are added together and the signal benchmark is overlaid. The cut position and direction is shown as blue line.

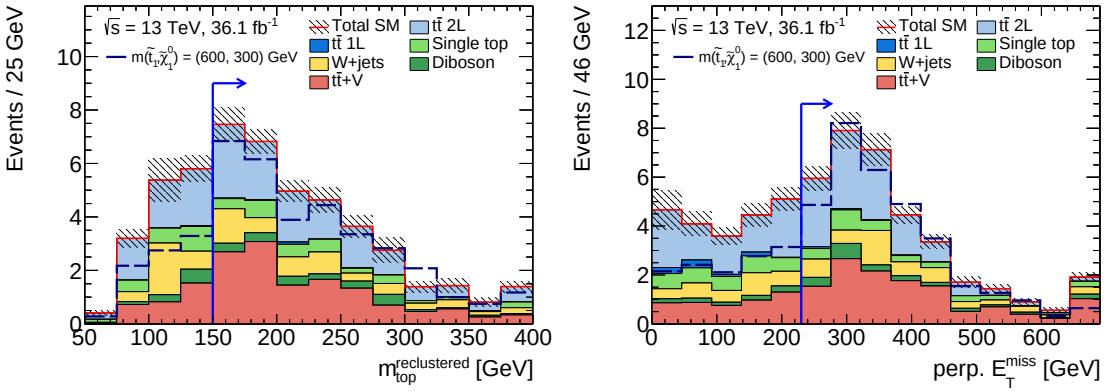

Figure 14.6: Distribution of the hadronic top mass and the $E_{T,\perp}^{\mathrm{miss}}$ after applying all tN_med cuts, except the one on the displayed distribution. The background processes are added together and the signal benchmark is overlaid. The cut position and direction is shown as blue line.

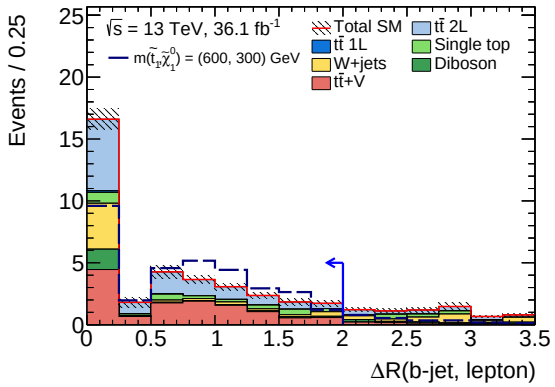

Figure 14.7: Distribution of the $\Delta R(b, \ell)$ after applying all tN_med cuts, except the one on the displayed distribution. The background processes are added together and the signal benchmark is overlaid. The cut position and direction is shown as blue line.

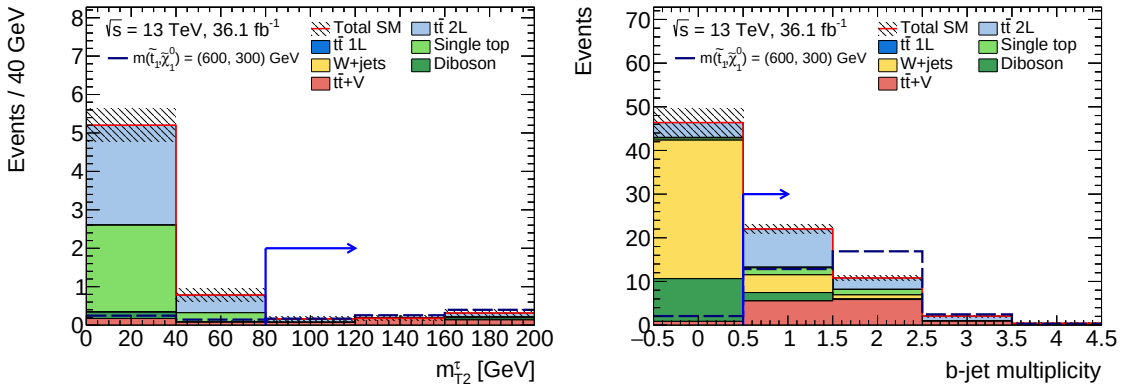

Figure 14.8: Distribution of the m_{T2}^{τ} and the b-jet multiplicity after applying all tN_med cuts, except the one on the displayed distribution. The background processes are added together and the signal benchmark is overlaid. The cut position and direction is shown as blue line.

In Figure 14.8, two preselection variables are shown without applying the preselection cut. Especially the m_{T2}^{τ} distribution shows that applying this cut helps to remove a large part of the dileptonic $t\bar{t}$ and the single top background without loosing much signal. The b-jet multiplicity shows, that this cut helps to remove a large fraction of W+jets and diboson events.

Figure 14.9 shows the transverse momenta of the four leading jets. For all jet momenta, the preselection cut is slightly increased to remove slightly more background events. The expected number of signal events is nearly unaffected by those cuts. The p_{T} cuts are kept the same among all signal, control and validation regions for tN_med in order to avoid any extrapolation over the jet momenta which would lead to larger jet related uncertainties.

The signal region optimisation is repeated for samples with higher top squark masses. Overall, similar cuts are found to be optimal in order to separate the signal from the background processes. One striking difference for the performed optimisation is the varying $E_{\mathrm{T}}^{\mathrm{miss}}$ cut. For increasing top squark masses, an increased $E_{\mathrm{T}}^{\mathrm{miss}}$ cut leads to a better performance. The signal region as defined above is based on a top squark mass of 600 GeV. In order to be sensitive towards higher top squark

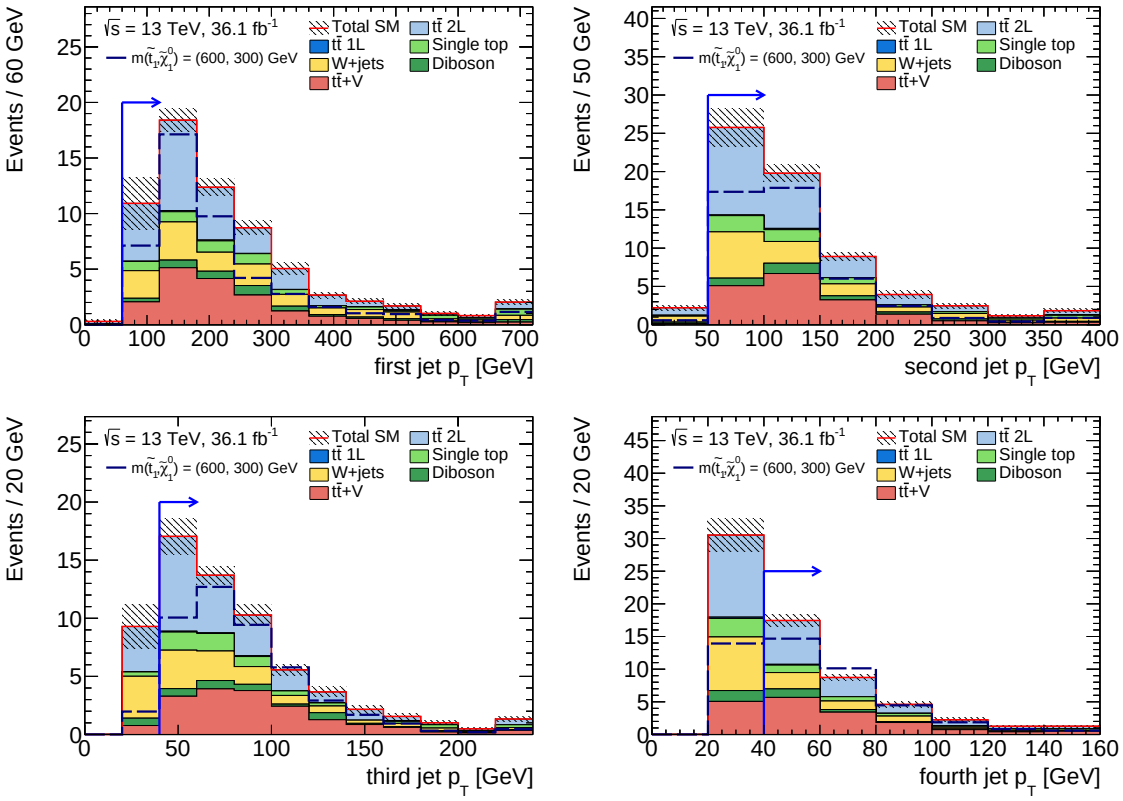

Figure 14.9: Distribution of the p_{T} of the leading four jets after applying all tN_med cuts, except the one on the displayed distribution. The background processes are added together and the signal benchmark is overlaid. The cut position and direction is shown as blue line.

masses, the $E_{\mathrm{T}}^{\mathrm{miss}}$ shape information can be used in a shape fit. For this, the tN_med signal region is divided into several bins in $E_{\mathrm{T}}^{\mathrm{miss}}$. The events entering the shape fit are the same which are selected for the single-bin analysis and thus the same background estimate is used.

14.3 Background Estimation

The background normalisation is estimated in dedicated control regions and then validated in corresponding validation regions. Those regions are defined to be kinematically close to the tN_med signal region. Some key variable cuts are inverted in order to reduce the signal contamination and enhance the yield and the purity of a particular background. The control regions are used combined in the simultaneous likelihood fit to constrain the background normalisation. A dedicated control region is defined for the main background – dileptonic $t\bar{t}$– and for the third and fourth leading background – W+jets and single top. The second leading background is $t\bar{t} + V$, which is estimated using a different final state and not relying only a kinematic inversion. For this background estimate, $t\bar{t} + Z(\rightarrow \ell\ell)$ evens are selected as detailed below.

The semi-leptonic $t\bar{t}$ contribution is large in the control regions for W+jets and single top. Therefore, the corresponding background normalisation is also estimated in a dedicated control region, even if the contribution in the signal region is small.

The signal and control regions are all used in the simultaneous fit and therefore the regions are designed orthogonal that each data event is only considered once. The validation regions are used to validate the estimated background normalisation. They are not used as part of the fit, but nonetheless they are kept statistically independent.

14.3.1 Control Regions

Control regions are defined to have a good purity of the dedicated background and a low signal contamination. For this, different variables are used to provide a good separation between the background processes. The approach to define control regions based on the kinematic inversion is illustrated in Figure 14.10. For all control regions, the jet momenta cut are kept unchanged in order to avoid any extrapolation over these momenta and all regions are defined orthogonal to each other. In order to enhance the statistic in these control and validation regions, some further cuts are relaxed on variables which are well modelled by the MC simulation.

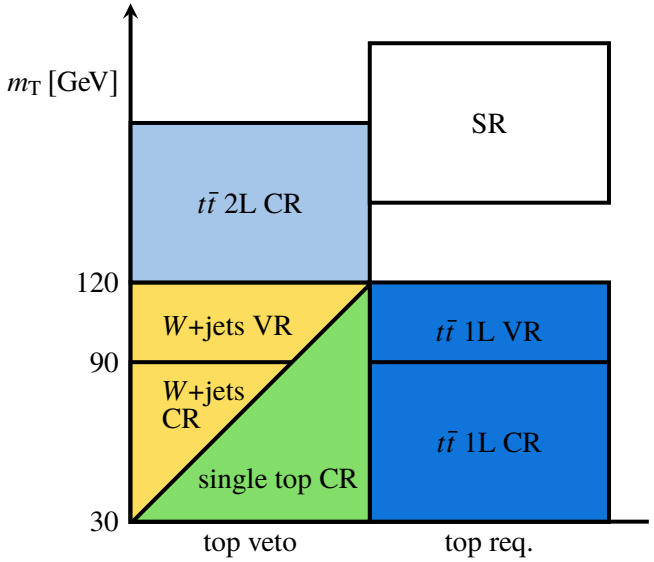

Figure 14.10: Illustration of the approach to define the control and validation regions for the tN_med signal region. The W+jets and single top regions are separated by the b-tagging requirement.

The control region definition is based on a top tagging approach using the recursive reclustering algorithm. For the signal region, as well as for the semi-leptonic $t\bar{t}$ control region, a hadronic top quark candidate with a mass larger 150 GeV is required. There is no hadronic top quark decay in events from dileptonic $t\bar{t}$ or W+jets processes. After the m_T cut, the main contribution of the single top process originates from dileptonic Wt events. Therefore, no hadronic top quark candidate is expected for the single top events in the signal region. A top veto is applied for the control regions for dileptonic $t\bar{t}$, W+jets and single top. For the top veto, it is required that no hadronic top quark

candidate was found or the candidate has a mass below 150 GeV. Previous analysis [1, 164] did not use the top tagging approach. Instead, the background normalisation for $t\bar{t}$ was estimated in a region dominated by semi-leptonic $t\bar{t}$ events. The W+jets background was estimated with a b-veto and thus an extrapolation over the number of light and heavy flavour jets was needed. With the top tagging method, the background composition in the control regions more closely resembles that in the signal region.

The main background when requiring a large m_{T} originates from dileptonic $t\bar{t}$ events. Therefore, a control region is built keeping the m_{T} requirement, but vetoing a hadronic top quark candidate. The other control regions are based on lower m_{T} requirements. In order to separate especially between $t\bar{t}$ and single top events, the am_{T2} variable is exploited. In single top events, the effective mass of the W boson and the b-quark can be higher as no second on-shell top is present. Thus a lower cut is used to separate $t\bar{t}$ events from the non-$t\bar{t}$ processes. In order to retain the orthogonality, an upper cut is introduced for all non-$t\bar{t}$ processes such as single top and W+jets. In general, the $t\bar{t}$ background can evade this am_{T2} kinematic bound, if the two b-tagged jets which are used for the reconstruction do not originate from the two top-quark decays. The two b-tagged jets can instead come from the b- and c-quarks from a hadronic top-quark decay. Only in these cases, the angular distance between the two b-tagged jets is expected to be small. Thus, an upper cut on this angular distance $\Delta R(b_1, b_2)$ is introduced to reduce the $t\bar{t}$ contribution in the single top control region. In order to reduce the W+jets contribution in the single top control region, the b-tag requirement is increased to at least two b-jets.

Selecting events with positively charged leptons helps to increase the purity of W+jets events in the W+jets control region, as other SM processes behave almost equally in the lepton charge. Leptons in W+jets events tend to have a positive charge due to the asymmetry in the production. This effect is enhanced with increasing $E_{\mathrm{T}}^{\mathrm{miss}}$. Due to the W polarisation, the neutrinos get higher momentum in events with positively charged leptons.

Table 14.4 summarises the event selections of the tN_med signal region and the associated control regions. The purity of the four control regions is illustrated in Figure 14.11. The purity in both $t\bar{t}$ control regions is large, as for both regions more than 75% events stem from the targeted $t\bar{t}$ process. Other, non-$t\bar{t}$ backgrounds are more difficult to separate. Thus the purity of the W+jets and single top control region is only 64% and 46% respectively. The largest contribution from other SM processes in the two latter control regions come from semi-leptonic $t\bar{t}$ followed by single top or W+jets. As the normalisation of the semi-leptonic $t\bar{t}$ process is estimated in a dedicated control region, the larger contribution is the other control regions is taken properly into account in the simultaneous fit.

As previously discussed, a background only fit is performed considering only the SM processes. From this fit, the normalisation factors can be extracted for the different backgrounds. The fitted normalisation factors are shown in Table 14.5. The normalisation factors for both $t\bar{t}$ processes are in agreement with unity and both agree within their uncertainties. The single top normalisation factor is slightly above unity, but also agrees with unity given the larger uncertainty. These uncertainties arise due to the lower purity in the single top control region and the larger effect of the corresponding theoretical uncertainties. The normalisation factor for W+jets is below unity and may indicate a bad modelling of this background process. Similar low normalisation factors are observed in the same publication for other signal regions [5] and were already observed in previous publications [1, 164]. The extracted values and their extrapolation to the signal region will be tested in dedicated validation regions. The expected yields are presented with and without those normalisation factors applied in

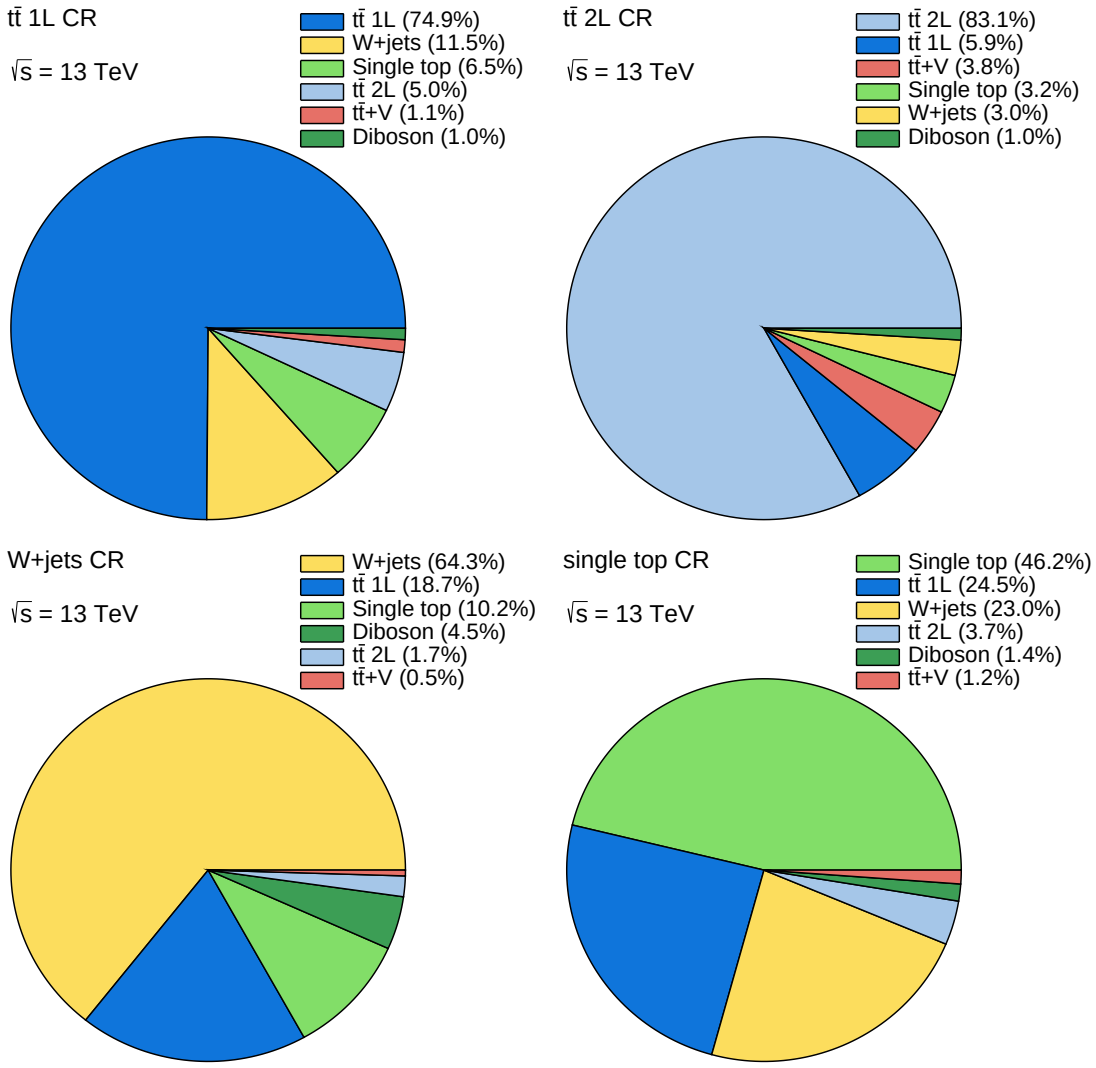

Figure 14.11: Breakdown of the individual SM contributions in the semi-leptonic $t\bar{t}$ (top left), dileptonic $t\bar{t}$ (top right), W+jets (bottom left) and single top (bottom right) control regions.

Table 14.4: Overview of the event selections defining tN_med and the associated control regions. The common event preselection as defined in Table 13.2 is applied. The veto on hadronic top candidates is fulfilled for events where no candidate is found, or if the candidate mass is below 150 GeV.

	tN_med	$t\bar{t}$ 1L CR	$t\bar{t}$ 2L CR	W+jets CR	Single top CR
$E_{\mathrm{T}}^{\mathrm{miss}}$			> 250 GeV		
$E_{T,\perp}^{\mathrm{miss}}$			> 230 GeV		
Jet p_{T}			$> 60, 50, 40, 40$ GeV		
m_{T}	> 160 GeV	$\in [30, 90]$ GeV	> 120 GeV	$\in [30, 90]$ GeV	$\in [30, 120]$ GeV
$H_{\mathrm{T,sig}}^{\mathrm{miss}}$	> 14	> 10	> 10	> 10	> 10
top cand. mass	> 150 GeV	> 150 GeV	veto	veto	veto
am_{T2}	> 175 GeV	< 200 GeV	< 200 GeV	> 200 GeV	> 200 GeV
b-tags @ 77%	≥ 1	≥ 1	≥ 1	≥ 1	≥ 2
$\Delta R(b, \ell)$	< 2	–	–	–	–
$\Delta R(b_1, b_2)$	–	–	–	< 1.2	> 1.2
Lepton charge	–	–	–	$= +1$	–

Table 14.5: Normalisation factors for the different background processes as estimated in the background only fit.

SM process	Normalisation factor
$t\bar{t}$ 1L	1.05 ± 0.09
$t\bar{t}$ 2L	0.96 ± 0.13
W+jets	0.85 ± 0.18
Single top	1.19 ± 0.37

Table 14.6, where also the number of observed events are shown. For the $t\bar{t} + V$ background the normalisation is already applied, where the corresponding control region method will be explained in Section 14.3.1. By design, a very good agreement can be observed for the data and the total background events including the normalisation factor. In the same table, the signal contribution of the benchmark signal is given for all control regions. This contribution is negligible for most of the regions with the largest contribution of 12.8% in the dileptonic $t\bar{t}$ control region. Overall only small signal contributions are observed and will be taken into account in the simultaneous fit when including the signal and all control regions.

In addition to comparing only the total event yield, the modelling of the kinematic distributions is checked applying the different control region selections. The most interesting variables for this are the ones where the requirements are changed between the control and the signal region. Mis-modelling in any of these variables could indicate problems when extrapolating over them into the signal region. The $H_{\mathrm{T,sig}}^{\mathrm{miss}}$ and $E_{\mathrm{T}}^{\mathrm{miss}}$ distribution are shown for the two $t\bar{t}$ control regions in Figure 14.12. Also the mass of the hadronic top candidate and the m_{T} distribution are shown

Table 14.6: Observed events and expected yields for all background processes in the presented control regions with and without the normalisation factors applied. The individual uncertainties are correlated and do not add up quadratically to the total uncertainty. The lowest row gives the signal contribution of the benchmark signal in the control regions.

Region	$t\bar{t}$ 1L CR	$t\bar{t}$ 2L CR	W+jets CR	Single top CR
Observed events	575	92	173	75
Total events	575 ± 24	92 ± 10	173 ± 13	75 ± 9
$t\bar{t}$ 2L events	27 ± 7	75 ± 10	3.1 ± 1.0	2.5 ± 0.9
$t\bar{t}$ 1L events	440 ± 40	5.9 ± 2.6	36 ± 11	18 ± 5
$t\bar{t}$ + V events	6.7 ± 2.0	4.1 ± 1.0	1.02 ± 0.33	0.93 ± 0.31
W+jets events	55 ± 15	2.4 ± 0.7	102 ± 19	13.8 ± 3.0
Single top events	43 ± 19	3.7 ± 1.8	23 ± 8	39 ± 11
Diboson events	5.3 ± 2.0	0.9 ± 0.4	8.3 ± 2.4	1.0 ± 0.4
MC exp. events	556 ± 25	94 ± 4	186 ± 18	71 ± 8
MC exp. $t\bar{t}$ 2L events	28 ± 7	78.5 ± 3.4	3.2 ± 0.9	2.6 ± 0.9
MC exp. $t\bar{t}$ 1L events	416 ± 11	5.6 ± 2.5	35 ± 9	17 ± 4
MC exp. $t\bar{t}$ + V events	5.9 ± 0.4	3.6 ± 0.4	0.90 ± 0.08	0.82 ± 0.16
MC exp. W+jets events	64 ± 13	2.8 ± 0.6	119 ± 14	16.2 ± 2.7
MC exp. single top events	36 ± 11	3.1 ± 1.0	19.0 ± 2.4	32.6 ± 2.9
MC exp. diboson events	5.3 ± 2.0	0.9 ± 0.4	8.3 ± 2.5	1.0 ± 0.4
Signal contribution	0.4%	12.8%	0.2%	1.6%

for the semi- and dileptonic $t\bar{t}$ control region, respectively. For the W+jets and single top control region, the $E_{\mathrm{T}}^{\mathrm{miss}}$ and the angular distance $\Delta R(b,\ell)$ are shown in Figure 14.13. Additionally, the $H_{\mathrm{T,sig}}^{\mathrm{miss}}$ distribution is shown for the W+jets and the am_{T2} distribution is shown for the single top control region. In all these distributions, a good agreement can be observed between the data and the backgrounds with the normalisation factors applied. Further distributions for the control regions can be found in Appendix C.2.

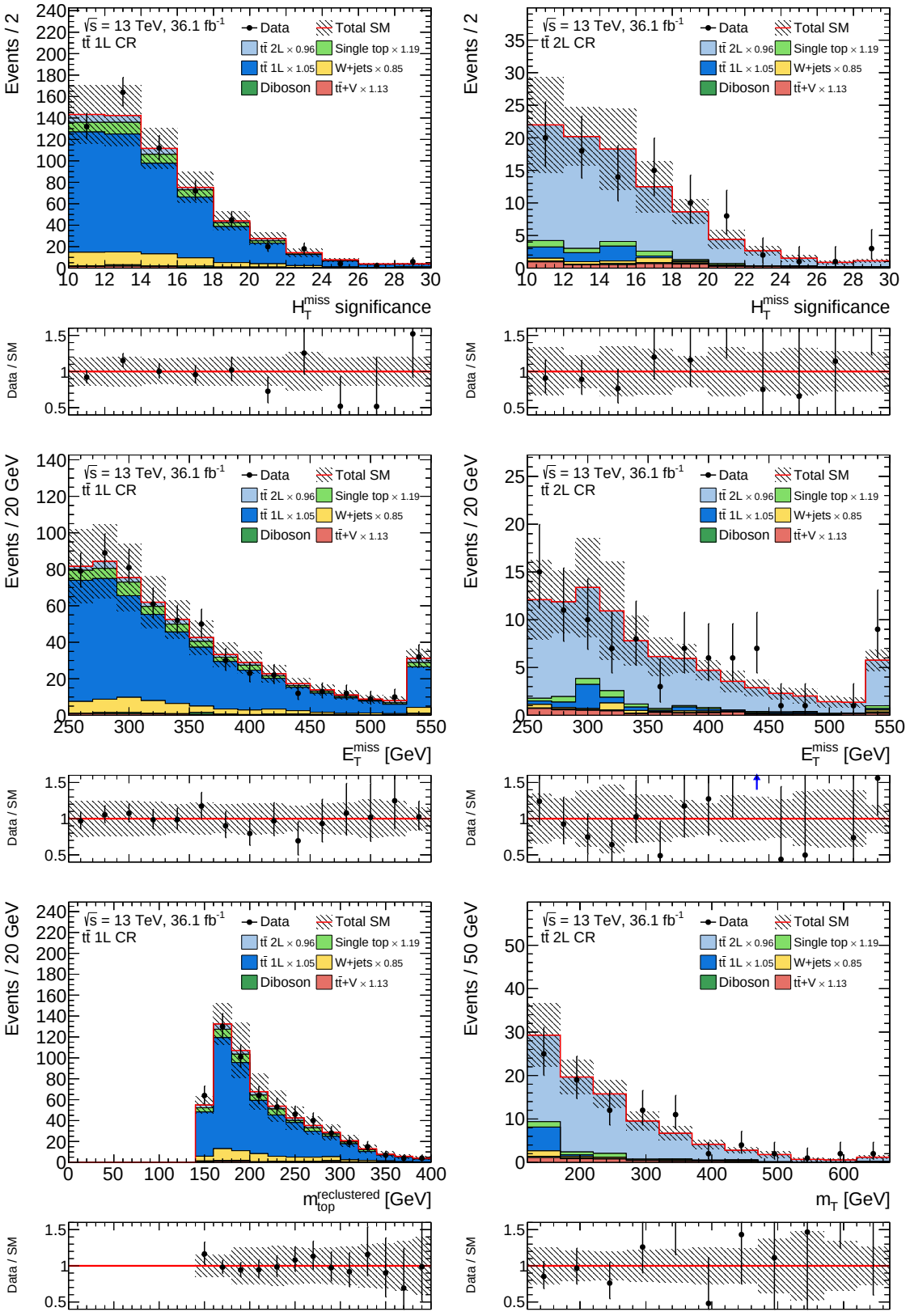

Figure 14.12: Comparison of data and simulation in the semi-leptonic (left) and dileptonic (right) $t\bar{t}$ control region after applying the normalisation obtained in the simultaneous fit. Statistical uncertainties as well as the systematic uncertainties from JES, JER and b-tagging are displayed. The last bin includes the overflow.

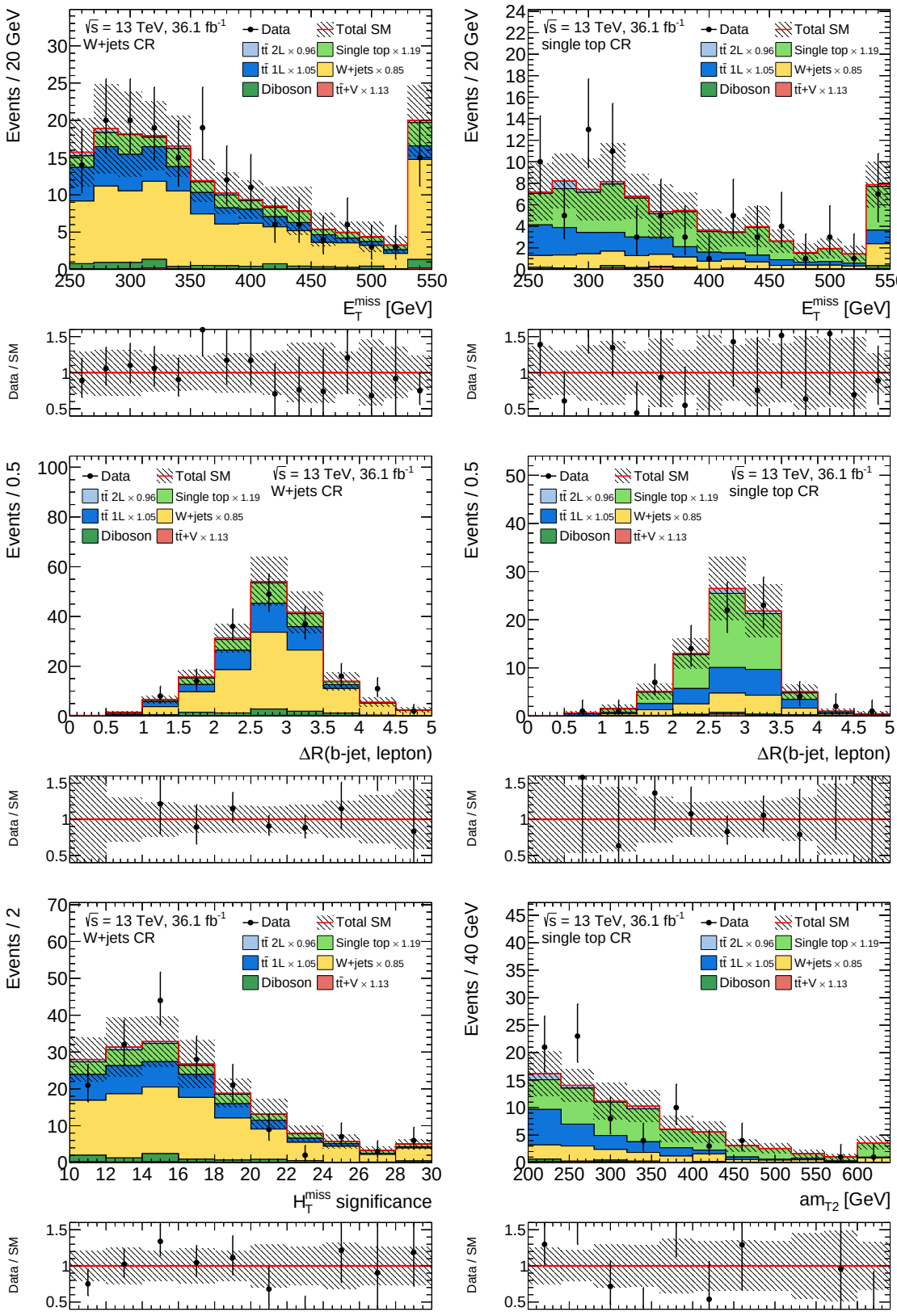

Figure 14.13: Comparison of data and simulation in the W+jets (left) and single top (right) control region after applying the normalisation obtained in the simultaneous fit. Statistical uncertainties as well as the systematic uncertainties from JES, JER and b-tagging are displayed. The last bin includes the overflow.

$t\bar{t} + Z$ Control Region

The second leading background for the tN_med signal region stems from $t\bar{t} + V$ events dominated by events with a Z boson decaying into two neutrinos. For this background, a different control region approach is defined. In order to estimate the normalisation, events with a Z boson decaying into two leptons are selected. The leptons are then treated as invisible and $E_{\mathrm{T}}^{\mathrm{miss}}$ related variables are re-computed in order to have a proxy for $t\bar{t} + Z(\rightarrow \nu\nu)$ events.

A common selection is designed for all signal regions in the publication [5] and only the jet p_{T} cuts are set specific for each signal region. The selection requires exactly three charged leptons, at least four jets and at least one b-tagged jet. Two of the leptons are required to have opposite charge, and the same flavour. The combined mass of those two leptons is required to be in the range $81 < m_{\ell\ell} < 101\,\mathrm{GeV}$ in order to form a suitable $Z \rightarrow \ell\ell$ candidate. Due to the different lepton selection, only the $t\bar{t} + V$ normalisation factor is shared between this control region and the other regions in the simultaneous fit. All other processes are treated as uncorrelated to the ones contributing to the single lepton selections.

In Figure 14.14, the background composition can be seen for this control region when applying the dedicated jet p_{T} requirements. The main contribution in this selection comes from $t\bar{t} + Z$ events where the Z boson decays into two leptons. The next leading process stems from diboson events.

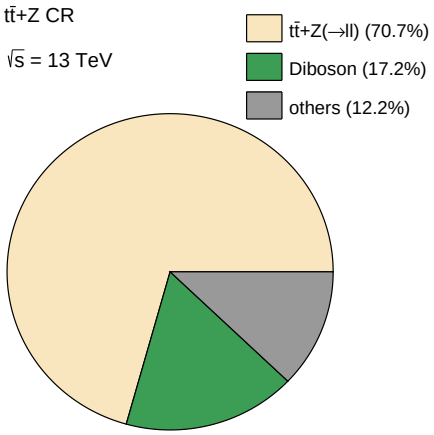

Figure 14.14: Breakdown of the individual SM contribution in the $t\bar{t} + Z$ control region.

Table 14.7: Observed events and expected yields for all background processes in the $t\bar{t} + Z$ control region with and without the normalisation factors for $t\bar{t} + V$ and diboson events applied. The individual uncertainties are correlated and do not add up quadratically to the total uncertainty.

Region	$t\bar{t} + Z$ CR
Observed events	55
Total events	55 ± 7
$t\bar{t} + V$ events	42.46 ± 11
$t\bar{t}$ 2L events	0.89 ± 0.28
Diboson events	7.0 ± 1.0
tWZ events	3^{+6}_{-3}
tZ events	$1.4^{+2.5}_{-1.4}$
MC exp. events	50 ± 9
MC exp. $t\bar{t} + V$ events	37.51 ± 2.8
MC exp. $t\bar{t}$ 2L events	0.89 ± 0.29
MC exp. diboson events	7.0 ± 1.0
MC exp. tWZ events	3^{+6}_{-3}
MC exp. tZ events	$1.4^{+2.5}_{-1.4}$

The normalisation of the diboson background is determined in a region with a b-veto instead of the b-tag requirement. This defines a region with a purity of 85% for diboson, where the normalisation for diboson is estimated to be 0.8, in common for all $t\bar{t} + Z$ control regions in the analysis. The normalisation factor for the $t\bar{t} + V$ background is calculated in the simultaneous fit to 1.13 ± 0.32. The expected and observed events are shown in Table 14.7.

In Figure 14.15, the mass and p_{T} of the dilepton system and the number of b-jets, as well as the $E_{\mathrm{T}}^{\mathrm{miss}}$ are shown in this control region. In order to calculate the $E_{\mathrm{T}}^{\mathrm{miss}}$, the two leptons from the Z boson decay are treated as invisible. Overall a good modelling in this control region can be seen. The full procedure is also validated by using $t\bar{t} + \gamma$ events where the photon is treated as an invisible particle [5].

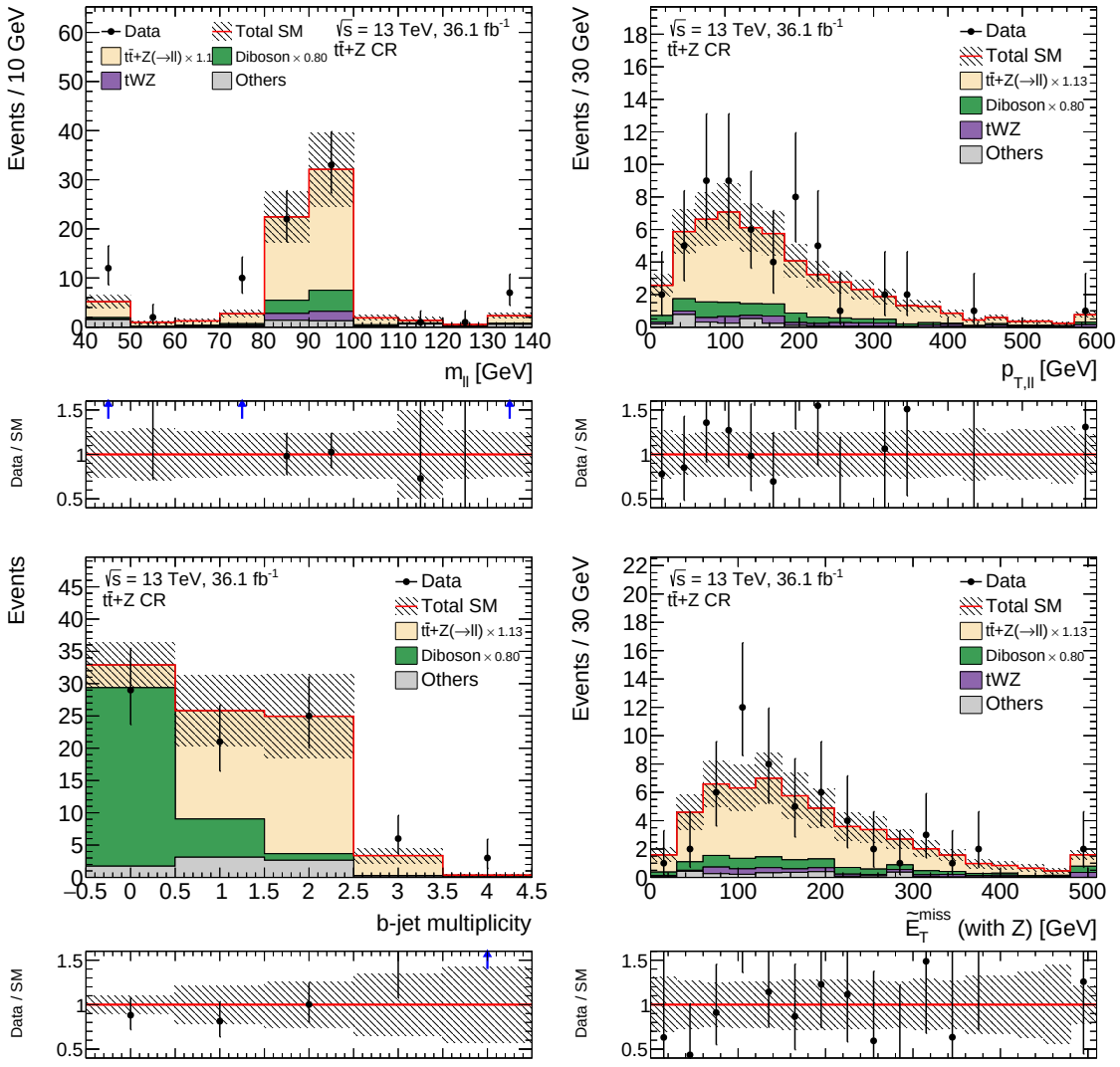

Figure 14.15: Comparison of data and simulation in the $t\bar{t} + Z$ CR after applying the normalisation factor as obtained in the simultaneous fit. Statistical uncertainties as well as the systematic uncertainties from JES, JER and b-tagging are displayed. The last bin includes the overflow. The b-jet multiplicity is shown without the number of b-tag requirement applied.

14.3.2 Validation Regions

In order to validate the normalisation of the backgrounds, dedicated validation regions are defined which are not used in the simultaneous fit. The background estimate from the control regions is extrapolated to the validation regions and the agreement between the data and the prediction is checked.

The definition of the validation regions follows a similar approach as for the control regions. Dedicated, orthogonal regions are defined for semi-leptonic $t\bar{t}$, dileptonic $t\bar{t}$ and for the W+jets background. These validation regions are also included in the sketch to illustrate the various regions (see Figure 14.10). As described above, the validation of the $t\bar{t}+Z$ background is done using $t\bar{t}+\gamma$ events.

Table 14.8 gives the details of the validation region selection. The main change with respect to the control region is a shift in the m_{T} window towards higher values ($90 < m_{\mathrm{T}} < 120\,\mathrm{GeV}$) for the semi-leptonic $t\bar{t}$ and W+jets validation region. No dedicated single top validation region was defined as the m_{T} windows between 30 and 120 GeV was already needed to get a reliable amount of events in the control region. Additionally, the single top process contributes less than 10% in the signal region. For the dileptonic $t\bar{t}$ validation region, the veto on a top candidate is inverted and a top candidate is required. The same mass requirements as for the signal region are applied. With a requirement on $am_{T2} < 130\,\mathrm{GeV}$, the orthogonality between the validation and the signal region is ensured. Defining the dileptonic $t\bar{t}$ region with a top candidate requirement validates the extrapolation over the requirement or veto of a hadronic top candidate.

The expected and observed yields with the previously determined background normalisation factors are given in Table 14.9. The observed data events are higher for the semi-leptonic $t\bar{t}$ and W+jets

Table 14.8: Overview of the event selections defining tN_med and the associated validation regions. The common event preselection as defined in Table 13.2 is applied in all cases. The veto on hadronic top candidates is fulfilled for events where no candidate is found, or if the candidate mass is below 150 GeV.

	tN_med	$t\bar{t}$ 1L VR	$t\bar{t}$ 2L VR	W+jets VR
$E_{\mathrm{T}}^{\mathrm{miss}}$		$> 250\,\mathrm{GeV}$		
$E_{T,\perp}^{\mathrm{miss}}$		$> 230\,\mathrm{GeV}$		
n. of b-tags @ 77%		≥ 1		
m_{T}	$> 160\,\mathrm{GeV}$	$\in [90, 120]\,\mathrm{GeV}$	$> 120\,\mathrm{GeV}$	$\in [90, 120]\,\mathrm{GeV}$
$H_{\mathrm{T,sig}}^{\mathrm{miss}}$	> 14	> 10	> 10	> 10
top candidate mass	$> 150\,\mathrm{GeV}$	$> 150\,\mathrm{GeV}$	$> 150\,\mathrm{GeV}$	veto
am_{T2}	$> 175\,\mathrm{GeV}$	$< 200\,\mathrm{GeV}$	$< 130\,\mathrm{GeV}$	$> 200\,\mathrm{GeV}$
$\Delta R(b, \ell)$	< 2	–	–	–
$\Delta R(b_1, b_2)$	–	–	–	< 1.2
Lepton charge	–	–	–	$= +1$

Table 14.9: Observed events and expected yields for all background processes in all validation regions with and without the normalisation factors applied. The normalisation is estimated in the simultaneous fit based on the control regions. The individual uncertainties are correlated and do not add up quadratically to the total uncertainty. The lowest row gives the signal contribution of the benchmark signal in the validation regions.

Region	$t\bar{t}$ 1L VR	$t\bar{t}$ 2L VR	W+jets VR
Observed events	94	29	28
Total background events	77 ± 13	38 ± 6	21.8 ± 3.4
$t\bar{t}$ 2L events	11.1 ± 3.0	31 ± 6	1.4 ± 0.7
$t\bar{t}$ 1L events	52 ± 14	2.1 ± 0.7	4.3 ± 1.6
$t\bar{t}+V$ events	1.4 ± 0.4	2.1 ± 0.8	0.32 ± 0.09
W+jets events	5.4 ± 1.8	1.1 ± 0.7	11.7 ± 3.0
Single top events	6.0 ± 3.2	1.3 ± 0.7	3.4 ± 1.3
Diboson events	0.7 ± 0.4	0.29 ± 0.14	0.7 ± 0.5
MC exp. background events	75 ± 14	39 ± 5	23 ± 4
MC exp. $t\bar{t}$ 2L events	11.5 ± 2.7	32 ± 5	1.5 ± 0.7
MC exp. $t\bar{t}$ 1L events	50 ± 13	2.0 ± 0.6	4.1 ± 1.4
MC exp. $t\bar{t}+V$ events	1.26 ± 0.33	1.9 ± 0.4	0.28 ± 0.05
MC exp. W+jets events	6.3 ± 1.6	1.2 ± 0.8	13.8 ± 2.6
MC exp. single top events	5.0 ± 2.1	1.1 ± 0.5	2.9 ± 0.6
MC exp. diboson events	0.7 ± 0.4	0.29 ± 0.14	0.7 ± 0.5
Signal contribution	2.1%	15.5%	1.4%

validation region, where less events are observed for the dileptonic $t\bar{t}$ region. All validation regions agree between the data and the MC prediction within 1.5 σ. The modelling is also checked in these regions for the variables defining the different regions. In Figure 14.16, the $E_{\mathrm{T}}^{\mathrm{miss}}$ distribution is shown for the three validation regions. In addition, the mass of the hadronic top candidate is also shown for the dileptonic $t\bar{t}$ region. The data agree with the normalised backgrounds within the uncertainties. Additional distributions for all validation regions can be found in Appendix C.3.

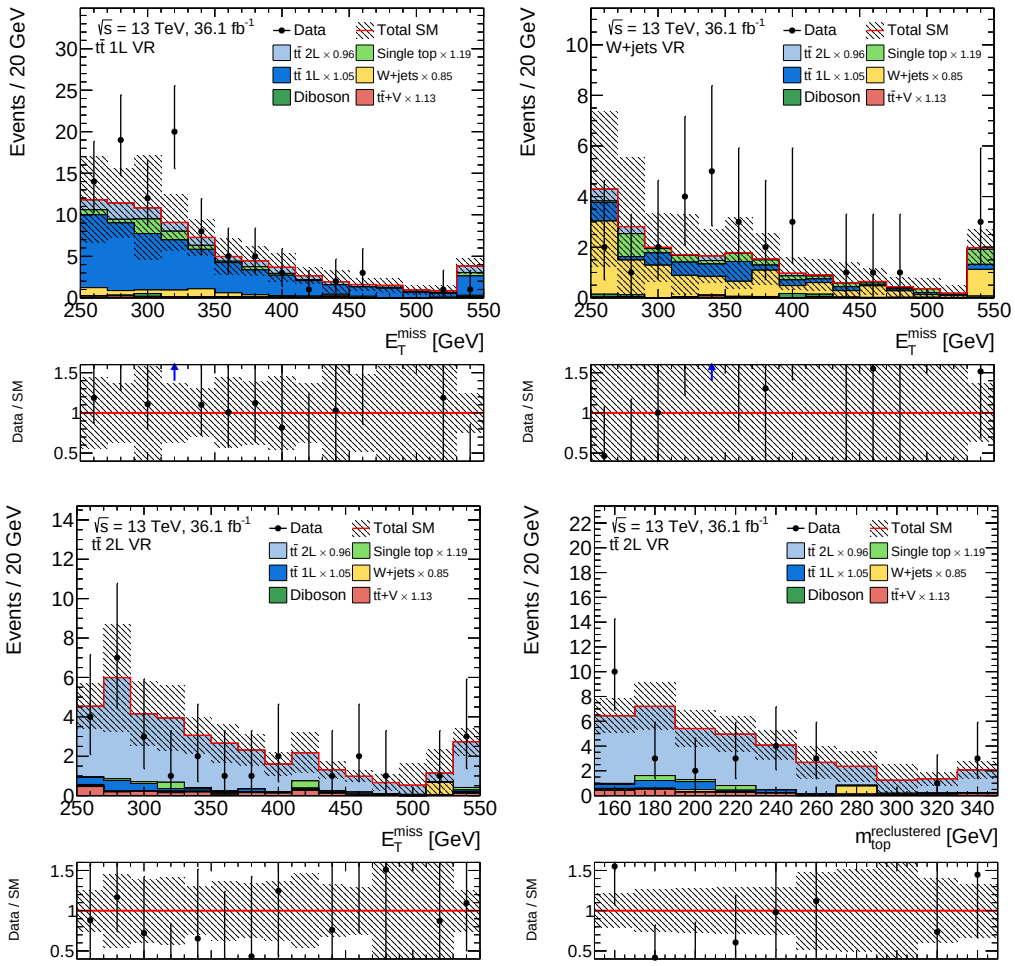

Figure 14.16: Comparison of data and simulation in the semi-leptonic $t\bar{t}$ (top left), W+jets (top right) and dileptonic $t\bar{t}$ (bottom) validation regions after applying the normalisation obtained in the simultaneous fit. Statistical uncertainties as well as the systematic uncertainties from JES, JER and b-tagging are displayed. The last bin includes the overflow.

14.4 Impact of Systematic Uncertainties

The sources of the experimental and theoretical uncertainties are discussed in Section 13.4. The experimental uncertainties are evaluated calculating the change in the expected events in the different regions when varying the sources of uncertainties. The theoretical uncertainties are evaluated by comparing different MC simulated samples. In order to reduce the influence of the limited statistics in these dataset, not the full event selection is used. Instead, starting with the preselection, only the requirement on one of the variables is added. The uncertainty is estimated by comparing the predictions of the different simulated samples. This procedure is repeated for all variables used to define the signal and control regions, and the resulting uncertainties are added in quadrature. With this procedure, any correlation effects between the requirements are neglected. The result

Table 14.10: Total background expectation with the statistical and systematic uncertainty. For the systematic uncertainty, the full breakdown of the leading uncertainties in the background prediction in the signal region is given. The individual uncertainties are correlated and thus do not necessarily add up in quadrature to the total uncertainty. All uncertainties which contribute less than 1% are not shown.

Uncertainty	**tN_med**
Total background expectation	36.31
Total statistical ($\sqrt{N_{\text{exp}}}$)	±6.03
Total background systematic	±6.61 [18.21%]
$t\bar{t}+V$ normalisation	±4.00 [11.0%]
$t\bar{t}+V$ modelling	±3.83 [10.6%]
$t\bar{t}$ 2L normalisation	±1.70 [4.7%]
$t\bar{t}$ radiation	±1.55 [4.3%]
$t\bar{t}$ MC generator	±1.31 [3.6%]
MC stat. (nominal samples)	±1.28 [3.5%]
Single top normalisation	±1.09 [3.0%]
Jet energy resolution	±1.01 [2.8%]
Jet energy scale (1^{st} component)	±1.01 [2.8%]
Pileup reweighting	±0.92 [2.5%]
W + jets normalisation	±0.92 [2.5%]
$t\bar{t}$ fragmentation	±0.89 [2.5%]
Flavour tagging c-jet mistag rate	±0.83 [2.3%]
Flavour tagging light-jet mistag rate	±0.72 [2.0%]
Diboson cross-section	±0.43 [1.2%]
Diboson modelling	±0.40 [1.1%]

agrees within the uncertainties with the estimate using the full selection, but has a lower statistical component [5].

The modelling uncertainties for the semi-leptonic and the dileptonic $t\bar{t}$ processes are treated as uncorrelated, as the systematic effects dominating the uncertainties differ for these processes. The semi-leptonic $t\bar{t}$ background is mainly sensitive to uncertainties affecting the m_{T} distribution, such as the jet energy resolution. On the other hand, dileptonic $t\bar{t}$ events enter the signal region only if one lepton is misidentified and additional jets are found.

In Table 14.10, the systematic uncertainties in the total background prediction are listed. The leading theoretical uncertainties are due to the normalisation and modelling of the $t\bar{t}$ + V background which is the leading background when applying the estimated normalisation factors. The leading experimental uncertainty comes from the jet energy resolution and the jet energy scale which both influence the hadronic top quark reconstruction and in case of the resolution also affects strongly the m_{T}. Overall, the statistical uncertainty is slightly smaller than the systematic uncertainties.

14.5 Results

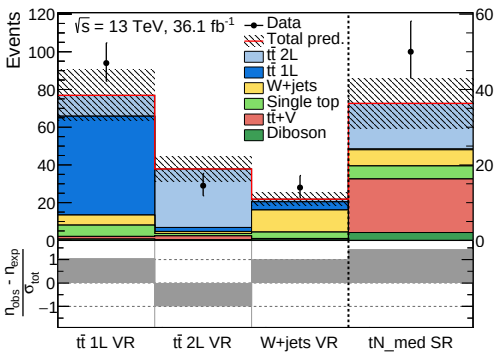

Figure 14.17: Comparison of the measured data (n_{obs}) with the background prediction (n_{exp}) in the validation regions and the signal region. The bottom panel shows the significance of the difference between data and the background prediction, where the significance is based on the total uncertainty (σ_{total}).

Table 14.11: Observed events and expected yields for all background processes in the signal region with the normalisation factors applied. The individual uncertainties are correlated and do not add up quadratically to the total uncertainty.

Region	tN_med
Observed events	50
Total background events	36 ± 7
$t\bar{t}$ 2L events	12.1 ± 2.9
$t\bar{t}$ 1L events	0.2 ± 0.1
$t\bar{t}$ + V events	14 ± 5
W+jets events	4.3 ± 1.1
Single top events	3.5 ± 1.2
Diboson events	2.1 ± 0.7

The results for the tN_med signal region are summarised in Figure 14.17 and Table 14.11. As previously discussed the validation regions show ±1 σ differences between the observed data and the normalised background expectation. In the signal region, 36 ± 7 events are expected, and 50 data events are observed. This result in an difference of 1.4 σ which is in reasonable agreement with the background-only hypothesis. The modelling of the distributions in the signal regions is verified, but overall no significant features are observed. The $E_{\mathrm{T}}^{\mathrm{miss}}$ distribution is shown as an example in Figure 14.18, all other distributions are shown in Appendix C.4.

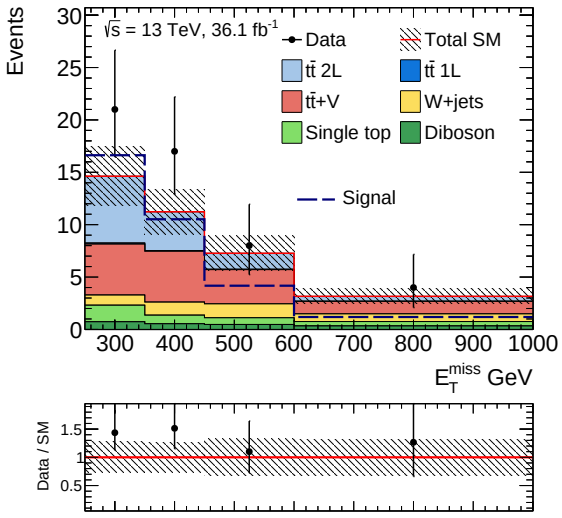

Figure 14.18: $E_{\mathrm{T}}^{\mathrm{miss}}$ distribution after applying all signal region requirements and the previously determined background normalisation. The shown binning is the one used for the shape fit. As signal, the benchmark signal for the tN_med region is overlaid with a top squark mass of 600 GeV and a neutralino mass of 300 GeV. The uncertainty band includes all statistical and systematic uncertainties.

The model-independent limit setting is performed with the single bin signal region tN_med as defined in Table 14.1 using the procedure explained in Section 4.2. For this, no signal model is assumed and any signal contribution in the control regions is neglected. A potential signal would thus lead to an increased background estimate, resulting in a conservative limit. The compatibility of the observed data with the background-only hypothesis is calculated to be $p_0 = 0.07$. The observed (expected) upper limit on non-SM events in the signal region is $N_{\text{non-SM}} < 31$ (< 19). With this single-bin setup, the exclusion limits are set on the top squark and neutralino masses as shown in Figure 14.19 on the left-hand side. With this setup, top squark masses up to 830 GeV (900 GeV) and neutralino masses up to 350 GeV (400 GeV) are excluded from the observed (expected) limit. Overall, a large improvement compared to the previous results can be seen.

As previously discussed, the tN_med signal region is designed with a relatively loose $E_{\mathrm{T}}^{\mathrm{miss}}$ requirement. As signal events with higher top squark masses tend towards higher $E_{\mathrm{T}}^{\mathrm{miss}}$ values, the $E_{\mathrm{T}}^{\mathrm{miss}}$ shape information can help to improve the exclusion potential towards higher values. In the configuration used, the $E_{\mathrm{T}}^{\mathrm{miss}}$ distribution is split into four bins. The binning of the $E_{\mathrm{T}}^{\mathrm{miss}}$ distribution is shown in Figure 14.18 when applying the tN_med signal requirements. A good shape agreement between the data and the background prediction can be seen. But overall more data are seen as predicted from the normalised MC simulation.

The shape fit is performed in the same way as the single tN_med signal region fit. The background normalisation is determined in the dedicated control regions and results to the same as for the single bin fit. The uncertainties are evaluated for all signal region bins separately. The result of the shape fit is shown in Figure 14.19 on the right-hand side. Top squark masses up to 980 GeV (1020 GeV) and neutralino masses up to 350 GeV (420 GeV) are excluded by the observed (expected) limit. Comparing the results with the single bin and the shape fit shows the expected improvement. The exclusion potential is increased by 150 GeV towards higher top squark masses.

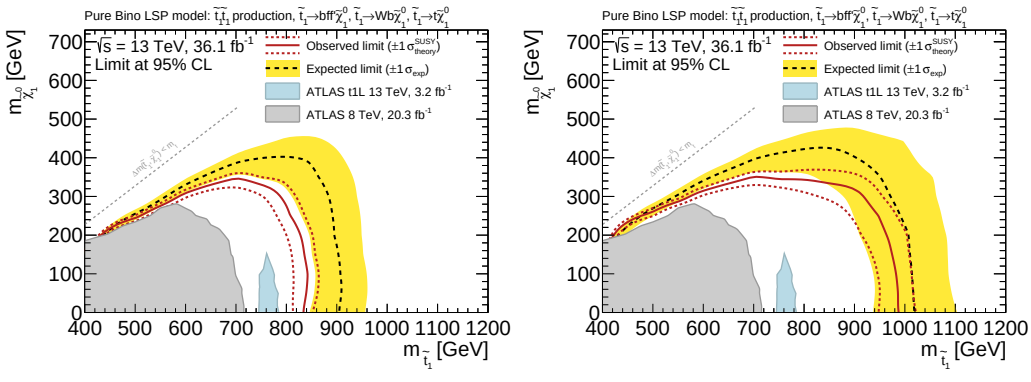

Figure 14.19: Expected and observed 95% excluded regions in the plane of $m_{\tilde{\chi}_1^0}$ versus $m_{\tilde{t}_1}$ for the direct top squark pair production assuming $\tilde{t}_1 \to t\tilde{\chi}_1^0$ decay with a branching ratio of 100%. The observed excluded regions from previous publications [163] are shown as grey and blue areas. The black line shows the expected limit and the yellow band includes all statistical and systematic uncertainties. The red line shows the observed limit, where the smaller dashed lines represent the uncertainty in the signal cross-section. The excluded region is shown for the single-bin (left) and the shape fit (right) setup.

14.5.1 Combination

The tN_med signal region is optimised for the $\tilde{t}_1 \to t\tilde{\chi}_1^0$ signal, assuming a 100% branching ratio where the neutralino mainly consists of a bino. Other similar signal models exist where the neutralino is a higgsino as discussed in Section 2.2. The tN_med signal region is sensitive for the decay into $t\tilde{\chi}_1^0$ and $t\tilde{\chi}_2^0$ with a hadronic decay of a Z or a Higgs boson. The decay signatures with a chargino are characterised by low-momentum objects, so-called soft objects. For the publication [5] three dedicated signal region are optimised targeting a soft lepton in the final state: bCsoft_diag, bCsoft_med and bCsoft_high. These regions target the $b\tilde{\chi}_1^{\pm}$ decay for various masses. Common for all regions is a soft lepton requirement with a minimal p_{T} of 4 GeV for muons and 5 GeV for electrons. The signal is characterised by low momentum leptons and large $E_{\mathrm{T}}^{\mathrm{miss}}$, where the SM backgrounds are dominated by events with leptonic W decays. Thus, the ratio of $p_{\mathrm{T}}^{\ell}/E_{\mathrm{T}}^{\mathrm{miss}}$ is a strong discriminant with low values for the signal. A shape-fit with three bins is used for each of the soft lepton regions using this variable. To achieve a good sensitivity to all possible decays, a combination of the tN_med signal region and the three soft lepton regions is performed.

The combination of the tN_med signal region with any of the three soft lepton regions is based on a combined fit. For this, the event selection for the signal and control regions should not overlap. The signal region selection is orthogonal to the soft lepton selection as they require an upper cut on $m_{\mathrm{T}} < 160$ GeV, while the tN_med signal region requires $m_{\mathrm{T}} > 160$ GeV. The definition of the control regions is not orthogonal. In order to reduce the overlap, events entering e.g. the tN_med top control region are removed from the top control region of the soft lepton selection. The overlap before and after the overlap removal between the various regions is shown in Appendix C.5. In most regions, no overlap is observed and the remaining overlap can be neglected as it is less than 2%.

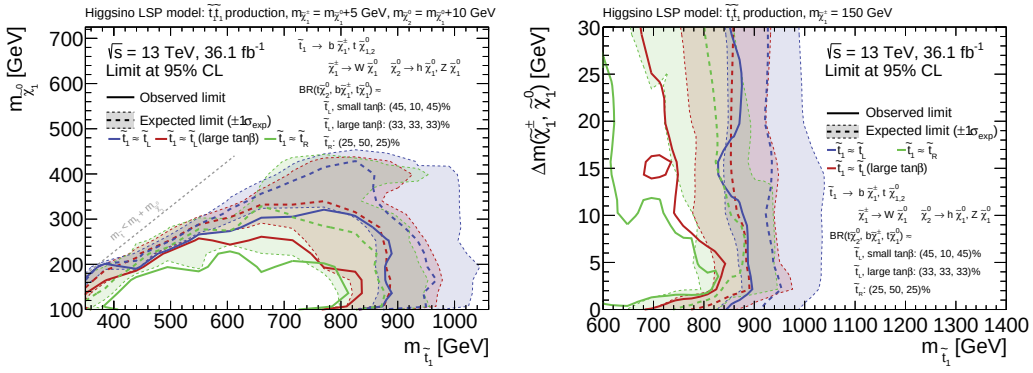

Figure 14.20: Expected and observed 95% excluded regions in the plane of $m_{\tilde{\chi}_1^0}$ versus $m_{\tilde{t}_1}$ (left) and $\Delta m(\tilde{\chi}_1^\pm, \tilde{\chi}_1^0)$ versus $m_{\tilde{t}_1}$ (right) for the direct top squark pair production in the higgsino LSP model using the tN_med combination with the three soft lepton selections. The dashed coloured lines shows the expected limit and the same coloured band includes all statistical and systematic uncertainties. The coloured line shows the observed limit, where the smaller dashed lines represent the uncertainty in the signal cross-section. The different colours represent different branching ratio scenarios.

In order to perform a statistical combination of the tN_med signal region with each of the soft lepton regions, all control and signal region bins are used in a combined likelihood fit which leads to three combination fits. The background processes differ and possible mismodelling can depend on the kinematic phase-space, thus the background normalisation factors for the soft and tN_med selection are determined individually. Only the signal normalisation is shared for the two selections. The experimental uncertainties are treated as fully correlated, while the theoretical uncertainties are assumed to be uncorrelated as different effects can play a role for the different selections. In order to validate the combination procedure, the fitted uncertainties as well as the normalisation factors are compared to the fits using only the tN_med or the soft lepton signal and control regions and good agreement is observed. Details for this validation are presented in Appendix C.5.

The final exclusion contours are shown for the higgsino LSP model in Figure 14.20. On the left-hand side, the mass differences are assumed to be $\Delta m(\tilde{\chi}_1^\pm, \tilde{\chi}_1^0) = 5\,\text{GeV}$ and $\Delta m(\tilde{\chi}_2^0, \tilde{\chi}_1^0) = 10\,\text{GeV}$. On the right-hand side, the chargino mass is fixed to 150 GeV. The mass relation $\Delta m(\tilde{\chi}_2^0, \tilde{\chi}_1^0) = 2 \cdot \Delta m(\tilde{\chi}_1^\pm, \tilde{\chi}_1^0)$ is assumed varying $\Delta m(\tilde{\chi}_1^\pm, \tilde{\chi}_1^0)$ between 0 and 30 GeV. The observed (expected) limit reach top squark masses up to 850 GeV (900 GeV). The sensitivity towards the $\tilde{t}_1 \simeq \tilde{t}_R$ scenario is mainly driven from the soft lepton regions, while the reach for the low tan β model is dominated from the tN_med selection. This is visible in the dependence of the exclusion on the mass splitting $\Delta m(\tilde{\chi}_1^\pm, \tilde{\chi}_1^0)$. The transverse momentum of the charged lepton is correlated to the mass splitting, thus the soft lepton selection is strongly sensitive to low mass differences. Towards higher mass differences, the sensitivity decreases, as visible for the $\tilde{t}_1 \simeq \tilde{t}_R$ scenario. The sensitivity for the tN_med selection is nearly unaffected from this mass difference therefore the sensitivity for the $\tilde{t}_1 \simeq \tilde{t}_L$ scenario is independent from the mass splitting. The large tan β scenario profits most from the combination, as all decay modes occur with the same probability.

The same combination of the signal regions can be used to set limits on the well tempered neutralino models which are introduced in Section 2.2. The results are shown in Figure 14.21 for the left- and right-handed hypotheses. For the left-handed scenario, both top and bottom squark productions are

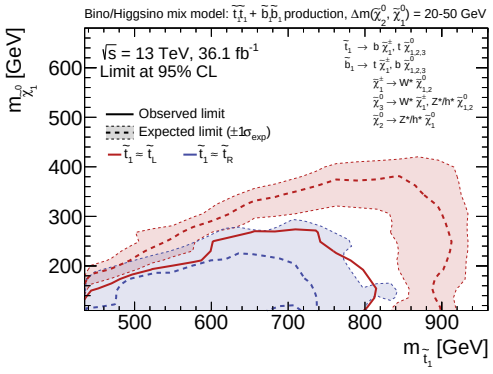

Figure 14.21: Expected and observed 95% excluded regions in the plane of $m_{\tilde{\chi}_1^0}$ versus $m_{\tilde{t}_1}$ for the direct top/bottom squark pair production in the well tempered neutralino model using the tN_med combination with the three soft lepton selections. The dashed coloured lines shows the expected limit and the same coloured band includes all statistical and systematic uncertainties. The coloured line shows the observed limit, where the smaller dashed lines represent the uncertainty in the signal cross-section. The different colours represent different signal hypotheses.

considered, while for the right-handed scenario only the top squark production is considered. The observed (expected) exclusion limit goes up to 800 GeV (900 GeV) for the left-handed scenario. The expected exclusion for the right-handed scenario goes up to 740 GeV, but due to the lower sensitivity and a slight excess in data, no observed exclusion limit can be set.

15 Compressed Region

15.1 Analysis Strategy

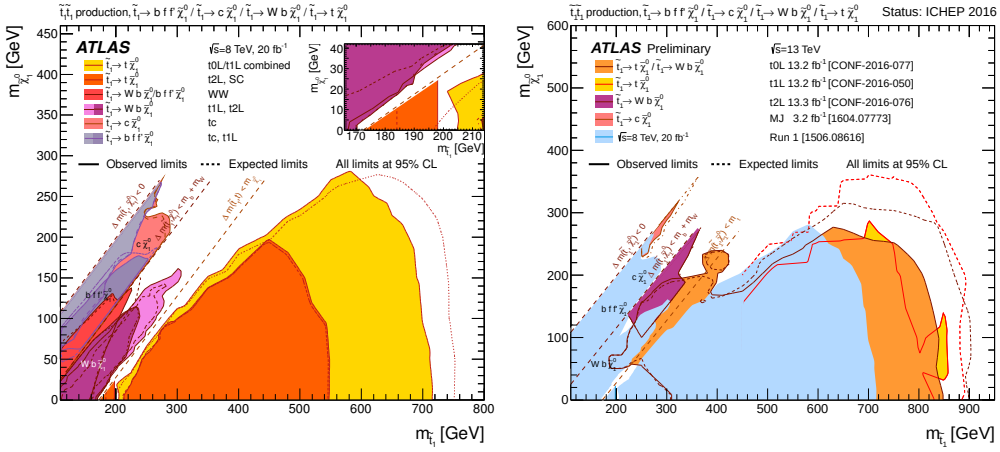

Figure 15.1: Summary of the dedicated ATLAS searches for top squark pair production based on data taken at $\sqrt{s} = 8$ TeV (left [171]) and $\sqrt{s} = 8$ and 13 TeV (right [163]). Exclusion limits at 95% CL are shown. The dashed and solid lines show the expected and observed limits, respectively, including all uncertainties except the theoretical signal cross-section uncertainty. The inset in the left plot shows a zoom into the low top squark mass region to the diagonal.

The region of parameter space where the mass difference of the top squark and the neutralino is close to the top quark mass is usually referred to as diagonal region as the kinematic boundary between the two- and the tree-body decay is shown via a diagonal line in the exclusion plots in the previous analyses [163, 171]. In this compressed $\tilde{t}_1 \rightarrow t + \tilde{\chi}_1^0$ scenario, the signal process has very similar kinematics as the Standard Model $t\bar{t}$ process.

In Figure 15.1, the exclusion contour of previous analyses is shown. No exclusion in the compressed region was possible from the analyses at $\sqrt{s} = 8$ TeV [171]. Different single bin approaches were tested, but found to be not sensitive. For the shown results, a more complicated approach was used with a shape fit in the $E_{\mathrm{T}}^{\mathrm{miss}}$ and m_{T} distribution using 12 bins in total. This more complex approach was not sufficient to fully exclude the compressed region. The exclusion limit starts around a top

squark mass of 200 GeV, but the mass difference between the top squark and the sum of the top quark and the neutralino is larger than 15 GeV. A dedicated analysis targeting the three-body decay also looses sensitivity towards the diagonal boundary. Therefore a non-excluded area is left between the different search regions. A measurement of the spin correlation in $t\bar{t}$ events is sensitive to the production of top squarks pairs for very low top squark masses. With this measurement, top squarks with a mass between the top quark mass up to a mass of 198 GeV can be excluded. Top squark masses above this value are not excluded from these previous analyses for the compressed decay.

Newer results at $\sqrt{s} = 13$ GeV from a similar search considering the fully hadronic top squark pair decay gained sensitivity over the diagonal region for higher top squark masses [172]. In this analysis, top squark masses down to a mass of 250 GeV are excluded for the compressed decay.

Taking into account these results, the compressed area for top squark masses from 198 to 250 GeV is not excluded. The aim of the presented analysis is to gain sensitivity towards lower top squark masses on the diagonal in order to exclude this region in the compressed parameter space. The analysis is optimised to be sensitive to this area for the two-body decay of the top squark, and is sensitive towards the thee-body decay as well.

The kinematics of the signal process and the background processes are very similar, due to the low mass difference of the top squark and the neutralino. To achieve optimal sensitivity, the full event information has to be exploited. This includes kinematic features, as well as the information in the correlation of observables. To render this task possible, a boosted decision tree (BDT, see Section 4.3) is used to classify the events into signal and background classes.

In this chapter, first the procedure of the optimisation of the inputs and settings for the BDT is detailed. Afterwards, the estimation for the background normalisation is explained. The BDT distribution and input variables are well validated, the validation approaches are explained in detail. As a more complex shape fit is performed for this analysis, the details of the fit procedure are given. Afterwards, the results of the analysis are presented and compared to similar searches.

15.2 Training of the BDT

The preselection used for the training is detailed in Section 13.2. The agreement between data and the MC prediction are checked after this selection and no shape differences are observed (see Appendix C.6).

A signal with a top squark mass of 250 GeV and a neutralino mass of 62 GeV is used for the training of the BDT. In order to perform a stable training which is not sensitive to statistical fluctuations, high statistics is produced for this sample. The signal is trained against the $t\bar{t}$ and W+jets background which are the two leading backgrounds after the preselection (see Figure 13.5 left-hand side) and both sum up to 20318 ± 173 expected events. Other background processes, such as $t\bar{t} + V$, single top and diboson events are not considered in the training, but are used for the final evaluation. The diboson process is the smallest of these backgrounds with 173 ± 3 events predicted from the MC simulation. Smaller backgrounds processes stemming from Z+jets, tZ, $t\bar{t} + WW$ or tWZ events are not considered as they are negligible compared to the others. After the preselection, 83 ± 16 events are expected in total from these smaller processes, with the largest amount from Z+jets events of 68%.

The selection of the BDT parameters, the preselection as well as the input variables are optimised. For each setting which should be tested, a dedicated BDT has to be trained. The performance of the BDT is quantified based on the maximal expected significance achievable when cutting at the BDT distribution evaluated with the test events.

For the optimisation, first a simple BDT with the `Gradient BoostType` is used with many input variables and the default `TMVA` settings. In the first optimisation step, the choice of the input variables is optimised. Low ranked and thus unimportant variables are removed when no change in the BDT performance is observed. In the ranking, the highest importance is assigned to variables which are easy to split on. This does not necessarily mean that these variables also provide the largest separation power. In order to estimate the expected sensitivity of a performed training, a cut is placed on the BDT output maximising the expected significance. The significance values are then compared independently of the cut position on the BDT score. After the lowest ranked variables is found to increase the expected sensitivity, a full set of so-called N-1 trainings is performed. For this, each variable is left out once and removed if no improvement is observed. This procedure is iterated until all input variables show improvement in the expected sensitivity.

Table 15.1: The different settings and values tested in the BDT hyper-parameter grid search.

Setting	Value
`BoostType`	Grad, Ada
`NTrees`	300, 400, 500, 600, 700, 800
`MinNodeSize`	2, 4, 6
`UseRandomisedTrees`	True, False
`UseNvars`	4, 6, 8, 10
`UseBaggedBoost`	True, False
`BaggedSampleFraction`	0.4, 0.5, 0.6
$E_{\mathrm{T}}^{\mathrm{miss}}$ cut	100, 120 GeV
m_{T} cut	90, 120 GeV

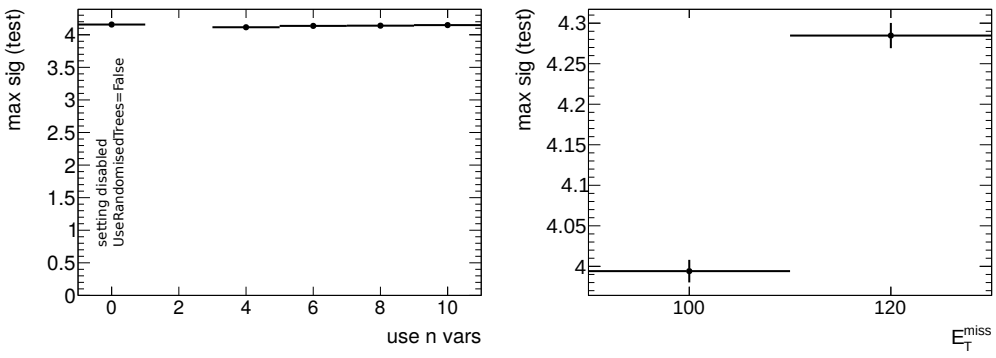

Figure 15.2: Tested values for the `UseNvars` and the $E_{\mathrm{T}}^{\mathrm{miss}}$ cut versus the maximal significance of an uncorrelated data sample (test).

Table 15.2: The different settings and specific values used for the BDT.

Setting	Value	Short description
`BoostType`	Grad	Boosting type for all trees in the forest
`NTrees`	400	Number of trees in the forest
`MinNodeSize`	4	Minimum percentage of training events required in a leaf node
`UseRandomisedTrees`	True	Determine at each node splitting the cut variable only as the best out of a random subset of variables
`UseNvars`	10	Size of the subset of variables used with RandomisedTree option
`UseBaggedBoost`	True	Use only a random subsample of all events for growing the trees in each iteration
`BaggedSampleFraction`	0.6	Relative size of bagged event sample to original size of the sample

In the second optimisation step, a general grid search is performed to determine the best BDT parameters. Additionally, the $E_{\mathrm{T}}^{\mathrm{miss}}$ and m_{T} preselection cuts are varied. The tested values can be found in Table 15.1. All combinations of these different settings are tested. For example, the dependence of the `UseNvars` and the $E_{\mathrm{T}}^{\mathrm{miss}}$ cut versus the significance of an uncorrelated data set can be seen in Figure 15.2. Changing the `UseNvars` does not strongly influence the achievable significance, while the $E_{\mathrm{T}}^{\mathrm{miss}}$ preselection affects this significance. In order to take into account the correlations of the various settings, all combinations are tested and the one with the highest total significance is taken. The chosen settings and a short description of their meaning are shown in Table 15.2. For the preselection, $m_{\mathrm{T}} > 120\,\mathrm{GeV}$ and $E_{\mathrm{T}}^{\mathrm{miss}} > 120\,\mathrm{GeV}$ show the best performance and are thus already presented previously (see Section 13.2).

The two optimisation steps, selecting the input variables and the BDT settings, are correlated to each other. Therefore, these processes have to be iterated until no further improvement is achieved. The N-1 trainings are repeated, resulting in similar significances. Thus, the final set of input variables is summarised in Table 15.3 showing the N-1 significances as well as the total calculated significance after applying a cut at the BDT distribution considering a flat background uncertainty of 25%.

The training of a BDT is susceptible to statistical fluctuations in the training data set. If the same simulated events are used in the training as well as in the statistical evaluation of the BDT, this can lead to a bias due to the differences between simulation and data. In order to avoid this overtraining effect, none of the events entering the training are used in the statistical evaluation. The simulated MC events are split into two parts according to their event numbers, a quantity available in all events that is not correlated to any physical observable. One of the parts is used for the training of the BDT and the other part for the evaluation, ensuring that no event is used twice. As this procedure would effectively decrease the statistical precision of the simulation by 50%, a second BDT is trained with identical settings and variables, but inverting the selection for the training and evaluation data sets. In the final evaluation, the same split according to the event number is applied to data and

Table 15.3: Input variables for the BDT. The N-1 significance column gives the significance as described above for a BDT trained without the corresponding variable used. The variables are ranked starting with the lowest significance, thus the most important variables. The lowest row gives the expected significance after applying a cut at the BDT distribution when all variables are used for the training.

Input variables	N-1 significance
$\Delta\phi(E_{\mathrm{T}}^{\mathrm{miss}}, t_{\mathrm{had}})$	3.1 ± 0.2
χ^2-based $m_{\mathrm{t,had}}$	3.3 ± 0.2
$E_{\mathrm{T}}^{\mathrm{miss}}$	3.5 ± 0.3
m_{T}	3.7 ± 0.2
Number of jets	3.7 ± 0.2
$\Delta R(b, \ell)$	3.8 ± 0.4
$\Delta\phi(t, \bar{t})$	4.0 ± 0.3
Fourth jet p_{T}	4.2 ± 0.4
Third jet p_{T}	4.4 ± 0.3
$H_{\mathrm{T,sig}}^{\mathrm{miss}}$	4.4 ± 0.4
All variables	5.8 ± 0.4

MC simulation. This makes sure that no bias due to differences in the BDT distributions of the two trainings can affect the analysis.

Figure 15.3 and Figure 15.4 show the shape distributions of the two BDT trainings, for signal and background events respectively. The events in the "Train" distribution are used to train the respective BDT, while the "Test" events are from the evaluation part of the sample. As the BDT shapes are similar, both between test and training set as well as between the two trainings, no influence of statistical fluctuations on the performance of the trainings are expected. The combination with even and odd event numbers is done same for the MC samples and the data events.

With the above procedure, a BDT is trained to be sensitive in the low top squark mass regime near the diagonal boundary. Signal events receive a higher score of the resulting BDT, while backgrounds are classified with a low score. The distribution of the BDT output is used in the analysis, in order to define control regions for the backgrounds, as well as a signal region. In the signal enriched region, the shape of the BDT output is used to enhance the sensitivity to the specific signal model.

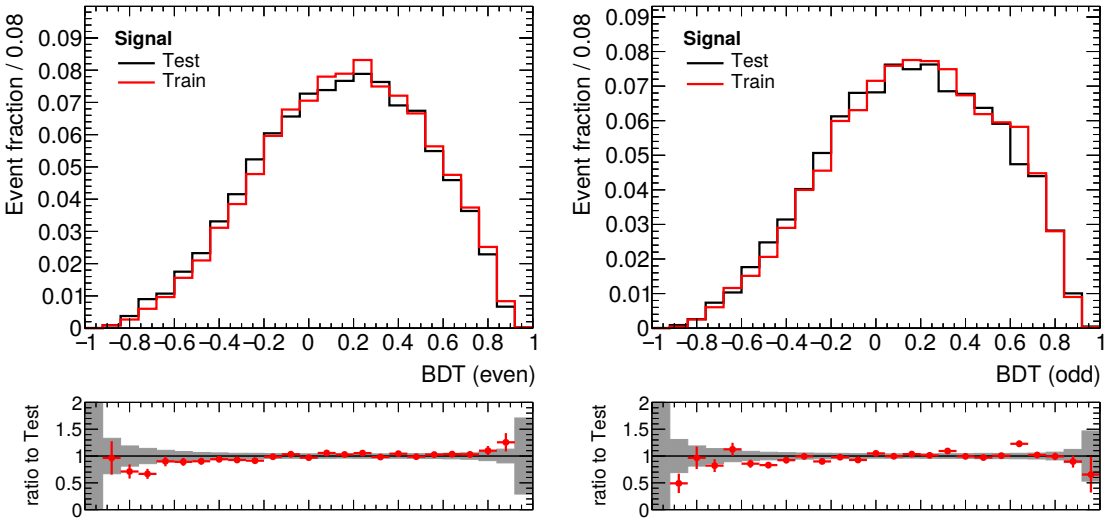

Figure 15.3: Signal shape for the BDT trained on even (left) and odd (right) event numbers comparing the corresponding test and train sample.

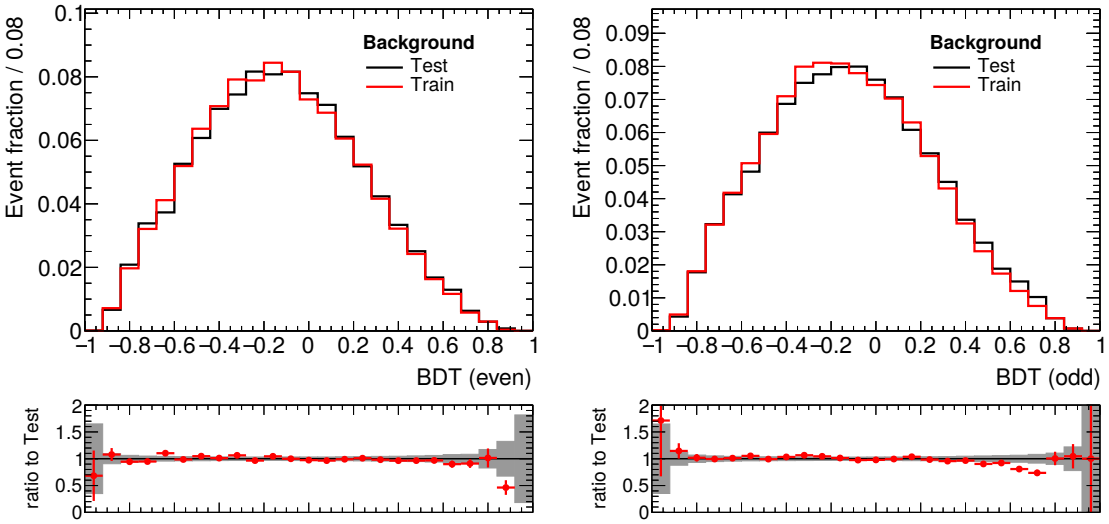

Figure 15.4: Background shape for the BDT trained on even (left) and odd (right) event numbers comparing the corresponding test and train sample.

15.3 Background Estimation

The full BDT distribution is presented in Figure 15.5 showing the sum of all backgrounds and the benchmark signal overlaid. Overall, the largest background stems from $t\bar{t}$ processes, where the semi-leptonic and dileptonic $t\bar{t}$ processes are both relevant and contribute to 55% and 30% respectively. The contribution of the other backgrounds is smaller compared to the signal for most of the BDT distribution. The normalisation of the $t\bar{t}$ background is estimated similarly to the tN_med region, in a data-driven way by defining $t\bar{t}$ enriched regions.

In Figure 15.6, the shape is compared between all backgrounds added and the benchmark signal. As already seen in the previous distribution, the signal to background ratio improves for higher BDT scores. Thus the higher BDT score values can be used to define a signal enriched region. As the separation between signal and background in general is difficult for this region, the definition of a $t\bar{t}$ enriched control region is also not trivial when using only requirements on kinematic distributions. With the BDT, a powerful tool is optimised for this separation and therefore control regions can be defined by using lower BDT scores. The right-hand plot in Figure 15.6 shows the shape difference between the benchmark signal and the two $t\bar{t}$ processes – semi- and dileptonic. As visible from these shapes, the semi- and dileptonic processes behave differently, as the dileptonic $t\bar{t}$ process tends towards even lower BDT values compared to the semi-leptonic $t\bar{t}$ process. Thus independent normalisation factors can be determined. Two control regions are defined using the BDT range from -1 to -0.4 and from -0.4 to 0.4.

Additional requirements on the transverse momenta are applied in order to bring the control regions kinematically closer to the signal region and to reduce modelling uncertainties. In Figure 15.7 the transverse momentum of the first two leading jets are shown after the preselection used for the training and a cut on BDT > 0.4. Applying additional requirements at the leading jet p_{T} larger 100 GeV and the second leading jet p_{T} larger 50 GeV remove background events without removing too many signal events. The transverse momenta requirement is 66% and 78% efficient for the background and the signal respectively. As the region with higher BDT scores is nearly not affected, only the control region kinematics are changed to be closer to the ones in the signal region.

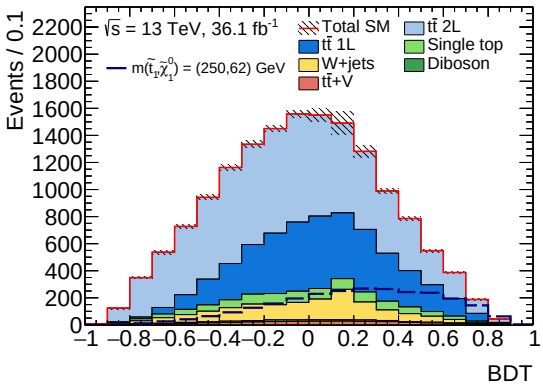

Figure 15.5: Full BDT distribution for the sum of all SM backgrounds and the benchmark signal overlaid.

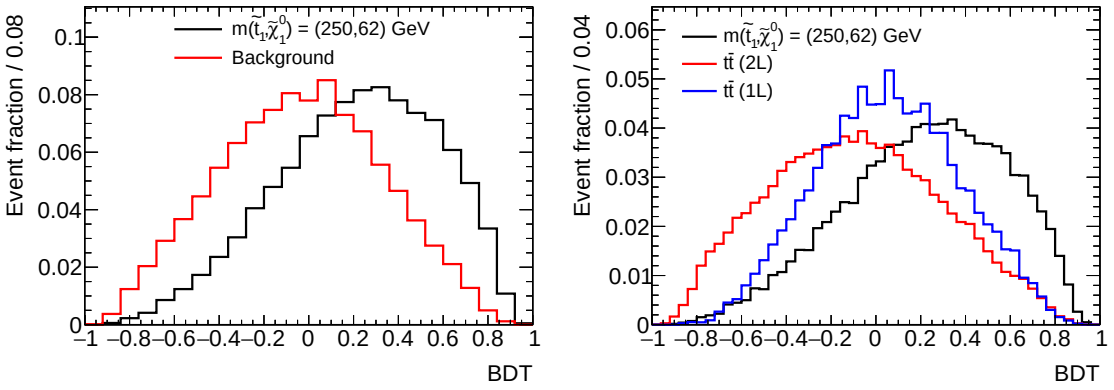

Figure 15.6: Shape comparison between the benchmark signal and the sum of all backgrounds (left) and for the semi- and dileptonic $t\bar{t}$ contribution separately (right).

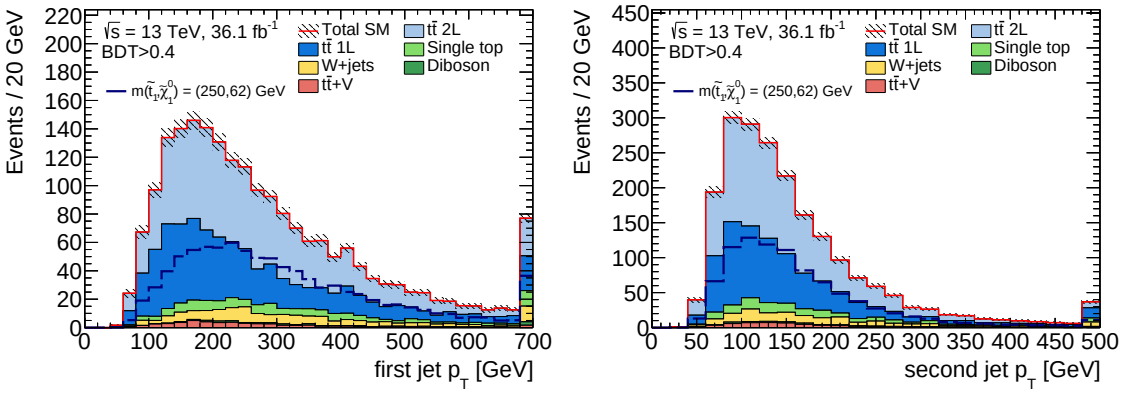

Figure 15.7: Leading (left) and sub leading (right) jet p_{T} after applying all preselection requirements and a cut on the BDT distribution of 0.4. The sum of all background processes is shown and the benchmark signal is overlaid.

The normalisation factors are determined in the fit to the control regions to 1.16 ± 0.16 for dileptonic $t\bar{t}$ and 1.16 ± 0.28 for semi-leptonic $t\bar{t}$. The values are slightly above unity but agree within the uncertainties with unity. The normalisation factors are in good agreement to each other. In order to not rely on the additional jet modelling, the normalisation is nonetheless kept separate for both $t\bar{t}$ processes. The observed and expected event yields are presented in Table 15.4 and a perfect agreement between the fitted and the observed yields can be seen by construction.

The modelling of the MC prediction is checked in these two control region bins requiring -1 < BDT < -0.4 (CR1) and -0.4 < BDT < 0.4 (CR2). The $E_{\mathrm{T}}^{\mathrm{miss}}$ and m_{T} distribution for those two regions are shown in Figure 15.8 and 15.9 respectively. Overall a good modelling can be observed for all variables (see Appendix C.7.2).

Table 15.4: Observed events and expected yields for all background processes in the control regions with the normalisation factors applied. The individual uncertainties are correlated and do not add up quadratically to the total uncertainty.

Region	CR1	CR2
Observed events	2855	11432
Total background events	2855 ± 53	11432 ± 107
$t\bar{t}$ 2L events	2072 ± 190	5900 ± 776
$t\bar{t}$ 1L events	395 ± 82	3796 ± 747
$t\bar{t}+V$ events	35 ± 18	176 ± 89
Single top events	123 ± 54	560 ± 218
W + jets events	206 ± 123	911 ± 423
Diboson events	25 ± 13	89 ± 48
MC exp. background events	2800	11382
MC exp. $t\bar{t}$ 2L events	2000	5697
MC exp. $t\bar{t}$ 1L events	411	3949
MC exp. $t\bar{t}+V$ events	35	176
MC exp. single top events	123	560
MC exp. W + jets events	206	911
MC exp. diboson events	25	89

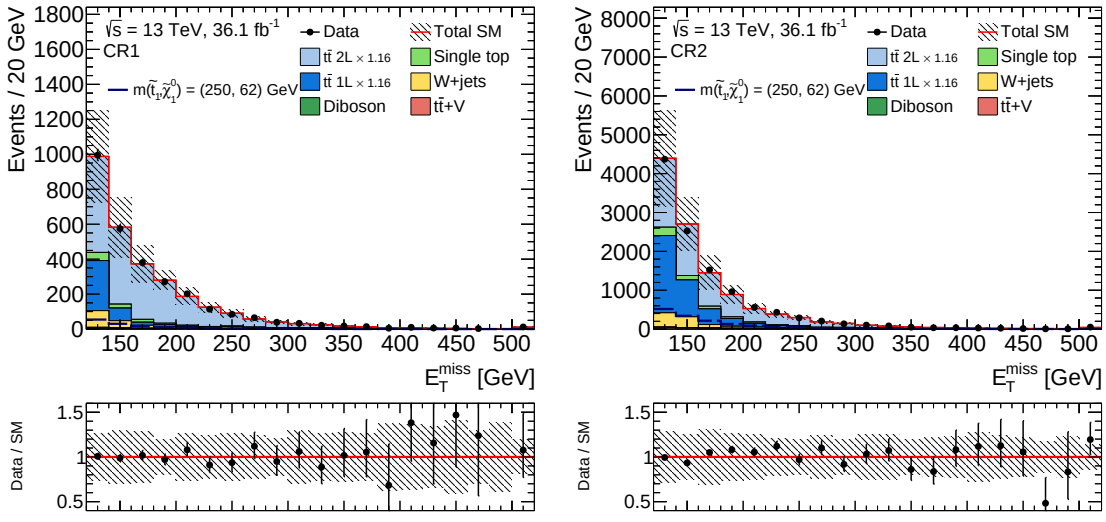

Figure 15.8: The $E_{\mathrm{T}}^{\mathrm{miss}}$ distribution in the two control region bins requiring -1 < BDT < -0.4 (CR1, left) and -0.4 < BDT < 0.4 (CR2, right). The normalisation factors for $t\bar{t}$ 1L and 2L are applied as determined in the simultaneous fit. The statistical uncertainty is shown as well as the uncertainties from JES/JER and b-tagging.

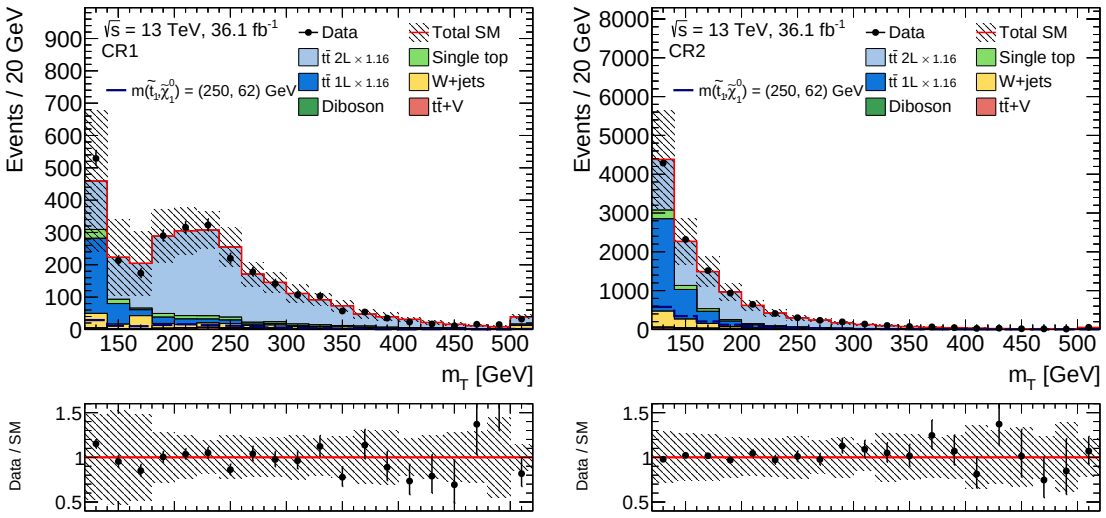

Figure 15.9: The m_{T} distribution in the two control region bins requiring -1 < BDT < -0.4 (CR1, left) and -0.4 < BDT < 0.4 (CR2, right). The normalisation factors for $t\bar{t}$ 1L and 2L are applied as determined in the simultaneous fit. The statistical uncertainty is shown as well as the uncertainties from JES/JER and *b*-tagging.

15.4 Validation

The modelling of the BDT distribution has to be well validated as both the background normalisation as well as the signal sensitivity is derived from this distribution. The BDT distribution, the input variables and the correlation between those are validated and various mis-modelling checks are performed. Illustrative plots are shown in this section.

Already before the training of the BDT, all input variables are checked after the preselection (see Table 13.2) is applied. The $E_{\mathrm{T}}^{\mathrm{miss}}$ and m_{T} distribution are shown in Figure 15.10. The shape of these distributions is modelled well, but an overall constant offset can be seen in the ratio between data and the SM prediction. This normalisation will be taken into account when using the determined $t\bar{t}$ normalisation which is slightly above the prediction for both semi- and dileptonic $t\bar{t}$. The other distributions after the preselection cut also show good shape agreements and can be found in Appendix C.6.

Furthermore, a combination of both control regions is checked (-1 < BDT < 0.4) and a less inclusive selection which is closer to the signal region requiring 0 < BDT < 0.4. The $E_{\mathrm{T}}^{\mathrm{miss}}$ distribution for those two selections is shown in Figure 15.11. All other distribution for those selections are presented in Appendix C.7.2 and an overall good modelling can be seen for all variables. The signal contamination in those regions is below 15%.

A dedicated validation region is constructed using the BDT distribution. As the control regions are defined for BDT scores < 0.4 and the signal region is defined with a high BDT score, the intermediate region is used as validation region to check the $t\bar{t}$ normalisation for this fit setup. This validation region is defined in the range of 0.4 < BDT < 0.6. To reduce the signal contamination

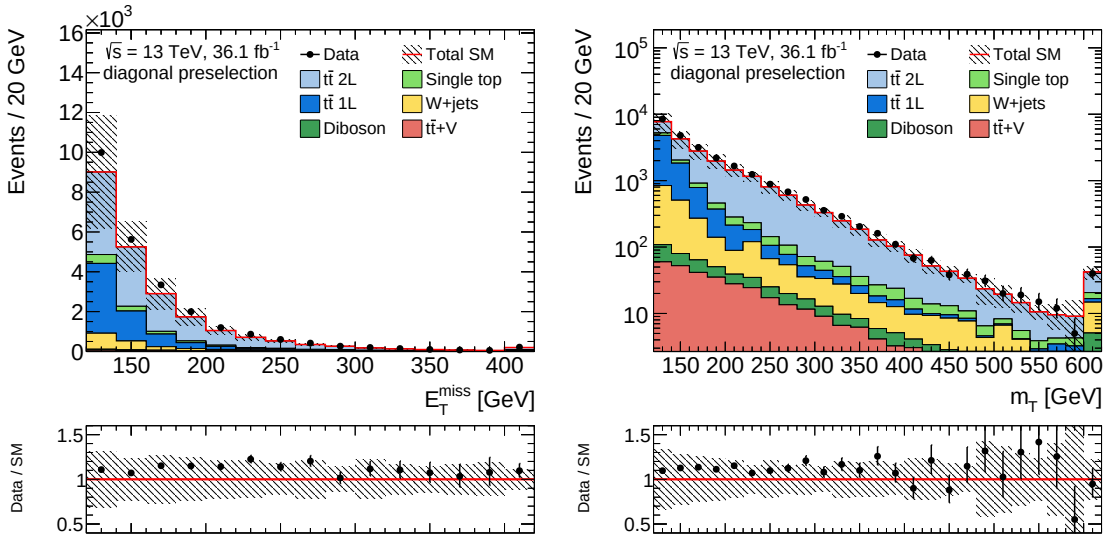

Figure 15.10: The $E_{\mathrm{T}}^{\mathrm{miss}}$ (left) and m_{T} (right) distribution after the low $E_{\mathrm{T}}^{\mathrm{miss}}$ preselection is applied (see Table 13.2). The statistical uncertainty is shown as well as the uncertainties from JES/JER and *b*-tagging.

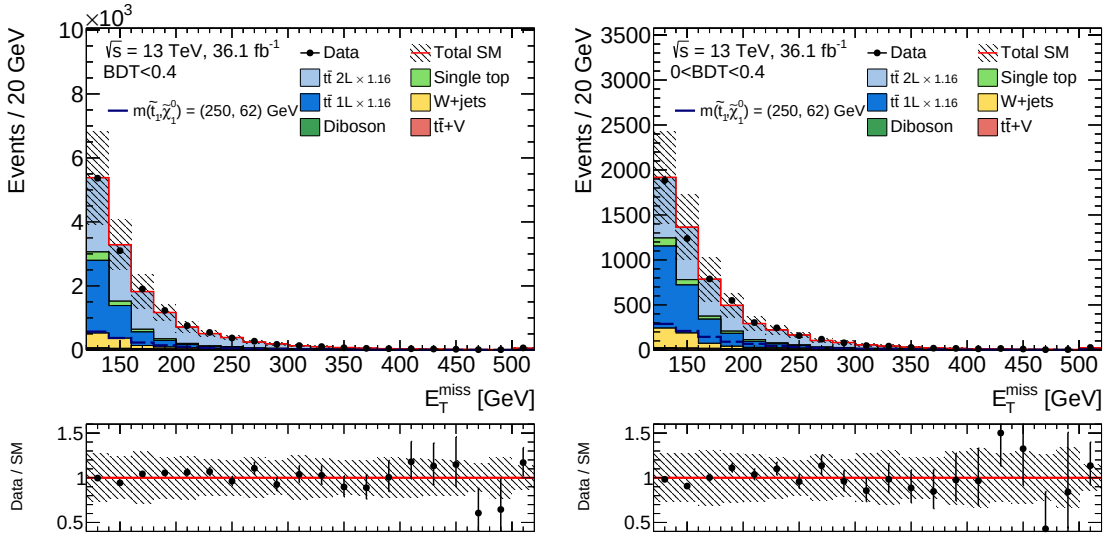

Figure 15.11: The $E_{\mathrm{T}}^{\mathrm{miss}}$ distribution in a BDT range of -1 to 0.4 (left) and 0 to 0.4 (right).The normalisation factors for semi- and dileptonic $t\bar{t}$ are applied as determined in the simultaneous fit. The statistical uncertainty is shown as well as the uncertainties from JES/JER and *b*-tagging.

higher BDT values are not considered. Using this range, the signal contamination reaches 31%. The modelling is checked in this region before the discovery fit is performed where no signal was found. Therefore, this region is then part of the exclusion fit setup in which the full shape is used in order to increase the sensitivity. The $E_{\mathrm{T}}^{\mathrm{miss}}$ and m_{T} distribution for this validation region is shown in Figure 15.12 where a good agreement can be seen. Further plots for this region are presented in Appendix C.7.1 where overall a good modelling is observed.

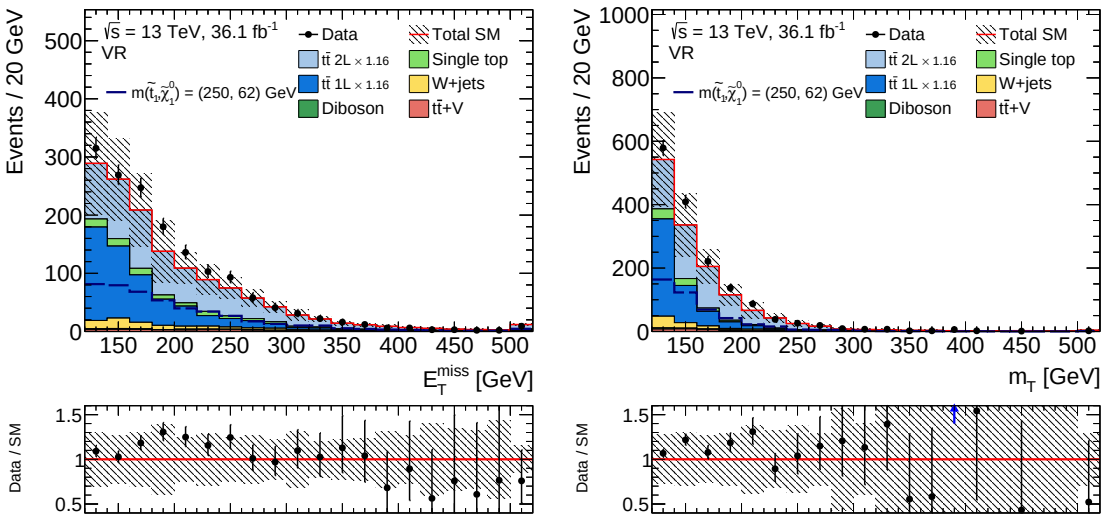

Figure 15.12: The $E_{\mathrm{T}}^{\mathrm{miss}}$ (left) and m_{T} (right) distribution in the BDT VR in the discovery fit setup. The normalisation factors for semi- and dileptonic $t\bar{t}$ are applied as determined in the simultaneous fit. The statistical uncertainty is shown as well as the uncertainties from JES/JER and b-tagging.

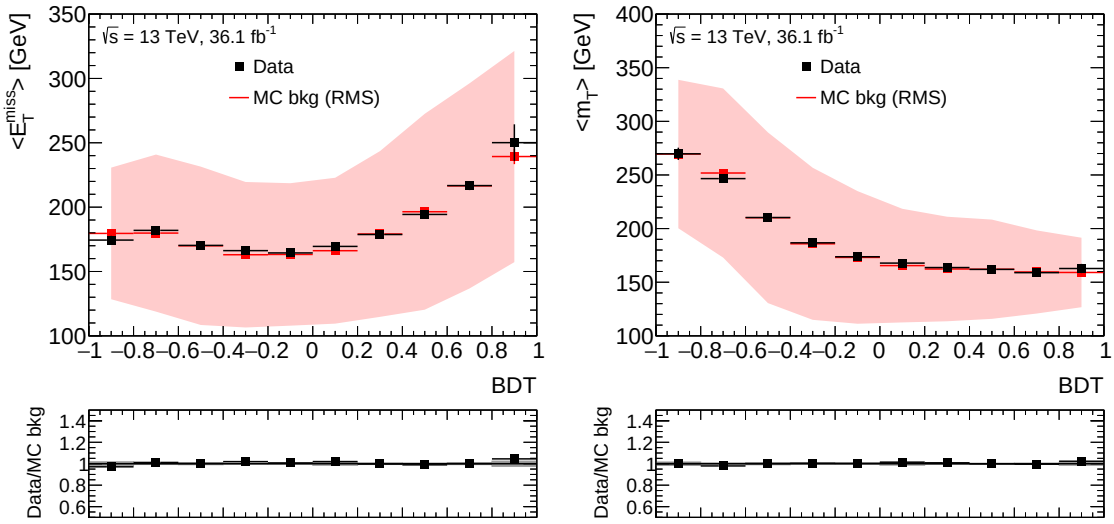

Figure 15.13: Average of $E_{\mathrm{T}}^{\mathrm{miss}}$ (left) and m_{T} (right) versus the BDT output.

Furthermore, the dependence of the average of each BDT input variable to the BDT distribution is compared between data and the SM prediction. Illustrative distributions are shown in Figure 15.13 and Figure 15.14, the remaining ones can be found in Appendix C.7.3. These plots check both the modelling of the input quantities in different BDT bins as well as the modelling of the correlation of each variable to the BDT distribution. On the other hand, they illustrate the general importance of the variables. Some variables show a stronger slope in these plots, e.g. the $E_{\mathrm{T}}^{\mathrm{miss}}$ and m_{T} distribution. Those variables could more easily be used in a cut-based analyses. Other variables have a flat structure, e.g. $\Delta\phi(t_{\mathrm{lep}}, t_{\mathrm{had}})$. This indicates that the correlation to other variables gives the additional information used for the BDT.

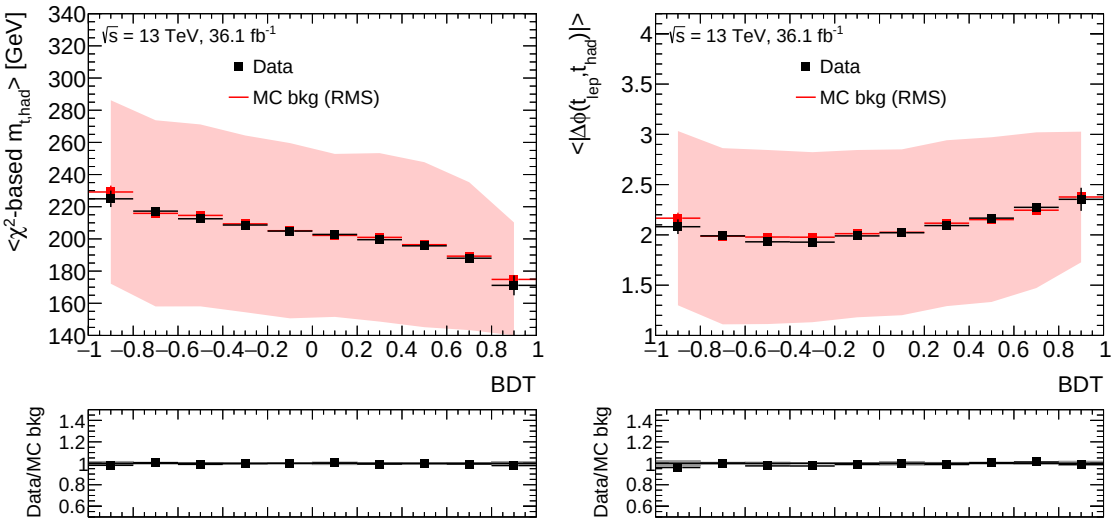

Figure 15.14: Average of χ^2-based $m_{\mathrm{t,had}}$ (left) and $\Delta\phi(t_{\mathrm{lep}}, t_{\mathrm{had}})$ (right) versus the BDT output.

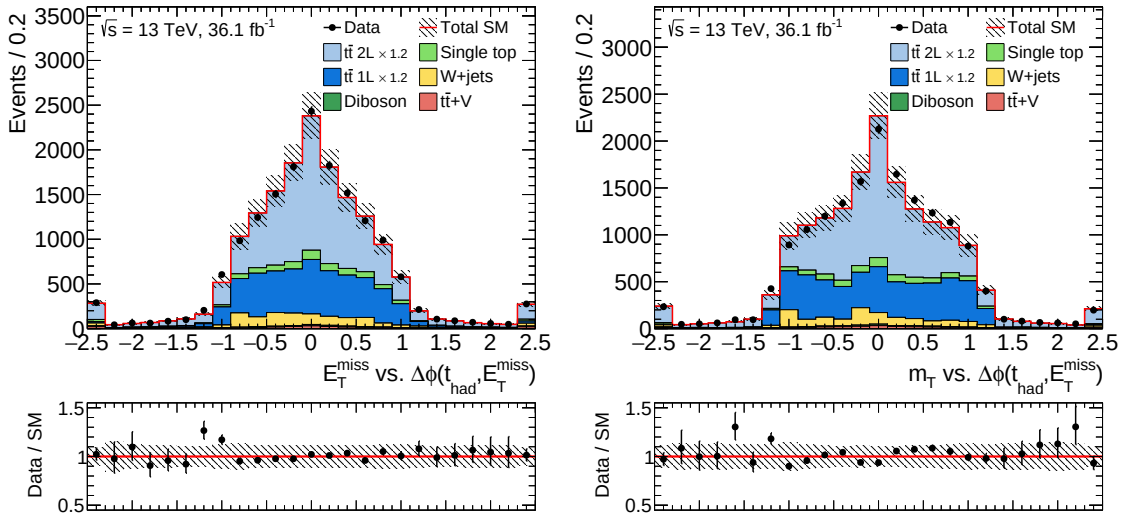

Figure 15.15: The correlation of $E_{\mathrm{T}}^{\mathrm{miss}}$ (left) and m_{T} (right) versus the $\Delta\phi(E_{\mathrm{T}}^{\mathrm{miss}}, t_{\mathrm{had}})$. Normalisation factors for semi- and dileptonic $t\bar{t}$ are applied, only statistical uncertainties are shown

In the training, the BDT learned the kinematic of the signal process and learned to separate this process from the background processes. The dependence of the input variables on the BDT distribution shows which features are considered signal like. High BDT values are correlated with higher $E_{\mathrm{T}}^{\mathrm{miss}}$ values. This is expected as the signal process tends slightly towards higher values than the $t\bar{t}$ background. The m_{T} average for high BDT scores is around 160 GeV. The background processes tends to values below the W boson mass, where the signal tends towards higher values, but not as high as e.g. for the tN_med signal (see the preselection plots in Section 13.2). Especially the χ^2-based $m_{\mathrm{t,had}}$ dependence show the good performance of the training by learning the correct mass of the expected top quark resonance. Towards high BDT values, the χ^2-based $m_{\mathrm{t,had}}$ average

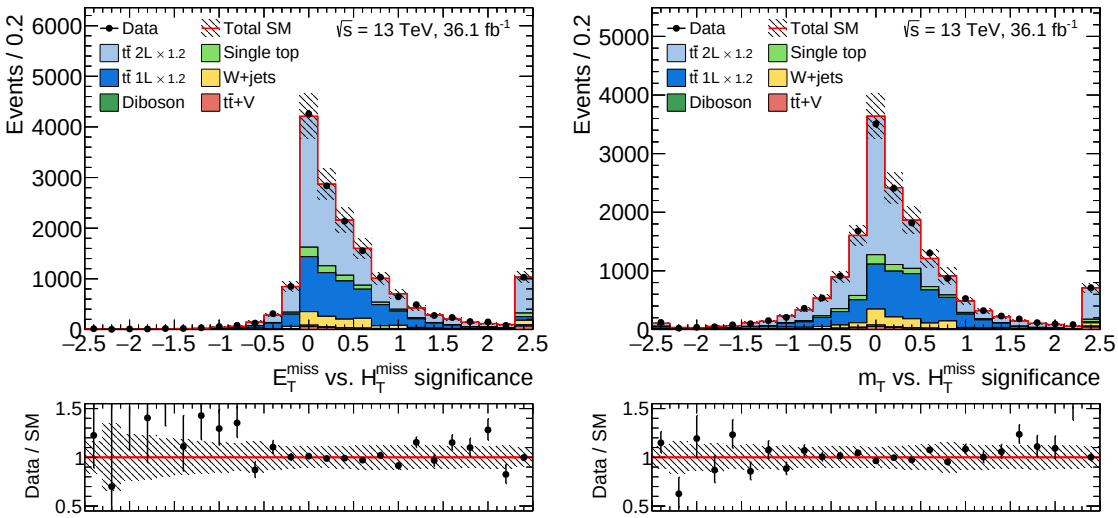

Figure 15.16: The correlation of $E_{\mathrm{T}}^{\mathrm{miss}}$ (left) and m_{T} (right) versus the $H_{\mathrm{T,sig}}^{\mathrm{miss}}$. Normalisation factors for semi- and dileptonic $t\bar{t}$ are applied, only statistical uncertainties are shown

is at 175 GeV. That means that the BDT expects a well reconstructed top quark for the signal classification.

Overall, these plots are a good tool to understand the internal structure of the BDT and show that the BDT learned the kinematic of the signal and is not trained on statistical artefacts. In addition, one can validate that the learned structure is well modelled as the same behaviour is predicted from the SM processes as it is seen in data.

The BDT relies on the correlation between the input variables. Therefore the modelling of the correlation is validated. This can be done by checking that the correlation between variables is well modelled by MC. For this, the Pearson correlation coefficient is calculated which is defined as $(x - \langle x \rangle) \cdot (y - \langle y \rangle)/(\mathrm{RMS}_x \cdot \mathrm{RMS}_y)$. This is a measure of the linear correlation of two variables. If a positive (negative) values is calculated, there is a positive (negative) linear correlation, where values around zero mean that there is no linear correlation. Illustratively, the correlation for $E_{\mathrm{T}}^{\mathrm{miss}}$ and m_{T} to the $\Delta\phi(E_{\mathrm{T}}^{\mathrm{miss}}, t_{\mathrm{had}})$ is shown in Figure 15.15 with values around zero. Therefore, no linear correlation between these variables can be seen. In Figure 15.16, the correlation between $E_{\mathrm{T}}^{\mathrm{miss}}$ and m_{T} to $H_{\mathrm{T,sig}}^{\mathrm{miss}}$ is shown. As $H_{\mathrm{T,sig}}^{\mathrm{miss}}$ and $E_{\mathrm{T}}^{\mathrm{miss}}$ are correlated to each other, the distribution tends towards positive values. The correlation to m_{T} is much less pronounced, therefore this distribution is centred around zero with a small trend towards positive values. The correlation of all input variables to $E_{\mathrm{T}}^{\mathrm{miss}}$ and m_{T} are shown in Appendix C.7.4. The data and the SM prediction agree well within the uncertainties, and no mis-modelling of these correlations can be observed.

15.4.1 Validation with 2L and 1L1τ Selections

The main background for high BDT values consists of events stemming from the dileptonic $t\bar{t}$ process. These processes can be only selected in the signal region when one lepton is not reconstructed and thus not selected, and additional jets are produced. Thus the modelling of the jet multiplicity and momenta of these events is validated in dedicated selections requiring either an electron and a muon or one lepton and one hadronic τ candidate. After the nominal preselection, 60% of the dileptonic $t\bar{t}$ events include a hadronic τ decay, approximately constant over the whole range of the BDT output.

In order to validate the dileptonic $t\bar{t}$ background without a hadronic τ, events are selected with an opposite charged $e\mu$ lepton pair ($e\mu$ (OS) selection). For the selection, the single lepton triggers are used and at least two jets are required with $p_{\mathrm{T}} > 50, 25\,\mathrm{GeV}$, where at least one is b-tagged. In Figure 15.17, the jet multiplicity is shown for two different $E_{\mathrm{T}}^{\mathrm{miss}}$ thresholds in order to check the modelling in dependence of the $E_{\mathrm{T}}^{\mathrm{miss}}$. A good agreement can be seen for the simulation and the measured data for up to more than eight selected jets. The modelling of the transverse momentum distribution of the third and fourth leading jet is shown in Figure 15.18. These distributions are checked as they are input in the BDT training and could lead to problems in case of mis-modelling for the leading background.

In order to validate the dileptonic $t\bar{t}$ background with a hadronic τ decay, events are selected using the BDT preselection with an inverted hadronic τ veto and thus requiring a hadronic τ candidate (1L1τ selection). The jet multiplicity is shown for two $E_{\mathrm{T}}^{\mathrm{miss}}$ thresholds in Figure 15.19 and the third and fourth leading jet p_{T} in Figure 15.20. Also for this selection, the simulation agrees well with the measured data and no significant deviations are observed.

These distributions confirm that the extra jet production, which is the important factor for the dileptonic $t\bar{t}$ contribution in a one lepton selection, is well described in the simulation.

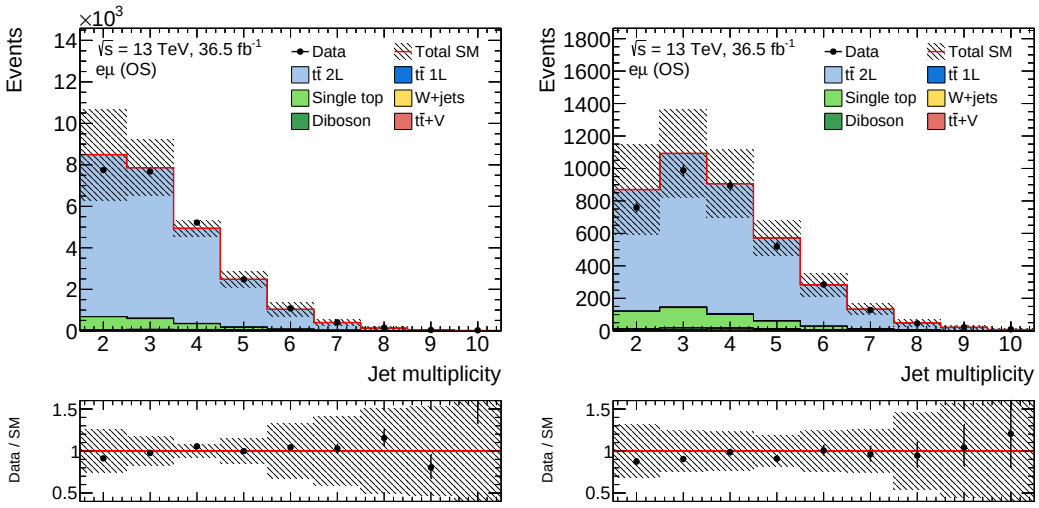

Figure 15.17: Jet multiplicity in the $e\mu$ (OS) selection for $E_{\mathrm{T}}^{\mathrm{miss}} > 120\,\mathrm{GeV}$ (left) and $E_{\mathrm{T}}^{\mathrm{miss}} > 200\,\mathrm{GeV}$ (right). The uncertainty band includes only the $t\bar{t}$ theory uncertainties.

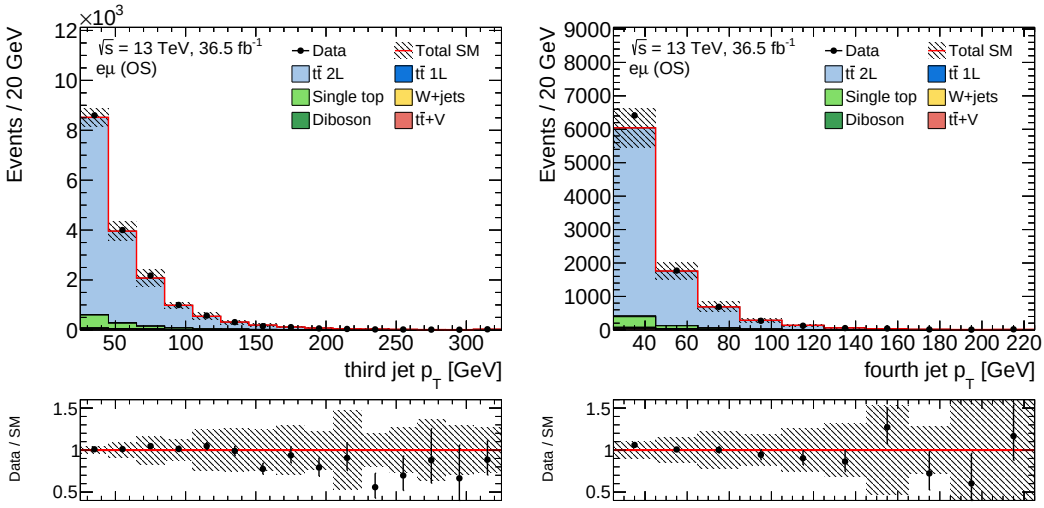

Figure 15.18: Distribution of the p_{T} of the third and fourth leading jet in the $e\mu$ (OS) selection for $E_{\mathrm{T}}^{\mathrm{miss}} > 120\,\mathrm{GeV}$. The uncertainty band includes only the $t\bar{t}$ theory uncertainties.

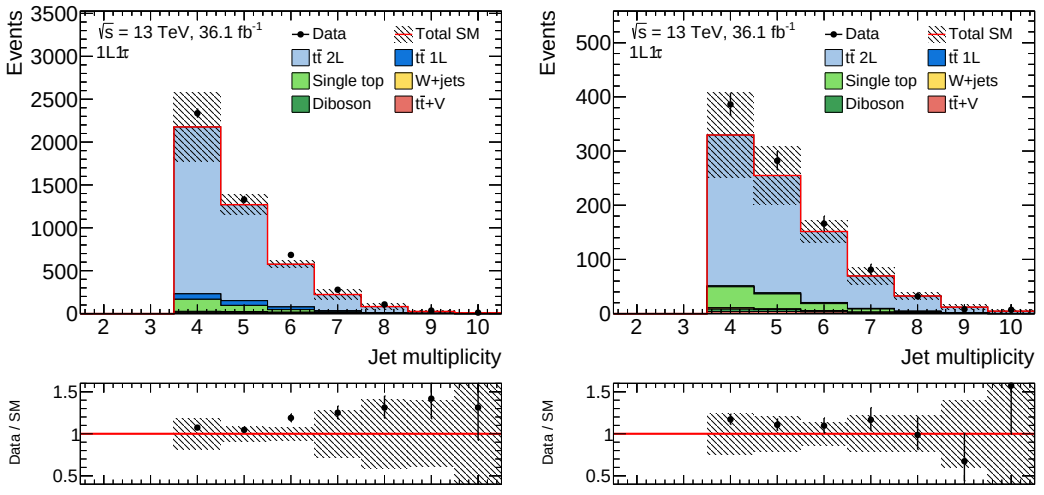

Figure 15.19: Jet multiplicity in the 1L1τ selection for $E_{\mathrm{T}}^{\mathrm{miss}} > 120\,\mathrm{GeV}$ (left) and $E_{\mathrm{T}}^{\mathrm{miss}} > 200\,\mathrm{GeV}$ (right). The uncertainty band includes only the $t\bar{t}$ theory uncertainties.

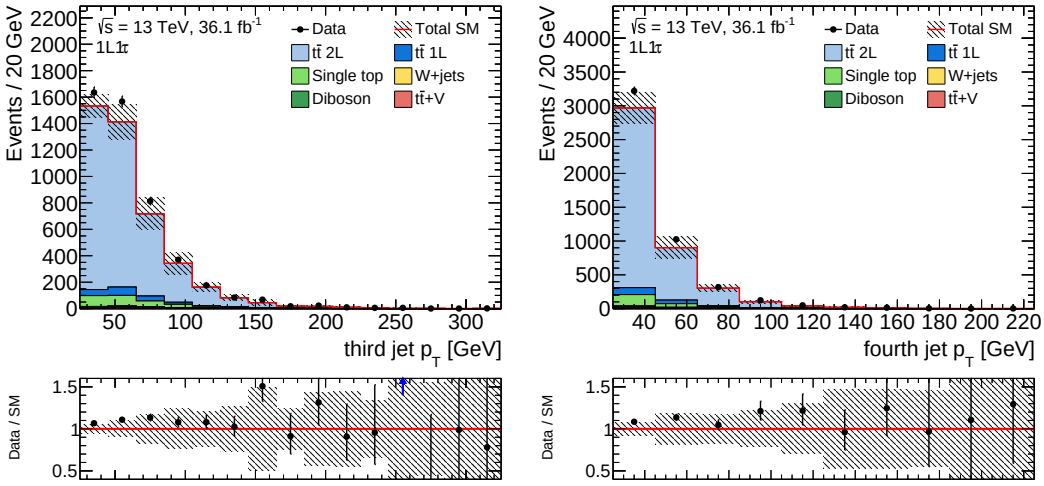

Figure 15.20: Distribution of the p_{T} of the third and fourth leading jet in the 1L1τ selection . The uncertainty band includes only the $t\bar{t}$ theory uncertainties.

15.4.2 Summary of the BDT Validation

The validation of the BDT is important as the full BDT distribution is used. Therefore the modelling of the input variables is tested in various regions. A good agreement between the simulation and the measured data can be seen in all these regions. Furthermore, the correlation of the input variables to the BDT distribution and to each other is studied and found to be well described by the simulation.

The jet multiplicity and the jet p_{T} information, as used in the BDT, are also validated in dedicated opposite sign $e\mu$ and 1L1τ selections. Also here, a good description of the data by the simulation is found.

15.5 Impact of Systematic Uncertainties

The sources of experimental and theoretical uncertainties are discussed in Section 13.4. All those uncertainties are evaluated by calculating the yield change for each control and signal region bin when varying the sources of uncertainties. The full shape and normalisation differences are then considered as systematic uncertainty. As the $t\bar{t}$ background normalisation is determined in the fit, for this background only the shape changes influence the result. In the same manner as for the tN_med signal region, the semi- and dileptonic $t\bar{t}$ systematic uncertainties are handled separately. Only for the minor backgrounds which contribute less than 2% in each individual bin – diboson and $t\bar{t}+V$ – the theoretical uncertainties are not evaluated in detail, but assumed to be flat with an uncertainty of 50% over the full region. This uncertainty is well above the corresponding cross-section uncertainty of 6% and 13% respectively. Interference effects between $t\bar{t}$ and single top Wt processes are evaluated on particle level to be below 10%, thus an overall flat uncertainty of 10% was assumed for this uncertainty.

The signal and the background processes are very similar in the compressed phase-space. This can potentially lead to a stronger dependence to additional jets (ISR) also in the signal process which could enhance e.g. the $E_{\mathrm{T}}^{\mathrm{miss}}$. To take into account such a dependence, signal systematic uncertainties are considered. For this, the factorisation, renormalisation and merging scale as well as the parton-shower tuning are varied in the event generation for the benchmark signal. Those uncertainties are then evaluated for the benchmark signal sample and amount to less than 10% in each bin.

In order to get a more reliable estimate of the uncertainties against the statistical fluctuation of the background samples, a smoothing procedure is applied for the uncertainties of the dominant backgrounds in the diagonal region. This smoothing procedure merges statistically insignificant bins and smooths the result with a Gaussian kernel. The advantage of this smoothing procedure will be explained in the next section.

In Table 15.5, the systematic uncertainties in the total background prediction are listed. The leading theoretical uncertainty comes from the normalisation of the dileptonic $t\bar{t}$ background which is the dominant background in this region. The leading experimental uncertainty comes again from the jet energy resolution. Overall, the statistical uncertainty is slightly larger than the systematic uncertainties.

Table 15.5: Total background expectation with the statistical and systematic uncertainty. For the systematic uncertainty, the full breakdown of the leading uncertainties in the background prediction in the discovery signal region is given. The individual uncertainties are correlated and thus do not necessarily add up in quadrature to the total uncertainty. All uncertainties which contribute less than 0.3% are not shown.

Uncertainty	Discovery region
Total background expectation	115.27
Total statistical ($\sqrt{N_{\mathrm{exp}}}$)	±10.74
Total background systematic	±10.05 [8.72%]
$t\bar{t}$ 2L normalisation	±9.00 [7.8%]
Jet energy resolution	±2.95 [2.6%]
MC stat. (nominal samples)	±2.78 [2.4%]
Jet η intercalibration	±2.78 [2.4%]
$t\bar{t}$ 1L normalisation	±2.50 [2.2%]
Pileup reweighting	±1.86 [1.6%]
$t\bar{t} + V$ theory	±1.26 [1.1%]
Single top interference	±0.84 [0.73%]
Flavour tagging c-jet mistag rate	±0.72 [0.62%]
Jet energy scale (1$^{\mathrm{st}}$ component)	±0.64 [0.55%]
W+jets MC generator	±0.56 [0.48%]
Diboson theory	±0.35 [0.30%]
W+jets renormalisation scale	±0.34 [0.30%]

15.6 Fit Setup

The comparison between the measured data and the SM expectation is evaluated using a profile likelihood fit as described in Section 4.2. For the so-called discovery fit setup, only one signal region bin is used to be model independent. All events with a BDT score larger than 0.75 are used in this case. When applying a cut on the BDT distribution, choosing this BDT score maximises the expected significance for the benchmark signal. The corresponding expected events are given in Table 15.6. The discovery fit is performed first in order to check the existence of a possible signal. In this case, the validation region as described in Section 15.4 in the region of BDT scores 0.4 to 0.6 is checked. As no problems are observed in this validation region and no signal is found using the discovery bin, the full BDT shape is used for the final exclusion fit.

For the exclusion fit, seven bins are chosen in order to improve the separation between the signal and the two $t\bar{t}$ background components. The lower BDT scores are dominated by $t\bar{t}$ background. The normalisation for semi- and dileptonic $t\bar{t}$ can mainly be determined in the two previously defined control region bins. Towards higher BDT scores, more signal is expected and thus these bins are more sensitive to a potential signal. The BDT output distribution is split into five bins at scores of 0.4, 0.5, 0.6, 0.7, 0.8 and 1. The full BDT distribution using the same binning as for the exclusion fit setup is shown in Figure 15.21 and the expected event yields are given in Table 15.7.

The fit procedure is tested first using only pseudo-data which are calculated from the Monte Carlo prediction. In Figure 15.22 on the left-hand side, the fit parameters obtained in the fit are shown. The black dots represent the Gaussian uncertainties corresponding to the experimental and theoretical uncertainties. The mean of the prior is set to zero with an uncertainty of 1 σ illustrated with the grey band. As pseudo-data are used, no shift away from zero is expected and no pull is observed. Some systematic uncertainties show an uncertainty smaller than one, e.g. the jet energy resolution

Table 15.6: Expected event yields for the discovery fit setup for all background processes and the benchmark signal $m(\tilde{t}_1, \tilde{\chi}_1^0) = (250, 62)$ GeV. The individual uncertainties are correlated and do not add up quadratically to the total uncertainty.

Discovery	BDT > 0.75
$t\bar{t}$ 2L	59 ± 3
$t\bar{t}$ 1L	31 ± 4
Single top	8.4 ± 1.3
W+jets	3.9 ± 0.5
Diboson	0.7 ± 0.1
$t\bar{t}$+V	2.5 ± 0.3
Total SM	106 ± 5
Signal	127 ± 4

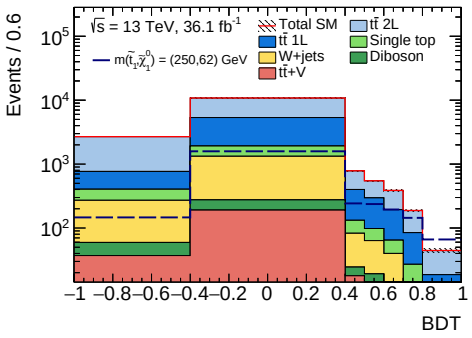

Figure 15.21: Full BDT distribution for all MC backgrounds added and the benchmark signal overlaid with the binning as used for the exclusion fit setup.

Table 15.7: Event yield table for the exclusion fit setup separating BDT scores above 0.4 into five signal region bins for all background processes and the benchmark signal $m(\tilde{t}_1, \tilde{\chi}_1^0) = (250, 62)$ GeV. The individual uncertainties are correlated and do not add up quadratically to the total uncertainty.

Exclusion	0.4<BDT<0.5	0.5<BDT<0.6	0.6<BDT<0.7	0.7<BDT<0.8	0.8<BDT<1
$t\bar{t}$ 2L	351 ± 10	231 ± 7	180 ± 7	97 ± 5	24 ± 2
$t\bar{t}$ 1L	255 ± 11	188 ± 9	126 ± 8	54 ± 5	12 ± 2
Single top	45.3 ± 3.1	33.8 ± 2.7	24.3 ± 2.2	11.9 ± 1.4	3.7 ± 0.8
W+jets	45.2 ± 2.9	33.3 ± 2.7	19.9 ± 1.5	6.4 ± 0.6	1.5 ± 0.3
Diboson	7.3 ± 0.7	5.2 ± 0.7	4.1 ± 0.6	1.5 ± 0.3	0.3 ± 0.1
$t\bar{t}$+V	16.3 ± 0.7	14.2 ± 0.6	8.8 ± 0.5	4.1 ± 0.4	1.0 ± 0.2
Total SM	719 ± 15	506 ± 12	362 ± 10	176 ± 7	42 ± 3
Signal	230 ± 5	230 ± 5	184 ± 5	141 ± 4	64 ± 3

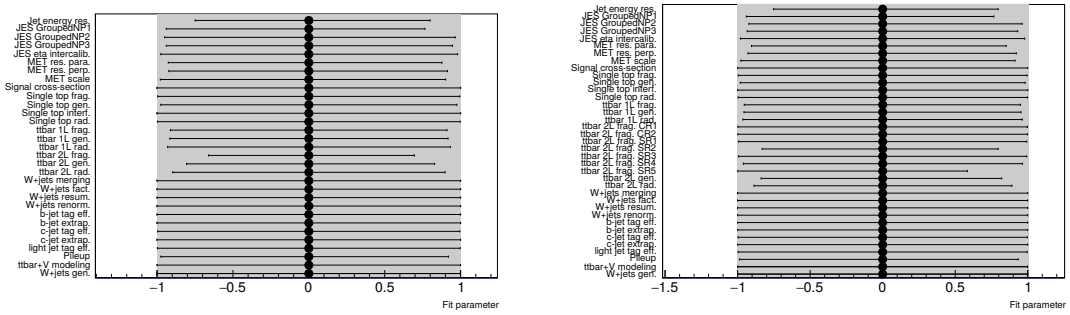

Figure 15.22: Fit parameter for the exclusion fit of the BDT for the benchmark signal using pseudo-data. The nominal setup (left) and a setup using one uncorrelated uncertainty per bin for the fragmentation uncertainty for semi-leptonic $t\bar{t}$ (right). The black dots show the best fit value and uncertainty of the nuisance parameters, encoding the various experimental and theoretical modelling uncertainties.

and the $t\bar{t}$ theory uncertainties. The largest constraint is seen for the parameter which comes from the dileptonic $t\bar{t}$ fragmentation uncertainty, labelled as "ttbar 2L frag.". In order to check the impact of such a constraint, a separate fit is performed where the uncertainty is taken as an uncorrelated uncertainty in each bin. For this, one variation for each bin is added individually. The resulting fit parameter plot is shown in Figure 15.22 on the right-hand side. The corresponding uncorrelated parameters are called "ttbar 2L frag. <bin>". The constraints are smaller but still visible for the signal region bins SR2 and SR5. In addition to the change of the constraints, the change in the expected significance is compared for a signal point with a top squark mass of 195 GeV and a neutralino mass of 1 GeV. Using the first setup, a significance of 2.39 σ is achieved. The uncorrelated uncertainties per bin result in an expected significance of 2.76 σ. Despite the larger constraint, the fit model where the systematic is correlated across the bins, yields a more conservative result and is therefore chosen.

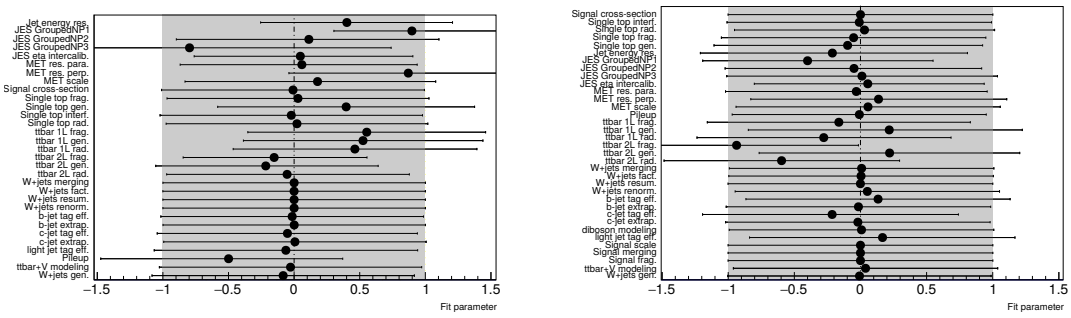

Figure 15.23: Fit parameter for the exclusion fit of the BDT for the benchmark signal for the fit without (left) and with (right) smoothed uncertainties. The black dots show the best fit value and uncertainty of the nuisance parameters, encoding the various experimental and theoretical modelling uncertainties.

When adding the measured data to the fit, the nuisance parameters are pulled as shown in Figure 15.23 on the left-hand side, pointing to imperfect agreement between the MC prediction and data. As previously described, a smoothing procedure is used for some of the uncertainties. This reduces the effect of statistical fluctuations on the uncertainties. Due to smaller fluctuations, an overall improved fit behaviour is observed. This can be seen in Figure 15.23 on the right-hand side. The fit parameters are shown when using the smoothing procedure for $t\bar{t}$ uncertainties, for pile-up and jet related uncertainties for single top and W+jets as well as for the single top theory uncertainties. All other uncertainties are taken directly from the MC samples as described above. The ordering of the uncertainties in both plots is changed, but overall smaller pulls and less strong constraints can be observed. The remaining largest pulls are due to the $t\bar{t}$ theory uncertainties, where the dileptonic $t\bar{t}$ fragmentation uncertainty is pulled most strongly.

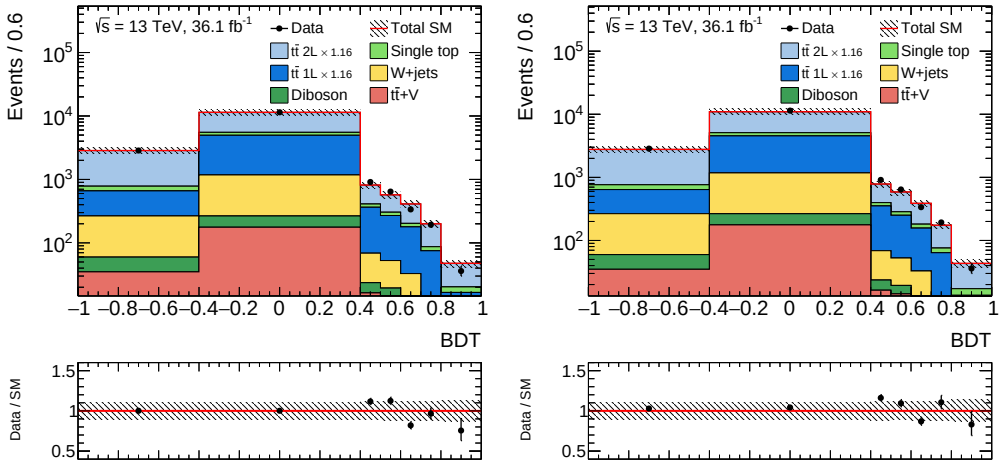

Figure 15.24: BDT distribution using the nominal samples (left) and using the sample for evaluating the theory fragmentation uncertainty for $t\bar{t}$ (right). The uncertainty band includes only statistical uncertainty in the MC statistics and the statistical uncertainty in the normalisation factors for $t\bar{t}$.

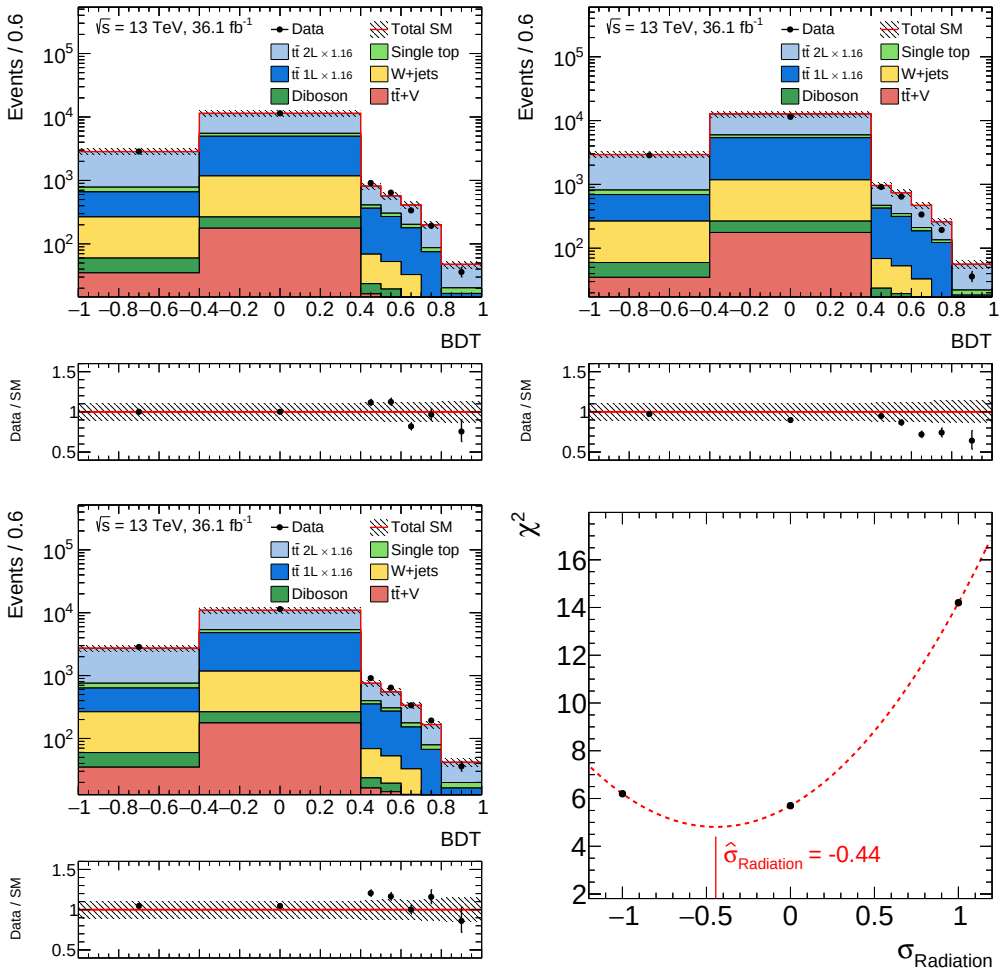

Figure 15.25: BDT distribution using the nominal samples (top left) and using the sample with radiation up (top right) and radiation down (bottom left), together with the χ^2 as a function of the radiation variation $\sigma_{\text{Radiation}}$ (bottom right). The uncertainty band includes only statistical uncertainty in the MC statistics and the statistical uncertainty in the normalisation factors for $t\bar{t}$.

The observed pull for the systematic uncertainties is caused by a disagreement of the measured data and the prediction. In some cases, a systematic variation shows better agreement and thus a shift is expected. The largest observed pull in Figure 15.23 is seen for the $t\bar{t}$ fragmentation and radiation uncertainty. In Figure 15.24, the BDT distribution is shown using the nominal MC predication and using the variation sample for the fragmentation uncertainty for $t\bar{t}$. The uncertainty band includes only statistical uncertainty in the MC statistics and the statistical uncertainty in the normalisation factors for $t\bar{t}$. The agreement between the different predictions is quantified with the χ^2 value. As not all uncertainties are included, the absolute value can not be used to judge the fit quality, and only the differences are meaningful. The χ^2 value calculates to 5.7 for the nominal sample and 5.0 when comparing the data to the prediction obtained using the alternative fragmentation sample. Overall, the agreement between the measured data and the MC predictions is similar, but in the signal region bins with the largest deviations, a better agreement can be seen when using the fragmentation variation sample for $t\bar{t}$. This can also be seen in the overall lower χ^2 value.

In Figure 15.25, the BDT distribution is shown using the nominal MC samples as well as the up and down variation samples for the radiation settings for $t\bar{t}$. The worst agreement between the data and the MC prediction is visible for the up variation of the $t\bar{t}$ radiation. Here, the last signal region bins do not agree within the statistical uncertainties. This results to a χ^2 value of 14.2. The down variation shows good agreement with a much lower χ^2 value of 6.2. The χ^2 values are also shown in the last panel in Figure 15.25, together with a quadratic fit. The position of the minimum of the quadratic form gives the best fit value, when neglecting any correlations to other parameters in the likelihood fit. The observed minimum of $\sigma_{\text{Radiation}}$ is at -0.44. This value matches the observed behaviour in the fit, when considering the approximations made. The parameters for dileptonic and semi-leptonic $t\bar{t}$ have best fit values of -0.6 and -0.25, respectively. Similar observation can be made for other uncertainties as shown for the first jet energy scale component in Appendix C.8.

15.7 Results

In the likelihood fit, the signal region bins are included and the two control region bins are used in order to determine the normalisation for semi- and dileptonic $t\bar{t}$ to 1.16 ± 0.28 and 1.16 ± 0.16 respectively. The expected and observed yields are listed in Table 15.8 for the discovery fit. The compatibility of the observed data with the background only hypothesis is calculated to be $p_0 = 0.5$, which is equivalent to a significance of zero. No significant deviation from the SM prediction is found, thus limits on the direct top squark pair production are derived. The observed (expected) upper limit on non-SM events in the signal region is $N_{\text{non-SM}} < 58$ (< 58).

Table 15.8: Observed events and expected event yields for all background processes in the discovery signal region with the normalisation factors applied. The individual uncertainties are correlated and do not add up quadratically to the total uncertainty.

Region	BDT>0.75
Observed events	115
Total background events	115 ± 10
$t\bar{t}$ 2L events	65 ± 9
$t\bar{t}$ 1L events	34 ± 2
$t\bar{t}$ + V events	2.6 ± 1.5
Single top events	8.2 ± 0.9
W + jets events	3.9 ± 1.7
Diboson events	0.7 ± 0.7
MC exp. background events	106 ± 5

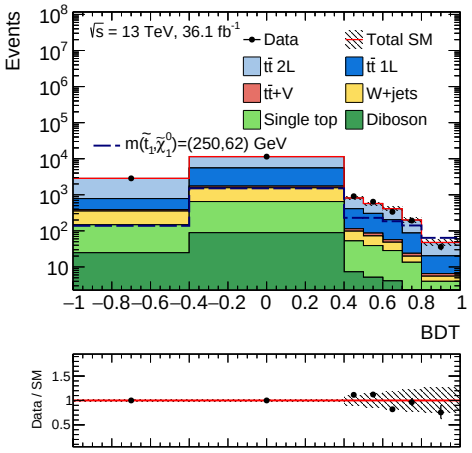

Figure 15.26: BDT distribution in the exclusion binning after applying the previously determined background normalisation. The uncertainty band includes all statistical and systematic uncertainties.

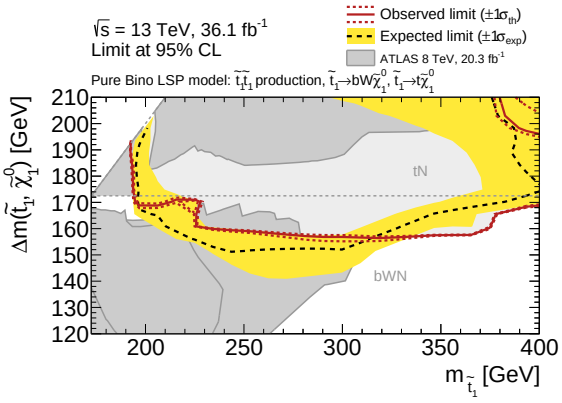

Figure 15.27: Expected and observed 95% excluded regions in the plane of $\Delta m(\tilde{t}_1, \tilde{\chi}_1^0)$ versus $m_{\tilde{t}_1}$ for the direct top squark pair production assuming either $\tilde{t}_1 \rightarrow t\tilde{\chi}_1^0$ or $\tilde{t}_1 \rightarrow bW\tilde{\chi}_1^0$ decay with a branching ratio of 100%. The observed excluded regions from previous publications [163] are shown as dark grey areas. The black line shows the expected limit and the yellow band includes all statistical and systematic uncertainties. The red line shows the observed limit, where the smaller dashed lines represent the uncertainty in the signal cross-section.

In order to achieve a good sensitivity for the exclusion across a large possible parameter space, the full BDT distribution is used with five signal region bins. The final BDT distribution including the previously determined normalisation factors for $t\bar{t}$ as well as all systematic uncertainties is shown in Figure 15.26. As the $t\bar{t}$ normalisation comes mainly from the first two bins, those bins show a perfect agreement between data and the MC prediction. The latter bins, corresponding to the signal enhanced bins show some fluctuations, but all differences are within the uncertainties.

The main focus of this analysis is the low top squark mass region, with a mass difference of $m_{\tilde{t}_1} - m_{\tilde{\chi}_1^0} \simeq m_t$. In order to better illustrate the exclusion reach in this compressed region, the exclusion contour is shown in the $\Delta m(\tilde{t}_1, \tilde{\chi}_1^0)$ versus $m_{\tilde{t}_1}$ plane in Figure 15.27. The limits from previous analyses are shown as grey areas. The expected exclusion goes down towards a top squark mass of 198 GeV. This can also be seen in Figure 15.28, where the upper limit on the cross-section is shown for signal samples next to the diagonal boundary with $\Delta m(\tilde{t}_1, \tilde{\chi}_1^0) - m_t = 500\,\text{MeV}$. For those samples, top squark masses from 198 GeV (198 GeV) can be excluded up to top squark masses of 463 GeV (408 GeV) in the observed (expected) limit. With these results, the remaining signal parameter space in the two-body region at low top squark masses is excluded.

The sensitivity towards the three-body decay side (labelled bWN in Figure 15.27) is also tested. As visible some signal points on the bWN side can be excluded by the signal region designed on the two-body decay side. The signal samples with a top squark mass of 220 GeV near the boundary between the two and three-body decay side are within the expected sensitivity. As already seen in the BDT shape (see Figure 15.26), the data do not agree with the MC prediction among all signal region bins. More data events are expected in the first two signal region bins, where less data events are expected in the third and last signal region bin. A good agreement can be observed for the fourth signal region bin. Considering the observed limit, the signal points around a top squark mass of 220 GeV on the three-body decay side cannot be excluded. Thus, these points and the small corner for very low top squark masses on the three-body decay side should be studied further in the future,

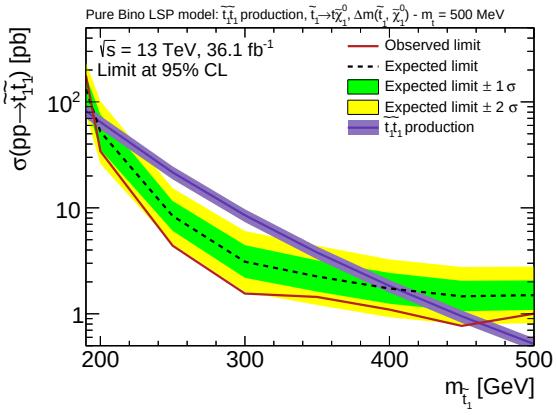

Figure 15.28: Observed and expected 95% CL upper limit on the cross-section for the top squark pair production as a function of the top squark mass. The signals are chosen such that the mass difference between the top squark, the neutralino and the top quark is equal to 500 MeV for all signal points. The thickness of the theory curve represents the uncertainty in the signal cross-section.

which can be done performing precision measurements of top properties. This feature is not visible in the cross-section limit in Figure 15.28, as this limit is evaluated on the two-body decay side.

15.7.1 Comparison to Similar Search Regions

In addition to the approach discussed here, two further analyses are included in the same publication [5] that target the compressed signal scenario between the two-body and the three-body decay of the top squark. The signal region presented is called "BDT_med" in this publication.

Based on the techniques discussed here, a second BDT is trained to achieve higher sensitivity at high top squark masses and is called "BDT_high". In addition to the variables discussed here, the correlation between the $E_{\mathrm{T}}^{\mathrm{miss}}$ and the momentum of the initial state radiation is exploited. This is linked to the ratio of neutralino and top squark masses and gets more relevant towards large top squark masses [172]. The training and validation of the BDT_high is based on the same principles as discussed here. For the final fit, three control region bins are used to estimate the combined $t\bar{t}$ normalisation where the selection is dominated by dileptonic $t\bar{t}$. Three signal region bins at higher BDT scores are used in the exclusion fit.

A third analysis targets very low top squark masses, $m_{\tilde{t}_1} \simeq 190\,\mathrm{GeV}$ and is called "BDT_low". Also here a BDT is trained, but not following the same procedure as described above and used for BDT_med and BDT_high. This region targets very low top squark masses between 190 and 200 GeV. The BDT is used to define one control region bin to determine a combined $t\bar{t}$ normalisation factor and one bin is used as signal region. As an input variable for the training, the mass of a reconstructed top quark is calculated. For the full reconstruction, the top squark and neutralino mass are fixed and a top squark mass of 200 GeV with a neutralino mass of 27 GeV is assumed for this signal region.

A dedicated region for the three-body decay is also optimised (bWN). It is designed similarly to the tN_med signal region, optimising a sensitive selection and using a shape fit in order to improve

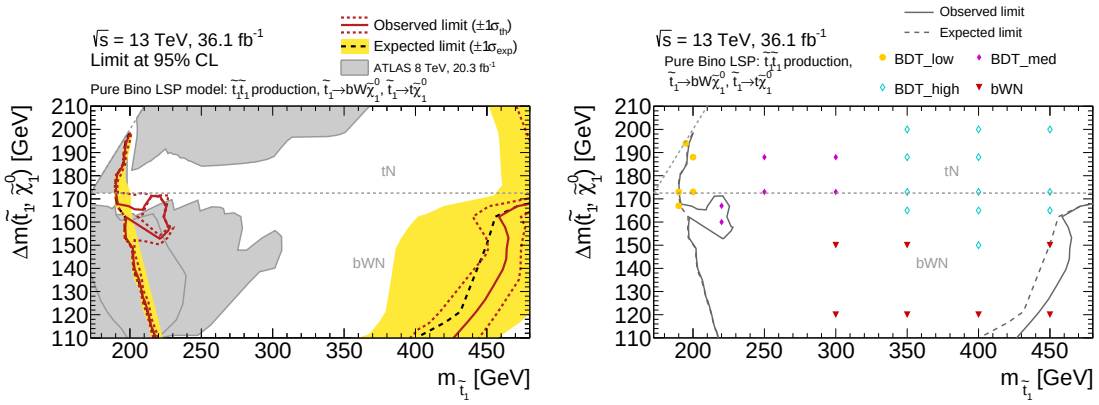

Figure 15.29: Expected and observed 95% excluded regions in the plane of $\Delta m(\tilde{t}_1, \tilde{\chi}_1^0)$ versus $m_{\tilde{t}_1}$ for the direct top squark pair production assuming either $\tilde{t}_1 \to t\tilde{\chi}_1^0$ or $\tilde{t}_1 \to bW\tilde{\chi}_1^0$ decay with a branching ratio of 100%. The excluded region is shown combining the three BDT and the bWN analyses (left). The observed excluded regions from previous publications [163] are shown as grey areas. The signal region with the best expected sensitivity and thus used for the combination is shown (right).

the exclusion sensitivity. The am_{T2} distribution is used for the shape fit, as the three-body decay produces lower values in am_{T2} than the background.

Figure 15.29 shows the combined exclusion contour. For each signal point, the signal region with the best expected sensitivity is used for the combination. The selection of the signal region is shown on the right-hand side. For top squark masses between 200 and 300 GeV, in the region to which previously no sensitivity was achieved, the analysis discussed here shows the best sensitivity. Expected significances in the range of $3\,\sigma$ to $5\,\sigma$ are achieved. At higher masses of the top squark, $m_{\tilde{t}_1} \gtrsim 350$ GeV, the BDT_high analysis is the most sensitive region. It is able to extend the expected exclusion limit by 100 GeV compared to BDT_med alone, up to a top squark mass of 500 GeV. In its target region, for $m_{\tilde{t}_1} \leq 200$ GeV, the BDT_low analysis achieves the best sensitivity. It extends the exclusion limit by 10 GeV down to $m_{\tilde{t}_1} \lesssim 190$ GeV, inside the parameter space excluded by a previous ATLAS analysis [171]. The analysis targeting the three-body decay side shows the best sensitivity for most of those points and extends the exclusion potential on the three-body side as it can exclude the full three-body decay area with top squark masses between 200 and 400 GeV.

15.7.2 Low Mass BDT

As previously described, the BDT_low region as published in the same paper [5] uses a different approach for the training, optimisation and evaluation. As a proof of concept, the same strategy, as developed for the BDT_med and applied to BDT_high, is applied also to the very low top squark masses near the diagonal.

For this check, a BDT is trained using the same settings and input variables as the previously presented analysis. Only the input samples are changed for the training in order to use the lowest available top squark masses. A combination of top squark masses of 190, 195 and 200 GeV is used,

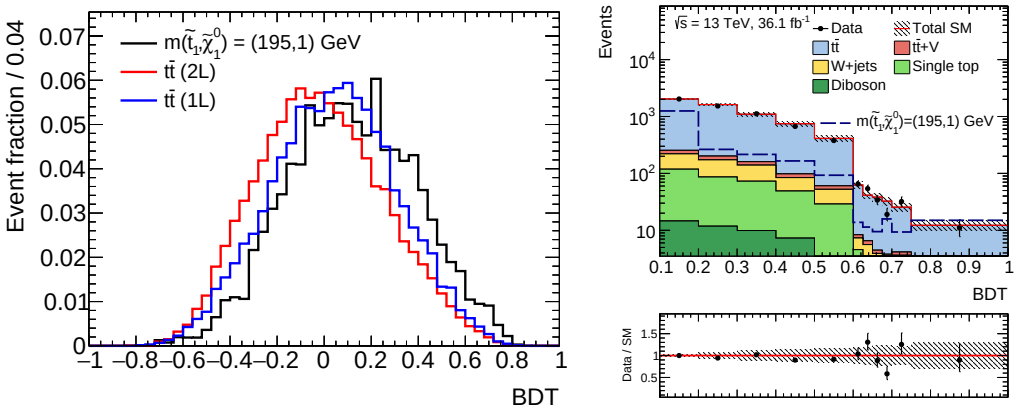

Figure 15.30: Shape comparison of the new trained BDT for semi- and dileptonic $t\bar{t}$ as well as for one signal sample (left). BDT distribution after applying all selection requirements and the determined background normalisation. The shown binning is the one used for the exclusion fit. The uncertainty band includes statistical and systematic uncertainties (right).

where for the latter two different neutralino masses are assumed. In total, four samples are used in order to have adequate statistical power in the training. In Figure 15.30, the shape of the resulting BDT distribution is shown for the semi- and dileptonic $t\bar{t}$ as well as for the signal sample with a top squark mass of 195 GeV. The differences between the semi-leptonic and dileptonic $t\bar{t}$ distributions are much smaller compared to the differences seen for the previous BDT. Therefore, in the fit only the combined normalisation for $t\bar{t}$ is determined. For this, one control region bin is defined in the region of BDT scores of 0.1 to 0.2. The intermediate BDT region from 0.2 to 0.6 is used as a validation region, as the signal behaves very similar to the background processes. The BDT region above 0.6 is then split into six bins as shown in Figure 15.30 and the shape information is used in order to check the sensitivity of this BDT.

Overall, a similar fit procedure is used as for the previous BDT. The only differences are the change to a combined $t\bar{t}$ normalisation factor. The theoretical systematic uncertainties for W+jets and single top are set to 50% instead of the exact evaluation. The high BDT scores has nearly no background except $t\bar{t}$. As no generated events are left in the high signal region bins, only a rough estimate of these uncertainties can be performed. These numbers agree with the numbers used for the BDT_low [5]. The theoretical signal uncertainties are also set to a flat uncertainty of 10% which is larger than the uncertainty calculated from a signal sample with a slightly higher top squark mass and cover a possible larger effect towards lower top squark masses. The same validation as for the BDT_med is done. A selection of the plots is shown in Appendix C.9. This setup is used to determine the expected sensitivity for the signal points where the BDT_low performs better than the BDT_med. The number for all three BDTs are presented in Table 15.9. Overall, the newly trained BDT shows a large improvement compared to the BDT_med for all signal points. As these samples are used for the training of the BDT, this behaviour is expected. Compared to BDT_low, the significances are very similar for the 195 GeV and 200 GeV mass points. As two signal points with a top squark mass of 200 GeV are used, the newly trained BDT is more sensitive for these points. The kinematic distributions change when going towards higher top squark masses, therefore the BDT_low performs still better for the mass point at a top squark mass of 190 GeV as only one of the 200 GeV mass points was included in the training for this BDT.

Table 15.9: Expected significances for the low top squark masses comparing the BDT_med, BDT_low [5] and the new trained BDT.

Sample: $m_{\tilde{t}_1}, m_{\tilde{\chi}_1^0}$	BDT_med	BDT_low [5]	new BDT
190 GeV, 17 GeV	0.7 σ	2.34 σ	1.56 σ
195 GeV, 1 GeV	1.22 σ	1.69 σ	1.68 σ
200 GeV, 12 GeV	2.65 σ	2.71 σ	2.77 σ
200 GeV, 27 GeV	2.07 σ	2.45 σ	2.41 σ

Further improvements for a BDT sensitive to the very low top squark masses can be made by improving the training sample selection. This can be achieved by enhancing the MC statistic of the lowest signal point. If a combination of signal samples is needed, these samples should be very similar in the kinematic behaviour, so that the training cannot focus on the signal kinematics with the highest statistics. For best results, the optimisation of the BDT settings and especially the input variables should be redone also for this low top squark mass region. The kinematics change when going towards lower top squark masses and thus also the preselection cuts have to be reconsidered. The signal tends towards lower m_{T} values and thus the $m_{\mathrm{T}} > 120$ GeV cut reduces the amount of signal events. When loosening the cut to $m_{\mathrm{T}} > 90$ GeV, 60% more signal events are expected for top squark masses of 190 GeV and 195 GeV. The background increases by about 60%, when reducing the m_{T} threshold. While such a reduction does not increase the sensitivity directly, the additional signal events could be recovered in the BDT training. For increasing top squark masses, the effect reduces, e.g. only a 40% increase is expected for top squark masses of 250 GeV. A reduced m_{T} threshold can increase the effects of the jet energy resolution uncertainty, which directly impacts the resolution of the m_{T}. The exact value of the m_{T} requirement is thus a trade-off between the increased signal efficiency and the uncertainty in the background estimate.

Overall, this check shows, that the same procedure as developed for the BDT_med can also be applied for lower top squark masses. As this area is anyhow excluded from the spin-correlation measurements from 8 TeV [171], no further effort was spent into improving this newly trained BDT.

16 Comparison of the Full Result

Summarising the result of the presented analyses, a combination using the tN_med and the BDT_med regions is shown on the left-hand side in Figure 16.1 by using the signal region with the best expected sensitivity. On the right-hand side, the results using all signal regions targeting the two-, three- or four-body decay are shown as presented in the combined publication [5]. Already the two presented signal regions cover a wide range of the excluded area. The dedicated region for the high top squark masses and especially for the three- and four-body decay extend the exclusion range into the corresponding regions.

Figure 16.2 shows similar results for the full hadronic ATLAS search [172] and the CMS search with one isolated lepton in the final state [173]. Overall, similar search strategies are used in all analyses. In the ATLAS all-hadronic search, for each signal region a preselection is defined. Each signal region is then split into several bins depending on the count of reconstructed top candidates or binned into ratio of $E_{\mathrm{T}}^{\mathrm{miss}}$ to the p_{T} of the initial state radiation. For the CMS one-lepton search, two preselections are defined. They are not orthogonal to each other, but target either the compressed or the non-compressed region. The fit is then split into bins of number of jets, $E_{\mathrm{T}}^{\mathrm{miss}}$, invariant mass of the lepton and closest b-tagged jet and a variable t_{mod} which tests the compatibility with the $t\bar{t} \rightarrow 2\ell$ hypothesis when one lepton is not reconstructed. In total, the CMS analysis is using 27 bins for the non-compressed region and 4 bins for the compressed parameter space.

The previously discussed signal regions are important for the intermediate top squark masses towards higher neutralino masses (tN_med) and for the low top squark masses in the compressed region (BDT_med). For intermediate top squark masses around 800 GeV, neutralino masses up to 420 GeV are expected to be excluded with the presented analysis. The full hadronic ATLAS analysis is very similar designed, and reaches neutralino masses up to 350 GeV. Due to the large multi-bin setup, the exclusion reach for CMS is better, as neutralino masses up to 480 GeV can be excluded calculating the expected limit.

For the low top squark masses, the full compressed area can be excluded for top squark masses between 200 GeV and 500 GeV. The reach of the full hadronic ATLAS search goes down towards top squark masses of 250 GeV which leaves a small not excluded area from this analysis to the old ATLAS limits. CMS does not publish any results for signal models for which $|m_{\tilde{t}_1} - m_{\tilde{\chi}_1^0} - m_t| \leq 25\,\mathrm{GeV}$ and $m_{\tilde{t}_1} \leq 275\,\mathrm{GeV}$. They observe significant differences between the fast simulation and the full simulation for these scenarios and thus no interpretation is provided.

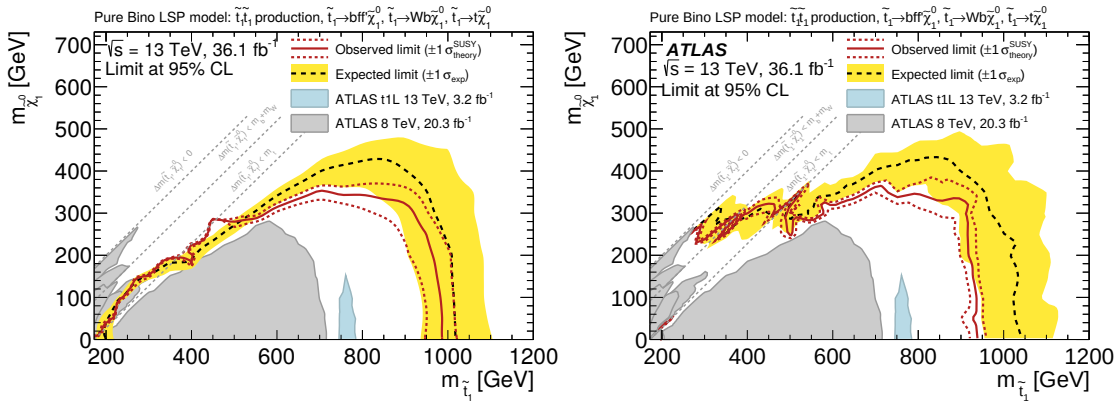

Figure 16.1: Expected and observed 95% excluded regions in the plane of $m_{\tilde{t}_1}$ versus $m_{\tilde{\chi}_1^0}$ for the direct top squark pair production assuming either $\tilde{t}_1 \to t\tilde{\chi}_1^0$, $\tilde{t}_1 \to bW\tilde{\chi}_1^0$ or $\tilde{t}_1 \to bff'\tilde{\chi}_1^0$ decay with a branching ratio of 100%. The observed excluded regions from previous publications [163] are shown as grey or blue areas. The black line shows the expected limit and the yellow band includes all statistical and systematic uncertainties. The red line shows the observed limit, where the smaller dashed lines represent the uncertainty in the signal cross-section. The excluded region is shown for the presented signal regions (tN_med and BDT_med, left) and for all signal regions from the publication [5] (right).

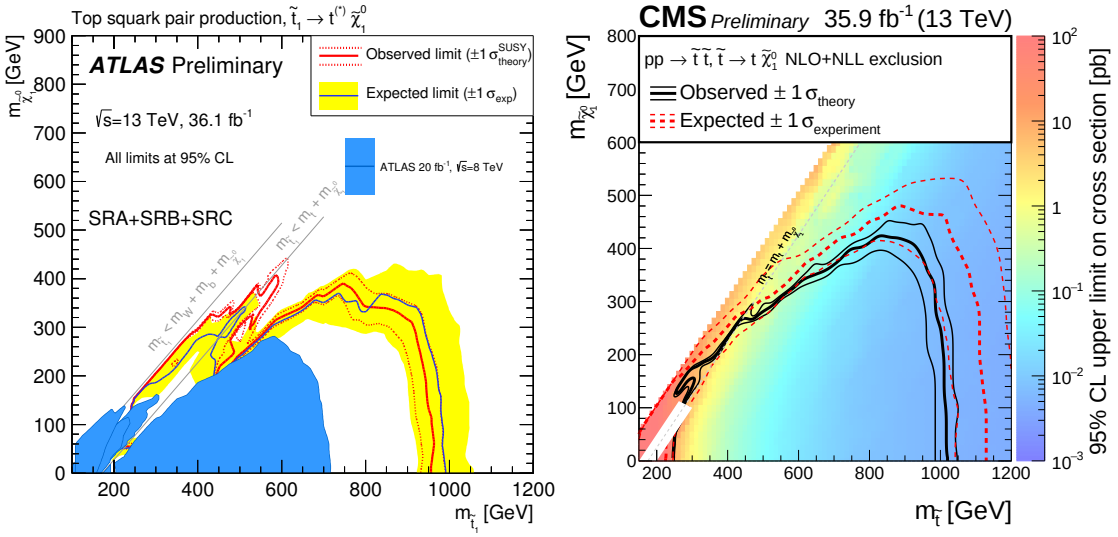

Figure 16.2: Expected and observed 95% excluded regions in the plane of $m_{\tilde{\chi}_1^0}$ versus $m_{\tilde{t}_1}$ for the direct top squark pair production assuming either $\tilde{t}_1 \to t\tilde{\chi}_1^0$ or $\tilde{t}_1 \to bW\tilde{\chi}_1^0$ decay with a branching ratio of 100%. The excluded area is shown for the full hadronic search from ATLAS [172] (left). Expected (observed) exclusion limits are shown as blue (red) line. Observed limits from previous searches [171] are overlaid for comparison in blue. The excluded area is shown for the one lepton search from CMS [173] (right). Expected (observed) exclusion limits are shown as red (black) lines. For both plots, the uncertainty bands corresponding to the $\pm 1\,\sigma$ variation on the expected limit and the sensitivity of the observed limit to $\pm 1\,\sigma$ variations of the signal theoretical uncertainties are shown.

Conclusion

Never memorise something that you can look up.

Albert Einstein

In this dissertation, the measurement of charged-particle distributions as well as a search for Supersymmetry are presented. Both analyses use data recorded with the ATLAS experiment at the LHC at a centre-of-mass energy of 13 TeV.

The measurement of charged-particle distributions is sensitive to non-perturbative QCD effects and is published in Ref. [4]. It extends the previous measurement at $\sqrt{s} = 13$ TeV [2] to charged-particles with transverse momenta as small as 100 MeV, providing important information for the description of the strong interaction in the low-momentum-transfer region of QCD. For the measurement, the observed data are corrected and unfolded in order to take any detector effects into account. The unfolding procedure is tested and validated. The charged-particle distributions are compared between the observed data and the prediction from different, QCD inspired models, implemented in Monte Carlo generators. The agreement depends strongly on the generator. Overall, the EPOS generator shows the best prediction compared to data. The mean particle density at $|\eta| < 0.2$ is calculated to $6.500 \pm 0.002(\text{stat.}) \pm 0.099(\text{syst.})$, and compared with different phase-spaces and centre-of-mass energies. The presented analysis has smaller uncertainties compared to measurements performed at other experiments.

The results of this measurement can be used to constrain free parameters of the underlying models of the different Monte Carlo generators. This will then improve the overall predictions and is thus an important input for further precision measurements and searches.

The second part of this dissertation details a search for Supersymmetry. Two dedicated analyses are presented, targeting different mass regions in models of light top squarks. Both are part of a publication together with other signal regions [5]. Both analyses rely on shape fit techniques in order to maximise the sensitivity to the signal models. The correct background estimate is crucial for both signal regions. The dominant backgrounds are normalised and the modelling is validated in dedicated regions. For both analyses, the compatibility of the observed data with the Standard Model hypothesis is checked. No excess is observed, and exclusion limits on models of Supersymmetry are set. The sensitivity of previous searches is extended by both analyses, excluding previously unconstrained regions in the model parameter space.

A signal region targeting intermediate to high top squark masses and a broad range of neutralino masses is defined (tN_med). As higher top squark masses and higher neutralino masses result into higher $E_{\text{T}}^{\text{miss}}$ values compared to the Standard Model background, the $E_{\text{T}}^{\text{miss}}$ distribution is used for the shape fit. The main background originates from dileptonic $t\bar{t}$ decays where one lepton is not reconstructed in the detector. It is reduced by variables sensitive to the top quark decays. The overall normalisation is derived in a region where dileptonic $t\bar{t}$ decays, with a lost lepton, dominate. Control regions for other backgrounds are defined similarly by inverting some of the signal region requirements. The control regions and the binned $E_{\text{T}}^{\text{miss}}$ distribution are used in a profile likelihood fit in order to determine the background normalisation and a possible signal contribution. With the tN_med signal region, top squark masses are excluded up to 980 GeV for low neutralino masses with an expected exclusion of 1020 GeV. Neutralino masses are excluded up to 350 GeV for a broad range of top squark masses with an expected exclusion of 420 GeV.

The signal region is designed to be sensitive to the simplified model in which only a top squark and the neutralino are considered. The targeted signature of $t\bar{t} + E_{\text{T}}^{\text{miss}}$ is general and a signature of other models of Supersymmetry as well. The analysis is sensitive to models with light higgsinos or a Dark Matter-inspired bino/higgsino mix. A statistical combination with signal regions selecting low-momentum leptons, top squark masses up to 800 GeV or 900 GeV are excluded, depending on the model and the decay branching ratio of the top squark.

The second analysis targets compressed top squark pair decays in models with a top squark mass around 200 GeV. These compressed mass scenarios result in models on the boundary between the decay into a top quark and a neutralino and the decay into an off-shell top quark and a neutralino. As the signal process is very similar to the Standard Model $t\bar{t}$ production, no single kinematic distribution can be found to separate these processes. A Boosted Decision Tree is trained based on the value and correlation of ten input variables. The distribution of the resulting classifier separates signal and background. A profile likelihood fit to the BDT distribution is then used to simultaneously constrain the background normalisation in the background enriched region, and to estimate a potential signal contribution. With this multivariate approach, top squark masses between 198 GeV and 460 GeV can be excluded for small mass differences ($m_{\tilde{t}_1} - (m_t + m_{\tilde{\chi}_1^0}) = 500\,\text{MeV}$). Together with previous limits and the tN_med results, top squarks with masses between the top quark mass and 980 GeV are excluded for massless neutralinos.

The measurement results and experimental search strategies developed in this dissertation provide a basis for the exploitation of the future LHC data. With the increased pile-up, the modelling of non-perturbative QCD effects influences the possible precision of measurements and searches. This is important for the remainder of Run 2 as well as for future LHC runs. With the increase in luminosity, it will be possible to further constrain difficult signals, which strongly resemble the Standard Model backgrounds. Multivariate methods, such as Boosted Decision Trees and shape fit techniques are crucial to gain sensitivity to such processes.

Appendix

A Monitoring for the IBL Detector

As qualification task, development for the new IBL readout software was done in two independent projects. As the first project, an additional scan was implemented and tested in the existing code structure. As the second project, a monitoring code for IBL was developed.

A.1 Cross-talk Scan

Several scans are already implemented for the IBL to test the principal functionality. A scan is performed by injecting and reading out single Pixel (or Pixel patterns) in the detector. Common for all implemented scans is that the Pixel which is injected is also read out. The aim of so-called cross-talk scans is to study the effect from one Pixel to the neighbouring ones. This can be achieved by injecting one Pixel and reading out the neighbouring ones. The code structure is adapted for this. For reading out other Pixels, the mask patterns used for the injected Pixels is shifted. This procedures is limited to only two mask iterations, but could be adapted for more steps.

The functionality of the scan is tested. The result are shown in Figure A.1 and A.2 for two different chips with high voltage off (left) and on (right). For each chip the number of measured hits is shown for each individual Pixel.

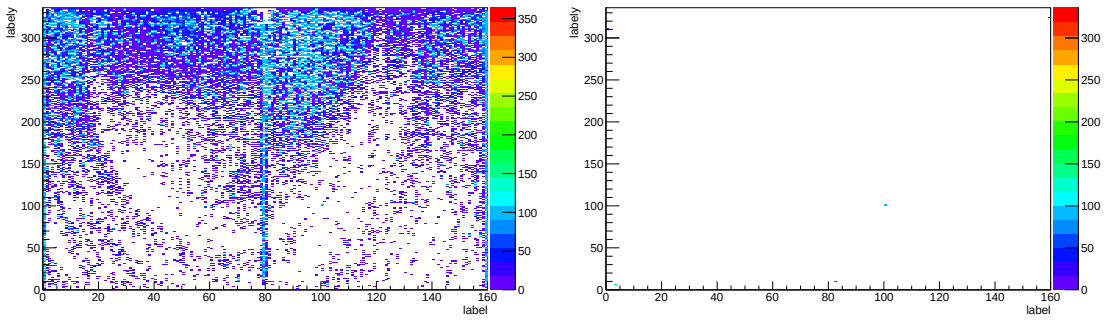

Figure A.1: Measured hits for the cross-talk scan for one chip with high voltage off (left) and on (right).

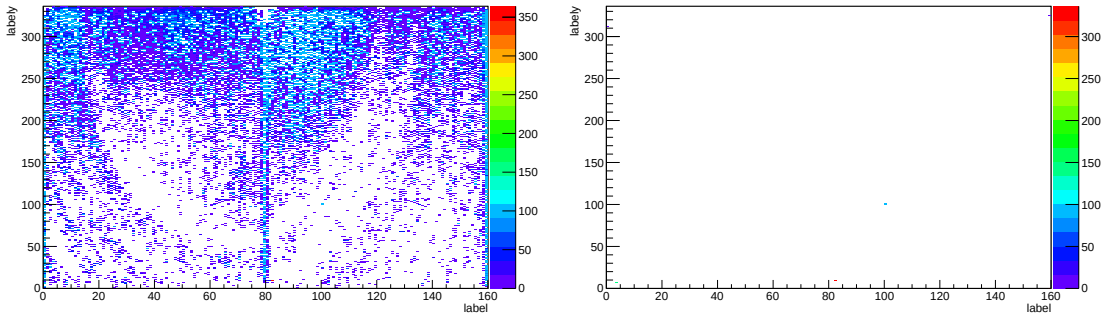

Figure A.2: Measured hits for the cross-talk scan for one chip with high voltage off (left) and on (right).

When the high voltage is off, the sensor is not fully depleted and thus one can see more cross-talk between the individual Pixels. When the high voltage is on, the Pixels are fully depleted and as result the cross-talk between the Pixels is less. This is easily visible as only few Pixels show any hits at all (right-hand plots). The tests with high voltage on and off show the expected behaviour, validating the scan implementation.

A.2 Quick Status – A Monitoring Tool

For the Pixel readout, a monitoring and automatic error correction program called *Quick Status* was already developed. The idea of this program is to run and monitor the status of the detector. In case of problems, error conditions are defined and commands developed to fix those errors.

A similar tool is also needed for the new readout system for the IBL detector. The principal design layout of quick status can be seen in the illustration in Figure A.3. There are different possible modes for quick status. In the OFF mode, the tool is disabled. In the monitoring mode, the detector readout is monitored and the status is logged. In case that problems are observed, the tool can take action automatically and fix the error conditions.

The user can change the configuration of the tool, even when it is running. This means that both the quick status mode and other parameters and thresholds can be changed during a data taking run. In addition, a user can perform actions directly to fix problems before the program detects them automatically.

For the monitoring code, different commands are either adapted from the Pixel code or newly developed. The occupancy of a specific frontend chip can be read out. It is possible to read out the status from a ROD, to get the busy status and percentage. Furthermore the decoding errors are monitored. All these information are monitored and they are also published in the information service (IS), making the information accessible for a longer time period.

Different so-called actions can be performed. These are scripts which fix specific problems. The quick status program can call specific scripts in case of problems automatically. This means, it can take existing scripts to e.g. resample the BOC phase. In case of unsolved problems, the automatic

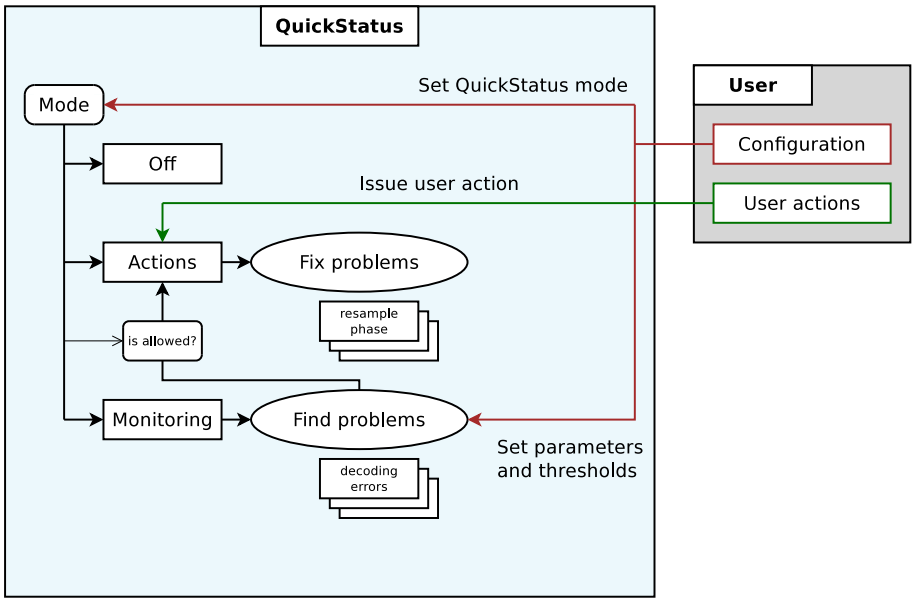

Figure A.3: Design for IBL quick status.

actions have to be developed first. During this qualification task, this was done for two different error conditions. First, in case of a full ROD being busy or causing other problems, the ROD is removed from data taking. Then, it is reset and moved back into data taking. The reset of the ROD is done when it is out of data taking in order to not disturb the physics data. This process is called *ROD recovery*. A similar problem was solved with the *stop-less removal*. This solves busy problems without affecting other modules when reconfiguring a single frontend chip during the run. This procedure is more complicated than resetting the full ROD, as the frontend chip has to be set in the appropriate state after the reconfiguration to be harmonised with all other frontends in the ROD.

As part of the quick status program, monitoring history is stored. In case of problems with e.g. the busy status of one ROD, the user can look up the status of the ROD and other information to the time directly before the problem. This can help to find the cause of the problem and is an important information for future developments. For this, a ring-buffer system is implemented, which is filled regularly and can be read out via a quick status user action.

The IBL quick status monitoring tool was implemented in the qualification task and tested successfully in a test setup. Only partial tests were executed using the real detector, making final, full test mandatory.

In the future, additional conditions to monitored can be defined and added to the existing code. In case of specific problems, actions are defined and it should be defined when which action should be performed automatically.

B Charged-particle Measurements

B.1 Closure Tests

In this Appendix, the auxiliary material for the correction procedure is shown. The closure tests are done for several combinations of Monte-Carlo generators which are used for the input distribution or the construction of the resolution matrix.

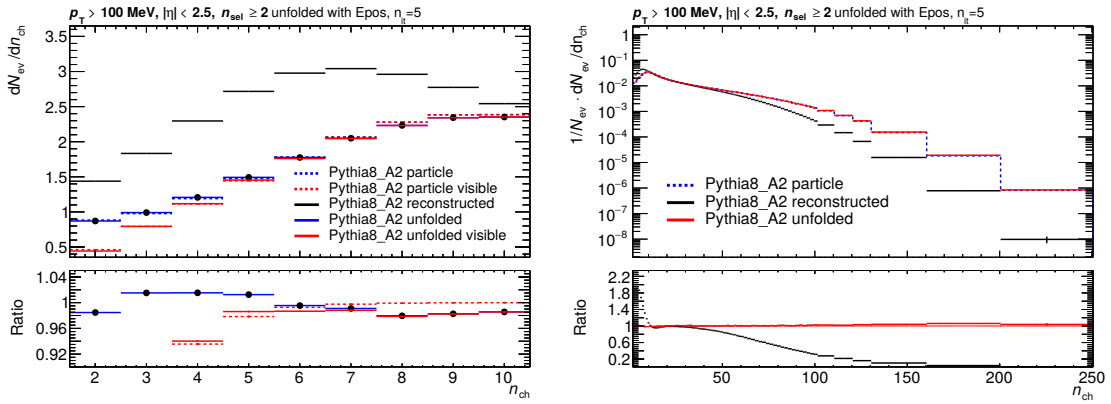

Figure B.1: Closure test using PYTHIA 8 A2 as the input distribution and EPOS generator to construct the unfolding matrix. The label "visible" is used for the subset of events with $n_{\text{sel}} \geq 2$ that do not migrate outside of the detector phase-space.

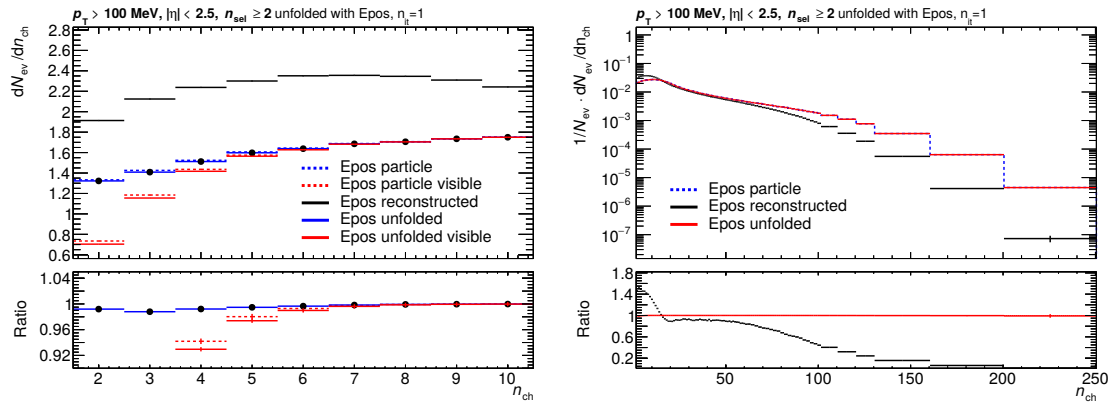

Figure B.2: Closure test using EPOS for both the input distribution and the generator to construct the unfolding matrix. The label "visible" is used for the subset of events with $n_{\mathrm{sel}} \geq 2$ that do not migrate outside of the detector phase-space.

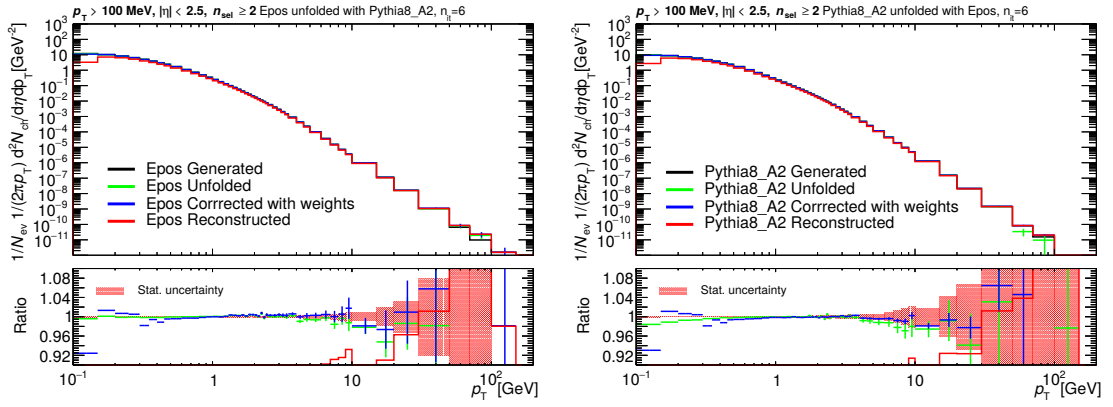

Figure B.3: Closure test using EPOS as the input distribution and PYTHIA 8 A2 generator to construct the unfolding matrix (left) and PYTHIA 8 A2 as the input and EPOS as generator to construct the unfolding matrix (right).

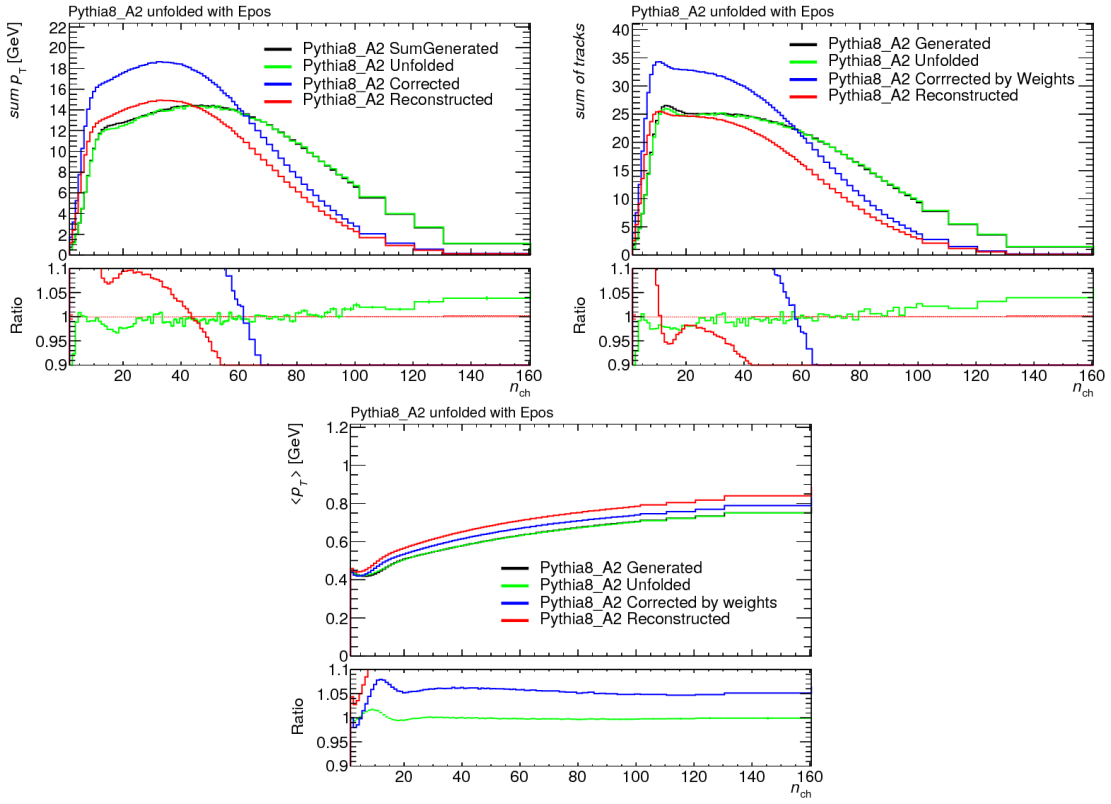

Figure B.4: Closure test for $\sum_{\text{tracks}} p_{\text{T}}$ versus n_{ch} and $\sum_{\text{tracks}} 1$ versus n_{ch} as well as for $\langle p_{\text{T}} \rangle (n_{\text{ch}})$ using PYTHIA 8 A2 as input distribution and EPOS constructing the unfolding matrix.

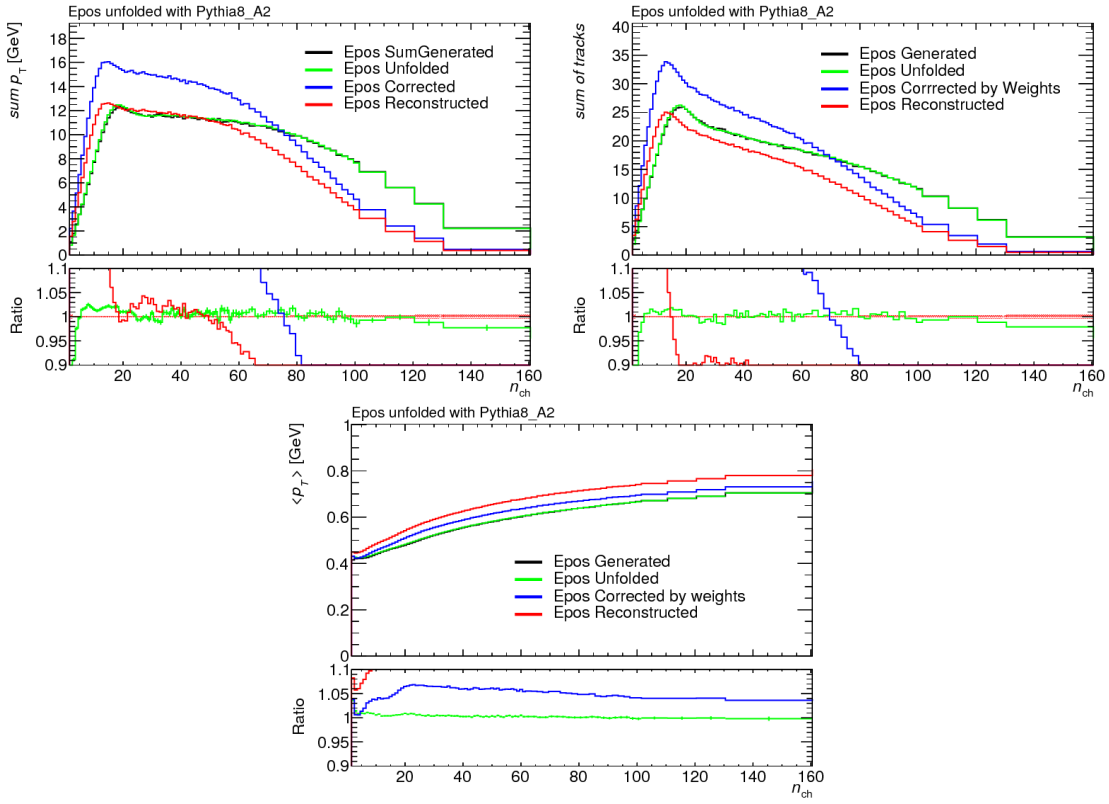

Figure B.5: Closure test for $\sum_{\text{tracks}} p_{\text{T}}$ versus n_{ch} and $\sum_{\text{tracks}} 1$ versus n_{ch} as well as for $\langle p_{\text{T}} \rangle (n_{\text{ch}})$ using EPOS as input distribution and PYTHIA 8 A2 for constructing the unfolding matrix.

B.2 Comparison Including Strange Baryons

In this Appendix, all measurements are presented including the extrapolation factor for the strange baryons. As for the mean particle density (see Section 11.1), the extrapolation is calculated using the EPOS generator where the MC distribution are compared when including and excluding strange baryons. The corresponding extrapolation factors are derived for each bin individually.

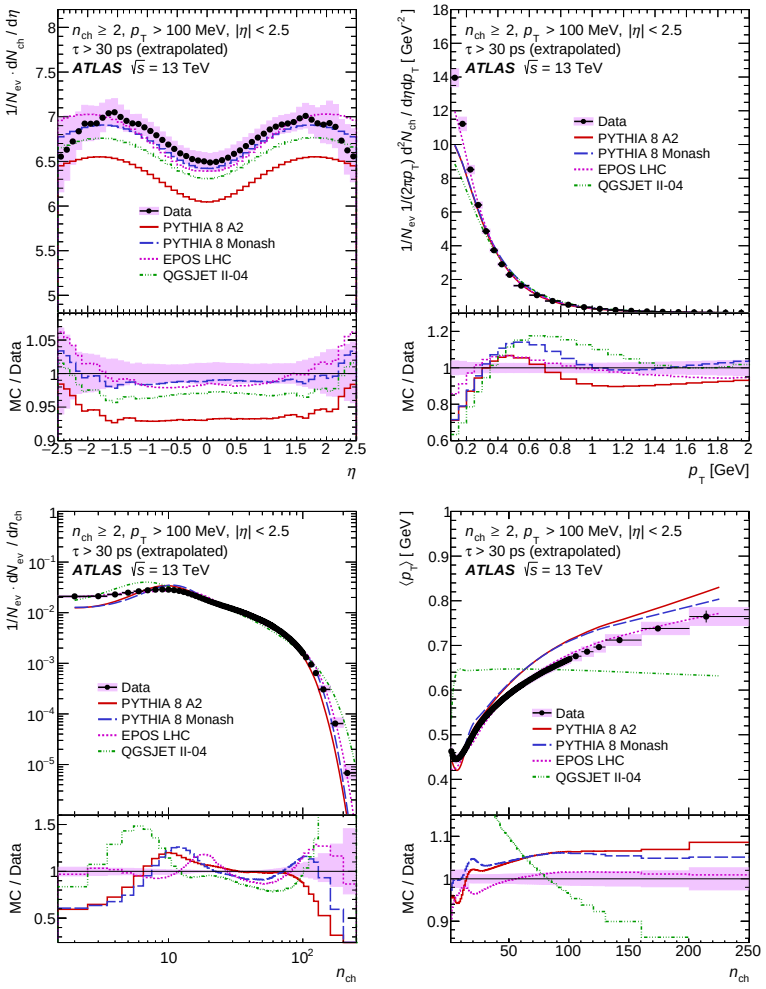

Figure B.6: Primary charged-particle multiplicities as a function of (left top) pseudorapidity η and (right top) transverse momentum p_T, (left bottom) the primary charged-particle multiplicity n_{ch} and (right bottom) the mean transverse momentum $\langle p_T \rangle$. The black dots represent the data and the coloured curves the different MC predictions. The vertical bars represent the statistical uncertainty, while the shaded areas show statistical and systematic uncertainties added in quadrature. The lower panel in each figure shows the ratio of the MC prediction to data. The strange baryon extrapolation factor is applied.

B.3 Comparison with Other Generators

In this Appendix, the measurements are shown without the extrapolation factor for the strange baryons. The comparison is done to other generators than presented in the main body.

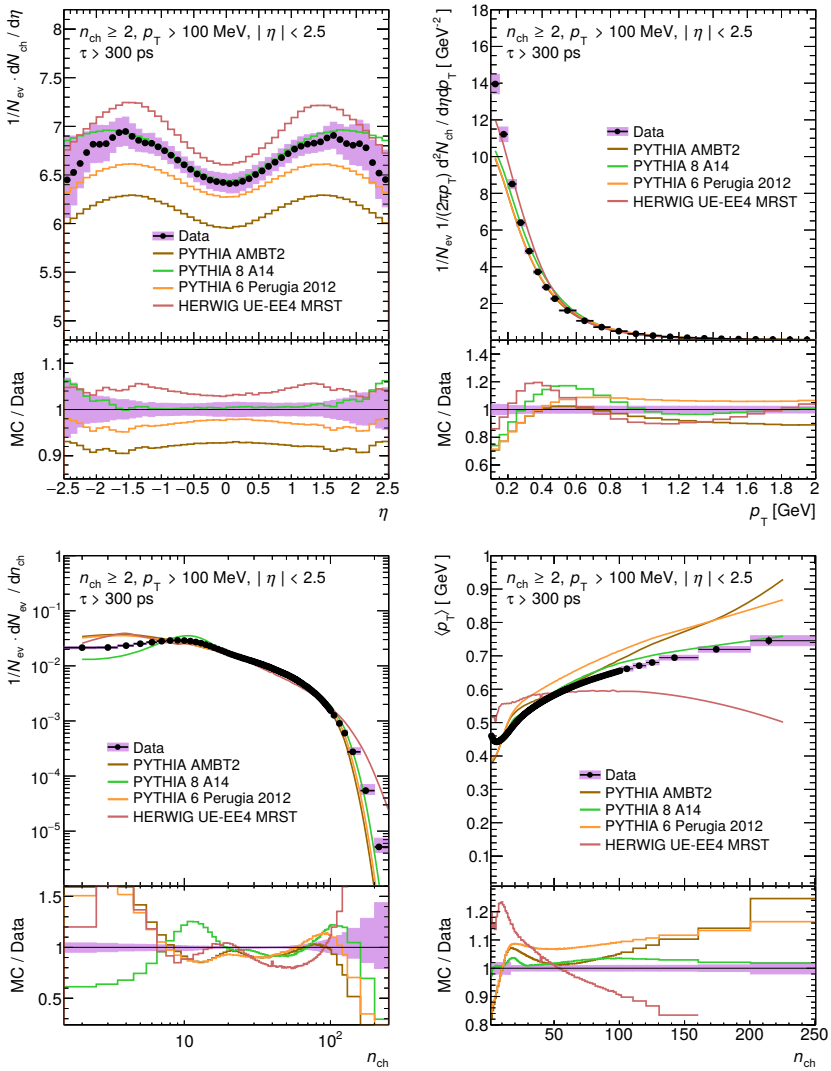

Figure B.7: Primary charged-particle multiplicities as a function of (left top) pseudorapidity η and (right top) transverse momentum p_T, (left bottom) the primary charged-particle multiplicity n_{ch} and (right bottom) the mean transverse momentum $\langle p_T \rangle$. The black dots represent the data and the coloured curves the different MC predictions. The vertical bars represent the statistical uncertainty, while the shaded areas show statistical and systematic uncertainties added in quadrature. The lower panel in each figure shows the ratio of the MC prediction to data.

C Search for Supersymmetry

C.1 Preselection Plots for tN_med

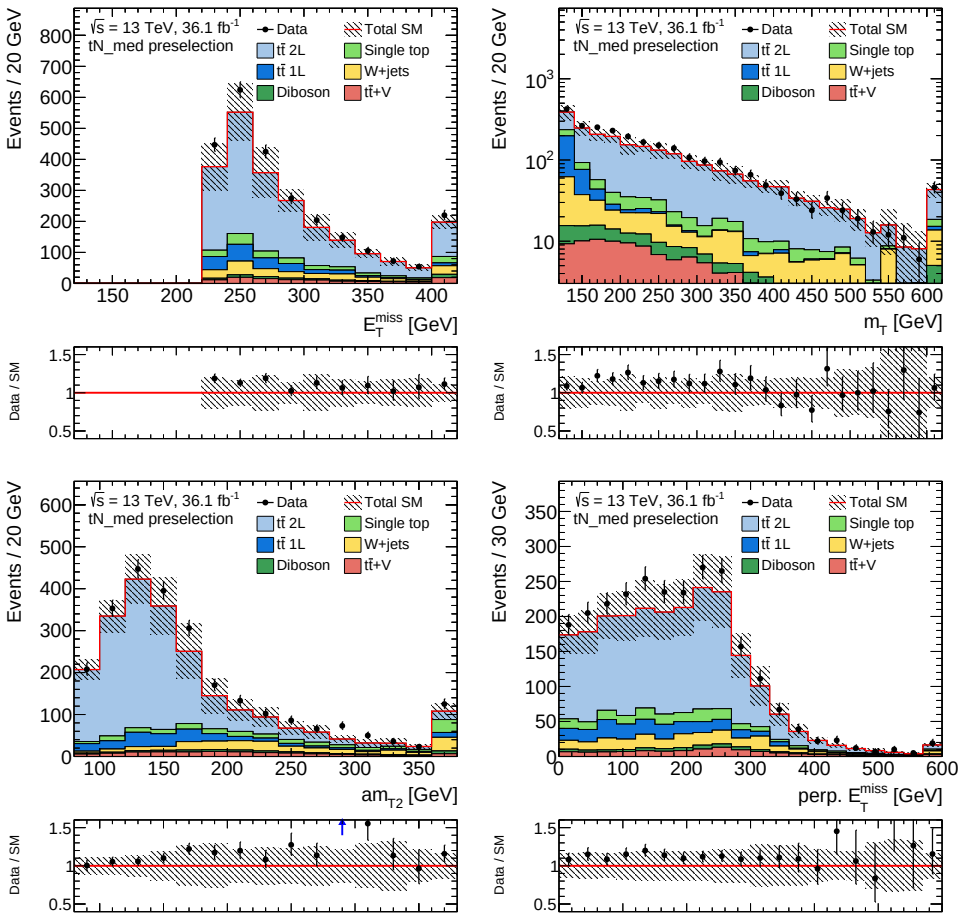

Figure C.1: Comparison of data and simulation applying only the preselection used for the tN_med signal region optimisation. Statistical uncertainties as well as the systematic uncertainties from JES, JER and *b*-tagging are displayed. The last bin includes the overflow.

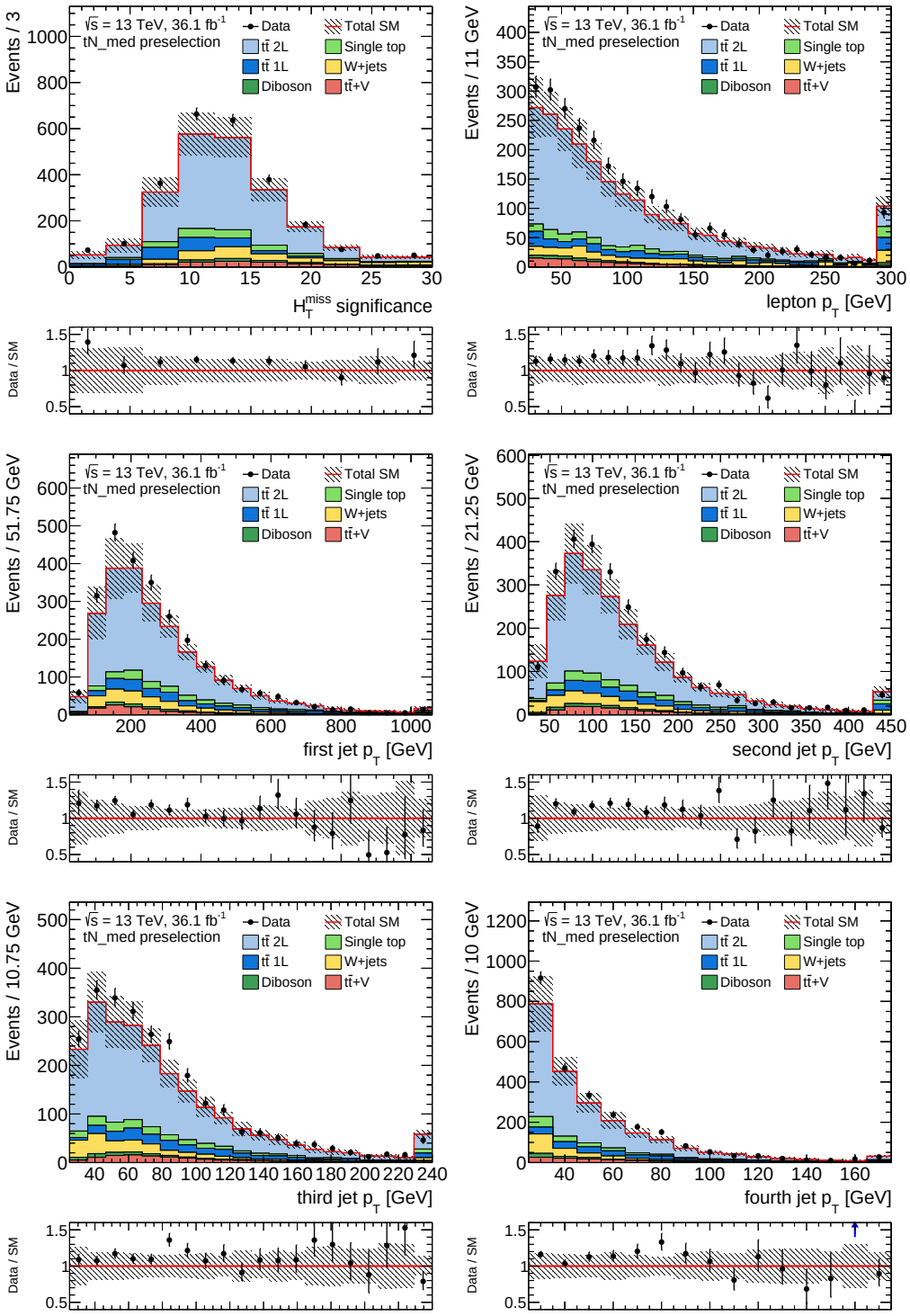

Figure C.2: Comparison of data and simulation applying only the preselection used for the tN_med signal region optimisation. Statistical uncertainties as well as the systematic uncertainties from JES, JER and *b*-tagging are displayed. The last bin includes the overflow.

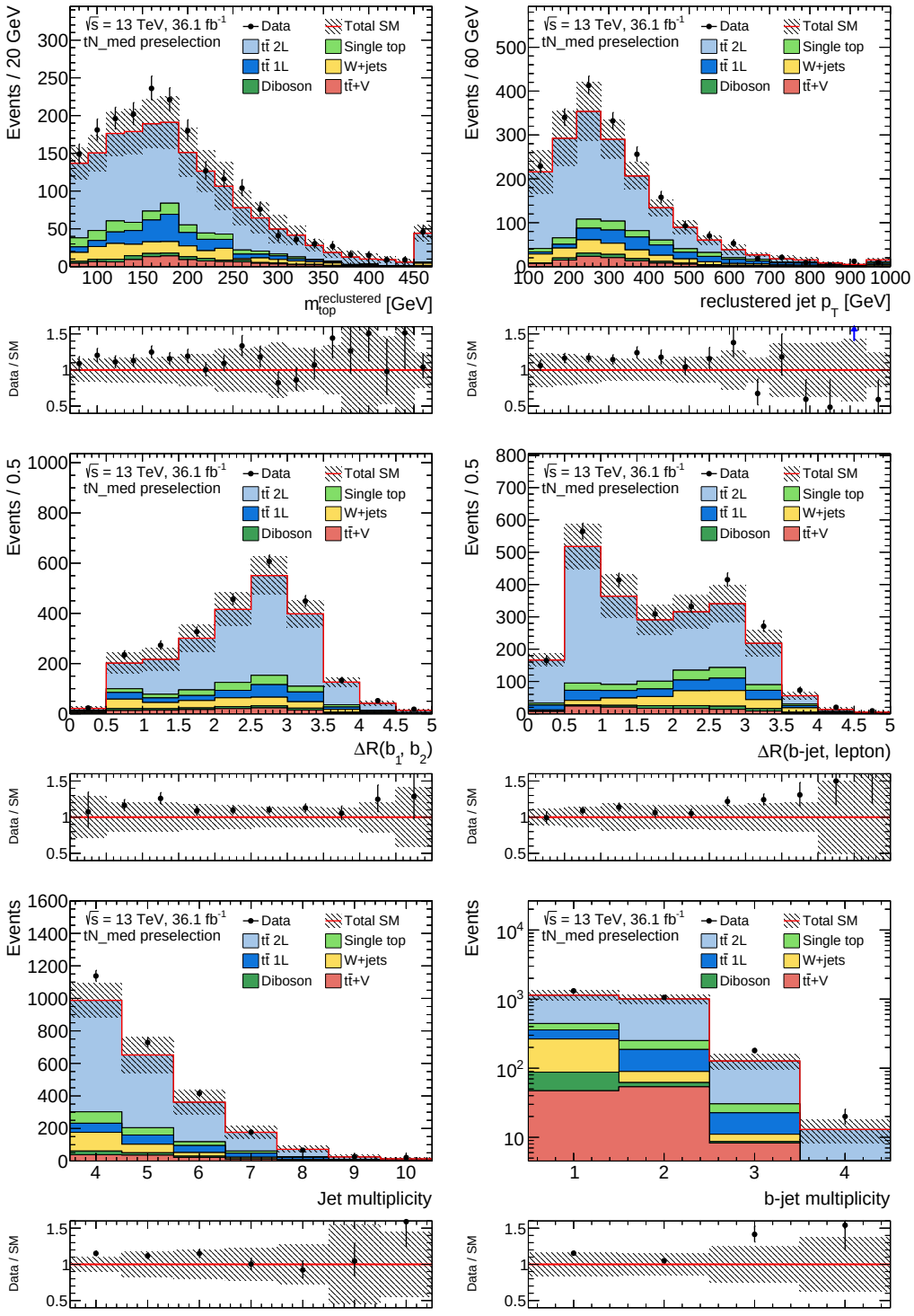

Figure C.3: Comparison of data and simulation applying only the preselection used for the tN_med signal region optimisation. Statistical uncertainties as well as the systematic uncertainties from JES, JER and *b*-tagging are displayed. The last bin includes the overflow.

C.2 Control Region Plots for tN_med

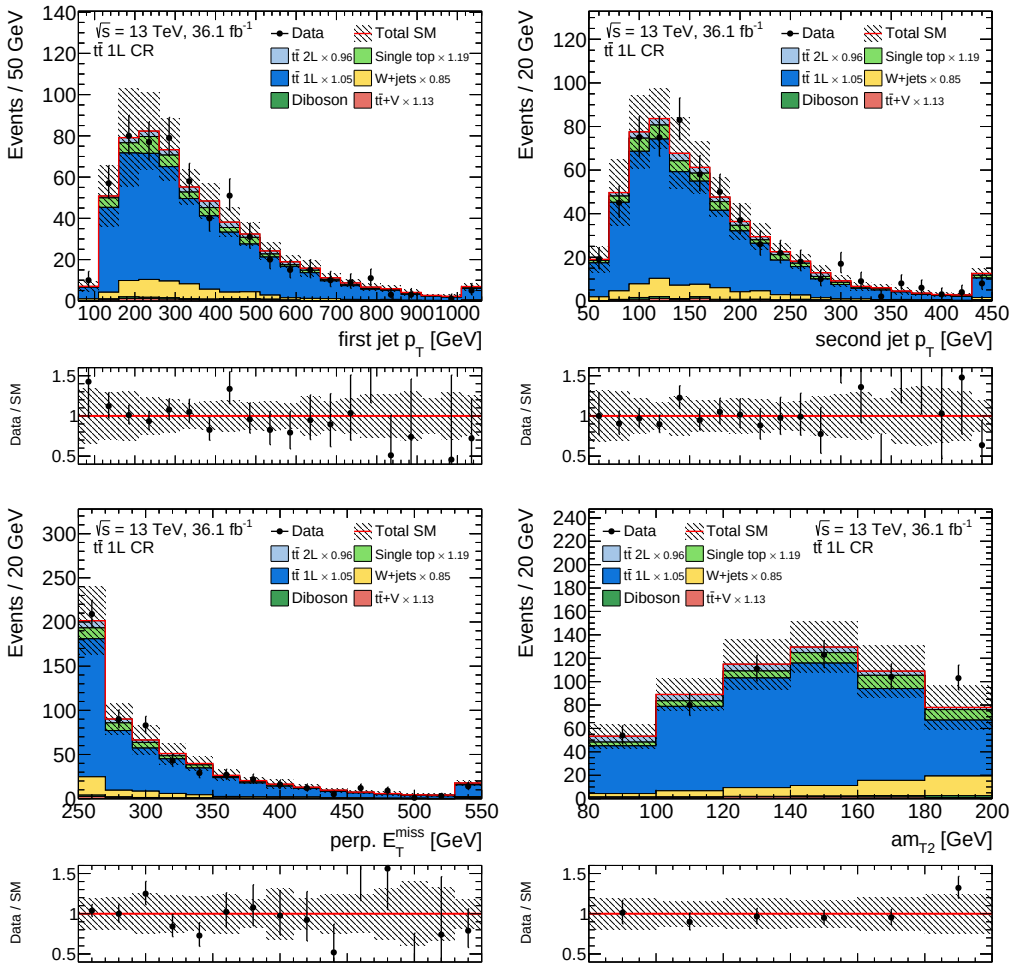

Figure C.4: Comparison of data and simulation for the semi-leptonic $t\bar{t}$ CR after applying the normalisation of the simultaneous fit. Statistical uncertainties as well as the systematic uncertainties from JES, JER and *b*-tagging are displayed. The last bin includes the overflow.

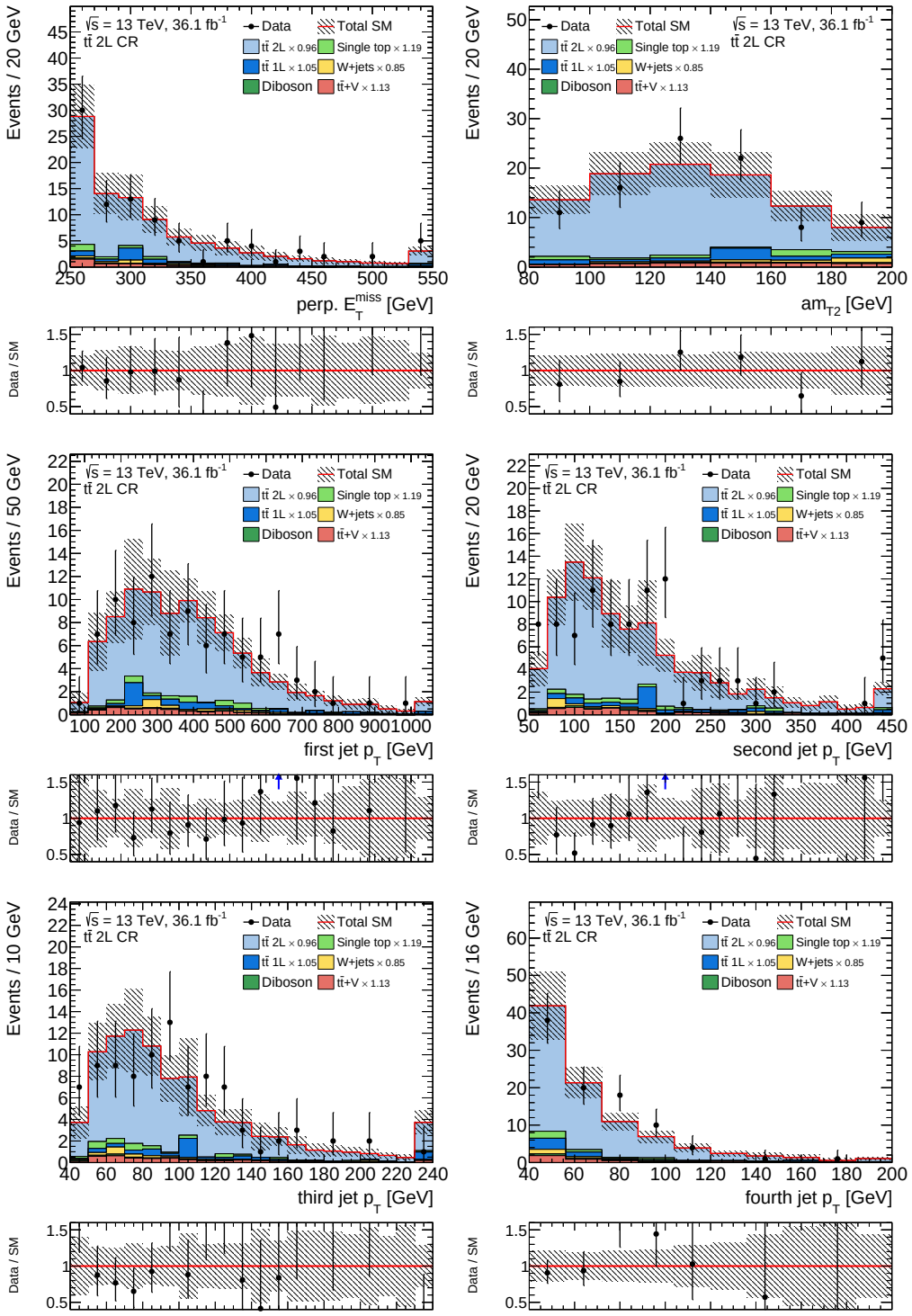

Figure C.5: Comparison of data and simulation for the dileptonic $t\bar{t}$ CR after applying the normalisation of the simultaneous fit. Statistical uncertainties as well as the systematic uncertainties from JES, JER and *b*-tagging are displayed. The last bin includes the overflow.

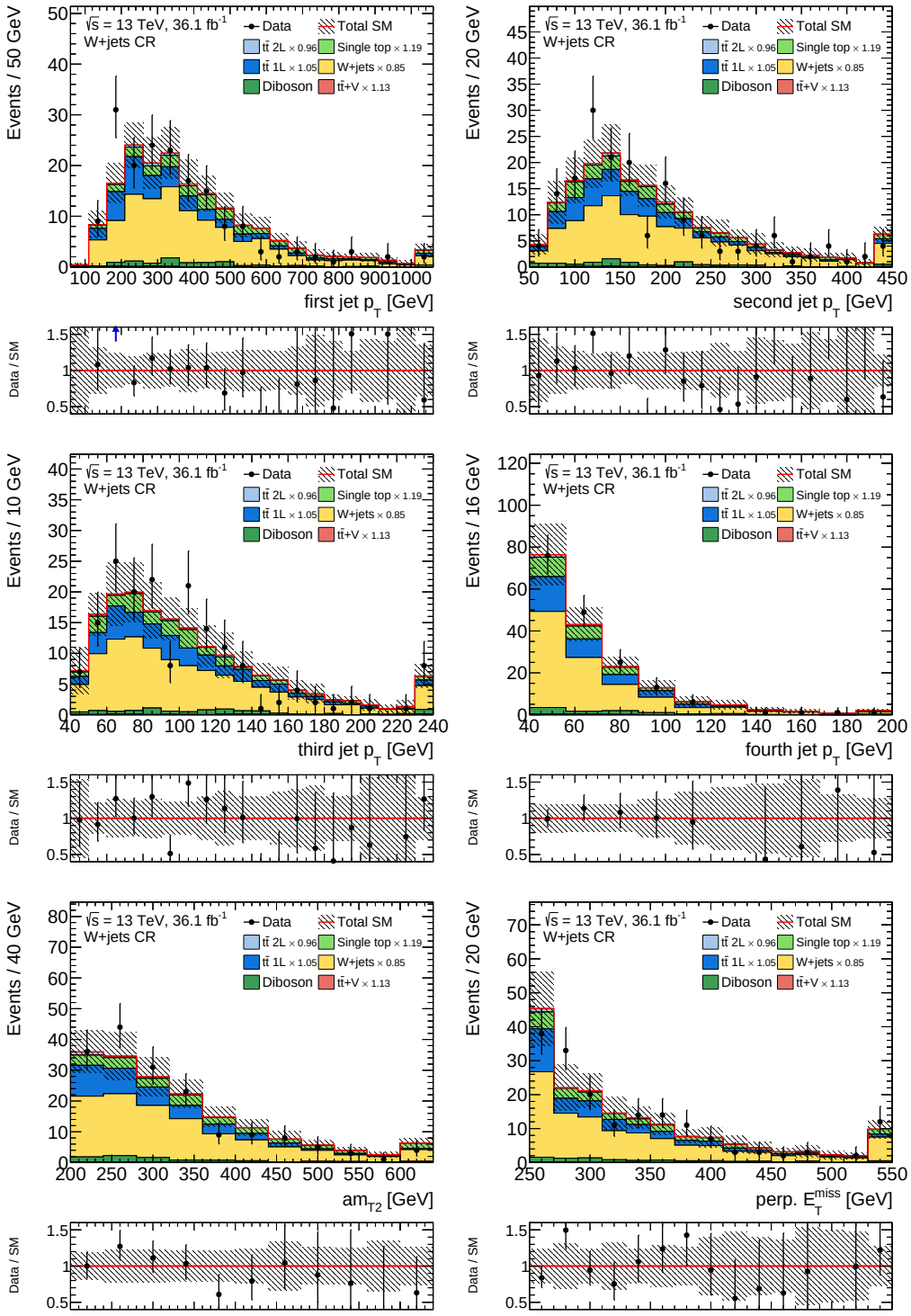

Figure C.6: Comparison of data and simulation for the W+jets CR after applying the normalisation of the simultaneous fit. Statistical uncertainties as well as the systematic uncertainties from JES, JER and b-tagging are displayed. The last bin includes the overflow.

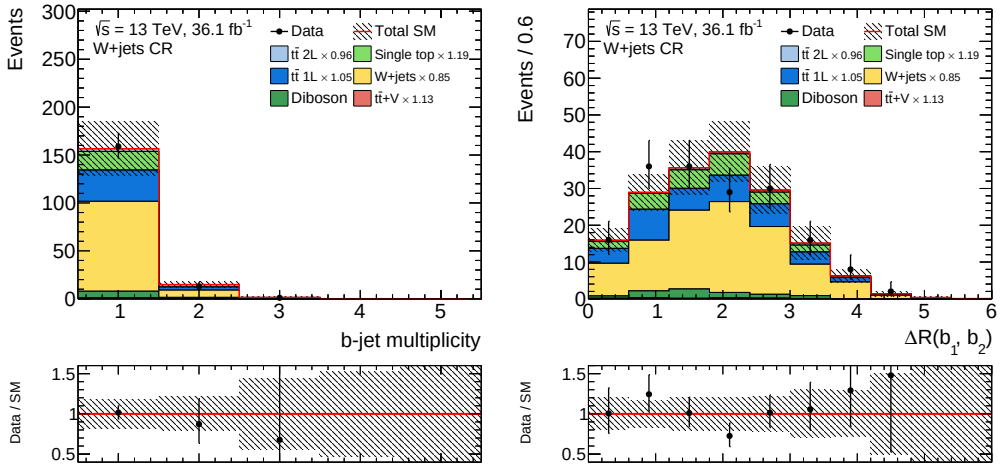

Figure C.7: Comparison of data and simulation for the W+jets CR after applying the normalisation of the simultaneous fit. Statistical uncertainties as well as the systematic uncertainties from JES, JER and b-tagging are displayed. The last bin includes the overflow.

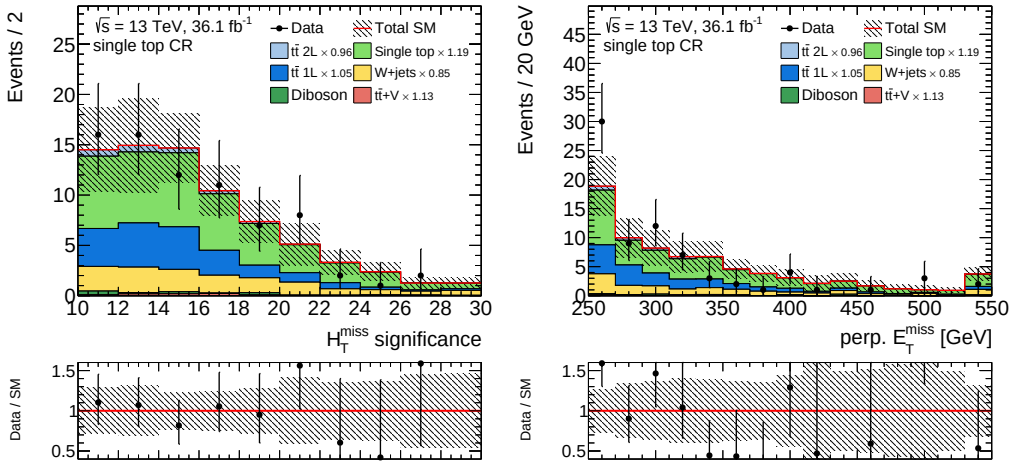

Figure C.8: Comparison of data and simulation for the single top CR after applying the normalisation of the simultaneous fit. Statistical uncertainties as well as the systematic uncertainties from JES, JER and b-tagging are displayed. The last bin includes the overflow.

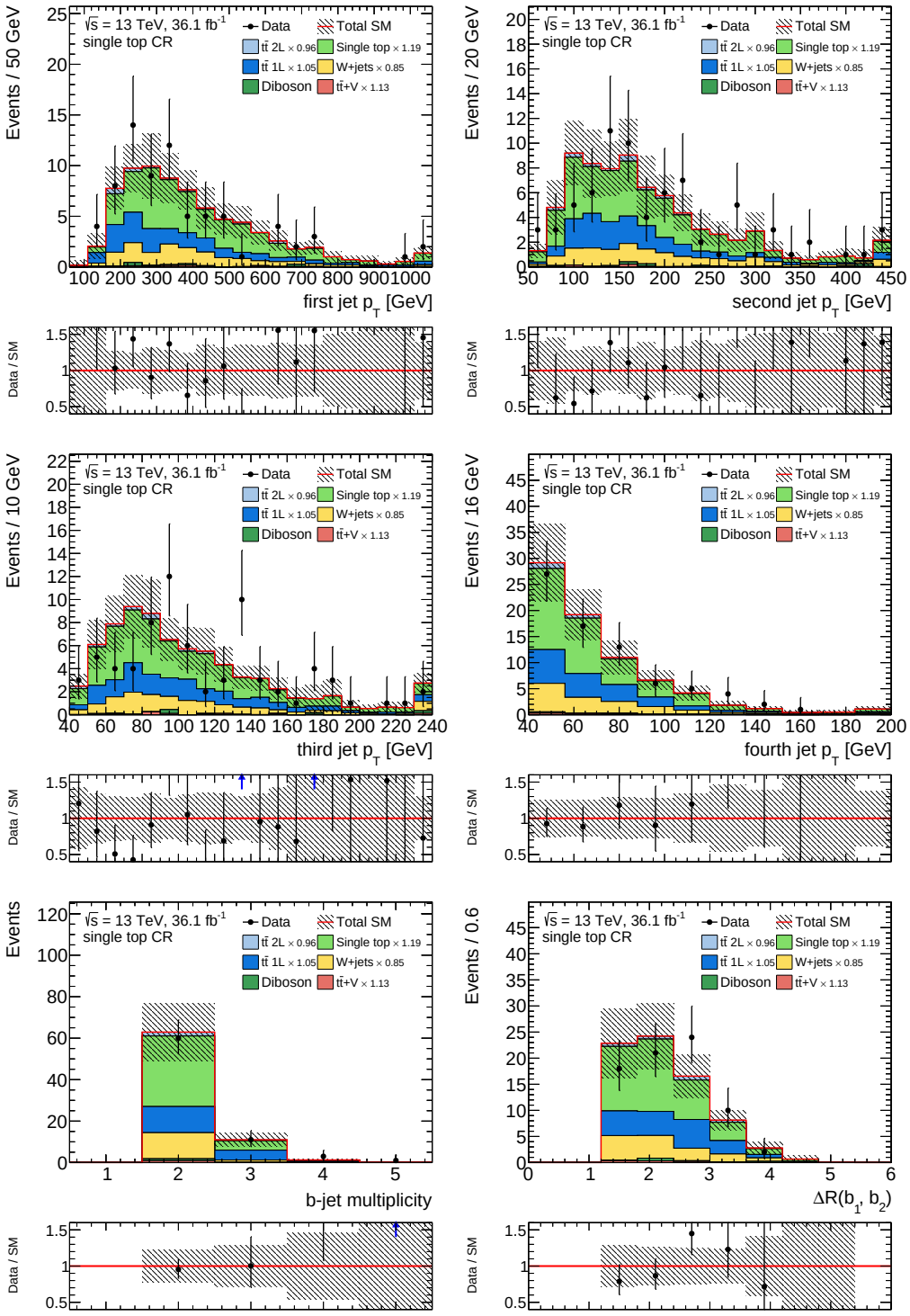

Figure C.9: Comparison of data and simulation for the single top CR after applying the normalisation of the simultaneous fit. Statistical uncertainties as well as the systematic uncertainties from JES, JER and *b*-tagging are displayed. The last bin includes the overflow.

C.3 Validation Region Plots for tN_med

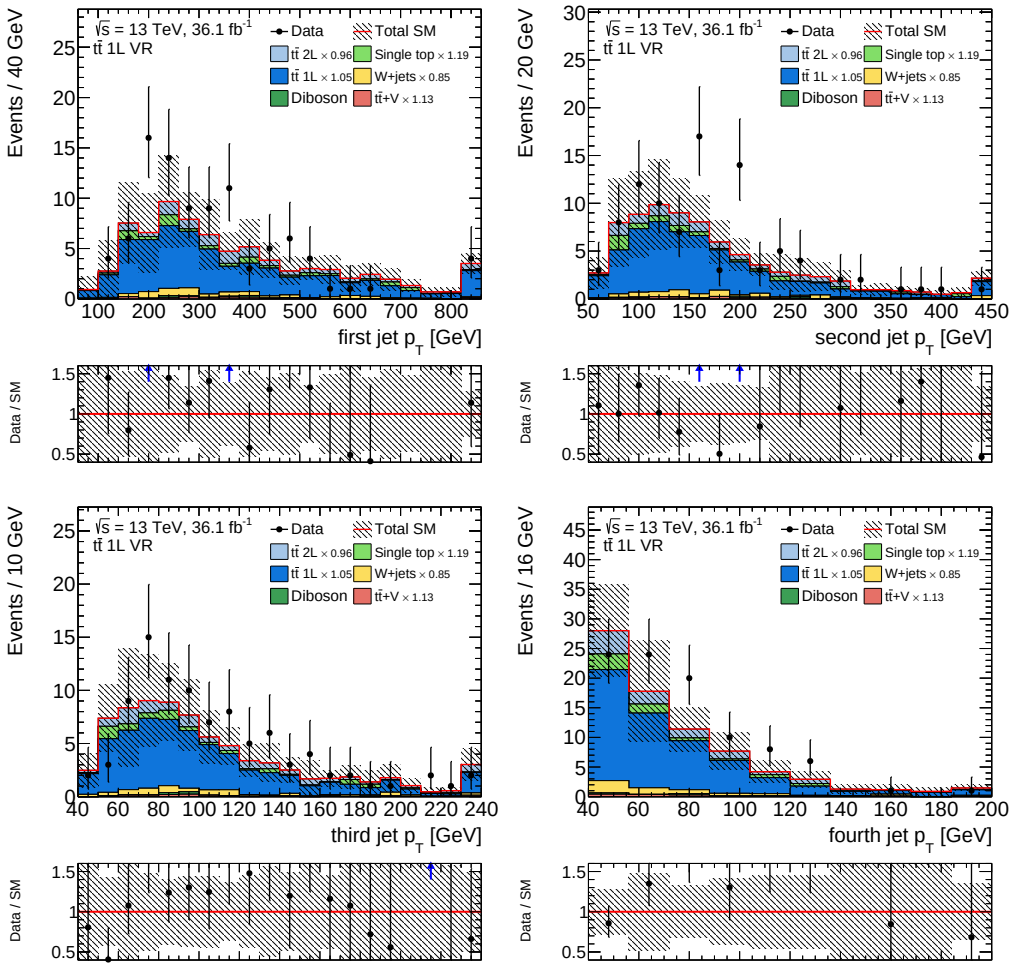

Figure C.10: Comparison of data and simulation for the semi-leptonic $t\bar{t}$ VR after applying the normalisation of the simultaneous fit. Statistical uncertainties as well as the systematic uncertainties from JES, JER and *b*-tagging are displayed. The last bin includes the overflow.

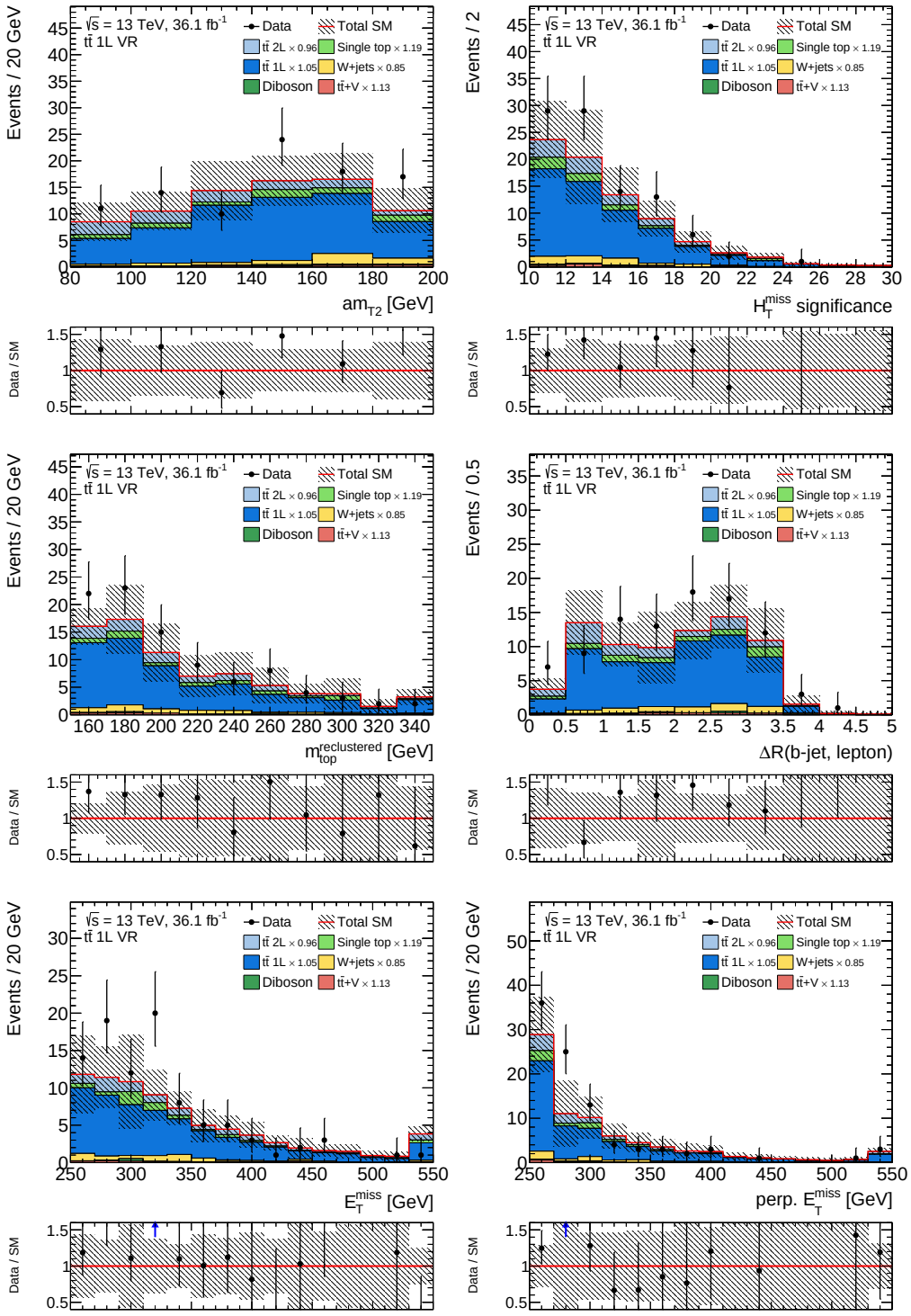

Figure C.11: Comparison of data and simulation for the semi-leptonic $t\bar{t}$ VR after applying the normalisation of the simultaneous fit. Statistical uncertainties as well as the systematic uncertainties from JES, JER and *b*-tagging are displayed. The last bin includes the overflow.

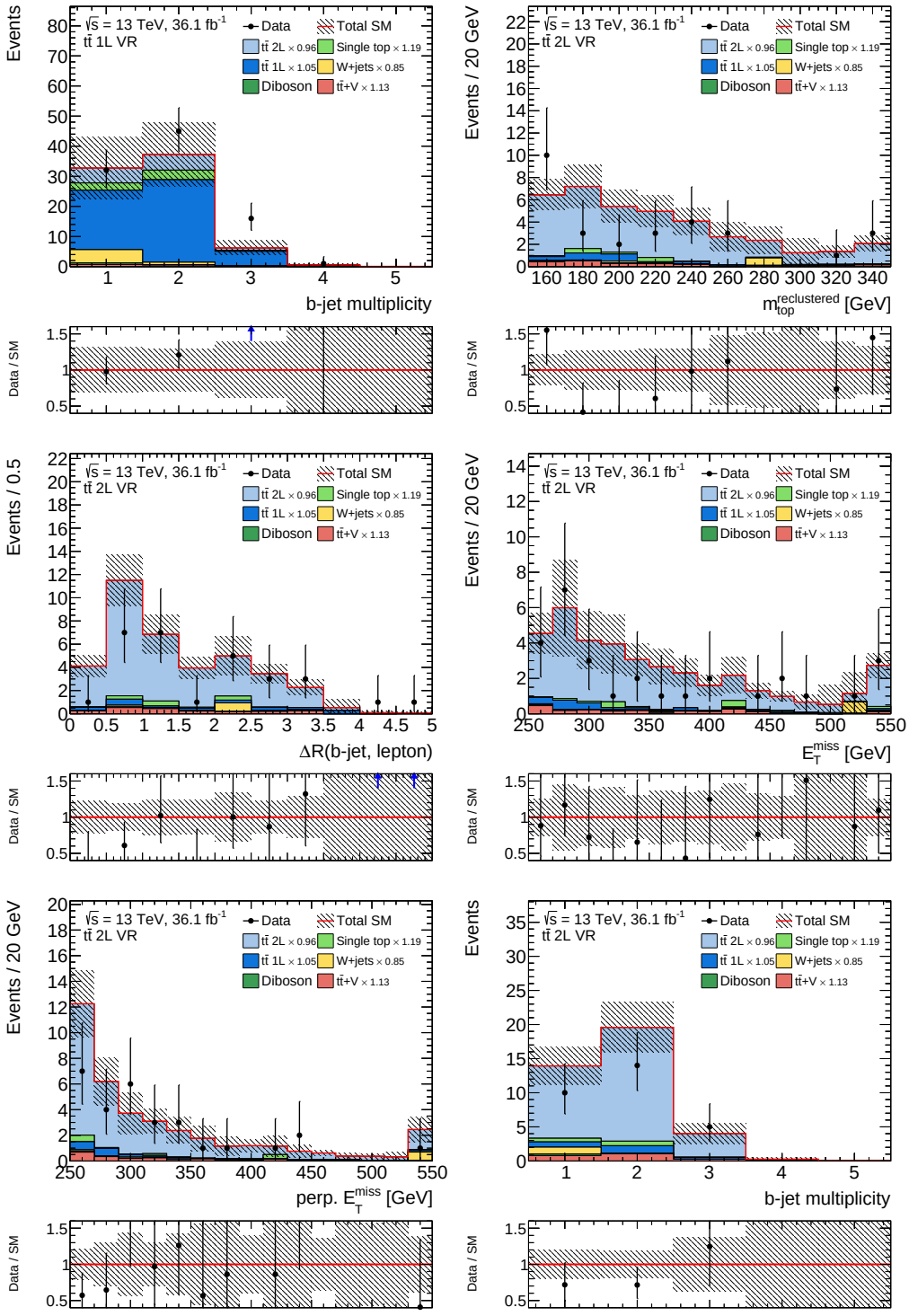

Figure C.12: Comparison of data and simulation for the semi-leptonic $t\bar{t}$ (top left) and the dileptonic $t\bar{t}$ VR after applying the normalisation of the simultaneous fit. Statistical uncertainties as well as the systematic uncertainties from JES, JER and *b*-tagging are displayed. The last bin includes the overflow.

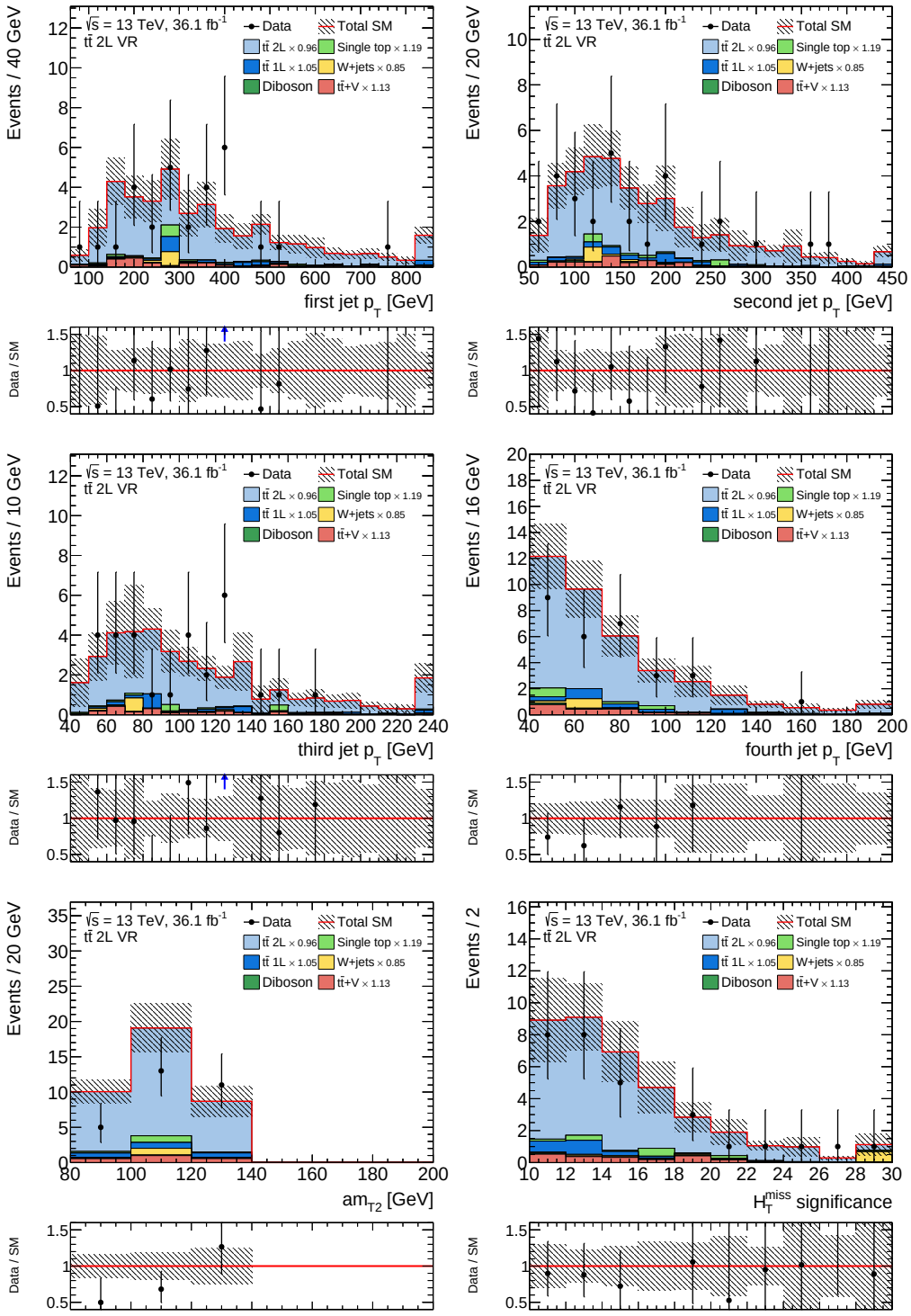

Figure C.13: Comparison of data and simulation for the dileptonic $t\bar{t}$ VR after applying the normalisation of the simultaneous fit. Statistical uncertainties as well as the systematic uncertainties from JES, JER and *b*-tagging are displayed. The last bin includes the overflow.

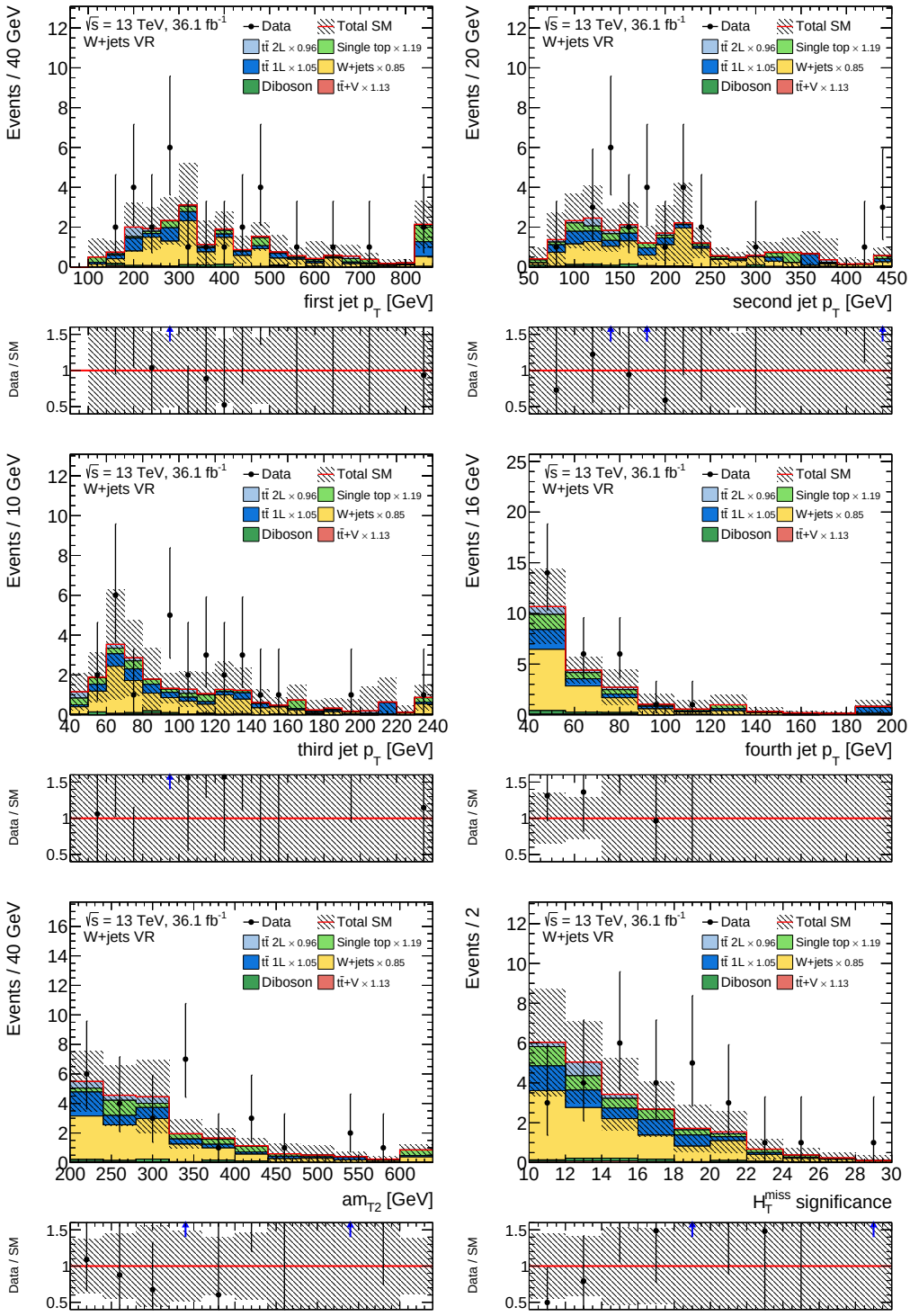

Figure C.14: Comparison of data and simulation for the W+jets VR after applying the normalisation of the simultaneous fit. Statistical uncertainties as well as the systematic uncertainties from JES, JER and b-tagging are displayed. The last bin includes the overflow.

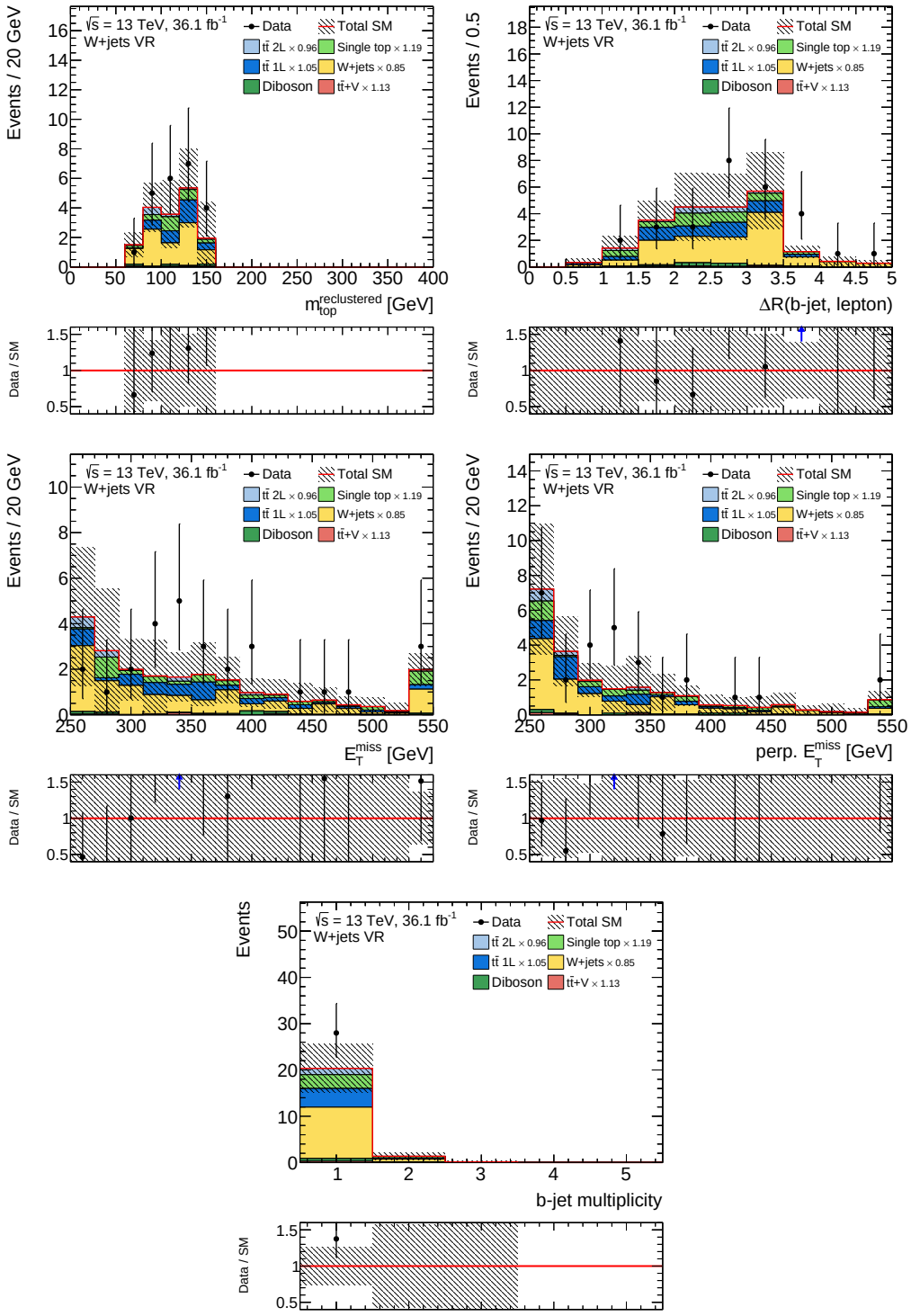

Figure C.15: Comparison of data and simulation for the W+jets VR after applying the normalisation of the simultaneous fit. Statistical uncertainties as well as the systematic uncertainties from JES, JER and b-tagging are displayed. The last bin includes the overflow.

C.4 Modelling in the tN_med Signal Region

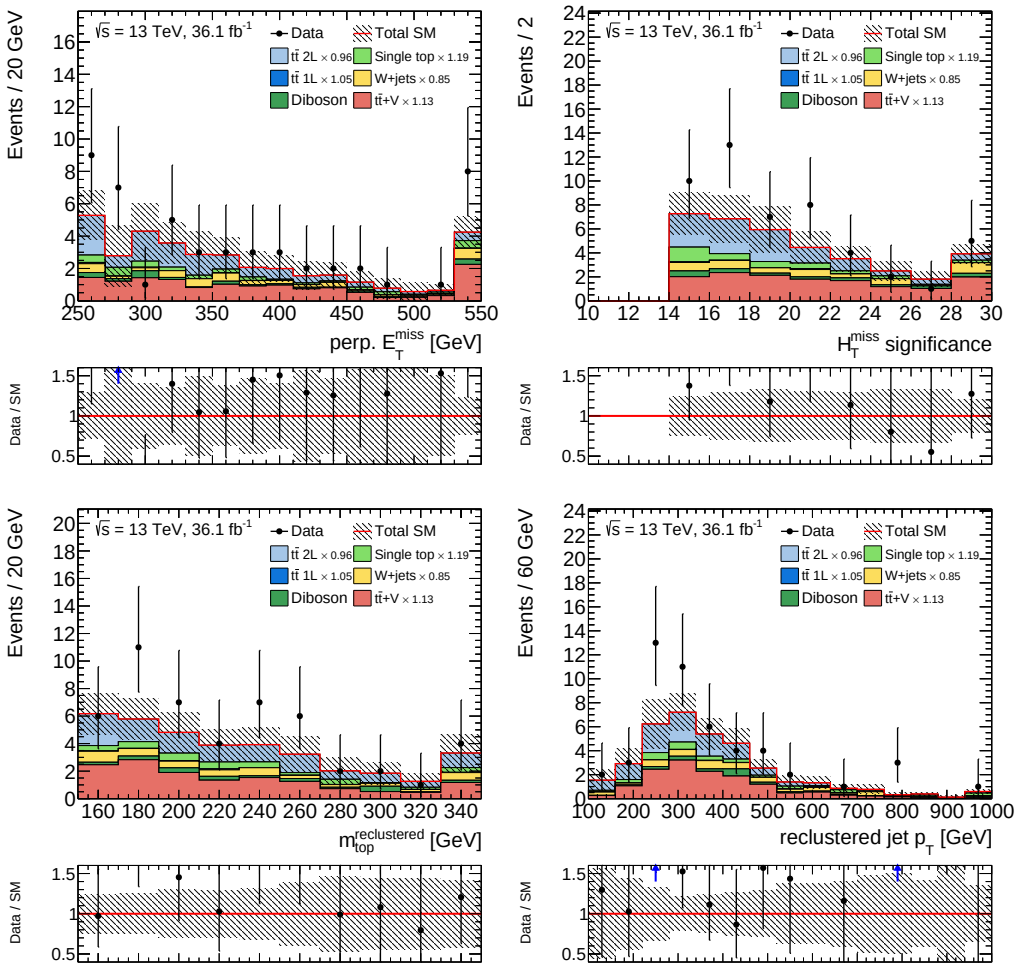

Figure C.16: Comparison of data and simulation for the signal region after applying the normalisation of the simultaneous fit. Statistical uncertainties as well as the systematic uncertainties from JES, JER and *b*-tagging are displayed. The last bin includes the overflow.

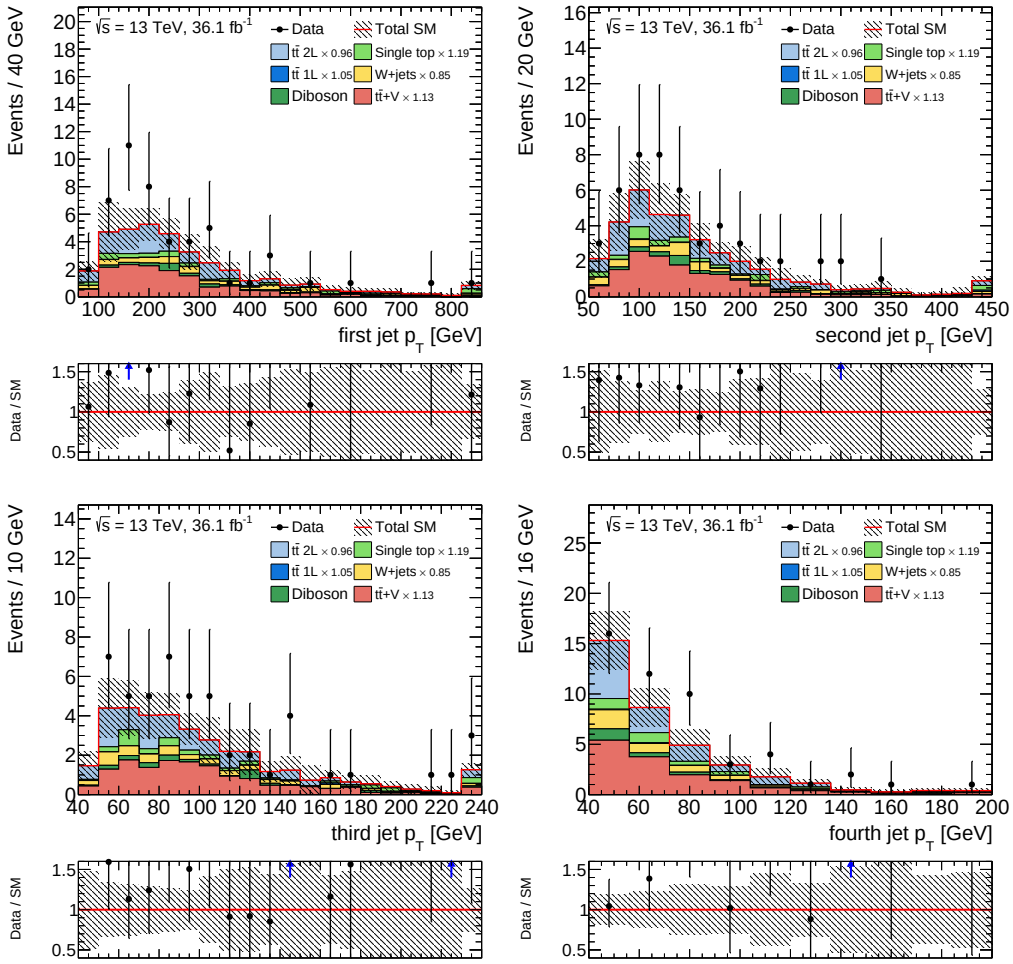

Figure C.17: Comparison of data and simulation for the signal region after applying the normalisation of the simultaneous fit. Statistical uncertainties as well as the systematic uncertainties from JES, JER and *b*-tagging are displayed. The last bin includes the overflow.

C.5 Combination of tN_med and the bCsoft Selections

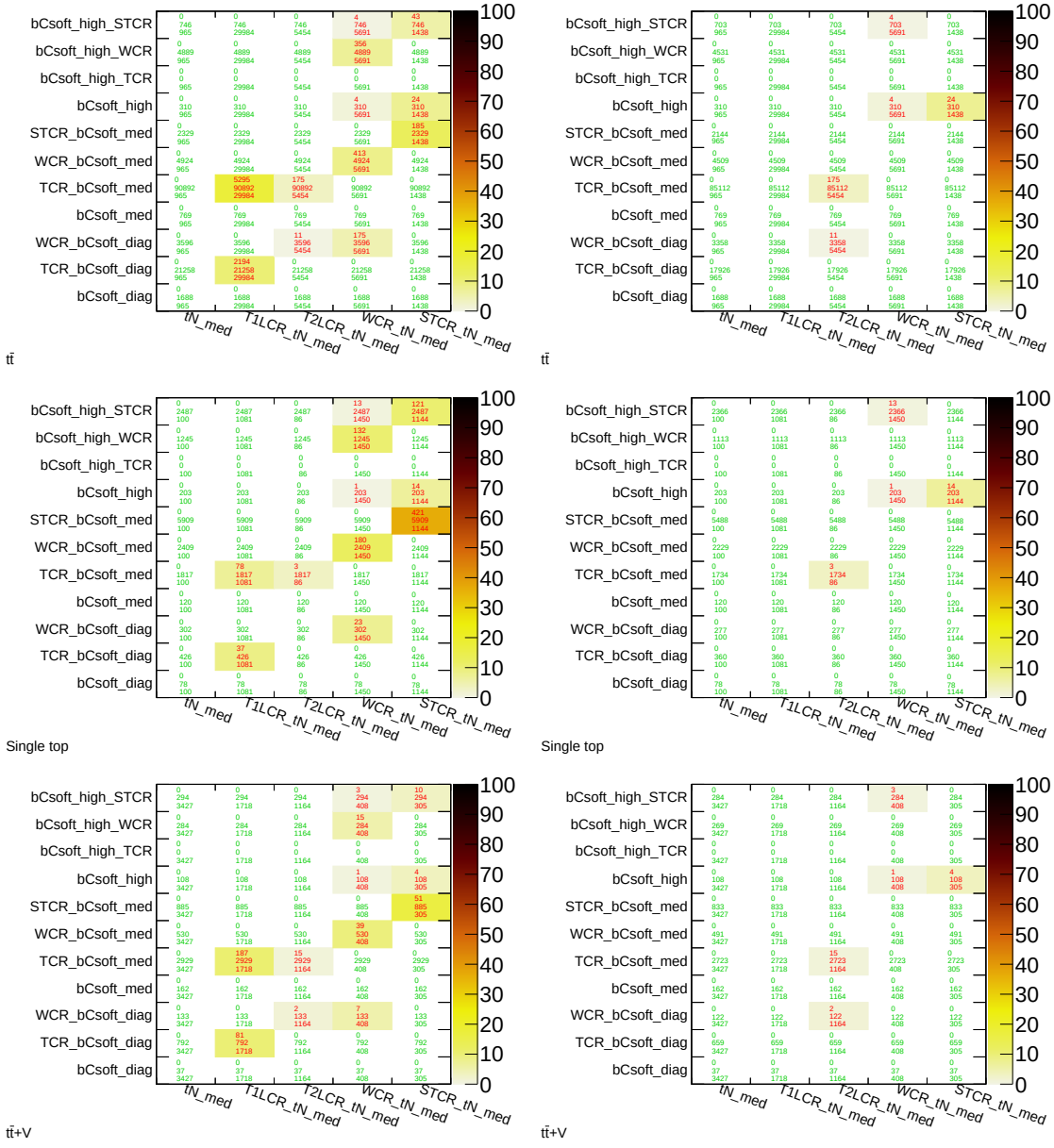

Figure C.18: Number of simulated events selected by any region of the three soft lepton selection and the tN_med selection for $t\bar{t}$ (top), single top (middle) and $t\bar{t} + V$ (bottom). The left-hand side shows the overlap using the standard selection, the right-hand side shows the remaining overlap after the tN_med control region veto applied for the soft lepton control regions. The numbers in each bin give the number of overlapping events and the number of events selected by the region indicated on the vertical axis and the horizontal axis from top to bottom. The colour scale indicates the fraction of overlapping events in a bin.

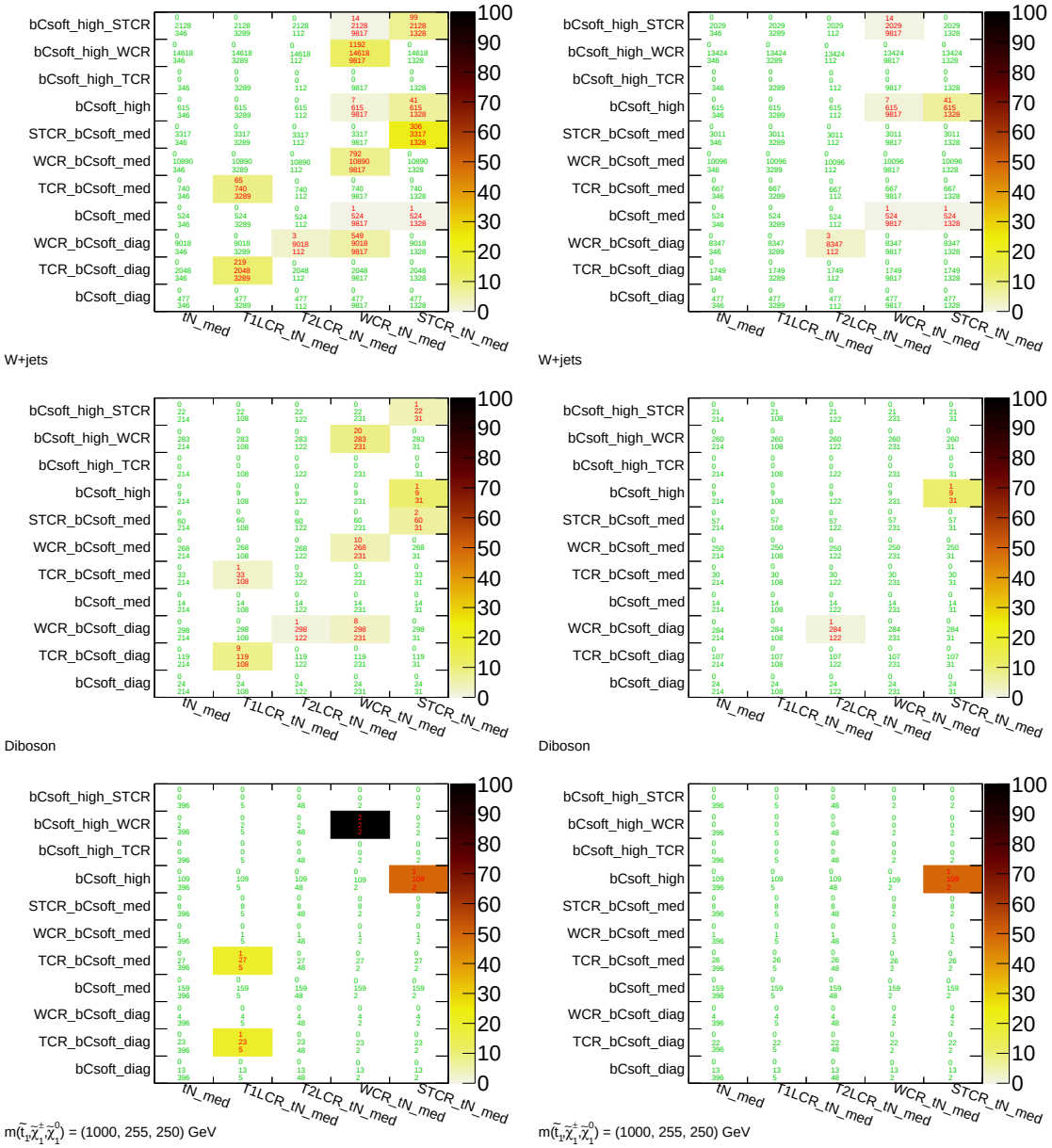

Figure C.19: Number of simulated events selected by any region of the three soft lepton selection and the tN_med selection for W+jets (top), diboson (middle) and a signal sample (bottom). The left-hand side shows the overlap using the standard selection, the right-hand side shows the remaining overlap after the tN_med control region veto applied for the soft lepton control regions. The numbers in each bin give the number of overlapping events and the number of events selected by the region indicated on the vertical axis and the horizontal axis from top to bottom. The colour scale indicates the fraction of overlapping events in a bin.

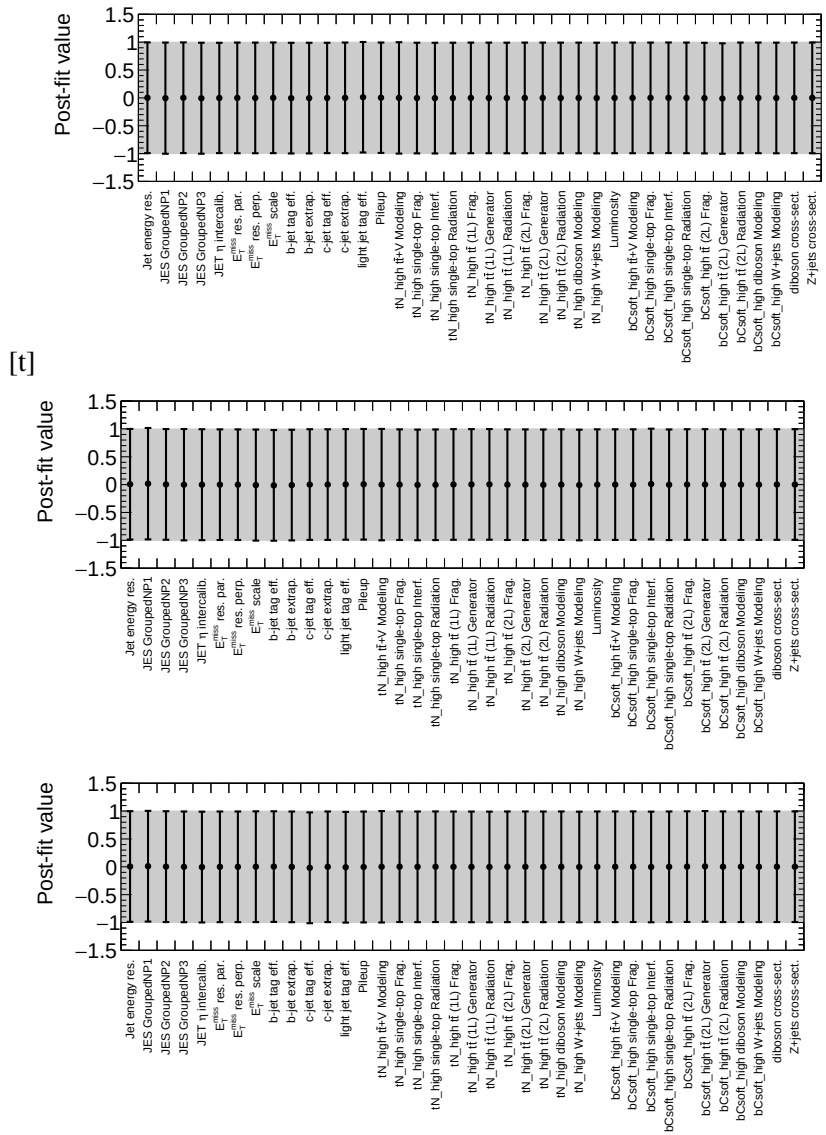

[t]

Figure C.20: The fit results for the three combination fits using the tN_med signal region as well as the bCsoft_diag (top), bCsoft_med (middle) or bCsoft_high (bottom) signal region.

The fit result and the corresponding uncertainties of the nuisance parameters are shown in Figure C.20 for the three combination fits. The Gaussian parameters have a best fit value of zero and an uncertainty of one. This means, that no pulls or constraints are introduced in the combination.

In Table C.21, the background normalisation factors are presented for the standalone fits for all four regions (three soft lepton and tN_med) and using the three combined fit setups. The normalisation for the tN_med selection does not differ for the three combination fits and is in agreement with the standalone results. The normalisation for the three soft lepton selections is in agreement comparing the combined and the standalone results. Small differences are expected due to the overlap removal in their control regions.

Figure C.21: Summary of the background normalisation factors for the standalone fits and the combination fit using one of the soft lepton selection with the tN_med selection.

	$t\bar{t}$ 1L	$t\bar{t}$ 2L	Single top	W+jets	$t\bar{t}+V$
Standalone					
tN_med	1.05 ± 0.09	0.96 ±0.13	1.18 ± 0.37	0.85 ± 0.18	1.13 ± 0.24
bCsoft_diag	0.66 ± 0.08		–	1.10 ± 0.20	–
bCsoft_med	0.87 ± 0.06		0.47 ± 0.12	1.30 ± 0.23	–
bCsoft_high	0.89 ± 0.14		0.32 ± 0.13	1.18 ± 0.21	–
Combination					
tN_med	1.05 ± 0.09	0.96 ±0.13	1.18 ± 0.37	0.85 ± 0.18	1.13 ± 0.24
bCsoft_diag	0.71 ± 0.12		–	1.18 ± 0.26	–
bCsoft_med	0.91 ± 0.07		0.51 ± 0.14	1.35 ± 0.24	–
bCsoft_high	0.93 ± 0.16		0.36 ± 0.16	1.19 ± 0.21	–

C.6 Preselection Plots for the Compressed Signal Region

Overall a good shape agreement between the data and the MC prediction can be seen. There is a constant offset visible in the ratio, but these differences are covered by scaling the $t\bar{t}$ contribution using a data-driven estimate.

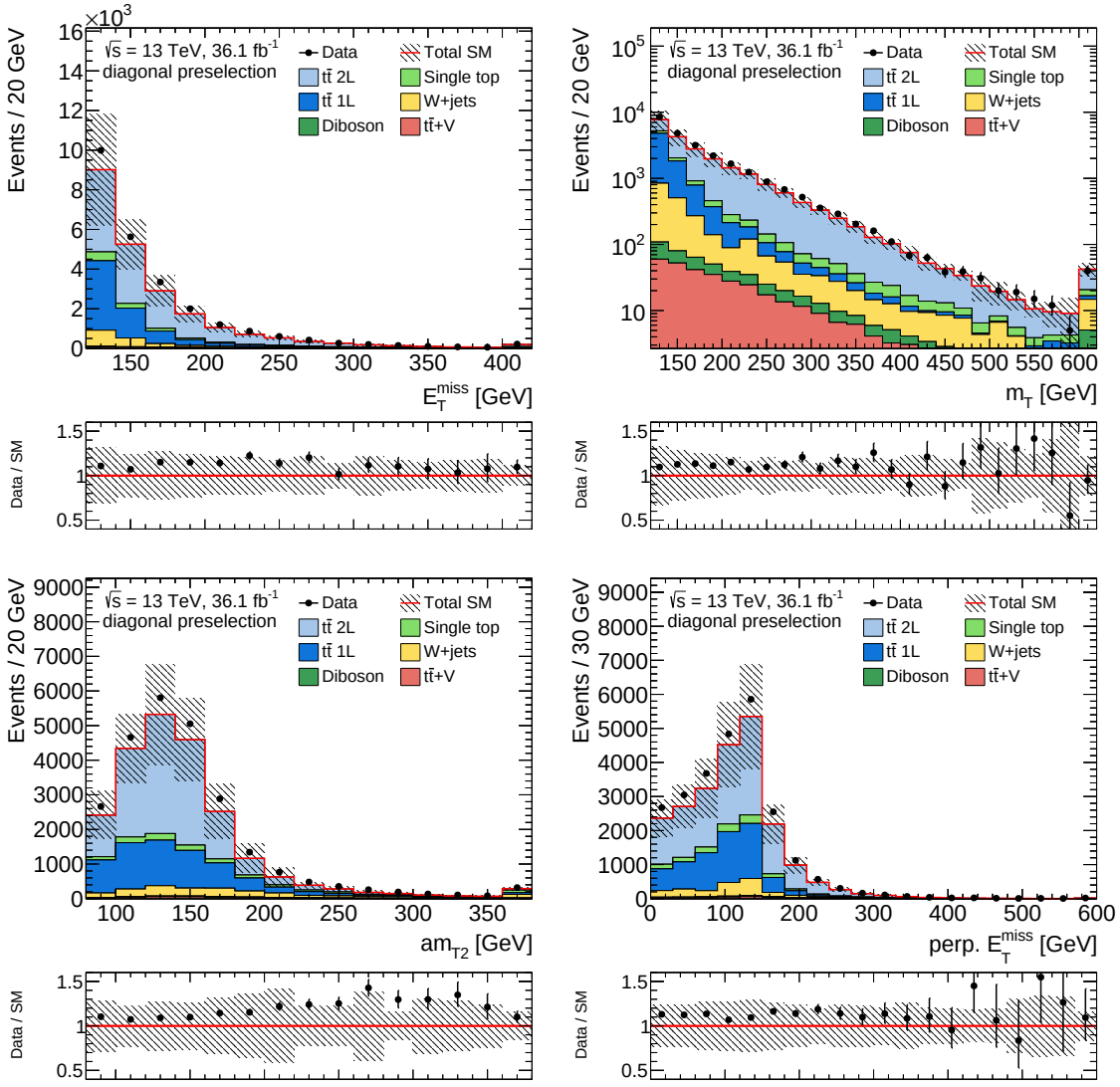

Figure C.22: Comparison of data and simulation applying only the preselection used for the compressed signal region optimisation. Statistical uncertainties as well as the systematic uncertainties from JES, JER and *b*-tagging are displayed. The last bin includes the overflow.

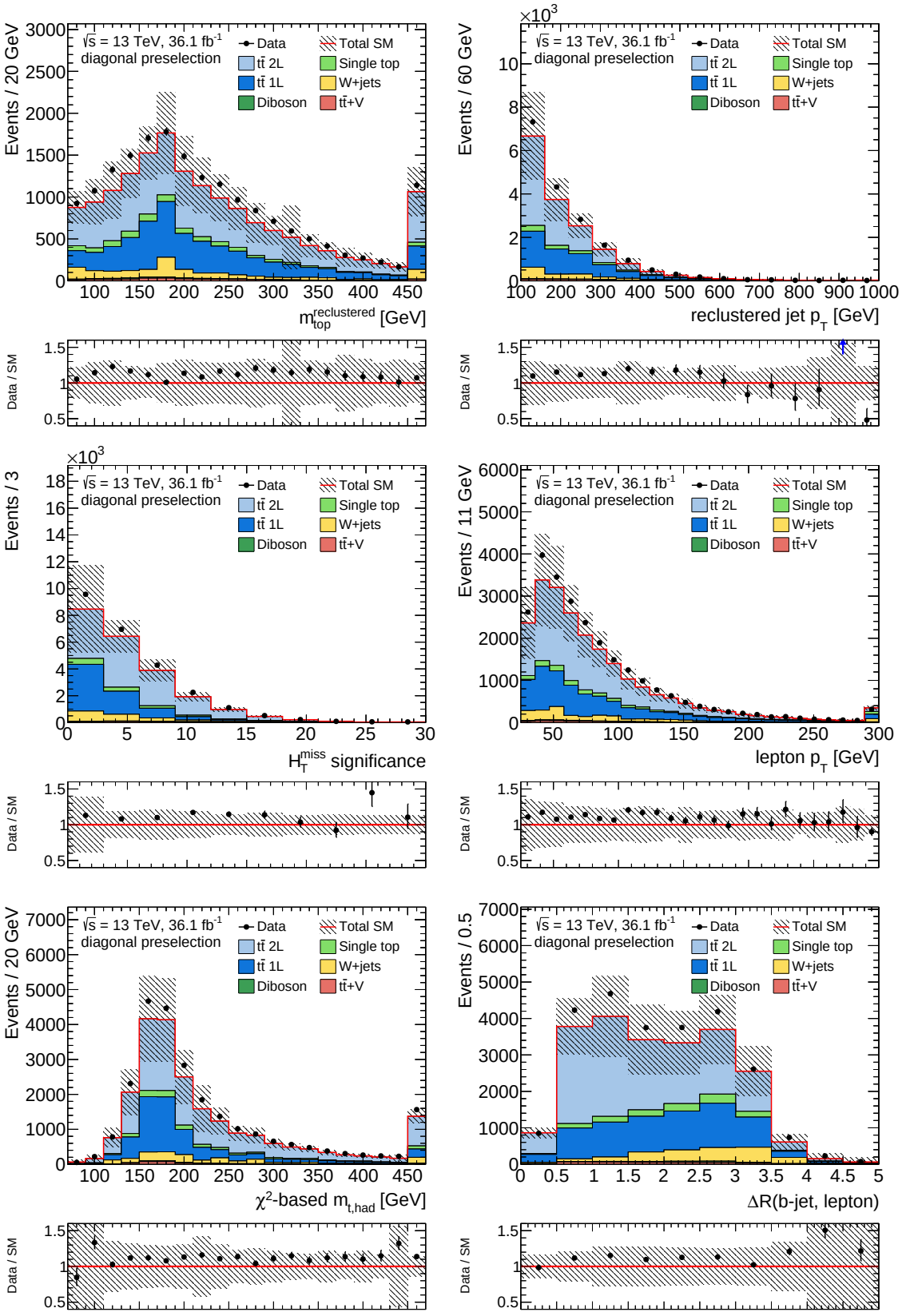

Figure C.23: Comparison of data and simulation applying only the preselection used for the compressed signal region optimisation. Statistical uncertainties as well as the systematic uncertainties from JES, JER and *b*-tagging are displayed. The last bin includes the overflow.

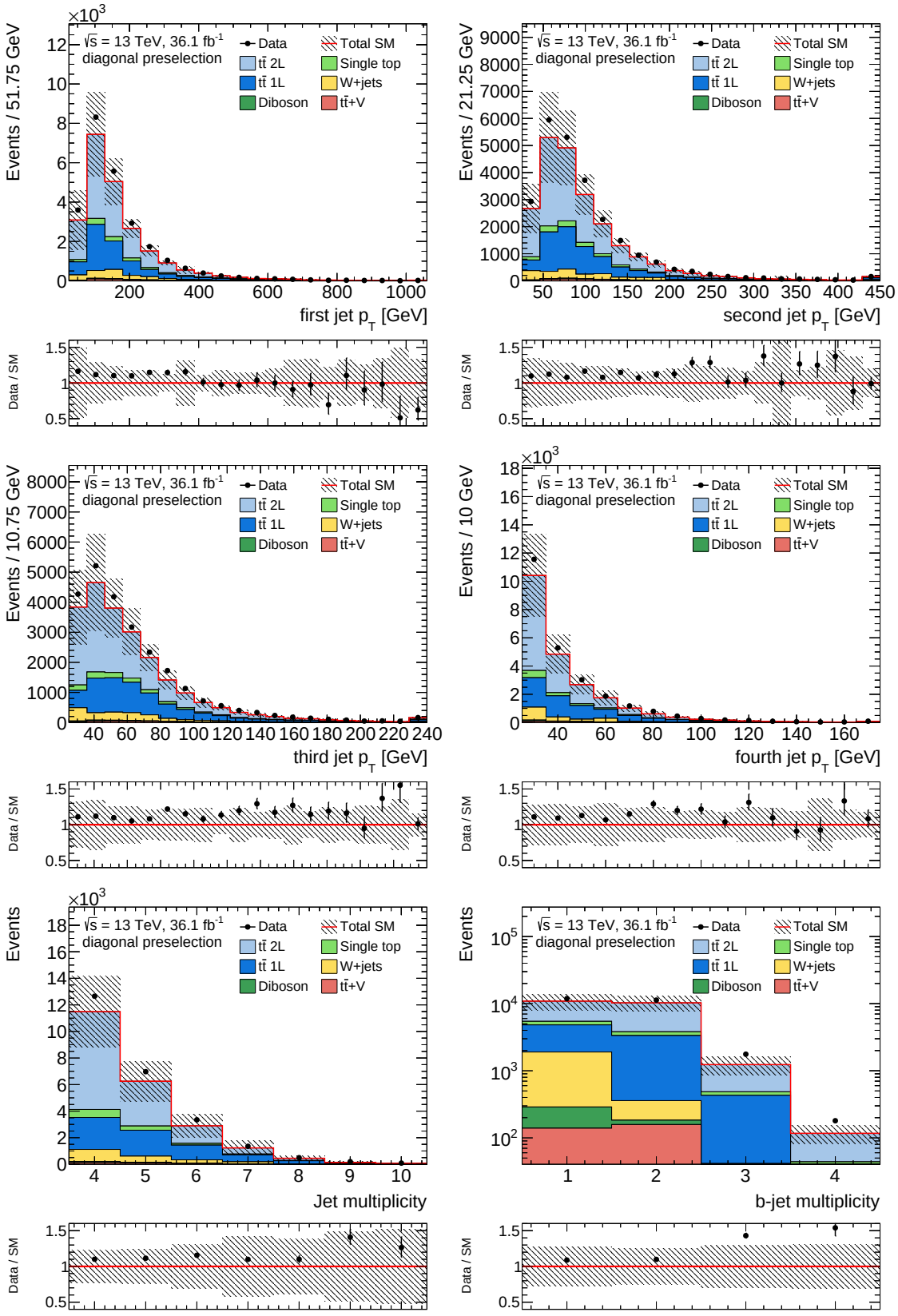

Figure C.24: Comparison of data and simulation applying only the preselection used for the compressed signal region optimisation. Statistical uncertainties as well as the systematic uncertainties from JES, JER and *b*-tagging are displayed. The last bin includes the overflow.

C.7 Validation Plots

C.7.1 VR for Discovery Fit Setup

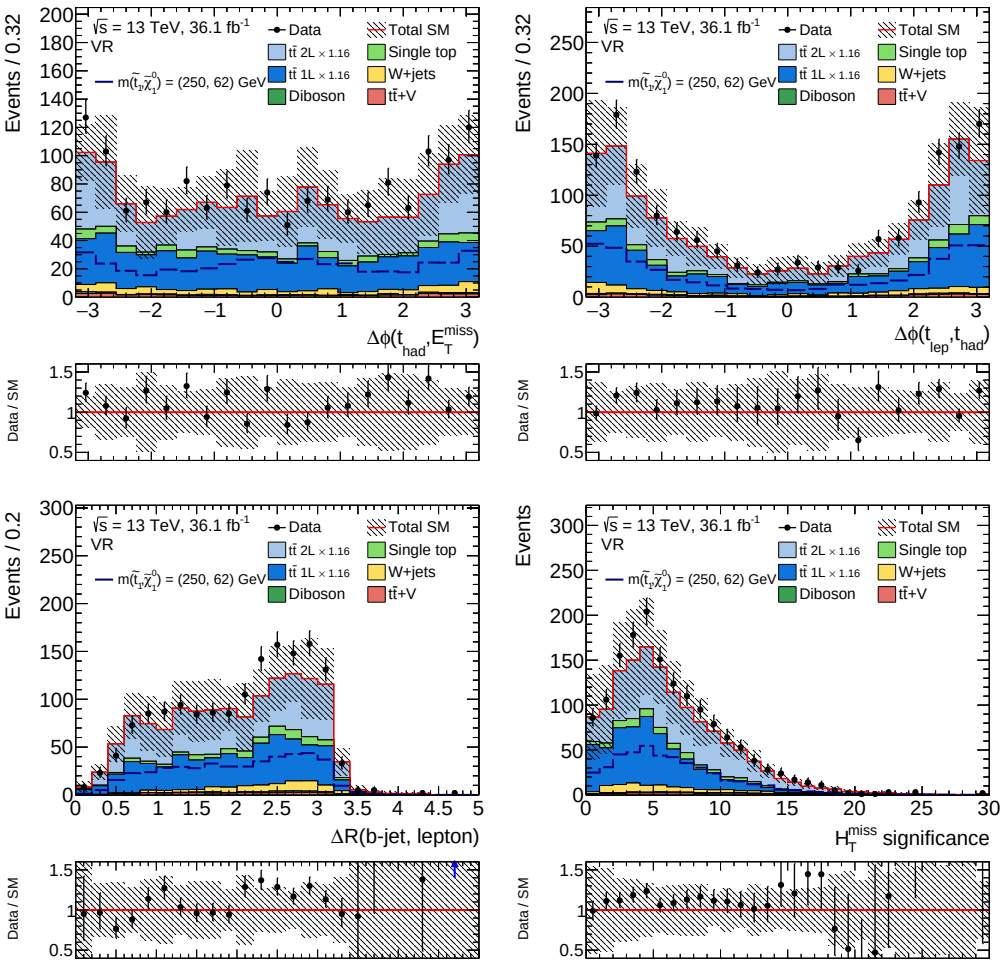

Figure C.25: The $\Delta\phi(E_{\mathrm{T}}^{\mathrm{miss}}, t_{\mathrm{had}})$ (top left) and $\Delta\phi(t_{\mathrm{lep}}, t_{\mathrm{had}})$ (top right), $\Delta R(b, \ell)$ (bottom left) and $H_{\mathrm{T,sig}}^{\mathrm{miss}}$ (bottom right) distribution in the BDT VR in the discovery fit setup. Normalisation factors for semi- and dileptonic $t\bar{t}$ are applied. The statistical uncertainty is shown as well as the uncertainties from JES/JER and b-tagging.

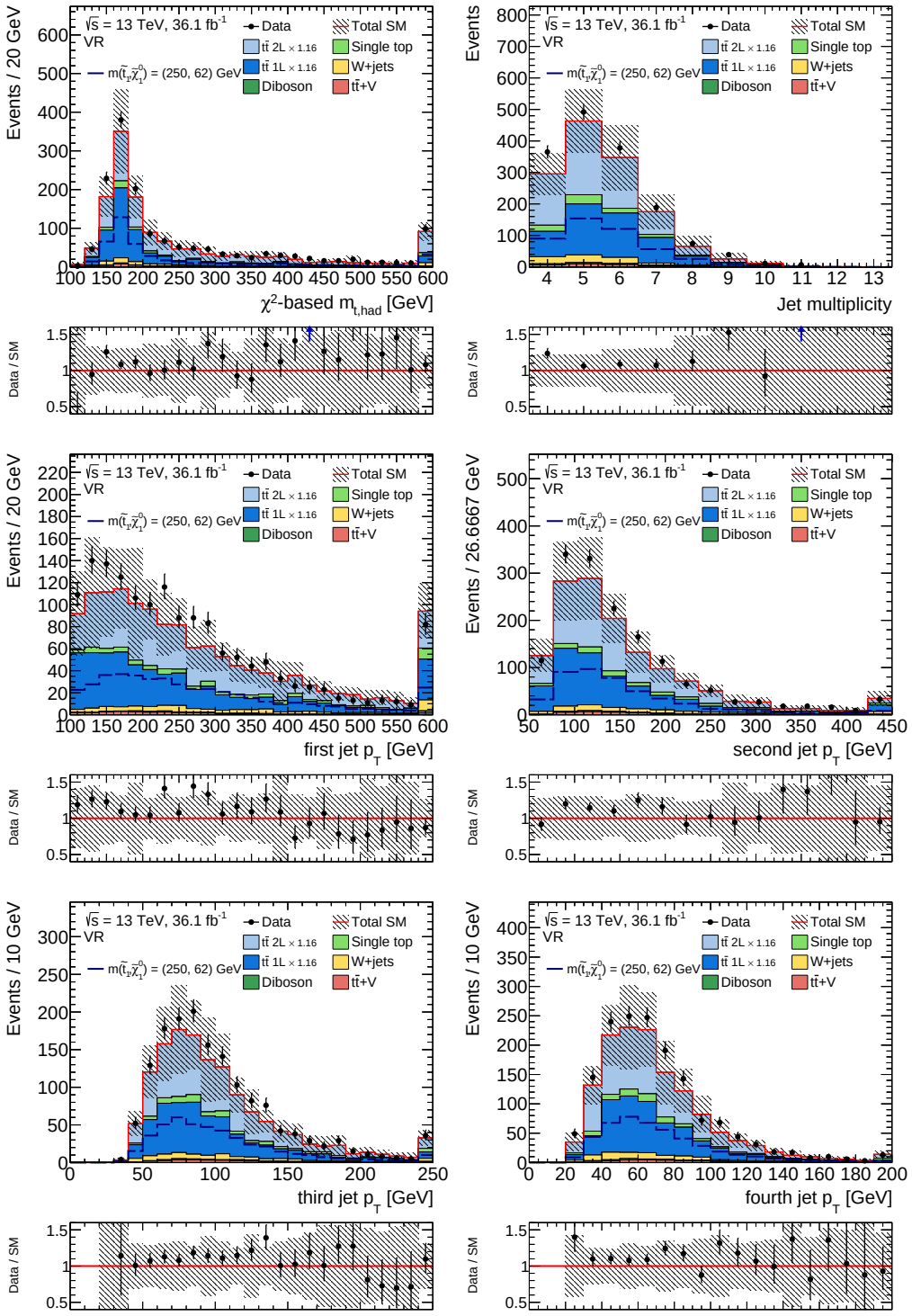

Figure C.26: The χ^2-based $m_{\mathrm{t,had}}$ (top left) and number of jet (top right), and the first (middle left), second (middle right), third (bottom left) and fourth (bottom right) jet p_{T} distribution in the BDT VR in the discovery fit setup. Normalisation factors for semi- and dileptonic $t\bar{t}$ are applied. The statistical uncertainty is shown as well as the uncertainties from JES/JER and b-tagging.

C.7.2 Validation Plots for Low BDT Values

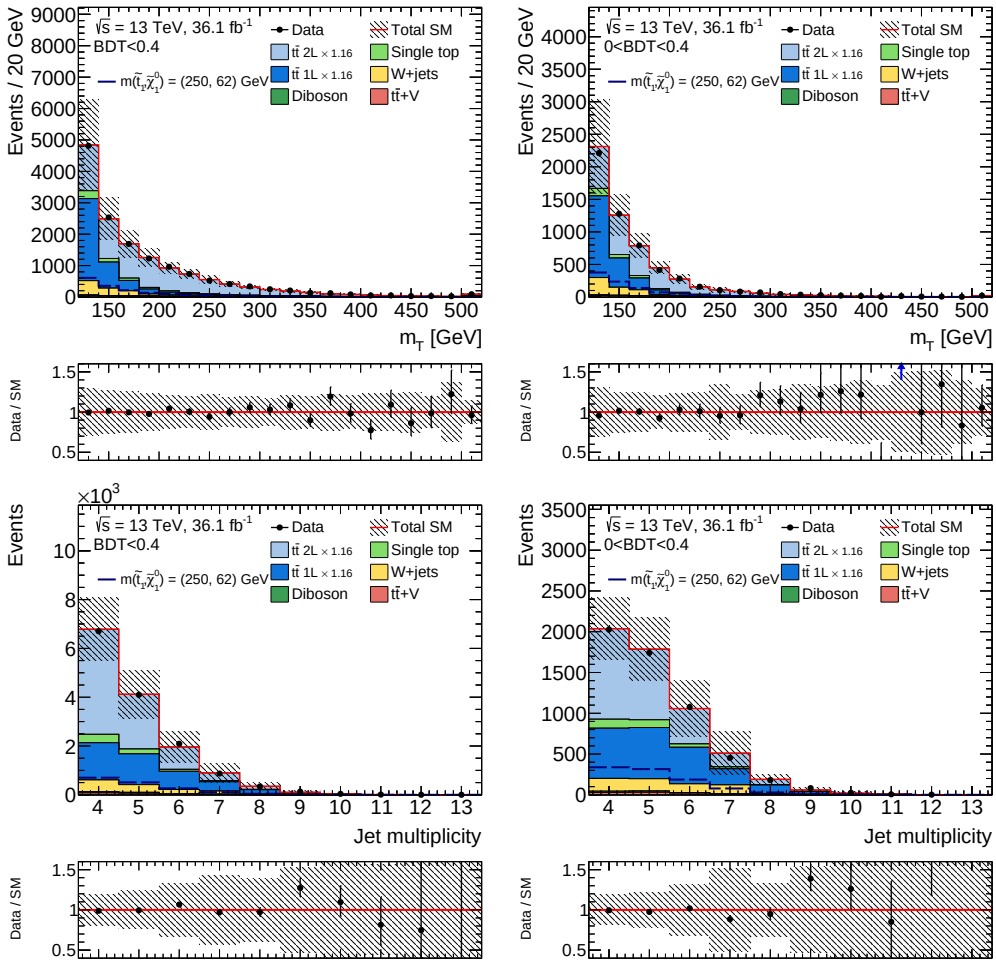

Figure C.27: The m_{T} (top) and number of jet (bottom) distribution in a BDT range of -1 to 0.4 (left) and 0 to 0.4 (right). Normalisation factors for semi- and dileptonic $t\bar{t}$ are applied. The statistical uncertainty is shown as well as the uncertainties from JES/JER and b-tagging.

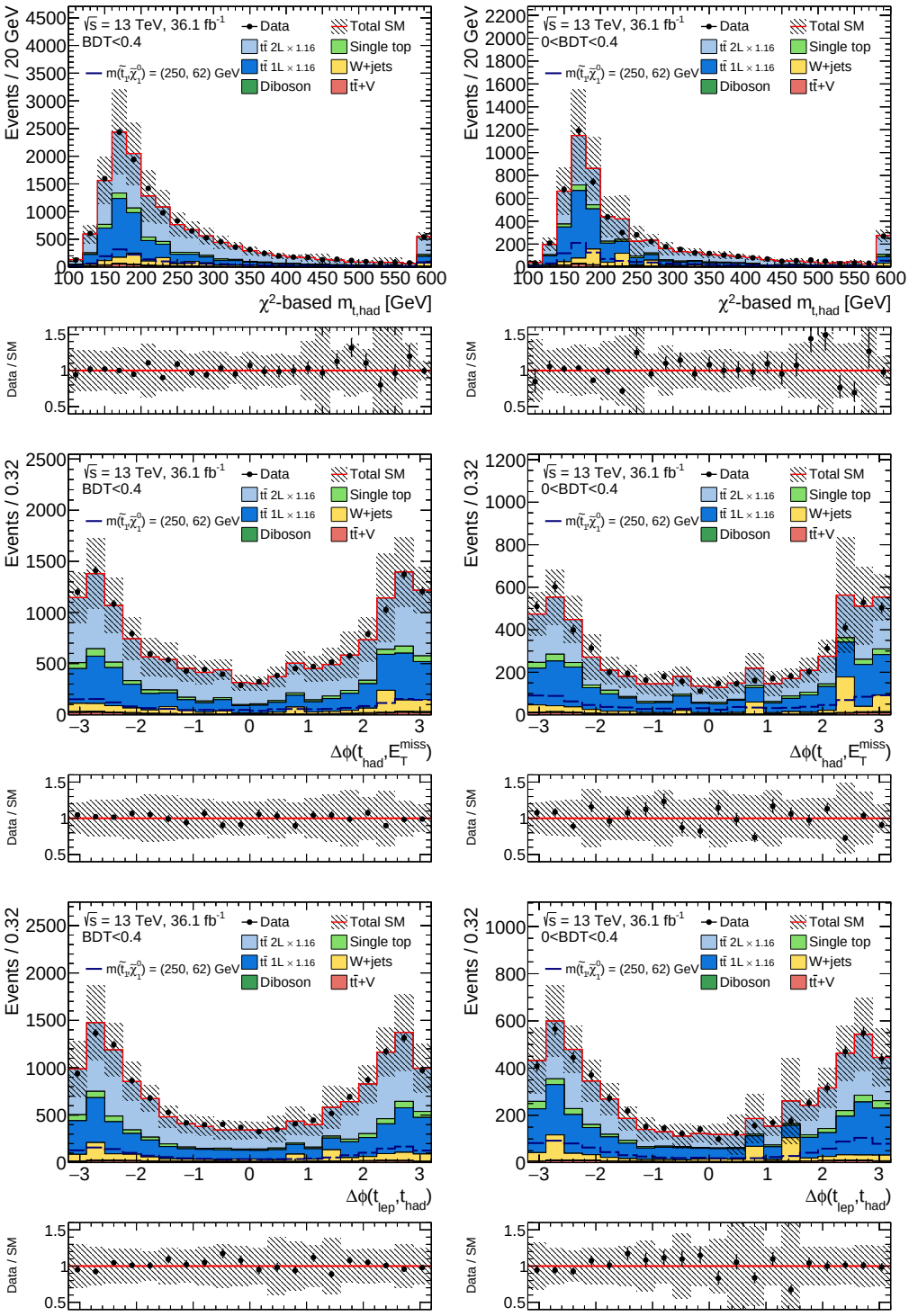

Figure C.28: The χ^2-based $m_{\mathrm{t,had}}$ (top), $\Delta\phi(E_{\mathrm{T}}^{\mathrm{miss}}, t_{\mathrm{had}})$ (middle), and $\Delta\phi(t_{\mathrm{lep}}, t_{\mathrm{had}})$ (bottom) distribution in a BDT range of -1 to 0.4 (left) and 0 to 0.4 (right). Normalisation factors for semi- and dileptonic $t\bar{t}$ are applied. The statistical uncertainty is shown as well as the uncertainties from JES/JER and b-tagging.

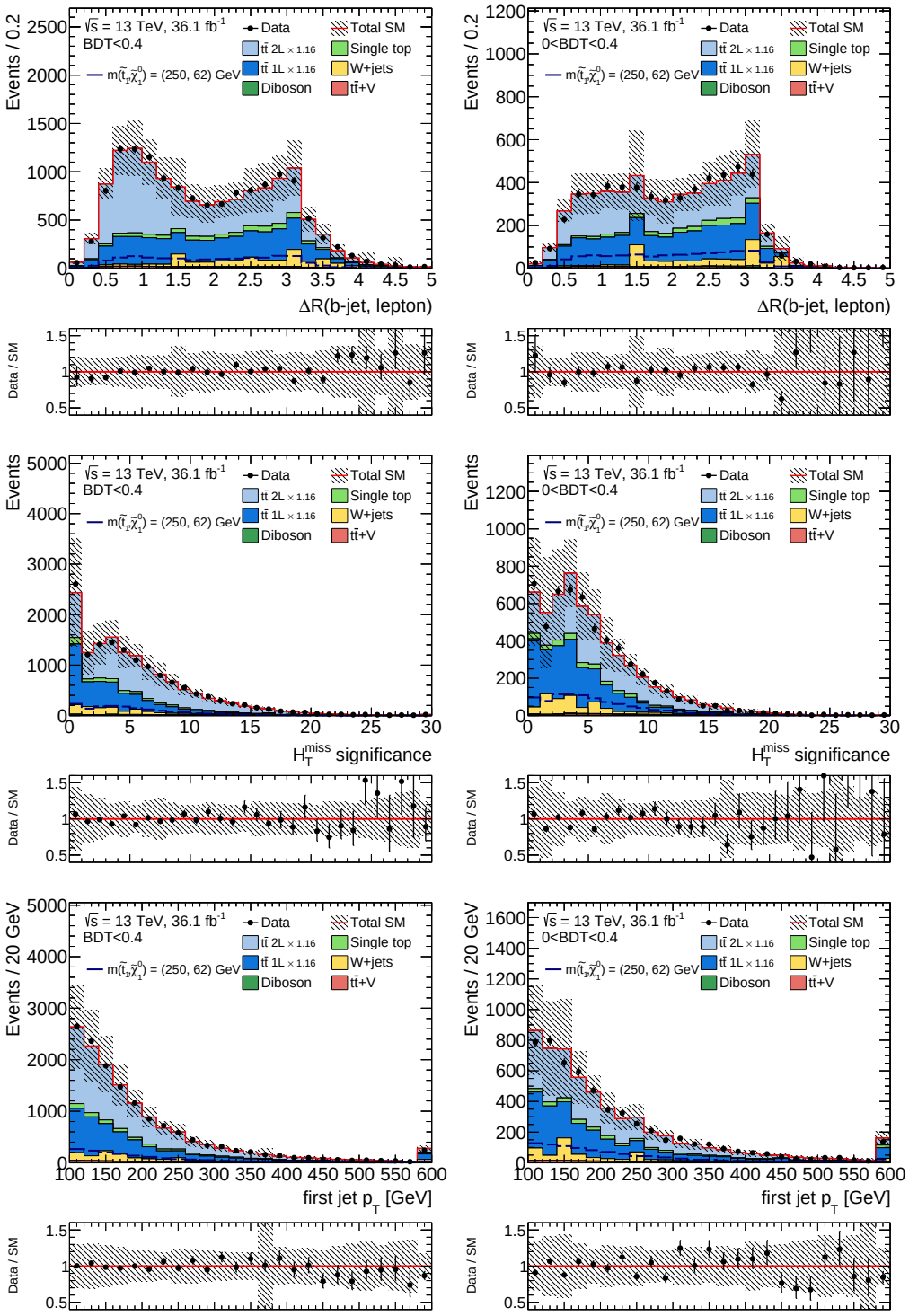

Figure C.29: The $\Delta R(b,\ell)$ (top), $H_{\mathrm{T,sig}}^{\mathrm{miss}}$ (middle) and first jet p_{T} (bottom) distribution in a BDT range of -1 to 0.4 (left) and 0 to 0.4 (right). Normalisation factors for semi- and dileptonic $t\bar{t}$ are applied. The statistical uncertainty is shown as well as the uncertainties from JES/JER and b-tagging.

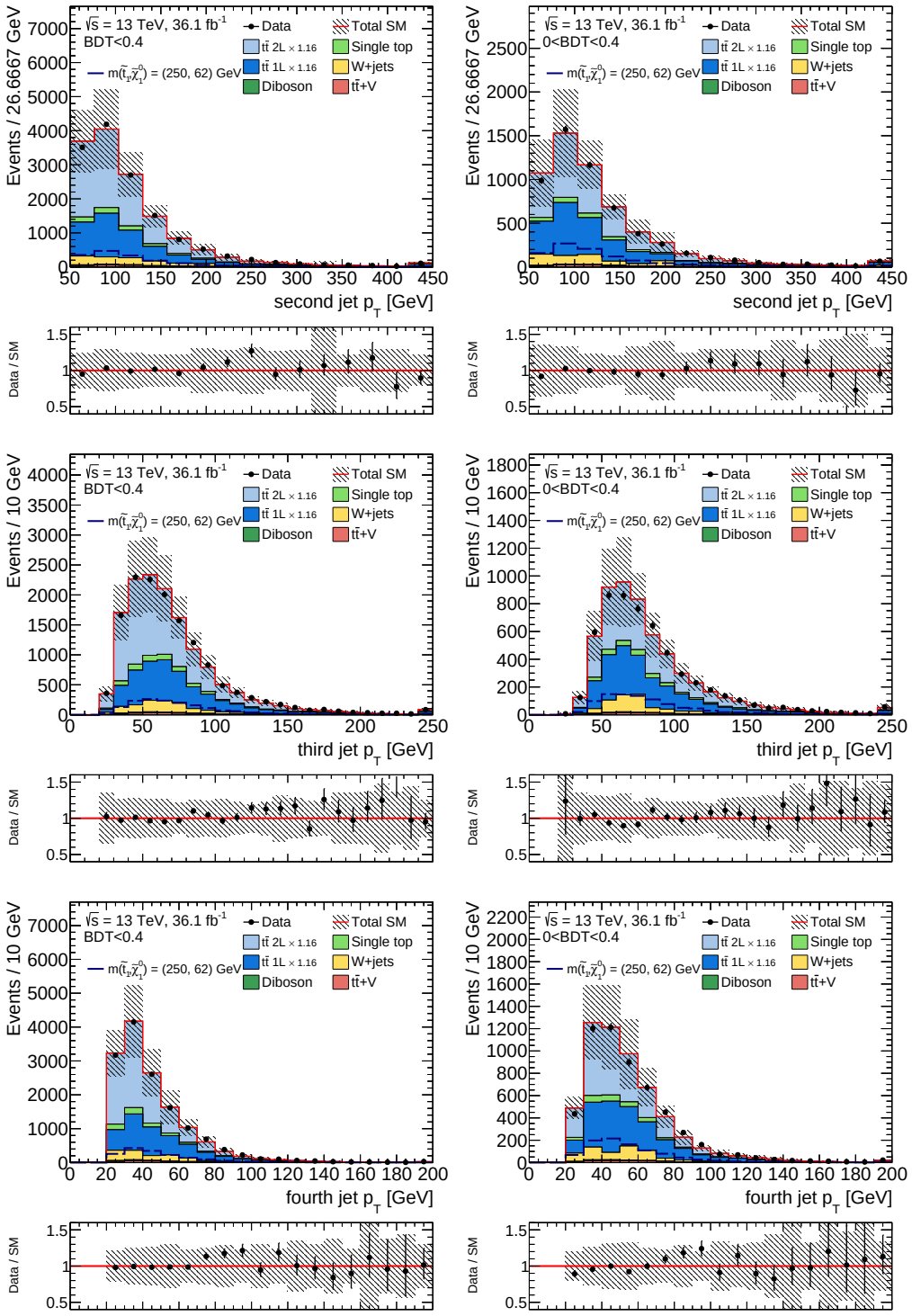

Figure C.30: The second (top), third (middle) and fourth (bottom) jet p_{T} distribution in a BDT range of -1 to 0.4 (left) and 0 to 0.4 (right). Normalisation factors for semi- and dileptonic $t\bar{t}$ are applied. The statistical uncertainty is shown as well as the uncertainties from JES/JER and *b*-tagging.

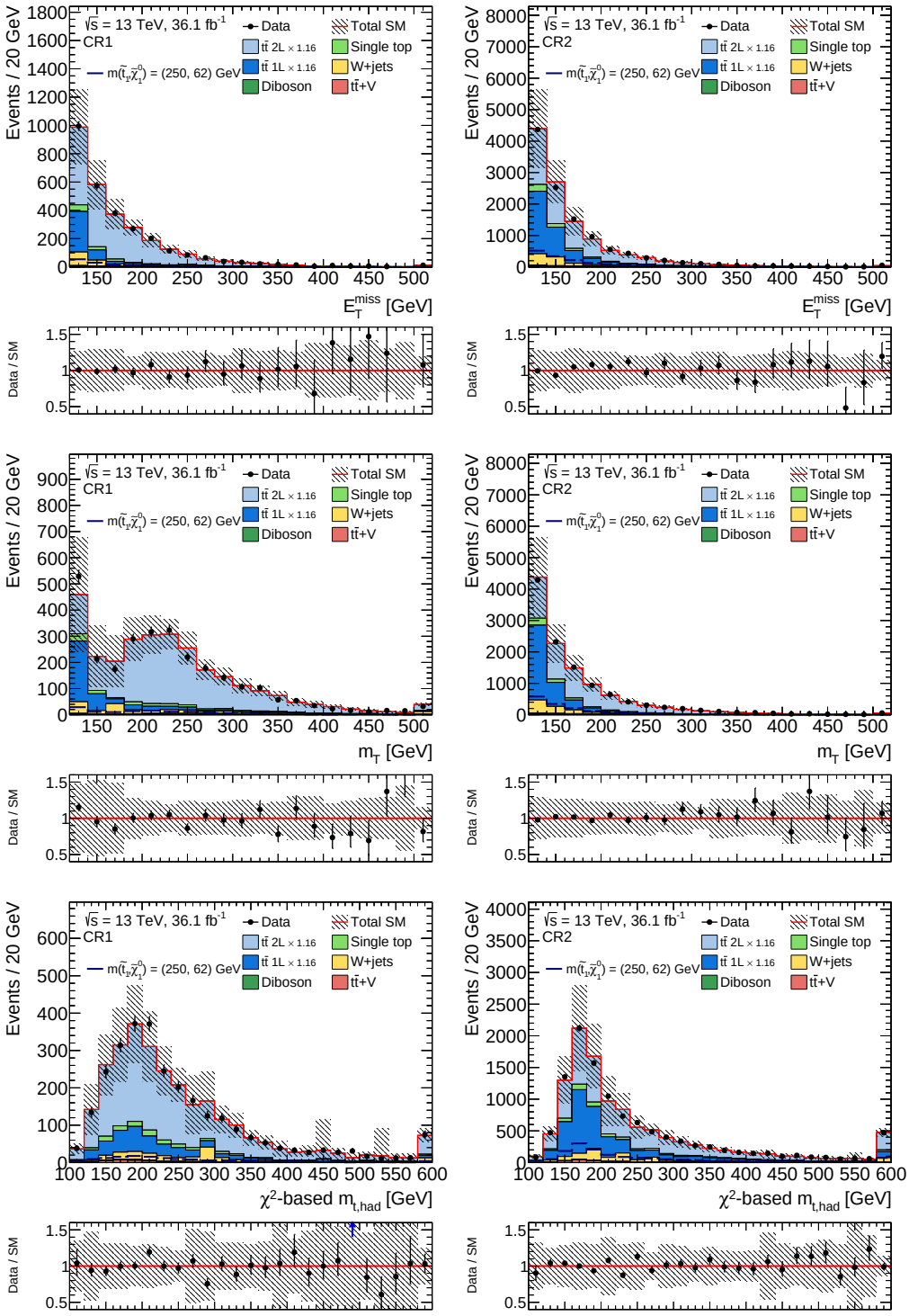

Figure C.31: The $E_{\mathrm{T}}^{\mathrm{miss}}$ (top), m_{T} (middle) and χ^2-based $m_{\mathrm{t,had}}$ (bottom) distribution in the CR1 and CR2 region. Normalisation factors for semi- and dileptonic $t\bar{t}$ are applied. The statistical uncertainty is shown as well as the uncertainties from JES/JER and b-tagging.

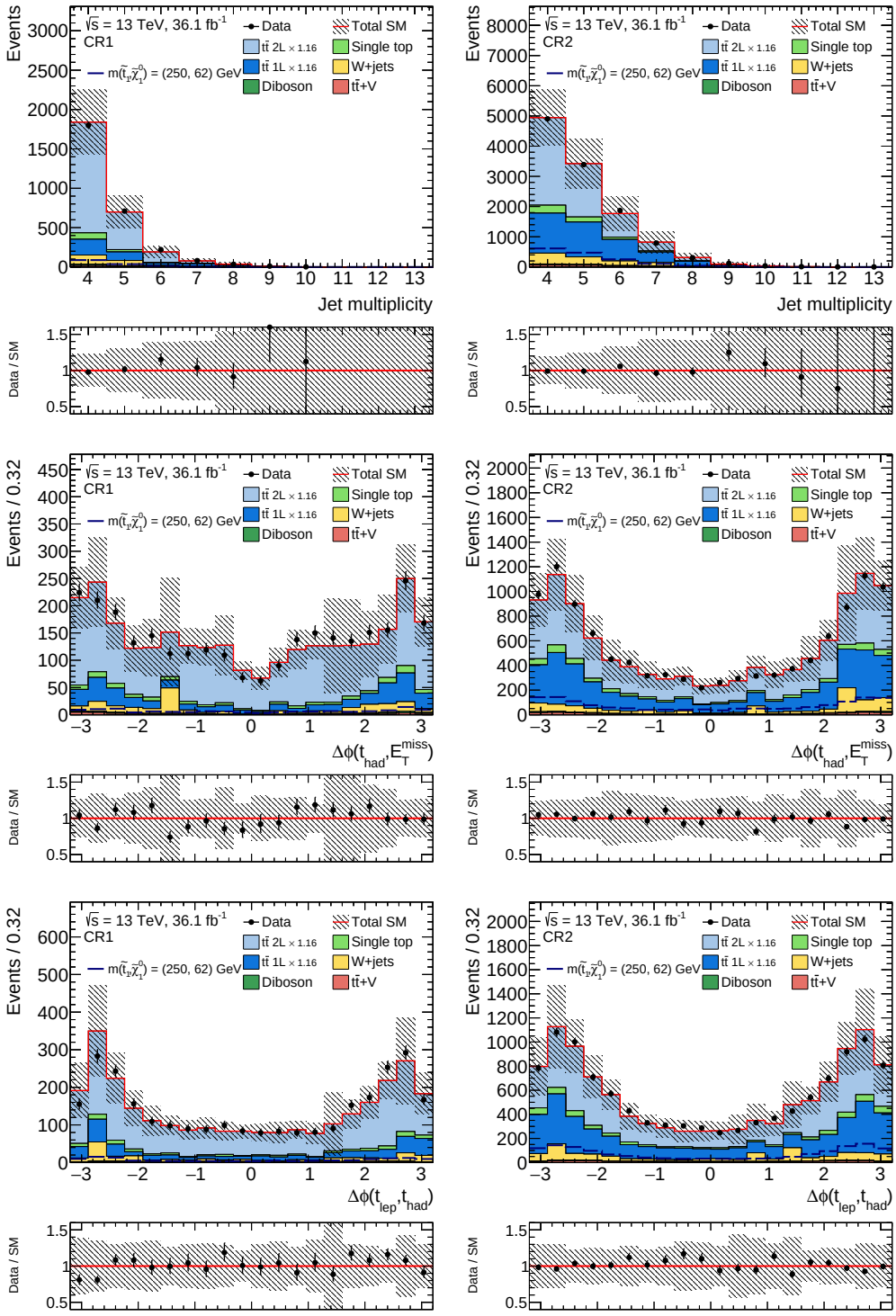

Figure C.32: The number of jet (top), $\Delta\phi(E_{\mathrm{T}}^{\mathrm{miss}}, t_{\mathrm{had}})$ (middle) and $\Delta\phi(t_{\mathrm{lep}}, t_{\mathrm{had}})$ (bottom) distribution in the CR1 and CR2 region. Normalisation factors for semi- and dileptonic $t\bar{t}$ are applied. The statistical uncertainty is shown as well as the uncertainties from JES/JER and b-tagging.

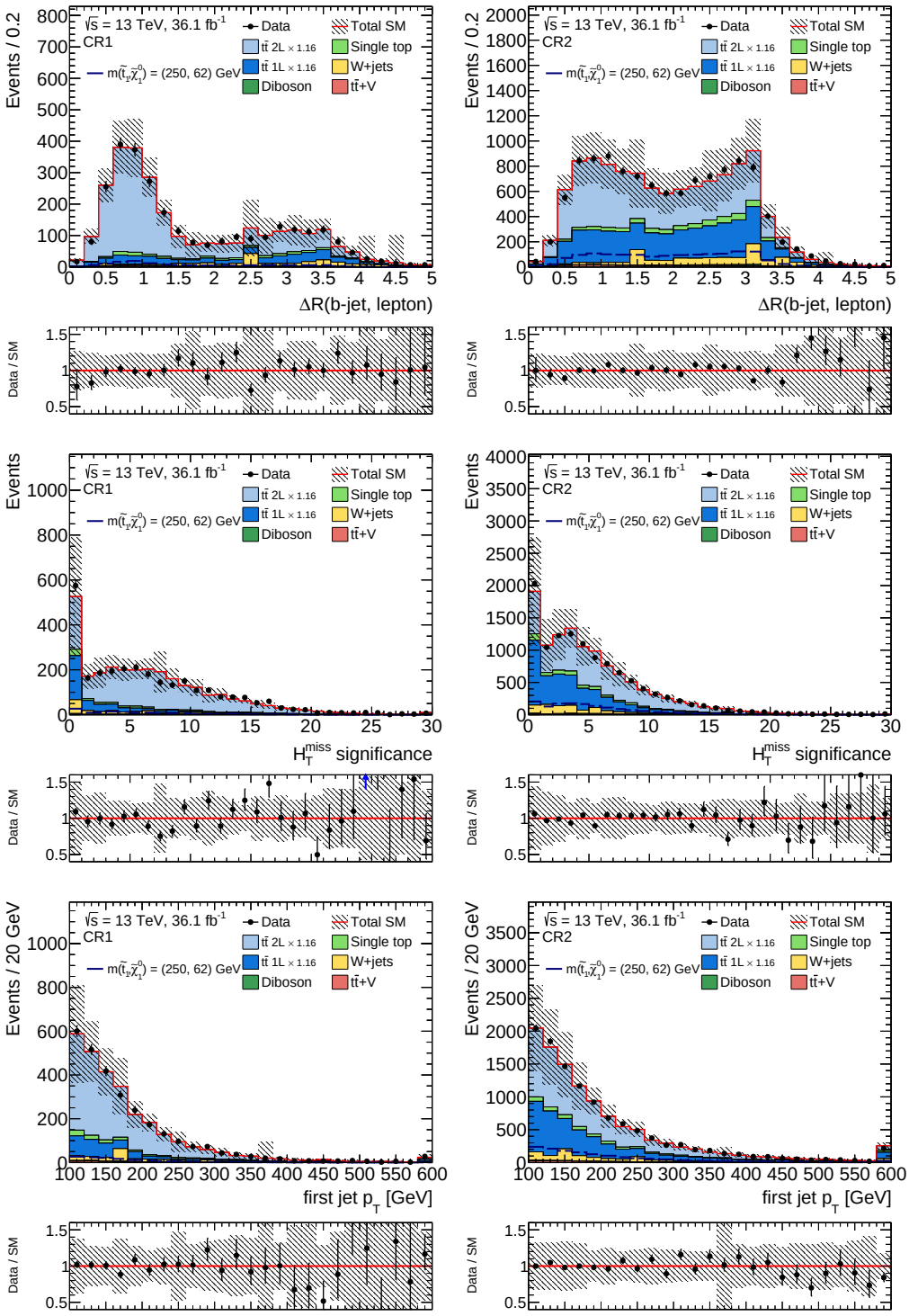

Figure C.33: The $\Delta R(b, \ell)$ (top), $H_{\mathrm{T,sig}}^{\mathrm{miss}}$ (middle) and first jet p_{T} (bottom) distribution in the CR1 and CR2 region. Normalisation factors for semi- and dileptonic $t\bar{t}$ are applied. The statistical uncertainty is shown as well as the uncertainties from JES/JER and b-tagging.

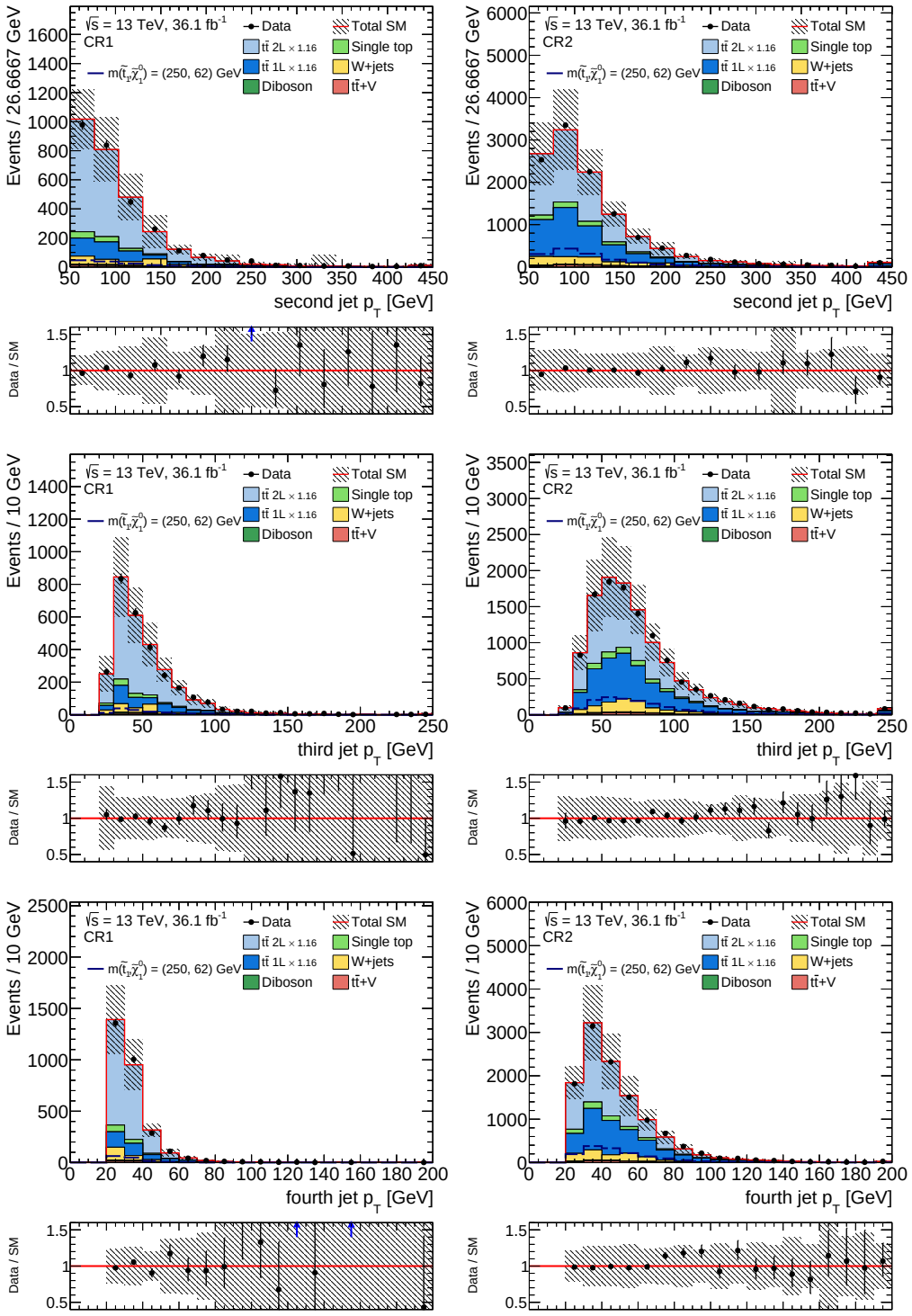

Figure C.34: The second (top), third (middle) and fourth (bottom) jet p_{T} distribution in the CR1 and CR2 region. Normalisation factors for semi- and dileptonic $t\bar{t}$ are applied. The statistical uncertainty is shown as well as the uncertainties from JES/JER and b-tagging.

C.7.3 Profile Plots

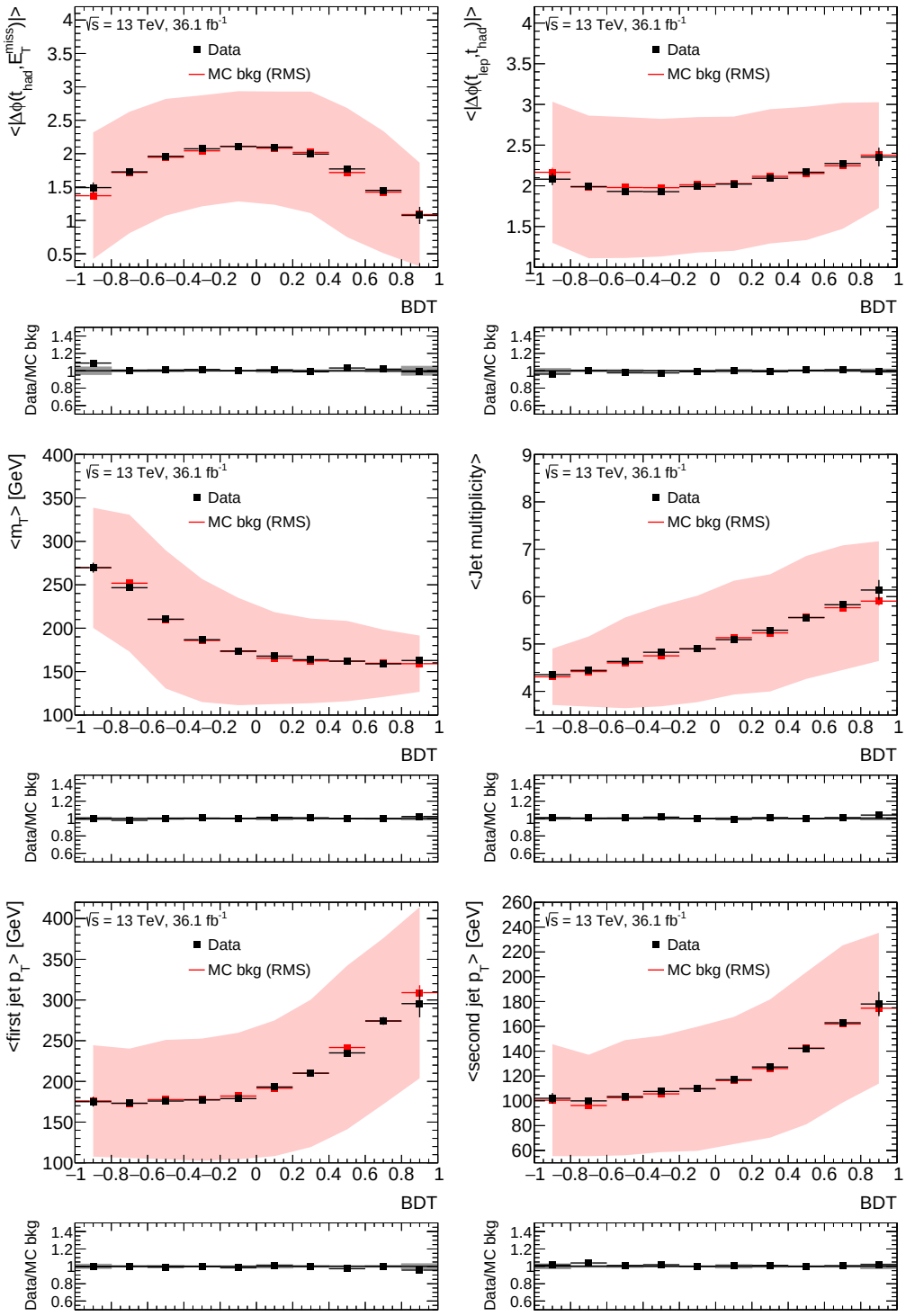

Figure C.35: Average of sensitive variables versus the BDT output.

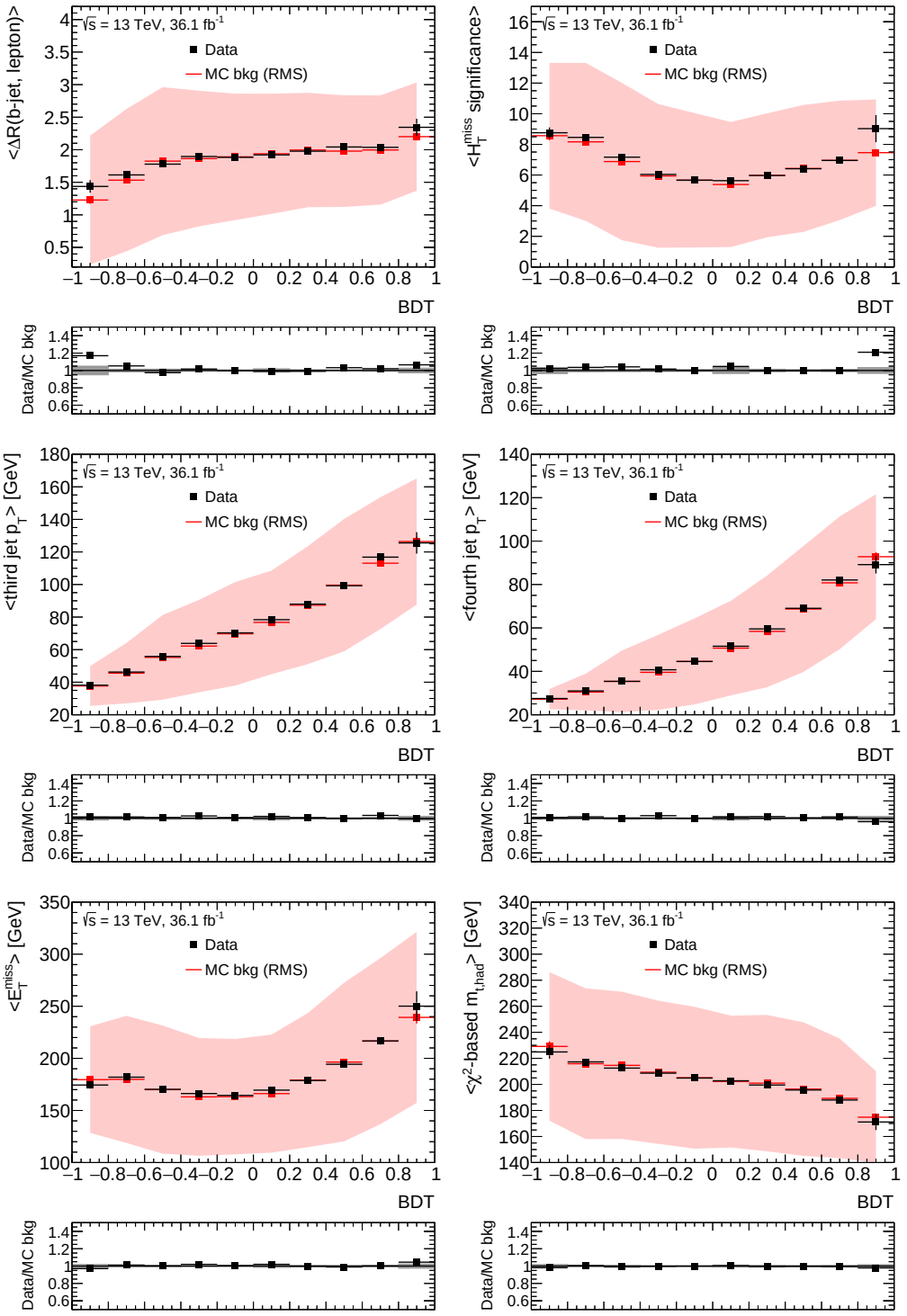

Figure C.36: Average of sensitive variables versus the BDT output.

C.7.4 Correlation Plots for BDT Input Variables

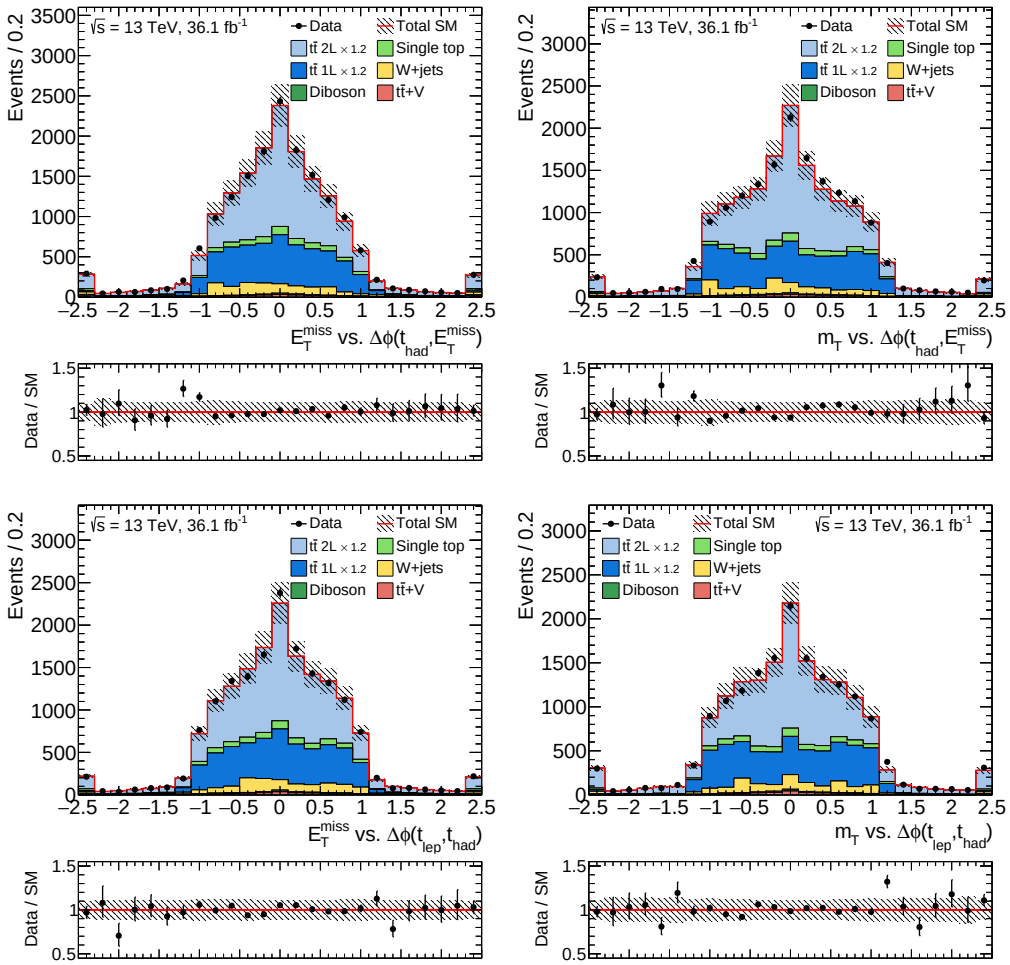

Figure C.37: The correlation of $E_{\mathrm{T}}^{\mathrm{miss}}$ (left) and m_{T} (right) versus the $\Delta\phi(E_{\mathrm{T}}^{\mathrm{miss}}, t_{\mathrm{had}})$ (top) and $\Delta\phi(t_{\mathrm{lep}}, t_{\mathrm{had}})$ (bottom) as described in the beginning of this section. Normalisation factors for semi- and dileptonic $t\bar{t}$ are applied. Only statistical uncertainties are shown.

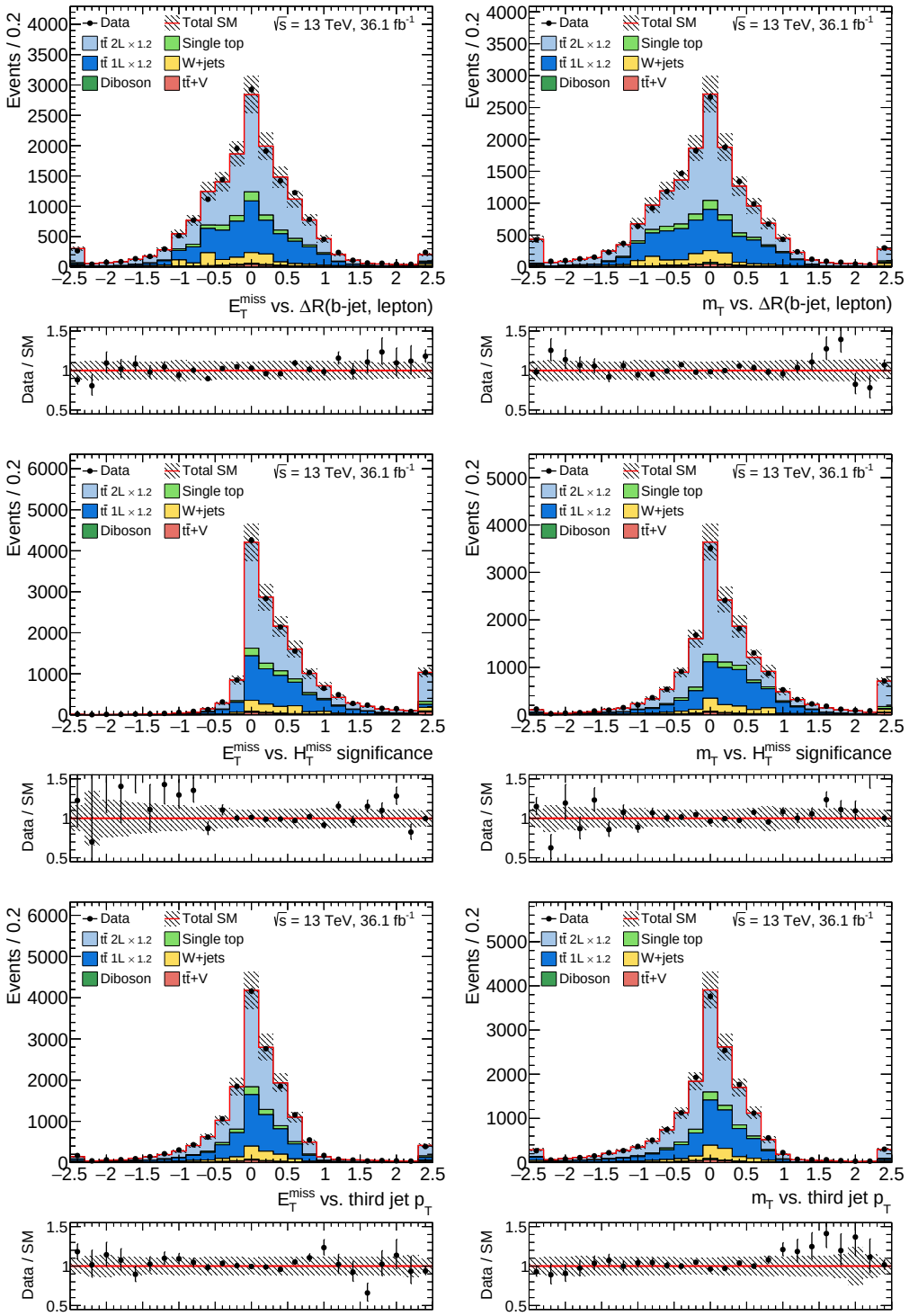

Figure C.38: The correlation of $E_{\mathrm{T}}^{\mathrm{miss}}$ (left) and m_{T} (right) versus the $\Delta R(b, \ell)$ (top), $H_{\mathrm{T,sig}}^{\mathrm{miss}}$ (middle) and third jet p_{T} (bottom) as described in the beginning of this section. Normalisation factors for semi- and dileptonic $t\bar{t}$ are applied. Only statistical uncertainties are shown.

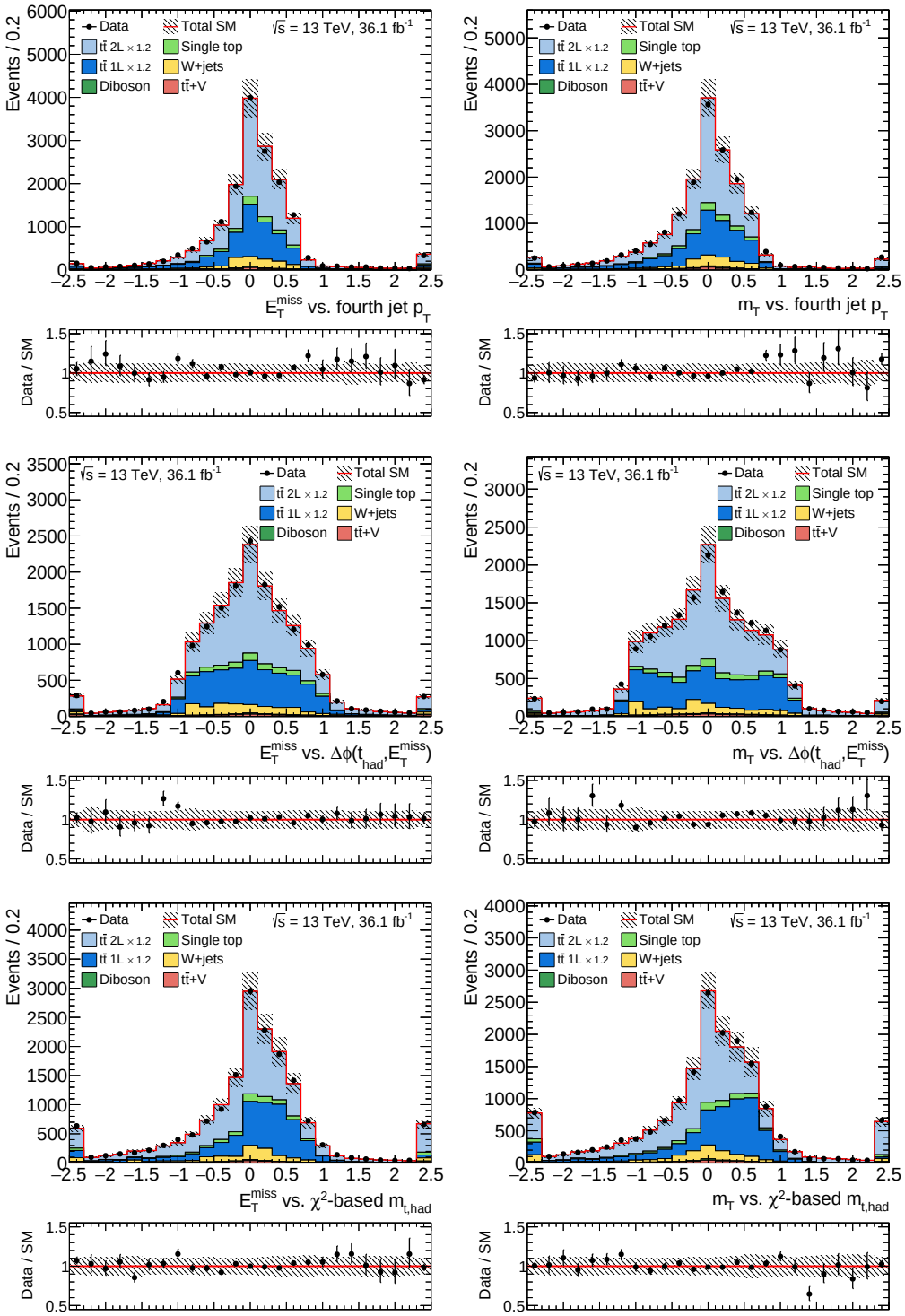

Figure C.39: The correlation of $E_{\mathrm{T}}^{\mathrm{miss}}$ (left) and m_{T} (right) versus the fourth jet p_{T} (top), $\Delta\phi(E_{\mathrm{T}}^{\mathrm{miss}}, t_{\mathrm{had}})$ (middle) and χ^2-based $m_{\mathrm{t,had}}$ (bottom) as described in the beginning of this section. Normalisation factors for semi- and dileptonic $t\bar{t}$ are applied. Only statistical uncertainties are shown.

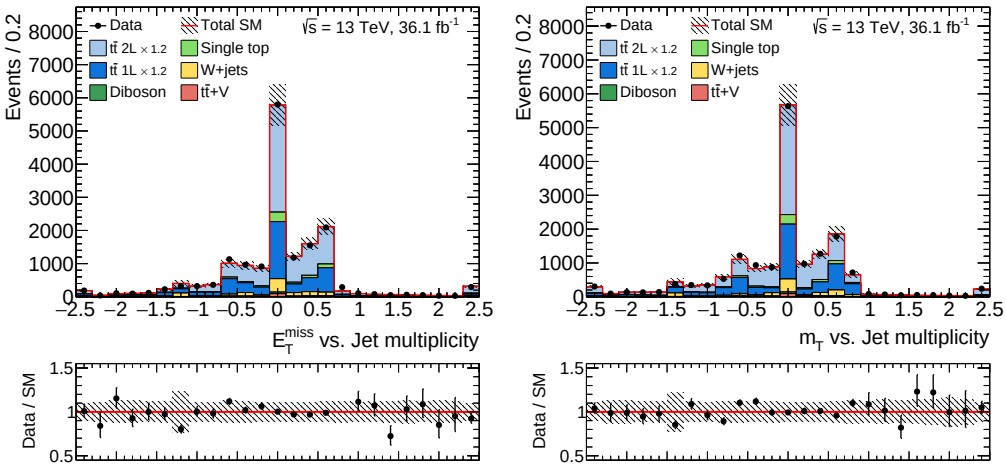

Figure C.40: The correlation of $E_{\mathrm{T}}^{\mathrm{miss}}$ (left) and m_{T} (right) versus the number of jets as described in the beginning of this section. Normalisation factors for semi- and dileptonic $t\bar{t}$ are applied. Only statistical uncertainties are shown.

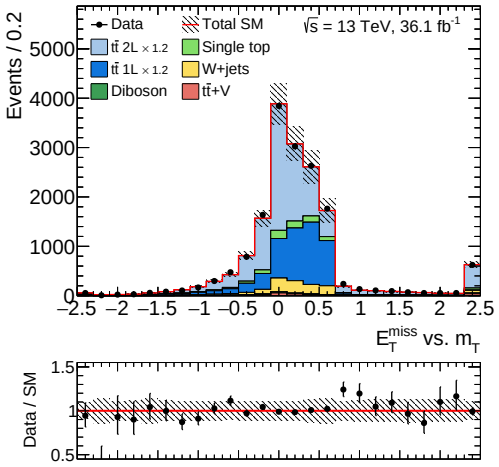

Figure C.41: The correlation of $E_{\mathrm{T}}^{\mathrm{miss}}$ versus m_{T} (right) as described in the beginning of this section. Normalisation factors for semi- and dileptonic $t\bar{t}$ are applied. Only statistical uncertainties are shown.

C.8 JES Dependence of the BDT Fit

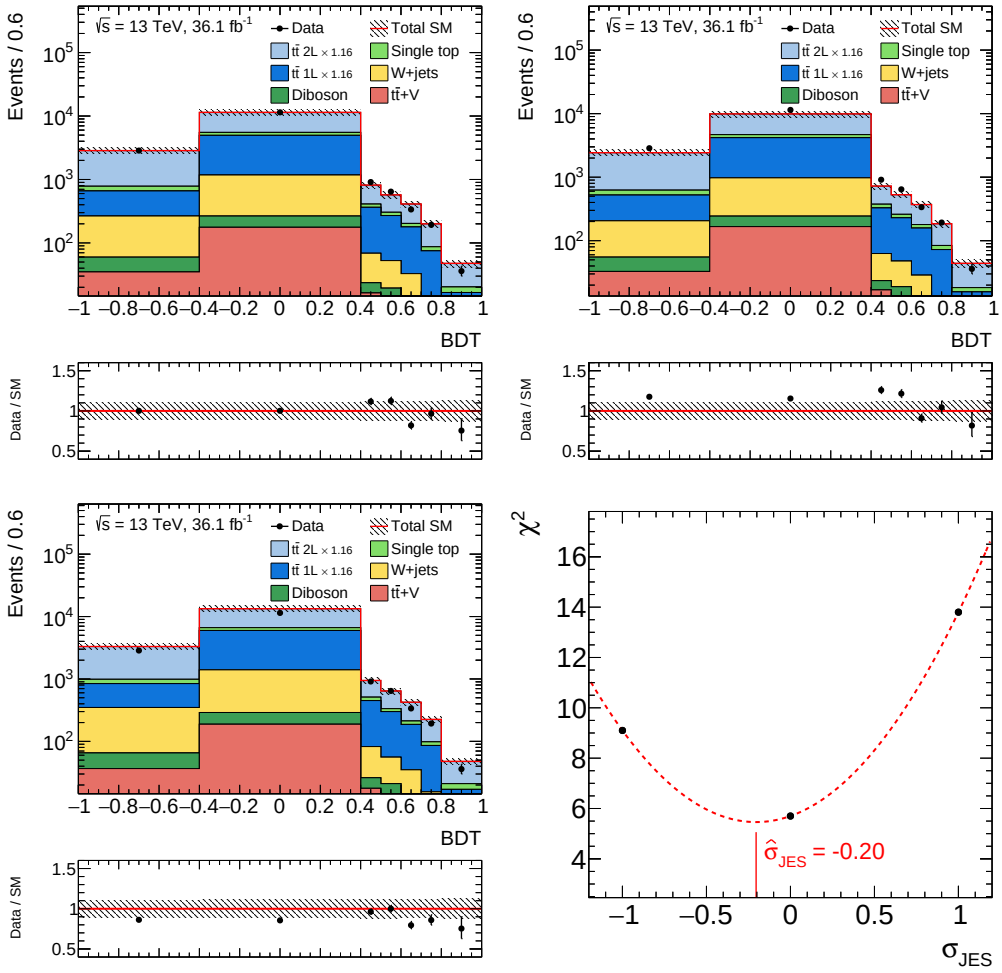

Figure C.42: BDT distribution using the nominal samples (top left) and using for all samples the up (top right) and down (bottom left) variation for the first jet energy scale component. The uncertainty band includes only statistical uncertainty in the MC statistics and the statistical uncertainty in the normalisation factors for $t\bar{t}$.

C.9 Results for Low Mass BDT

The same validation was done for the new retrained BDT as for the one discussed (BDT_med). Overall, a good agreement between the MC prediction and the measured data can be seen for all distributions. Some example distributions are shown in the CR (Figure C.43) and VR (Figure C.44) bin as well as the correlation plots (Figure C.45 and C.46).

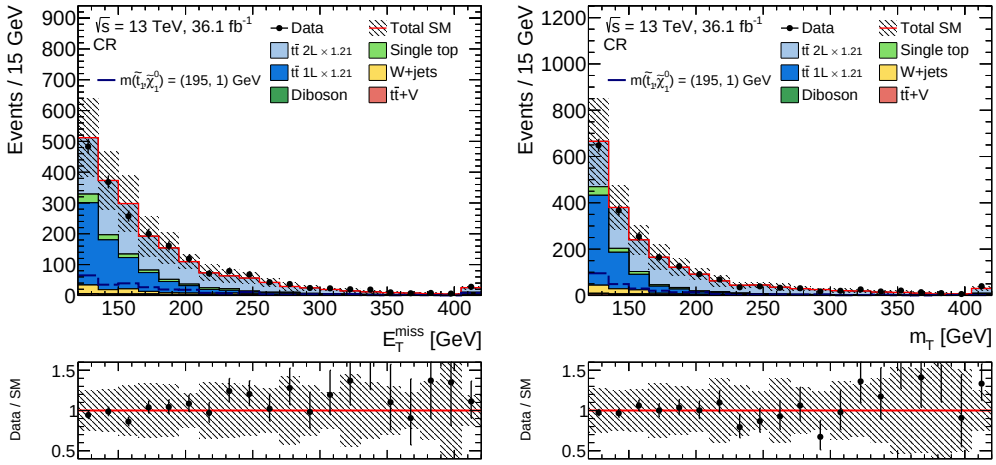

Figure C.43: The $E_{\mathrm{T}}^{\mathrm{miss}}$ (left) and m_{T} (right) distribution for the BDT CR. The normalisation factors for $t\bar{t}$ is applied as determined in the simultaneous fit. The statistical uncertainty is shown as well as the uncertainties coming from JES/JER and b-tagging.

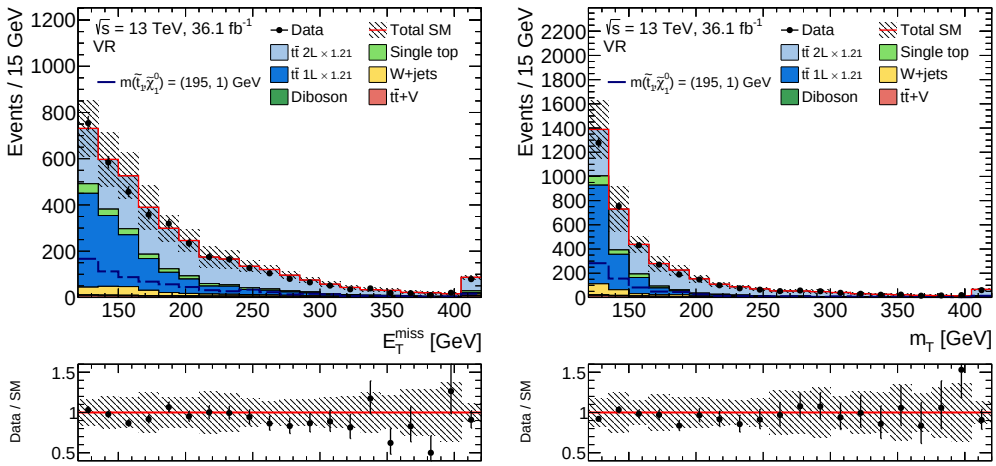

Figure C.44: The $E_{\mathrm{T}}^{\mathrm{miss}}$ (left) and m_{T} (right) distribution for the BDT VR. The normalisation factors for $t\bar{t}$ is applied as determined in the simultaneous fit. The statistical uncertainty is shown as well as the uncertainties coming from JES/JER and b-tagging.

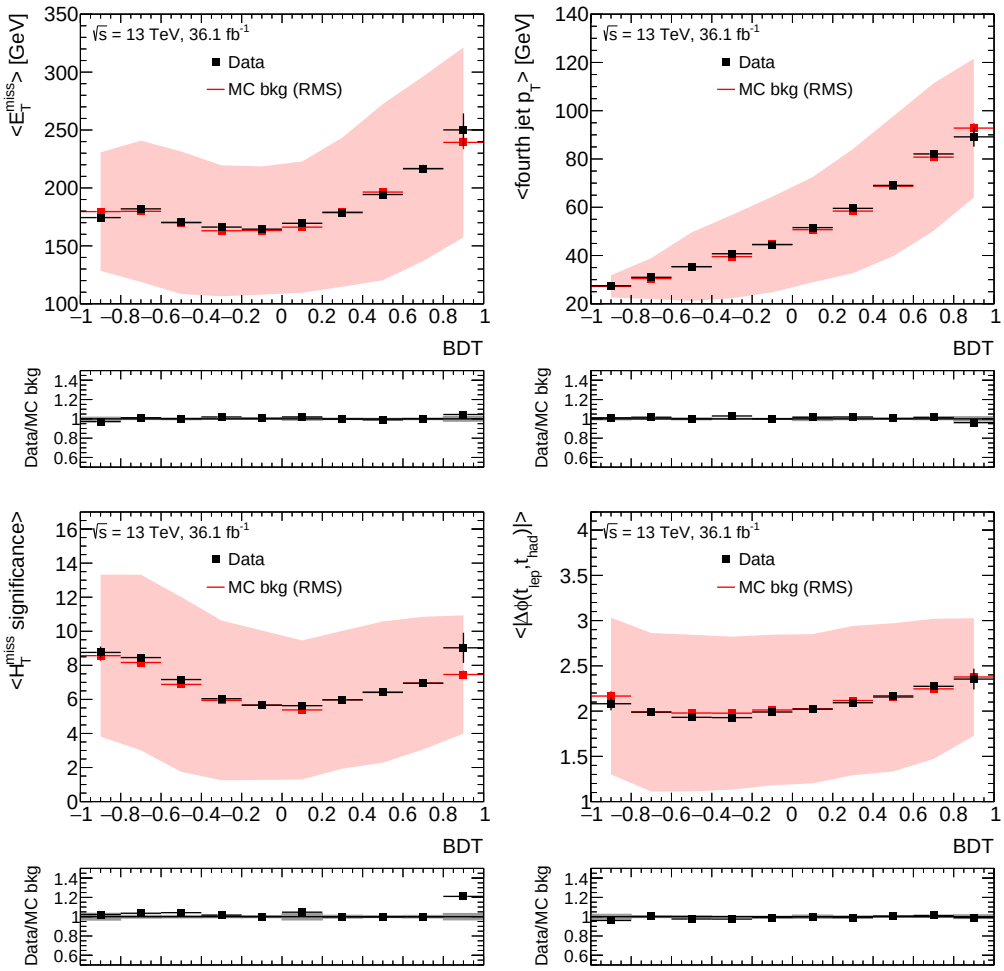

Figure C.45: Average of $E_{\mathrm{T}}^{\mathrm{miss}}$ (top left), third jet p_{T} (top right), $H_{\mathrm{T,sig}}^{\mathrm{miss}}$ (bottom left) and $\Delta\phi(t,\bar{t})$ (bottom right) versus the BDT distribution.

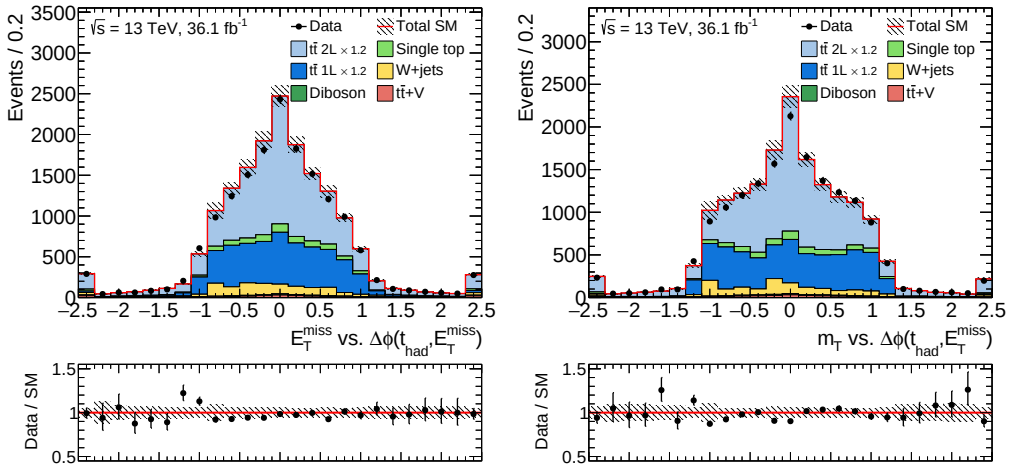

Figure C.46: The correlation of $E_{\mathrm{T}}^{\mathrm{miss}}$ (left) and m_{T} (right) versus the $\Delta\phi(E_{\mathrm{T}}^{\mathrm{miss}}, t_{\mathrm{had}})$. The normalisation factors for $t\bar{t}$ is applied, only statistical uncertainties are shown

Table C.1: Observed events and expected yields for all background processes in the control and validation region with and without the normalisation factors applied.

Region	CR	VR
Observed events	2031	3693
Total background events	2031 ± 45	3877 ± 265
$t\bar{t}$ events	1777 ± 78	3357 ± 316
$t\bar{t}$ + V events	34 ± 17	71 ± 35
Single top events	104 ± 34	205 ± 66
W + jets events	102 ± 30	212 ± 74
Diboson events	14.6 ± 7.7	31.6 ± 16.9
MC exp. background events	1720	3287
MC exp. $t\bar{t}$ events	1465	2767
MC exp. $t\bar{t}$ + V events	34	71
MC exp. single top events	104	206
MC exp. W + jets events	102	212
MC exp. diboson events	14.6	31.6

The observed and expected yields for all background processes are given in Table C.1 and C.2 for the control and validation region as well as for the various signal region bins.

Table C.2: Observed events and expected yields for all background processes in the signal region bins with and without the normalisation factors applied.

Region	SR1	SR2	SR3	SR4	SR5	SR6
Observed events	65	54	34	19	32	11
Total bkg events	62.7 ± 8.5	41.4 ± 5.7	38.4 ± 6.2	32.5 ± 5.3	25.5 ± 3.8	12.3 ± 2.5
$t\bar{t}$ events	54.4 ± 8.7	34.9 ± 5.7	34.0 ± 6.1	28.7 ± 5.2	21.4 ± 3.8	9.9 ± 2.2
$t\bar{t}$ + V events	1.0 ± 0.6	0.9 ± 0.5	0.5 ± 0.3	0.6 ± 0.3	0.5 ± 0.3	0.2 ± 0.1
Single top events	4.2 ± 1.7	2.3 ± 0.8	2.1 ± 0.7	2.0 ± 0.9	1.6 ± 0.6	1.2 ± 0.4
W + jets events	2.7 ± 1.5	2.8 ± 1.6	1.6 ± 1.0	0.9 ± 0.6	1.7 ± 1.2	0.8 ± 0.7
Diboson events	0.4 ± 0.3	0.4 ± 0.3	$0.2^{+0.3}_{-0.2}$	0.3 ± 0.3	0.3 ± 0.2	0.2 ± 0.1
MC exp. bkg events	53.2	35.3	32.4	27.5	21.8	10.5
MC exp. $t\bar{t}$ events	44.8	28.7	27.9	23.7	17.6	8.1
MC exp. $t\bar{t}$ + V events	1.02	0.93	0.54	0.56	0.50	0.19
MC exp. single top events	4.2	2.3	2.1	2.0	1.6	1.2
MC exp. W + jets events	2.8	2.8	1.6	0.9	1.8	0.8
MC exp. diboson events	0.41	0.43	0.20	0.31	0.28	0.22

Bibliography

[1] ATLAS Collaboration, *Search for top squarks in final states with one isolated lepton, jets, and missing transverse momentum in $\sqrt{s}$ = 13 TeV pp collisions with the ATLAS detector*, Phys. Rev. D **94** (2016) p. 052009, arXiv: 1606.03903 [hep-ex].

[2] ATLAS Collaboration, *Charged-particle distributions in $\sqrt{s}$ = 13 TeV pp interactions measured with the ATLAS detector at the LHC*, Phys. Lett. B **758** (2016) p. 67, arXiv: 1602.01633 [hep-ex].

[3] ATLAS Collaboration, *Search for pair production of vector-like top quarks in events with one lepton, jets, and missing transverse momentum in $\sqrt{s}$ = 13 TeV pp collisions with the ATLAS detector*, JHEP **08** (2017) p. 052, arXiv: 1705.10751 [hep-ex].

[4] ATLAS Collaboration, *Charged-particle distributions at low transverse momentum in $\sqrt{s}$ = 13 TeV pp interactions measured with the ATLAS detector at the LHC*, Eur. Phys. J. C **76** (2016) p. 502, arXiv: 1606.01133 [hep-ex].

[5] ATLAS Collaboration, *Search for top-squark pair production in final states with one lepton, jets, and missing transverse momentum using 36 fb^{-1} of $\sqrt{s}$ = 13 TeV pp collision data with the ATLAS detector*, JHEP **06** (2018) p. 108, arXiv: 1711.11520 [hep-ex].

[6] ATLAS Collaboration, *Track Reconstruction Performance of the ATLAS Inner Detector at $\sqrt{s}$ = 13 TeV*, ATL-PHYS-PUB-2015-018, 2015, URL: http://cds.cern.ch/record/2037683.

[7] ATLAS Collaboration, *A method for the construction of strongly reduced representations of ATLAS experimental uncertainties and the application thereof to the jet energy scale*, ATL-PHYS-PUB-2015-014, 2015, URL: https://cds.cern.ch/record/2037436.

[8] S. L. Glashow, *Partial Symmetries of Weak Interactions*, Nucl. Phys. **22** (1961) p. 579.

[9] S. Weinberg, *A Model of Leptons*, Phys. Rev. Lett. **19** (1967) p. 1264.

[10] A. Salam, *Gauge Unification of Fundamental Forces*, Rev. Mod. Phys. **52** (1980) p. 525.

[11] A. Salam and J. C. Ward, *Weak and electromagnetic interactions*, Nuovo Cim. **11** (1959) p. 568.

[12] M. E. Peskin and D. V. Schroeder, *An Introduction to quantum field theory*, Addison-Wesley, 1995, ISBN: 9780201503975, 0201503972.

[13] A. Zee, *Quantum field theory in a nutshell*, 2003, ISBN: 0691140340, 9780691140346.

[14] ATLAS Collaboration, *Observation of a new particle in the search for the Standard Model Higgs boson with the ATLAS detector at the LHC*, Phys. Lett. B **716** (2012) p. 1, arXiv: 1207.7214 [hep-ex].

[15] CMS Collaboration,
Observation of a new boson at a mass of 125 GeV with the CMS experiment at the LHC,
Phys. Lett. B **716** (2012) p. 30, arXiv: 1207.7235 [hep-ex].
[16] C. Patrignani et al., *Review of Particle Physics*, Chin. Phys. C **40** (2016) p. 100001.
[17] J. Goldstone, *Field Theories with Superconductor Solutions*,
Nuovo Cim. **19** (1961) p. 154.
[18] J. Goldstone, A. Salam, and S. Weinberg, *Broken Symmetries*,
Phys. Rev. **127** (1962) p. 965.
[19] SLAC Collaboration, *Discovery of a Narrow Resonance in e^+e^- Annihilation*,
Phys. Rev. Lett. **33** (1974) p. 1406.
[20] MIT Collaboration, *Experimental Observation of a Heavy Particle J*,
Phys. Rev. Lett. **33** (1974) p. 1404.
[21] M. Kobayashi and T. Maskawa,
CP Violation in the Renormalizable Theory of Weak Interaction,
Prog. Theor. Phys. **49** (1973) p. 652.
[22] Perl, M. L., et al., *Evidence for Anomalous Lepton Production in $e^+ - e^-$ Annihilation*,
Phys. Rev. Lett. **35** (1975) p. 1489.
[23] Herb, S. W., et al.,
Observation of a Dimuon Resonance at 9.5 GeV in 400-GeV Proton-Nucleus Collisions,
Phys. Rev. Lett. **39** (1977) p. 252.
[24] UA1 Collaboration, *Experimental observation of isolated large transverse energy electrons with associated missing energy at $\sqrt{s}$=540 GeV*,
Physics Letters B **122** (1983) p. 103, ISSN: 0370-2693.
[25] D0 Collaboration, *Observation of the Top Quark*, Phys. Rev. Lett. **74** (1995) p. 2632.
[26] CDF Collaboration, *Observation of Top Quark Production in $\overline{p}p$ Collisions with the Collider Detector at Fermilab*, Phys. Rev. Lett. **74** (1995) p. 2626.
[27] M. Baak et al., *Results for the Global Electroweak Standard Model Fit*, 2017, URL:
http://project-gfitter.web.cern.ch/project-gfitter/Standard_Model/.
[28] ATLAS Collaboration, *Measurement of the Higgs boson mass in the $H \to ZZ^* \to 4\ell$ and $H \to \gamma\gamma$ channels with $\sqrt{s}$=13TeV pp collisions using the ATLAS detector*, 2017,
URL: http://cds.cern.ch/record/2273853.
[29] ATLAS Collaboration, *Summary plots from the ATLAS Standard Model physics group*,
2017, URL: https:
//atlas.web.cern.ch/Atlas/GROUPS/PHYSICS/CombinedSummaryPlots/SM/.
[30] Y. Fukuda et al., *Evidence for oscillation of atmospheric neutrinos*,
Phys. Rev. Lett. **81** (1998) p. 1562, arXiv: hep-ex/9807003 [hep-ex].
[31] Planck Collaboration, *Planck 2015 results. XIII. Cosmological parameters*,
Astron. Astrophys. **594** (2016) A13, arXiv: 1502.01589 [astro-ph.CO].
[32] S. P. Martin, *A Supersymmetry primer*,
(1997), [Adv. Ser. Direct. High Energy Phys.18,1(1998)],
arXiv: hep-ph/9709356 [hep-ph].
[33] R. Haag, J. T. Łopuszański, and M. Sohnius,
"All possible generators of supersymmetries of the S-matrix",
Dynamical Groups and Spectrum Generating Algebras, World Scientific, 1988 p. 987.
[34] S. Coleman and J. Mandula, "All possible symmetries of the S matrix",
Dynamical Groups and Spectrum Generating Algebras, World Scientific, 1988 p. 469.

[35] Super-Kamiokande, *Search for proton decay via $p \to e^+\pi^0$ and $p \to \mu^+\pi^0$ in 0.31 megaton - years exposure of the Super-Kamiokande water Cherenkov detector*, Phys. Rev. D **95** (2017) p. 012004, arXiv: 1610.03597 [hep-ex].

[36] J. Alwall, P. Schuster, and N. Toro, *Simplified Models for a First Characterization of New Physics at the LHC*, Phys. Rev. D **79** (2009) p. 075020, arXiv: 0810.3921 [hep-ph].

[37] D. Alves, *Simplified Models for LHC New Physics Searches*, J. Phys. G **39** (2012) p. 105005, ed. by N. Arkani-Hamed et al., arXiv: 1105.2838 [hep-ph].

[38] C. Borschensky et al., *Squark and gluino production cross sections in pp collisions at $\sqrt{s}$ = 13, 14, 33 and 100 TeV*, Eur. Phys. J. C **74** (2014) p. 3174, arXiv: 1407.5066 [hep-ph].

[39] M. Papucci, J. T. Ruderman, and A. Weiler, *Natural SUSY Endures*, JHEP **09** (2012) p. 035, arXiv: 1110.6926 [hep-ph].

[40] A. Djouadi et al., "The Minimal supersymmetric standard model: Group summary report", *GDR (Groupement De Recherche) - Supersymetrie Montpellier, France, April 15-17, 1998*, 1998, arXiv: hep-ph/9901246 [hep-ph].

[41] C. F. Berger et al., *Supersymmetry Without Prejudice*, JHEP **02** (2009) p. 023, arXiv: 0812.0980 [hep-ph].

[42] N. Arkani-Hamed, A. Delgado, and G. F. Giudice, *The Well-tempered neutralino*, Nucl. Phys. B **741** (2006) p. 108, arXiv: hep-ph/0601041 [hep-ph].

[43] Planck Collaboration, *Planck 2013 results. XVI. Cosmological parameters*, Astron. Astrophys. **571** (2014) A16, arXiv: 1303.5076 [astro-ph.CO].

[44] A. Buckley et al., *General-purpose event generators for LHC physics*, Phys. Rept. **504** (2011) p. 145, arXiv: 1101.2599 [hep-ph].

[45] J. C. Collins, D. E. Soper, and G. F. Sterman, *Factorization of Hard Processes in QCD*, Adv. Ser. Direct. High Energy Phys. **5** (1989) p. 1, arXiv: hep-ph/0409313 [hep-ph].

[46] A. Buckley et al., *LHAPDF6: parton density access in the LHC precision era*, Eur. Phys. J. C **75** (2015) p. 132, arXiv: 1412.7420 [hep-ph].

[47] S. Dulat et al., *New parton distribution functions from a global analysis of quantum chromodynamics*, Phys. Rev. D **93** (2016) p. 033006, arXiv: 1506.07443 [hep-ph].

[48] Y. L. Dokshitzer, *Calculation of the Structure Functions for Deep Inelastic Scattering and e+ e- Annihilation by Perturbation Theory in Quantum Chromodynamics.*, Sov. Phys. JETP **46** (1977) p. 641, [Zh. Eksp. Teor. Fiz.73,1216(1977)].

[49] V. N. Gribov and L. N. Lipatov, *Deep inelastic electron scattering in perturbation theory*, Phys. Lett. B **37** (1971) p. 78.

[50] G. Altarelli and G. Parisi, *Asymptotic Freedom in Parton Language*, Nucl. Phys. B **126** (1977) p. 298.

[51] T. Kinoshita, *Mass singularities of Feynman amplitudes*, J. Math. Phys. **3** (1962) p. 650.

[52] T. D. Lee and M. Nauenberg, *Degenerate Systems and Mass Singularities*, Phys. Rev. B **133** (1964) p. 1549, [,25(1964)].

[53] B. Andersson et al., *Parton Fragmentation and String Dynamics*, Phys. Rept. **97** (1983) p. 31.

[54] B. R. Webber, *A QCD Model for Jet Fragmentation Including Soft Gluon Interference*, Nucl. Phys. B **238** (1984) p. 492.

[55] ATLAS Collaboration,
Measurement of charged-particle distributions sensitive to the underlying event in $\sqrt{s}$ = 13 TeV proton-proton collisions with the ATLAS detector at the LHC, JHEP **03** (2017) p. 157, arXiv: 1701.05390 [hep-ex].

[56] J. M. Butterworth, J. R. Forshaw, and M. H. Seymour,
Multiparton interactions in photoproduction at HERA,
Zeitschrift für Physik C: Particles and Fields **72** (1996) p. 637, ISSN: 1431-5858, URL: https://doi.org/10.1007/s002880050286.

[57] S. Agostinelli et al., *GEANT4: A Simulation toolkit*,
Nucl. Instrum. Meth. A **506** (2003) p. 250.

[58] ATLAS Collaboration, *The ATLAS Simulation Infrastructure*,
Eur. Phys. J. C **70** (2010) p. 823, arXiv: 1005.4568 [physics.ins-det].

[59] G. D'Agostini, *A Multidimensional unfolding method based on Bayes' theorem*,
Nucl. Instr. Meth. A **362** (1995) p. 487.

[60] G. D'Agostini, *Improved iterative Bayesian unfolding*, (2010), arXiv: 1010.0632.

[61] G. Cowan et al., *Asymptotic formulae for likelihood-based tests of new physics*,
Eur. Phys. J. C **71** (2011) p. 1554, [Erratum: Eur. Phys. J.C73,2501(2013)],
arXiv: 1007.1727 [physics.data-an].

[62] T. Junk, *Confidence level computation for combining searches with small statistics*,
Nuclear Instruments and Methods in Physics Research Section A: Accelerators, Spectrometers, Detectors and Associated Equipment **434** (1999) p. 435.

[63] M. Baak et al., *HistFitter software framework for statistical data analysis*,
Eur. Phys. J. C **75** (2015) p. 153, arXiv: 1410.1280 [hep-ex].

[64] A. Hoecker et al., *TMVA: Toolkit for Multivariate Data Analysis*,
PoS **ACAT** (2007) p. 040, arXiv: physics/0703039.

[65] L. Evans and P. Bryant, *LHC Machine*, Journal of Instrumentation **3** (2008) S08001.

[66] ALICE Collaboration, *The ALICE experiment at the CERN LHC*,
Journal of Instrumentation **3** (2008) S08002.

[67] ATLAS Collaboration, *The ATLAS Experiment at the CERN Large Hadron Collider*,
JINST **3** (2008) S08003.

[68] CMS Collaboration, *The CMS experiment at the CERN LHC*,
Journal of Instrumentation **3** (2008) S08004.

[69] LHCb Collaboration, *The LHCb Detector at the LHC*,
Journal of Instrumentation **3** (2008) S08005.

[70] C. Lefèvre, "The CERN accelerator complex. Complexe des accélérateurs du CERN", 2008, URL: http://cds.cern.ch/record/1260465.

[71] D. Nisbet, "2016 operation: Operational efficiency and lessons learnt", 2017, URL: https://indico.cern.ch/event/580313/contributions/2359285/.

[72] S. van der Meer, *Calibration of the effective beam height in the ISR*, 1968, URL: https://cds.cern.ch/record/296752.

[73] ATLAS Collaboration, *Delivered Luminosity versus time for 2011-2017 (pp data only)*, 2017, URL: https://twiki.cern.ch/twiki/bin/view/AtlasPublic/LuminosityPublicResultsRun2.

[74] ATLAS Collaboration, *Number of Interactions per Crossing*, 2017, URL: https://twiki.cern.ch/twiki/bin/view/AtlasPublic/LuminosityPublicResultsRun2.

[75] J. Pequenao, "Computer generated image of the whole ATLAS detector", 2008, URL: http://cds.cern.ch/record/1095924.

[76] ATLAS Collaboration, *ATLAS inner detector: Technical Design Report, 1*, ATLAS-TDR-4, 1997, URL: https://cds.cern.ch/record/331063.

[77] ATLAS Collaboration, *ATLAS inner detector: Technical Design Report, 2*, ATLAS-TDR-5, 1997, URL: https://cds.cern.ch/record/331064.

[78] ATLAS Collaboration, *Performance of the ATLAS Track Reconstruction Algorithms in Dense Environments in LHC Run 2*, Eur. Phys. J. C **77** (2017) p. 673, arXiv: 1704.07983 [hep-ex].

[79] ATLAS Collaboration, *Study of the material of the ATLAS inner detector for Run 2 of the LHC*, (2017), arXiv: 1707.02826 [hep-ex].

[80] ATLAS IBL Collaboration, *Production and Integration of the ATLAS Insertable B-Layer*, JINST **13** (2018) T05008, arXiv: 1803.00844 [physics.ins-det].

[81] ATLAS Collaboration, *ATLAS liquid-argon calorimeter: Technical Design Report*, ATLAS-TDR-2, 1996, URL: https://cds.cern.ch/record/331061.

[82] ATLAS Collaboration, *ATLAS tile calorimeter: Technical Design Report*, ATLAS-TDR-3, 1996, URL: https://cds.cern.ch/record/331062.

[83] ATLAS Collaboration, *ATLAS magnet system: Technical Design Report, 1*, Technical Design Report ATLAS, CERN, 1997, URL: https://cds.cern.ch/record/338080.

[84] ATLAS Collaboration, *Luminosity determination in pp collisions at $\sqrt{s} = 8$ TeV using the ATLAS detector at the LHC*, Eur. Phys. J. C **76** (2016) p. 653, arXiv: 1608.03953 [hep-ex].

[85] ATLAS Collaboration, *Improved luminosity determination in pp collisions at $\sqrt{(s)} = 7$ TeV using the ATLAS detector at the LHC*, Eur. Phys. J. C **73** (2013) p. 2518, arXiv: 1302.4393 [hep-ex].

[86] ATLAS Collaboration, *Performance of the ATLAS Trigger System in 2015*, Eur. Phys. J. C **77** (2017) p. 317, arXiv: 1611.09661 [hep-ex].

[87] H. M. Gray and E. W. Hughes, "The Charged Particle Multiplicity at Center of Mass Energies from 900 GeV to 7 TeV measured with the ATLAS Experiment at the Large Hadron Collider", Presented on 09 Nov 2010, 2010, URL: https://cds.cern.ch/record/1309943.

[88] T. Cornelissen et al., *Concepts, Design and Implementation of the ATLAS New Tracking (NEWT)*, 2007, URL: https://cds.cern.ch/record/1020106.

[89] T. Cornelissen et al., *The new ATLAS track reconstruction (NEWT)*, Journal of Physics: Conference Series **119** (2008) p. 032014, URL: http://stacks.iop.org/1742-6596/119/i=3/a=032014.

[90] R. Frühwirth, *Application of Kalman filtering to track and vertex fitting*, Nuclear Instruments and Methods in Physics Research Section A: Accelerators, Spectrometers, Detectors and Associated Equipment **262** (1987) p. 444 , ISSN: 0168-9002, URL: http://www.sciencedirect.com/science/article/pii/0168900287908874.

[91] ATLAS Collaboration, *Early Inner Detector Tracking Performance in the 2015 data at $\sqrt{s} = 13$ TeV*, 2015, URL: https://cds.cern.ch/record/2110140.

[92] ATLAS Collaboration,
Track Reconstruction Performance of the ATLAS Inner Detector at $\sqrt{s}$ = 13 TeV, 2015,
URL: https://cds.cern.ch/record/2037683.

[93] G Piacquadio, K Prokofiev, and A Wildauer,
Primary vertex reconstruction in the ATLAS experiment at LHC,
Journal of Physics: Conference Series **119** (2008) p. 032033,
URL: http://stacks.iop.org/1742-6596/119/i=3/a=032033.

[94] ATLAS Collaboration, *Reconstruction of primary vertices at the ATLAS experiment in Run 1 proton-proton collisions at the LHC*, Eur. Phys. J. C **77** (2017) p. 332,
arXiv: 1611.10235 [physics.ins-det].

[95] ATLAS Collaboration, *Electron efficiency measurements with the ATLAS detector using the 2015 LHC proton-proton collision data*, 2016,
URL: https://cds.cern.ch/record/2157687.

[96] ATLAS Collaboration,
Electron and photon energy calibration with the ATLAS detector using LHC Run 1 data,
Eur. Phys. J. C **74** (2014) p. 3071, arXiv: 1407.5063 [hep-ex].

[97] ATLAS Collaboration, *Muon reconstruction performance of the ATLAS detector in proton-proton collision data at $\sqrt{s}$ =13 TeV*, Eur. Phys. J. C **76** (2016) p. 292,
arXiv: 1603.05598 [hep-ex].

[98] ATLAS Collaboration,
Topological cell clustering in the ATLAS calorimeters and its performance in LHC Run 1,
Eur. Phys. J. C **77** (2017) p. 490, arXiv: 1603.02934 [hep-ex].

[99] M. Cacciari, G. P. Salam, and G. Soyez, *The Anti-k(t) jet clustering algorithm*,
JHEP **0804** (2008) p. 063, arXiv: 0802.1189 [hep-ph].

[100] ATLAS Collaboration, *Jet energy scale measurements and their systematic uncertainties in proton-proton collisions at $\sqrt{s}$ = 13 TeV with the ATLAS detector*,
Phys. Rev. D **96** (2017) p. 072002, arXiv: 1703.09665 [hep-ex].

[101] ATLAS Collaboration, *Performance of pile-up mitigation techniques for jets in pp collisions at $\sqrt{s}$ = 8 TeV using the ATLAS detector*, Eur. Phys. J. C **76** (2016) p. 581,
arXiv: 1510.03823 [hep-ex].

[102] ATLAS Collaboration, *b-tagging in dense environments*, 2014,
URL: https://cds.cern.ch/record/1750682.

[103] ATLAS Collaboration,
Expected performance of the ATLAS b-tagging algorithms in Run-2, 2015,
URL: https://cds.cern.ch/record/2037697.

[104] ATLAS Collaboration,
Optimisation of the ATLAS b-tagging performance for the 2016 LHC Run, 2016,
URL: http://cds.cern.ch/record/2160731.

[105] ATLAS Collaboration, *Calibration of the performance of b-tagging for c and light-flavour jets in the 2012 ATLAS data*, 2014, URL: https://cds.cern.ch/record/1741020.

[106] ATLAS Collaboration, *b-tagging calibration plots using dileptonic $t\bar{t}$ events produced in pp collisions at $\sqrt{s}$ = 13 TeV and a combinatorial likelihood approach*, 2016, URL:
http://atlas.web.cern.ch/Atlas/GROUPS/PHYSICS/PLOTS/FTAG-2016-003/.

[107] ATLAS Collaboration, *b-tagging calibration plots in light-flavour jets from 2015+2016 data using the negative-tag method*, 2017, URL:
http://atlas.web.cern.ch/Atlas/GROUPS/PHYSICS/PLOTS/FTAG-2017-002/.

[108] ATLAS Collaboration, *Reconstruction, Energy Calibration, and Identification of Hadronically Decaying Tau Leptons in the ATLAS Experiment for Run-2 of the LHC*, 2015, URL: http://cds.cern.ch/record/2064383.

[109] ATLAS Collaboration, *Measurement of the tau lepton reconstruction and identification performance in the ATLAS experiment using pp collisions at* $\sqrt{s}$ = 13 TeV, 2017, URL: http://cds.cern.ch/record/2261772.

[110] ATLAS Collaboration, *Performance of missing transverse momentum reconstruction for the ATLAS detector in the first proton-proton collisions at at* $\sqrt{s}$*= 13 TeV*, 2015, URL: http://cds.cern.ch/record/2037904.

[111] ATLAS Collaboration, *Expected performance of missing transverse momentum reconstruction for the ATLAS detector at* $\sqrt{s}$ = 13 *TeV*, 2015, URL: https://cds.cern.ch/record/2037700.

[112] ATLAS Collaboration, *Charged-particle multiplicities in pp interactions measured with the ATLAS detector at the LHC*, New J. Phys. **13** (2011) p. 053033, arXiv: 1012.5104 [hep-ex].

[113] ATLAS Collaboration, *Charged-particle distributions in pp interactions at* $\sqrt{s}$ = 8 *TeV measured with the ATLAS detector at the LHC*, (2016), arXiv: 1603.02439 [hep-ex].

[114] CMS Collaboration, *Pseudorapidity distribution of charged hadrons in proton-proton collisions at* $\sqrt{s}$ *= 13 TeV*, Phys. Lett. B **751** (2015) p. 143, arXiv: 1507.05915 [hep-ex].

[115] CMS Collaboration, *Charged particle multiplicities in pp interactions at* $\sqrt{s}$ = 0.9*, 2.36, and 7 TeV*, JHEP **1101** (2011) p. 079, arXiv: 1011.5531 [hep-ex].

[116] CMS Collaboration, *Transverse momentum and pseudorapidity distributions of charged hadrons in pp collisions at* $\sqrt{s}$ *= 7 TeV*, Phys. Rev. Lett. **105** (2010) p. 022002, arXiv: 1005.3299 [hep-ex].

[117] CMS Collaboration, *Transverse momentum and pseudorapidity distributions of charged hadrons in pp collisions at* $\sqrt{s}$ = 0.9 *and 2.36 TeV*, JHEP **1002** (2010) p. 041, arXiv: 1002.0621 [hep-ex].

[118] ALICE Collaboration, *Charged-particle multiplicity measured in proton-proton collisions at* $\sqrt{s}$ *= 7 TeV with ALICE at LHC*, Eur. Phys. J. C **68** (2010) p. 345, arXiv: 1004.3514 [hep-ex].

[119] CDF Collaboration, *Measurement of Particle Production and Inclusive Differential Cross Sections in* $p\bar{p}$ *Collisions at* $\sqrt{s}$ *=1.96 TeV*, Phys. Rev. D **79** (2009) p. 112005, arXiv: 0904.1098 [hep-ex].

[120] UA1 Collaboration, *A study of the general characteristics of proton-antiproton collisions at* $\sqrt{s}$*= 0.2 to 0.9 TeV*, Nucl. Phys. B **335** (1990) p. 261.

[121] UA5 Collaboration, *Charged particle multiplicity distributions at 200 and 900 GeV c.m. energy*, Zeit. Phys. **43** (1989) p. 357.

[122] T. Sjöstrand, S. Mrenna, and P. Z. Skands, *A Brief Introduction to PYTHIA 8.1*, Comput. Phys. Commun. **178** (2008) p. 852, arXiv: 0710.3820 [hep-ph].

[123] S. Porteboeuf, T. Pierog, and K. Werner, *Producing Hard Processes Regarding the Complete Event: The EPOS Event Generator*, (2010), arXiv: 1006.2967 [hep-ph].

[124] R. Corke and T. Sjöstrand, *Interleaved parton showers and tuning prospects*, JHEP **1103** (2011) p. 032, arXiv: 1011.1759.

[125] H. J. Drescher et al., *Parton-based Gribov–Regge theory*, Phys. Rept. **350** (2001) p. 93, arXiv: hep-ph/0007198 [hep-ph].

[126] S. Ostapchenko, *Monte Carlo treatment of hadronic interactions in enhanced Pomeron scheme: QGSJET-II model*, Phys. Rev. D **83** (2011) p. 014018, arXiv: 1010.1869 [hep-ph].

[127] V. N. Gribov, *A Reggeon Diagram Technique*, JETP **26** (1968) p. 414.

[128] ATLAS Collaboration, *Further ATLAS tunes of Pythia 6 and Pythia 8*, ATL-PHYS-PUB-2011-014, 2011, URL: http://cds.cern.ch/record/1400677.

[129] A. D. Martin, W. J. Stirling, R. S. Thorne and G. Watt, *Parton distributions for the LHC*, Eur. Phys. J. C **63** (2009) p. 189, arXiv: 0901.0002 [hep-ph].

[130] P. Skands, S. Carrazza, and J. Rojo, *Tuning PYTHIA 8.1: the Monash 2013 Tune*, Eur. Phys. J. C **74** (2014) p. 3024, arXiv: 1404.5630 [hep-ph].

[131] NNPDF Collaboration, R. D. Ball et al., *Parton distributions with LHC data*, Nucl. Phys. B **867** (2013) p. 244, arXiv: 1207.1303 [hep-ph].

[132] B. Abelev et al., *Multi-strange baryon production in pp collisions at $\sqrt{s}$ = 7 TeV with ALICE*, Phys. Lett. B **712** (2012) p. 309, arXiv: 1204.0282 [nucl-ex].

[133] A. K. Morley and S. Pagan Griso, *Summary of Run 1 ID material description discussion*, 2013, URL: https://cds.cern.ch/record/2008451.

[134] W. Lukas, *ATLAS inner tracking detectors: Run 1 performance and developments for Run 2*, 2014, URL: https://cds.cern.ch/record/1956718.

[135] A. Buckley et al., *Rivet user manual*, Comput. Phys. Commun. **184** (2013) p. 2803, arXiv: 1003.0694 [hep-ph].

[136] P. Z. Skands, "QCD for Collider Physics", *Proceedings, High-energy Physics. Proceedings, 18th European School (ESHEP 2010): Raseborg, Finland, June 20 - July 3, 2010*, 2011, arXiv: 1104.2863 [hep-ph], URL: https://inspirehep.net/record/896215/files/arXiv:1104.2863.pdf.

[137] ALICE Collaboration, *Pseudorapidity and transverse-momentum distributions of charged particles in proton-proton collisions at $\sqrt{s}$ =13 TeV*, Physics Letters B **753** (2016) p. 319 , ISSN: 0370-2693, URL: http://www.sciencedirect.com/science/article/pii/S0370269315009788.

[138] S. Alioli et al., *A general framework for implementing NLO calculations in shower Monte Carlo programs: the POWHEG BOX*, JHEP **1006** (2010) p. 043, arXiv: 1002.2581 [hep-ph].

[139] H.-L. Lai et al., *New parton distributions for collider physics*, Phys. Rev. D **82** (2010) p. 074024, arXiv: 1007.2241 [hep-ph].

[140] T. Sjöstrand, S. Mrenna, and P. Z. Skands, *PYTHIA 6.4 Physics and Manual*, JHEP **0605** (2006) p. 026, arXiv: hep-ph/0603175.

[141] P. Z. Skands, *Tuning Monte Carlo Generators: The Perugia Tunes*, Phys. Rev. D **82** (2010) p. 074018, arXiv: 1005.3457 [hep-ph].

[142] M. Czakon, P. Fiedler, and A. Mitov, *Total Top-Quark Pair-Production Cross Section at Hadron Colliders Through $O(\alpha_S^4)$*, Phys. Rev. Lett. **110** (2013) p. 252004, arXiv: 1303.6254 [hep-ph].

[143] M. Czakon and A. Mitov,
NNLO corrections to top pair production at hadron colliders: the quark-gluon reaction,
JHEP **1301** (2013) p. 080, arXiv: 1210.6832 [hep-ph].

[144] M. Czakon and A. Mitov, *NNLO corrections to top-pair production at hadron colliders: the all-fermionic scattering channels*, JHEP **1212** (2012) p. 054,
arXiv: 1207.0236 [hep-ph].

[145] P. Bärnreuther, M. Czakon, and A. Mitov, *Percent Level Precision Physics at the Tevatron: First Genuine NNLO QCD Corrections to $q\bar{q} \to t\bar{t} + X$*,
Phys. Rev. Lett. **109** (2012) p. 132001, arXiv: 1204.5201 [hep-ph].

[146] M. Cacciari et al., *Top-pair production at hadron colliders with next-to-next-to-leading logarithmic soft-gluon resummation*, Phys. Lett. B **710** (2012) p. 612,
arXiv: 1111.5869 [hep-ph].

[147] M. Czakon and A. Mitov,
Top++: A Program for the Calculation of the Top-Pair Cross-Section at Hadron Colliders,
Comput. Phys. Commun. **185** (2014) p. 2930, arXiv: 1112.5675 [hep-ph].

[148] S. Frixione et al., *Single-top hadroproduction in association with a W boson*,
JHEP **0807** (2008) p. 029, arXiv: 0805.3067 [hep-ph].

[149] N. Kidonakis, *Two-loop soft anomalous dimensions for single top quark associated production with a W- or H-*, Phys. Rev. D **82** (2010) p. 054018,
arXiv: 1005.4451 [hep-ph].

[150] N. Kidonakis, *NNLL resummation for s-channel single top quark production*,
Phys. Rev. D **81** (2010) p. 054028, arXiv: 1001.5034 [hep-ph].

[151] N. Kidonakis, *Next-to-next-to-leading-order collinear and soft gluon corrections for t-channel single top quark production*, Phys. Rev. D **83** (2011) p. 091503,
arXiv: 1103.2792 [hep-ph].

[152] M. Bahr et al., *Herwig++ Physics and Manual*, Eur. Phys. J. C **58** (2008) p. 639,
arXiv: 0803.0883 [hep-ph].

[153] J. Bellm et al., *Herwig 7.0/Herwig++ 3.0 release note*, Eur. Phys. J. C **76** (2016) p. 196,
arXiv: 1512.01178 [hep-ph].

[154] T. Gleisberg et al., *Event generation with SHERPA 1.1*, JHEP **0902** (2009) p. 007,
arXiv: 0811.4622 [hep-ph].

[155] R. D. Ball et al., *Parton distributions for the LHC Run II*, JHEP **1504** (2015) p. 040,
arXiv: 1410.8849 [hep-ph].

[156] S. Catani et al.,
Vector boson production at hadron colliders: a fully exclusive QCD calculation at NNLO,
Phys. Rev. Lett. **103** (2009) p. 082001, arXiv: 0903.2120 [hep-ph].

[157] J. Alwall et al., *The automated computation of tree-level and next-to-leading order differential cross sections, and their matching to parton shower simulations*,
JHEP **1407** (2014) p. 079, arXiv: 1405.0301 [hep-ph].

[158] ATLAS Collaboration, *ATLAS Run 1 Pythia8 tunes*, 2014,
URL: https://cds.cern.ch/record/1966419.

[159] I. Low, *Polarized charginos (and top quarks) in scalar top quark decays*,
Phys. Rev. D **88** (2013) p. 095018, arXiv: 1304.0491 [hep-ph].

[160] P. Artoisenet et al.,
Automatic spin-entangled decays of heavy resonances in Monte Carlo simulations,
JHEP **03** (2013) p. 015, arXiv: 1212.3460 [hep-ph].

[161] D. J. Lange, *The EvtGen particle decay simulation package*, Nucl. Instrum. Meth. A **462** (2001) p. 152.

[162] C. G. Lester and D. J. Summers, *Measuring masses of semiinvisibly decaying particles pair produced at hadron colliders*, Phys. Lett. B **463** (1999) p. 99, arXiv: hep-ph/9906349 [hep-ph].

[163] ATLAS Collaboration, *Summary plots from the ATLAS Supersymmetry physics group*, 2017, URL: https://atlas.web.cern.ch/Atlas/GROUPS/PHYSICS/CombinedSummaryPlots/SUSY/.

[164] ATLAS Collaboration, *Search for top squark pair production in final states with one isolated lepton, jets, and missing transverse momentum in $\sqrt{s}$ =8 TeV pp collisions with the ATLAS detector*, JHEP **11** (2014) p. 118, arXiv: 1407.0583 [hep-ex].

[165] D. Börner, P. Mättig, and S. Pataraia, "Search for the decay of a top quark superpartner into a top quark and a neutralino using multivariate techniques at the ATLAS experiment", Presented 22 Sep 2014, 2014, URL: https://cds.cern.ch/record/1994909.

[166] ATLAS Collaboration, *Jet Calibration and Systematic Uncertainties for Jets Reconstructed in the ATLAS Detector at $\sqrt{s}$ = 13 TeV*, 2015, URL: https://cds.cern.ch/record/2037613.

[167] ATLAS Collaboration, *Jet energy scale measurements and their systematic uncertainties in proton-proton collisions at $\sqrt{s}$=13 TeV with the ATLAS detector*, (2016), arXiv: 1703.09665 [hep-ex].

[168] ATLAS Collaboration, *Calibration of b-tagging using dileptonic top pair events in a combinatorial likelihood approach with the ATLAS experiment*, 2014, URL: https://cds.cern.ch/record/1664335.

[169] ATLAS Collaboration, *Simulation of top quark production for the ATLAS experiment at $\sqrt{(s)}$ = 13 TeV*, 2016, URL: https://cds.cern.ch/record/2120417.

[170] J Butterworth et al., *Single Boson and Diboson Production Cross Sections in pp Collisions at $\sqrt{s}$ = 7 TeV*, 2010, URL: https://cds.cern.ch/record/1287902.

[171] ATLAS Collaboration, *ATLAS Run 1 searches for direct pair production of third-generation squarks at the Large Hadron Collider*, Eur. Phys. J. C **75** (2015) p. 510, [Erratum: Eur. Phys. J.C76,no.3,153(2016)], arXiv: 1506.08616 [hep-ex].

[172] ATLAS Collaboration, *Search for a scalar partner of the top quark in the jets plus missing transverse momentum final state at $\sqrt{s}$=13 TeV with the ATLAS detector*, JHEP **12** (2017) p. 085, arXiv: 1709.04183 [hep-ex].

[173] CMS Collaboration, *Search for top squark pair production in pp collisions at sqrt(s)=13 TeV using single lepton events*, (2017), arXiv: 1706.04402 [hep-ex].

The image on page 43 has been adapted from:

Sergio Cittolin, *Drawings of the elements of CMS detector, in the style of Leonardo da Vinci. Dessins des éléments de CMS détecteur, dans le style de Leonardo da Vinci*, CMS-PHO-OREACH-2009-001, URL: https://cds.cern.ch/record/1157741

Acknowledgements

I want to thank Peter Mättig for all the support during my time at the university (from my bachelor thesis to my dissertation). Especially the possibility to stay a long time at CERN was a great opportunity for me. I learned a lot of physics there but also the personal development was important. I want to thank Tobias Golling and Dan Tovey for agreeing being the second and third referee of my dissertation.

I also want to thank the full Uni Wuppertal group and especially my office-mates: thanks for sharing the time (even during annoying meetings) and also for helping out and bringing some fun into the live at work.

A huge thank to all the people at CERN I worked with, especially the stop-1-lepton and the minimum bias groups. Thanks for supporting me and helping me solve any problems, even if they were not only physics related.

I want to especially thank all the people reading over my dissertation, namely Frank, Heather, Javier, Keisuke and Sophie. I know that you are very busy and I'm glad that you found the time to help me.

The dissertation would not have been possible without the continuous support from my family and my friends. I cannot thank you enough for all the help during this time (all the cooking and shopping when I did not find the time). Besides the daily stuff and reading over the dissertation, you all helped me so much that I kept working on the dissertation and helped me through the frustrating moments.

Finally the biggest thank goes to Jan. Your support and encouragement was essential for me to continue studying physics and finalising my PhD. Thanks for all the help in good and bad times and especially when I was annoying. Beside all problems and stress, it was (and is!) a great time with you.